Regional gravity field modeling using airborne gravimetry data

Regional gravity field modeling using airborne gravimetry data

Bas Alberts

Acknowledgments

Many years ago someone mentioned to me, 'Isn't it great that gravity can be measured in such a dynamic environment as aboard an aircraft?'. This caught my attention, and since then I have been working on various projects related to airborne gravimetry, finally resulting in this PhD thesis. I can now confirm that measuring gravity aboard an aircraft is a great feat indeed. A book on this topic and the research it represents cannot be completed successfully without the support from a large number of people.

Foremost, I would like to thank Roland Klees for his supervision and guidance during my PhD. It is impossible not to get affected by his enthusiasm and both his encouragement and expertise have helped me very much in completing this work. Many thanks go to Pavel Ditmar, whose feedback, resourcefulness and creativity contributed greatly to my work. I consider myself very lucky having had two supervisors who were always willing to listen and give valuable advice. I especially appreciated the weekly meetings with both of them, which were the source of many good ideas and fruitful discussions.

Furthermore, I thank all my (former) colleagues at DEOS and especially the PSG group for their support and for providing an enjoyable working environment. Special thanks go to Jasper van Loon, with whom it has been a pleasure sharing an office throughout the past seven years. I really enjoyed the discussions which ranged from work to soccer, but also the trips to conferences in Europe and Australia. I also thank everyone involved in the GAIN project, especially Brian Gunter for his support and discussions on strapdown airborne gravimetry. I hope the GAIN project will be very successful and many test flights will be performed in the near future. I thank Relly van Wingaarden and Fiona Tuynman for the administrative support.

I am grateful to GFZ Potsdam for providing the airborne gravity data of the AGMASCO and CHICAGO campaigns. I thank Jürgen Neumayer of GFZ and Uwe Meyer of BGR for explaining the airborne gravity pre-processing sofware (AGS) to me and Guochang Xu of GFZ for his help with GPS data processing.

I appreciate the willingness of my two paranymphs Freek van Leijen and Luc Alberts to read the manuscript, which helped reduce the number of remaining errors significantly.

Thanks to all my friends for the many nice times outside working hours such as during

holidays, bar evenings, board games, cycling, soccer, snowboarding (ok, skiing as well), barbecues and all the other relaxing moments. Focusing is only possible if there are moments that you do not have to focus.

I would like to say special thanks to my mother and John, to my brother Luc, and to my father and Anjenet, for their overall support, encouragement and showing so much interest in my work.

Finally, I would like to thank Hanne for helping me with the graphics, correcting my English, but foremost for her support throughout last year. The final year of my PhD was the one I enjoyed most.

Contents

Summary

Regional gravity field modeling using airborne gravimetry data

Airborne gravimetry is the most efficient technique to provide accurate high-resolution gravity data in regions that lack good data coverage and that are difficult to access otherwise. With current airborne gravimetry systems gravity can be obtained at a spatial resolution of 2 km with an accuracy of 1-2 mGal. It is therefore an ideal technique to complement ongoing satellite gravity missions and establish the basis for many applications of regional gravity field modeling.

Gravity field determination using airborne gravity data can be divided in two major steps. The first step comprises the pre-processing of raw in-flight gravity sensor measurements to obtain gravity disturbances at flight level and the second step consists of the inversion of these observations into gravity functionals at ground level. The pre-processing of airborne gravity data consists of several independent steps such as low-pass filtering, a cross-over adjustment to minimize misfits at cross-overs of intersecting lines, and gridding. Each of these steps may introduce errors that accumulate in the course of processing, which can limit the accuracy and the resolution of the resulting gravity field.

For the inversion of the airborne gravity data at flight level into gravity functionals at the Earth's surface, several approaches can be used. Methods that have been successfully applied to airborne gravity data are integral methods and least-squares collocation, but both methods have some disadvantages. Integral methods require that the data are available in a much larger area than for which the gravity functionals are computed. A large cap size is required to reduce edge effects that result from missing data outside the target area. Least-squares collocation suffers much less from these errors and can yield accurate results, provided that the auto-covariance function gives a good representation of data in- and outside the area. However, the number of base functions equals the number of observations, which makes least-squares collocation numerically less efficient.

In this thesis a new methodology for processing airborne gravity data is proposed. It combines separate pre-processing steps with the estimation of gravity field parameters in one algorithm. Importantly, the concept of low-pass filtering is replaced by a frequency-dependent data weighting to handle the strong colored noise in the data. Frequencies at which the noise level is high get a lower weight than frequencies at which the noise level is low. Furthermore, bias parameters are estimated jointly with gravity field parameters instead of applying a cross-over adjustment. To parameterize the gravity potential a spectral representation is used, which means that the estimation results in a set of coeffi-

cients. These coefficients are used to compute gravity functionals at any location on the Earth's surface within the survey area. The advantage of the developed approach is that it requires a minimum of pre-processing and that all data can be used as obtained at the locations where they are observed.

The performance of the developed methodology is tested using simulated data and data acquired in airborne gravimetry surveys. The goal of the simulations is to test the approach in a controlled environment and to make optimal choices for the processing of real data. For the numerical studies with simulated data, the new methodology outperforms the more traditional approaches for airborne gravity data processing. For the application of the developed methodology to real data, three data sets are used. The first data set comprises airborne gravity measurements over the Skagerrak area, obtained as part of a joint project between several European institutions in 1996. This survey provided accurate airborne gravity data, and because good surface gravity data are available within the area, the data set is very useful to test the performance of the approach. The second data set was obtained by the GeoForschungsZentrum Potsdam during a survey off the coast of Chile in 2002. This data set, which has a lower accuracy than the first data set, is used to investigate the estimation of non-gravitational parameters such as biases and scaling factors. The final data set that is used consists of airborne gravity data acquired by Sander Geophysics Limited in 2003. The survey area is located near Timmins, Ontario and is much smaller than the area of the other data sets. The small size of the area and the high accuracy of the data make it a challenging data set for regional gravity modeling.

The computational experiments with real data show that the performance of the developed methodology is at the same level as traditional methods in terms of gravity field errors. However, it provides a more flexible and powerful approach to airborne gravity data processing. It requires a minimum of pre-processing and all observations are used in the determination of a regional gravity field. The frequency-dependent data weighting is successfully applied to each data set. The approach provides a statistically optimal solution and is a formalized way to handle colored noise. A noise model can be estimated from a posteriori least-squares residuals in an iterative way. The procedure is purely data-driven and, unlike low-pass filtering, does not depend on previous experience of the user. The developed methodology allows for the simultaneous estimation of non-gravitational parameters with the gravity field parameters. A testing procedure should be applied, however, to avoid insignificant estimations and high correlations. For the Chile data set a significant improvement of the estimated gravity field is obtained when bias and scale factors are estimated from the observations. The results of the computations with the real data sets show the high potential of using airborne gravimetry to obtain accurate gravity for geodetic and geophysical applications.

Samenvatting

Regionale zwaartekrachtveldmodellering met behulp van vliegtuiggravime–triegegevens

Vliegtuiggravimetrie is een van de meest efficiënte technieken om nauwkeurige zwaartekrachtgegevens in te winnen met een hoge resolutie in regio's waar een goede dekking van deze gegevens ontbreekt en die op een andere manier moeilijk te bereiken zijn. Met de huidige vliegtuiggravimetriesystemen kunnen zwaartekrachtgegevens met een ruimtelijke resolutie van $2\,\mathrm{km}$ en een nauwkeurigheid van $1\text{-}2\,\mathrm{mGal}$ worden verkregen. Het is dus een ideale techniek om huidige satellietzwaartekrachtmissies aan te vullen en de basis te vormen voor regionale zwaartekrachtveldmodellering.

Zwaartekrachtveldbepaling met behulp van vliegtuiggravimetriegegevens kan worden onderverdeeld in twee stappen. De eerste stap bestaat uit de voorbewerking van de ruwe data, gemeten met de zwaartekrachtsensoren, wat resulteert in zwaartekrachtanomalieën op vlieghoogte. De voorbewerking van vliegtuiggravimetriegegevens bestaat uit verschillende onafhankelijke stappen zoals laagdoorlaatfilteren, een cross-oververeffening om misfits op kruispunten van profielen te minimaliseren, en gridden. Elk van deze stappen kan fouten introduceren die accumuleren in de loop van de gegevensverwerking, wat de nauwkeurigheid en resolutie van het resulterende zwaartekrachtveld kan beperken.

De tweede stap bestaat uit de omrekening van de waarnemingen op vlieghoogte in zwaartekrachtwaarden op het aardoppervlak. Voor deze omrekening kunnen verschillende methoden worden gebruikt. Methoden die met succes zijn toegepast op vliegtuiggravimetriegegevens zijn integraalmethoden en kleinstekwadratencollocatie, maar beide methoden hebben een aantal nadelen. Integraalmethoden vereisen dat de gegevens in een veel groter gebied beschikbaar zijn dan waarvoor de zwaartekrachtwaarden worden berekend. Een grote blokgrootte is nodig om randeffecten als gevolg van ontbrekende gegevens buiten het doelgebied te verminderen. Kleinstekwadratencollocatie lijdt veel minder onder deze fouten en kan nauwkeurige resultaten opleveren, op voorwaarde dat de auto-covariantiefunctie een goede weergave geeft van de gegevens in en buiten het gebied. Daarentegen is het aantal basisfuncties gelijk aan het aantal waarnemingen, waardoor kleinstekwadratencollocatie numeriek minder efficiënt is.

In dit proefschrift wordt een nieuwe methode voor de verwerking van vliegtuiggravimetriegegevens voorgesteld. De methode combineert verschillende voorbewerkingsstappen met de schatting van de zwaartekrachtveldparameters in één algoritme. Daar-

naast wordt het concept van laagdoorlaatfilteren vervangen door een frequentie-afhanke-lijke weging van waarnemingen om de invloed van dominante, gekleurde ruis te verminderen. Frequenties waarop de ruis groot is krijgen een lager gewicht dan de frequenties waarop de ruis laag is. Bovendien worden systematische fouten gezamenlijk met de zwaartekrachtveldparameters geschat in plaats van een cross-oververeffening toe te passen. Om de zwaartekrachtpotentiaal te parametriseren wordt een spectrale representatie gebruikt, hetgeen betekent dat de schatting resulteert in een set van coëfficiënten. Deze worden gebruikt om zwaartekrachtwaarden te berekenen op vooraf bepaalde locaties op het aardoppervlak binnen het gebied. Het voordeel van de ontwikkelde methode is dat het een minimum van voorbewerkingsstappen vereist en dat alle gegevens kunnen worden gebruikt zoals ze verkregen zijn in de waarnemingspunten.

De prestaties van de ontwikkelde methode zijn getest met gesimuleerde data en data verkregen in vliegtuiggravimetriemeetcampagnes. Het doel van de simulaties is om de methode te testen in een gecontroleerde omgeving en om optimale keuzes te maken voor de verwerking van echte data. Voor de numerieke studies met gesimuleerde data presteert de ontwikkelde methode beter dan de meer traditionele methoden voor de verwerking van vliegtuiggravimetriegegevens. De ontwikkelde methode is tevens toegepast op drie echte datasets. De eerste dataset bestaat uit vliegtuiggravimetriemetingen in de Skagerrak, gemeten in 1996 als onderdeel van een gezamenlijk project van verscheidene Europese instellingen. Omdat deze meetcampagne nauwkeurige zwaartekrachtmetingen opleverde en omdat goede oppervlaktezwaartekrachtgegevens beschikbaar zijn in dit gebied, is deze dataset zeer geschikt voor het testen van de ontwikkelde methode. De tweede dataset is gemeten door het GeoForschungsZentrum Potsdam in 2002 tijdens een meetcampagne buiten de kust van Chili. Deze gegevens, die een lagere nauwkeurigheid hebben dan de eerste dataset, zijn gebruikt om de schatting van niet-gravitationele parameters zoals systematische fouten en schaalfactoren te testen. De laatste dataset die is gebruikt bestaat uit de vliegtuiggravimetriegegevens verworven door Sander Geophysics Limited in 2003. Het gebied waar de meetcampagne is uitgevoerd ligt nabij Timmins, Ontario en is veel kleiner dan de meetgebieden van de andere twee datasets. De kleine omvang van het gebied en de hoge nauwkeurigheid van de gegevens maken het een uitdagende dataset voor regionale zwaartekrachtveldmodellering.

Uit de berekeningen met echte data blijkt dat de prestaties van de ontwikkelde methode vergelijkbaar zijn met traditionele methoden met betrekking tot fouten in de berekende zwaartekrachtwaarden. De methode biedt echter een meer flexibele en effectieve aanpak voor de verwerking van vliegtuiggravimetriegegevens. Er is een minimum aan voorbewerking vereist en alle waarnemingen worden gebruikt voor de schatting van een regionaal zwaartekrachtveld. De frequentie-afhankelijke weging van metingen is met succes toegepast op elke dataset. Er wordt een statistisch optimale oplossing verkregen en de methode biedt een formele benadering voor het verwerken van gekleurde ruis. Een ruismodel kan worden geschat op iteratieve wijze met behulp van a posteriori residuen uit een kleinstekwadratenvereffening. De procedure wordt geheel door data gedreven en hangt in tegenstelling tot laagdoorlaatfilters niet af van de expertise van de gebruiker. De

ontwikkelde methode maakt het mogelijk om niet-gravitationele parameters gelijktijdig te schatten met zwaartekrachtveldparameters. Een testprocedure moet echter worden toegepast om niet-significante schattingen en hoge correlaties te voorkomen. Voor de Chili-dataset kan een belangrijke verbetering van het geschatte zwaartekrachtveld worden verkregen als systematische fouten en schaalfactoren worden geschat op basis van de waarnemingen. De resultaten van de berekeningen met echte data tonen het grote potentieel aan van het gebruik van vliegtuiggravimetrie voor het verkrijgen van nauwkeurige zwaartekrachtgegevens voor geodetische en geofysische toepassingen.

Nomenclature

Acronyms

ACF	Auto-Covariance Function
AGMASCO	Airborne Geoid Mapping System for Coastal Oceanography
AGS	Airborne Gravity Software
AIRGrav	Airborne Inertially Referenced Gravimeter
ARMA	AutoRegressive MovingAverage
BLUE	Best Linear Unbiased Estimate
DGPS	Differential GPS
EGM96	Earth Gravitational Model 1996
FDW	Frequency-dependent Data Weighting
FIR	Finite Impulse Response
FOT	First-Order Tikhonov
GCV	Generalized Cross-Validation
GGM	Global Gravity field Model
GPM	Geo-Potential Model
GPS	Global Positioning System
IIR	Infinite Impulse Response
INS	Inertial Navigation System
LCR	LaCoste and Romberg
LPF	Low-Pass Filter
LS	Least-Squares
LSC	Least-Squares Collocation
PCCG	Pre-Conditioned Conjugate Gradients
PSD	Power Spectral Density
RISG	Rotation Invariant Strapdown Gravimetry
RKHS	Reproducing Kernel HS
RMS	Root Mean Square
SINS	Strapdown INS
SISG	Strapdown INS Scalar Gravimetry
SMA	Sequential Multipole Analysis
UAV	Unmanned Airborne Vehicle
VCE	Variance Component Estimation
ZOT	Zero-Order Tikhonov

Notation and symbols

Scalars

a	aircraft acceleration ($\ddot{x}$)
b	bias
B	beam position
$\dot{B}$	beam velocity
c	spring tension scale factor
c_l	signal degree variance
c_i	cross-coupling coefficient
C_{lm}	harmonic series coefficient
d	drift
D_x, D_y	size of the area in the x and y direction
f	frequency
f_U	specific force in the upward direction
g	gravity
G	gravitational constant
h	height
k	k-factor
l	spatial distance
l	degree of harmonic series
m	order of harmonic series
M	mass of the Earth
N	geoid height
n	number of observations
r	radius
R	radius of the Earth
R_B	radius of the Bjerhammar sphere
S	spring tension
t	time
T	disturbing potential
$\mathrm{d}T$	time synchronization error
u	number of unknown parameters
v	aircraft velocity ($\dot{x}$)
α	regularization parameter
δ_{ij}	Kronecker delta
δg	gravity disturbance

Δg	gravity anomaly
ϵ_l	error degree variance
ϵ_{cc}	cross-coupling correction
ϵ_{Eot}	Eötvös correction
ϵ_{tilt}	tilt correction
ε_n	white noise process
γ	normal gravity
φ	latitude
λ	longitude
μ_i^n	multipole moment
ω_{ie}	Earth rotation
ψ	spherical distance
ρ_{xy}	correlation coefficient
σ	integration interval
σ^2	variance
σ_i^2	variance component
ξ_n	colored noise process

Functions

$C(\psi)$	covariance function
$K(P, Q))$	kernel function
$P_l(\cos\psi)$	Legendre polynomial
$\mathcal{H}(\psi)$	Hotine function
$\mathcal{P}(\psi)$	Poisson function

Matrices and vectors

$\mathbf{A}$	design matrix
$\mathbf{e}$	vector of residuals
$\mathbf{f}$	specific force vector
$\mathbf{g}$	gravity vector
$\boldsymbol{\delta g}$	gravity disturbance vector
$\boldsymbol{\gamma}$	normal gravity vector
$\mathbf{M}$	mask matrix
$\mathbf{N}$	normal matrix
$\mathbf{Q_x}$	variance-covariance matrix of $\mathbf{x}$
$\mathbf{R}$	regularization matrix
$\mathbf{R}_j^i$	rotation matrix
$\mathbf{x}$	vector of unknown parameters

xv

$\hat{\mathbf{x}}$	least-squares estimate
$\hat{\mathbf{x}}_\alpha$	regularized least-squares estimate
$\mathbf{y}$	vector of observations

Operators and mathematical notations

$\mathbf{A}^{-1}$	inverse of $\mathbf{A}$
$\mathbf{A}^T$	transpose of $\mathbf{A}$
$E\{\cdot\}$	expectation
$D\{\cdot\}$	dispersion
$M\{\cdot\}$	averaging
$|\cdot|$	absolute value
$\|\cdot\|$	norm
$\langle\cdot,\cdot\rangle$	inner product
∇	gradient operator
Δ	Laplace operator
$\mathcal{H}$	Hilbert space
$\square^i$	refers to inertial frame
$\square^l$	refers to local-level frame
$\square^b$	refers to body frame

Introduction

1.1 Background

Airborne gravimetry has developed into a technique that is capable of providing accurate gravity data at a high spatial resolution of 2 km or better. Airborne gravity measurements can be obtained in regions that lack good data coverage and which are difficult to access otherwise, such as mountainous areas, rain forests, and the polar regions. It is therefore an ideal technique to complement satellite-only gravity models which are limited to full wavelengths of approximately 150 km, and to provide the basis for regional gravity field modeling. Furthermore, airborne gravity can be used to validate existing data sets, such as marine surveys, and it is the only efficient tool to provide a seamless transition between terrestrial and marine gravity data.

The idea to use aircraft for gravity measurements is not new. Already in the late 1950s it was recognized that if the appropriate level of accuracy could be achieved airborne gravimetry would be vastly superior in economy and efficiency to point-wise terrestrial gravimetry. Although the first experiments gave promising results, it did not develop into a major tool for gravity field mapping for the following thirty years, due to the lack of accurate navigation data. This changed in the late eighties and early nineties when carrier phase Differential Global Positioning System (DGPS) became available. Since then many wide-area airborne gravity surveys have been performed with increasing resolution and accuracy.

In principle, gravimeters are highly sensitive accelerometers. If an accelerometer is put stationary on the surface of the Earth and it is level (i.e. the sensitive axis coincides with the direction of the gravity vector), the magnitude of gravity can be determined. For airborne gravimetry, the situation becomes more complex because the accelerometer is moving. Both aircraft and gravitational accelerations are sensed and the instrument is not easily kept level. Therefore, an airborne gravity system requires several components: an accelerometer for measuring what is called the specific force, a system to keep the accelerometer level (or for computing its attitude) and a system that measures the inertial acceleration of the aircraft. Since the improvement in GPS-technology, all airborne gravity systems nowadays depend on DGPS to determine the latter acceleration. By differencing the acceleration outputs of the two systems (accelerometer and GPS), common

accelerations are eliminated and gravity and the effect of system errors remain.

Attitude stabilization is traditionally done with damped two-axes platform systems. A gravity sensor, often a modified shipborne gravimeter, is mounted on the platform, which is mechanically stabilized using accelerometers and gyros. Over the years these systems have been improved and due to the excellent results that have been reported with these systems, they have become the established technique for airborne gravimetry. An alternative to a stabilized platform system is a strapdown inertial navigation system (INS). A comparison with the traditional system has shown that a strapdown system can reach the same level of accuracy. The advantage of a strapdown INS is that the full gravity vector can be determined and that it has the potential to increase the spatial resolution, whereas the platform systems usually have a better long-term stability.

Because airborne measurements are taken in a very dynamic environment, the noise in the data is extremely large. Typically, noise-to-signal ratios of 1000 or more are observed. To extract the signal from such noise is one of the major challenges in gravity field modeling from airborne gravity measurements. Fortunately, the largest contribution to the noise consists of high frequency noise, caused by aircraft vibration and the amplification of noise in the GPS positions when computing accelerations. The most common approach to remove these noise effects is to apply a low-pass filter. However, such a filtering deteriorates the gravity signal and limits the resolution that can be obtained.

In geodesy, one of the main applications of airborne gravity data is local geoid determination. The geoid can be defined as the equipotential surface of the gravity field that corresponds most closely to mean sea level. It is used as a reference surface for heights. Combined with the accurate low-frequency information from satellite gravity models, the geoid can be determined from airborne gravimetry data with decimeter-level accuracy or better. In the field of geophysics, airborne gravimetry is mainly used for regional geological studies and resource exploration, but the required resolution and accuracy can only just be met.

The resolution and accuracy of airborne gravimetry may be improved in two ways: by improvement of the sensors and by developing improved methodologies for the processing of airborne gravity data. The research presented in this thesis is focused on the latter.

1.2 Objectives

Traditionally, the pre-processing of airborne gravity data consists of various independent steps, such as low-pass filtering and the adjustment of data by minimizing misfits at cross-over points. The result of data pre-processing is generally a set of gravity field values along profiles at flight level, which is used as input for the inversion into gravity functionals of interest at ground level. The objective of this thesis is to develop a new technique that combines separate data processing steps with the estimation of gravity parameters in one algorithm. Importantly, a frequency-dependent data weighting to handle colored noise is applied instead of the traditional filtering. The developed methodology

is compared with established methods for airborne gravity data processing.

The following topics related to the general objective are addressed in this study:

Representation of the gravity field
A suitable representation of the disturbing potential for airborne gravity field determination must be chosen. In this thesis, a spectral representation of the gravity field is used, i.e the disturbing potential $T(\mathbf{x})$ is expressed as a linear combination of harmonic functions $\varphi(\mathbf{x})$:

$$T(\mathbf{x}) = \sum_k a_k \varphi_k(\mathbf{x}), \tag{1.1}$$

where a_k are the coefficients to be determined. The explicit expressions of the base functions $\varphi(\mathbf{x})$ can be chosen depending on the coordinate system under consideration. For a Cartesian coordinate system they are given as a product of trigonometric and exponential functions, which are fundamental solutions of Laplace's equation in Cartesian coordinates. The application of such a representation to airborne gravity data is investigated.

Regularization
For the computation of an accurate gravity field solution, regularization is needed since the goal is to determine the gravity field on or near the Earth's surface, not at aircraft altitude. Without regularization the estimation of a gravity field solution may become erroneous because data errors and unmodeled signal get amplified in the process of downward continuation. The issue of optimal regularization is an important part of this study. Various ways to define the regularization matrix and algorithms for the automatic selection of the regularization parameter will be considered.

Frequency-dependent data weighting
The standard approach to handle colored noise in airborne gravity measurements is to apply a low-pass filter. Such a filter, however, deteriorates the signal. A filter of a sufficiently large length reduces the noise in the obtained data, but the signal gets attenuated as well. As such, the results may be distorted even at frequencies where the noise is small. In this research the concept of filtering is replaced by the concept of frequency-dependent data weighting. Frequencies at which the noise is large get less weight than frequencies at which the noise is small. This approach to handle noise has already been applied successfully in gravity field modeling from satellite data, but is new in airborne gravity field determination. Essential in this procedure is the estimation of a noise model for which several strategies will be explored.

Bias and drift handling
The traditional approach of airborne gravity data processing often includes a cross-over adjustment to estimate bias and/or drift parameters. This method of adjustment of cross-over misfits has several disadvantages such as the requirement of a close coincidence of

3

measurement points at crossing lines, the low redundancy in the estimation, the necessity to interpolate data, and the possible aliasing of random errors into the solution. In this thesis an alternative method is derived, which combines the handling of bias parameters with the estimation of gravity field parameters. Its performance is compared with the traditional method of cross-over adjustment.

Comparison and validation

The developed methodology is tested and compared with traditional methods using simulated and real data sets. The goal of the simulation study is to analyze and optimize the performance of the developed methodology in a controlled environment. The results of real data processing are compared and validated using results from traditional algorithms and available surface gravity data.

1.3   Outline

The outline of this thesis is as follows. In chapter 2 the principle of airborne gravimetry is described. The various system concepts are discussed as well as the general measurement model and error model of airborne gravimetry. Furthermore, a historical overview is given and the most important applications of airborne gravity measurements are outlined.

The processing of airborne gravity data is discussed in chapter 3. The processing consists of two steps; the pre-processing, which generally results in a set of filtered observations at flight level; and the inversion of airborne gravity data into gravity functionals at the Earth's surface. For the latter several methods are summarized that have been successfully applied to airborne gravity data, such as integral methods, least-squares collocation and least-squares adjustment using radial base functions.

In chapter 4 a new methodology for the processing of airborne gravity data is proposed. The approach combines several pre-processing steps with the estimation of gravity field parameters. The base functions that are used to represent the disturbing potential are the fundamental solutions of Laplace's equation in Cartesian coordinates. Frequency-dependent data weighting to handle colored noise in the observations is introduced, as well as regularization methods to obtain a stable solution. This chapter forms the theoretical framework for the computations and analyses in the remainder of the thesis.

The developed methodology is tested and compared with traditional methods using simulated data sets. The results of these computations are presented in chapter 5. The goal of this chapter is to determine the optimal strategy for airborne gravity data processing. Tests are performed with noise free data as well as with data corrupted by white noise and colored noise.

Chapter 6 describes the application of the optimal strategy to real airborne gravimetric survey data. Several data sets are used. The first data set consists of airborne gravity measurements acquired in 1996 during a survey over the Skagerrak area. For this region good ground truth data is available, which is used to derive a noise model and to validate the results. The second data set was obtained during a campaign off the coast of Chile in

2002. The last data set that is used in this chapter is a geophysical data set from a survey flown over a relatively small area in Ontario, Canada in 2003.

Finally, the conclusions and recommendations are given in chapter 7.

5

Airborne gravimetry

2

This chapter provides an introduction to airborne gravimetry. First, a historical overview is given, starting from the first ideas in the late 1950s and concluding with the latest developments in this field. The general principle is discussed in section 2.2, focusing on sensor orientation and separation of kinematic and gravitational accelerations. Furthermore, an overview of techniques that are used to measure gravity from aircraft is given. The mathematical concept of both the measurement and the error model is explained in section 2.3.1, resulting in the fundamental equations for airborne gravity pre-processing and the most important error sources that affect airborne gravity measurements. The chapter concludes with a discussion of geodetic and geophysical applications of airborne gravimetry and opportunities for future developments.

2.1 Historical overview

Already in the 1950s, both geophysicists and geodesists were looking for solutions to measure gravity from the air. The first reported test of airborne gravity measurements is described in Lundberg (1957), where a system based on the principle of gradiometry was used. However, Lundberg's test was received with general skepticism in the exploration industry (Hammer, 1983). Following the successful use of a gravity meter aboard submarines and ships in the 1950s, the Air Force Cambridge Research Center initiated a program to develop an airborne gravity meter system. The first test was performed in 1958 by the U.S. Air Force, using a LaCoste and Romberg gimbal-supported sea gravimeter (S5), with navigation data provided by a Doppler system on the aircraft and a camera tracking range on the ground (Thompson and LaCoste, 1960). Shortly after this test a second test was done by Fairchild Aerial Surveys (Nettleton et al., 1960). The gravimeter used was again a LaCoste and Romberg instrument, but the aircraft was equipped with a mapping camera for positioning and a radar altimeter and hypsometer to determine the altitude.

The main problems for airborne gravimetry at the time were the navigation of the aircraft, including velocity, elevation and space positioning, the Eötvös effect, in-flight accelerations of the aircraft, and the lack of a gravimeter able to work in a dynamic environment (Thompson and LaCoste, 1960). However, it appeared that a relatively

low accuracy of about 10 mGal could be obtained using existing navigation systems, complemented by accurate ground control techniques, such as optical and radar tracking ranges.Furthermore, experience with large aircraft at high altitudes indicated that smooth flight conditions could be obtained, thus reducing large accelerations. The Eötvös effect, which is directly related to the aircraft velocity, was considered to be a major problem for gravity measurements in an aircraft. However, with proper flight programming, accurate Eötvös corrections could be made. As mentioned above, the gravimeters used in the first tests were modified sea gravimeters using a gimbal suspension to handle horizontal accelerations. This system had been developed and tested by LaCoste and Romberg for use at sea. Later, these systems were replaced by stabilized platform systems (cf. figure 2.1), which performed much better (LaCoste, 1967).
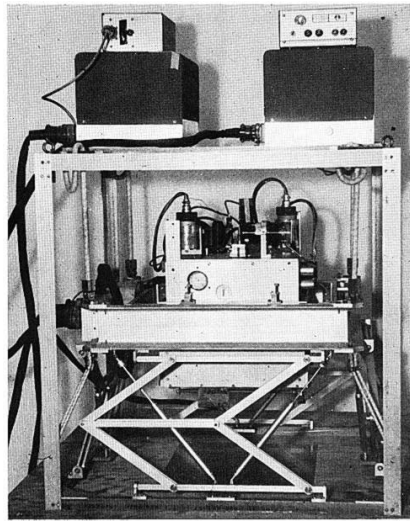
Figure 2.1: Stabilized platform gravity meter (LaCoste et al., 1967).

The tests in the beginning of the 1960s were performed with gravity meters installed in fixed-wing aircraft. The first successful measurement of gravity from a helicopter was performed in 1965 by the U.S. Naval Oceanographic Office, using a gimbal-suspended LaCoste and Romberg Sea Gravimeter (Gumert and Cobb, 1970; Gumert, 1998). A more thorough test followed in 1966, providing gravity data with accuracies of about 3 mGal, leading to the development of a complete helicopter gravity measuring system (HGMS), described in Gumert and Cobb (1970). The instrumentation consisted of a LaCoste and Romberg stable-platform gravity meter, a laser altimeter, a camera and a HIRAN navigation system. The advantages of a helicopter over fixed-wing aircraft are the better terrain-following capability, the increased spatial resolution resulting from flying at lower altitude and lower speed and the fact that a helicopter is less affected by turbulent condi-

tions than most other types of aircraft (Lee et al., 2006). Its only disadvantage may be a somewhat smaller range.

Despite improvements in scalar gravity system design, and the development of high resolution radar altimeters for vertical acceleration determination in the eighties (see e.g. Brozena (1984)), airborne gravimetry did not become fully operational until the introduction of GPS. Especially the use of carrier phase measurements and Differential GPS (DGPS) opened new ways to resolve navigational problems (see e.g. Brozena et al. (1989), Schwarz et al. (1989), Kleusberg et al. (1990)). The impact of the new positioning technology led to two important developments in airborne gravimetry (Schwarz and Li, 1997). The first one was the perfection of existing scalar gravimeter systems, which could be used, on the one hand, for geophysical exploration and, on the other hand, for large regional surveys as required by geodesy. The second development was the combination of GPS with inertial measuring units (IMU) for sensor stabilization and gravity vector determination.

One of the first large-scale airborne gravity surveys was the campaign over Greenland in 1991 and 1992, performed by the U.S. Naval Research Laboratory (NRL) in cooperation with the Danish National Survey and Cadastre (KMS) (currently part of the TU Denmark (DTU Space)), which proved the suitability of airborne gravimetry for gravity field mapping (see Brozena (1992), Brozena and Peters (1994), Forsberg and Kenyon (1994)). Other examples of wide-area surveys are the gravity survey of Switzerland, a joint project between the Swiss Federal Institute of Technology and LaCoste and Romberg Gravity Meters Inc. in 1992 (Klingelé et al., 1995), the AGMASCO project over the Skagerrak (1996) and the Azores (1997) conducted by a joint program of various European institutes (Forsberg et al. (1997), Hehl et al. (1997)) and the gravity surveys over the West Antarctic ice sheet (1991-1997) flown by the Lamont-Doherty Earth Observatory in collaboration with the Institute for Geophysics of the University of Texas (Bell et al., 1999). Recent major projects are the nationwide geoid and regional surveys of Malaysia (2002-2003), Mongolia (2004-2005) and Ethiopia (2006-2007) performed by DNSC (Olesen and Forsberg, 2007b), and the survey of Taiwan (Hwang et al., 2007). The reported accuracies of these campaigns were 1.5-2 mGal at 5-6 km spatial resolution.

In the nineties, several alternative system concepts were developed, based on the combination of inertial technology and DGPS. The Inertial Technology Center (ITC) in Moscow implemented and tested an inertially stabilized platform system in cooperation with the University of Calgary and Canagrav Research Ltd. in Calgary. For details of this test see Salychev et al. (1994). A similar system, called AIRGrav, was developed by Sander Geophysics Ltd. (Ferguson and Hammada, 2001). Both systems have been demonstrated to yield medium and high resolution estimates of the gravity field with an accuracy of 0.5-1.5 mGal (Bruton, 2000).

The use of a strapdown Inertial Navigation System (SINS) for airborne gravimetry was pioneered at the University of Calgary (see e.g. Schwarz et al. (1991)), where development and testing continued until the beginning of this decade. The advantage of

such a system is its smaller size and relatively low costs. Results of the first airborne test in 1995, using a Honeywell LASEREF III inertial system, showed that relative gravity can be obtained with an accuracy of 2-3 mGal at a half-wavelength resolution of 5 km (Wei and Schwarz, 1998). A side-by-side comparison of a strapdown INS system with a LaCoste and Romberg stable platform gravimeter, described by Glennie and Schwarz (1999), demonstrated that both systems performed equally well in terms of RMS errors, but the LCR system showed a better long-term stability. Later, Bruton et al. (2002) showed that with the same SINS system, the strapdown approach can yield accuracies of 1.5 mGal at a half-wavelength of 2 km and 2.5 mGal at a half-wavelength of 1.4 km, demonstrating the potential of this approach for high-resolution applications. The SINS approach also allows for the determination of the gravity vector, but in that case the system requirements are more stringent, as discussed by Schwarz et al. (1991) and Jekeli (1994). Nevertheless, Jekeli and Kwon (1999) obtained the full gravity vector at an accuracy level of 7-8 mGal for the horizontal component and 3 mGal for the vertical component, using the same data as Wei and Schwarz (1998).

2.2   The principle of airborne gravimetry

In principle, gravimeters are highly sensitive accelerometers. If an accelerometer is put stationary on the Earth's surface and it is level (i.e. the sensitive axis coincides with the direction of the gravity vector), the magnitude of gravity can be determined directly. However, the situation becomes much more complex when the accelerometer is moving, since an accelerometer cannot distinguish between kinematic and gravitational accelerations and because the instrument is not easily kept level. Thus, in airborne gravimetry, the solution of the following two problems is fundamental (Schwarz and Li, 1997):

1. Sensor orientation or stabilization under aircraft dynamics.

2. Separation of gravitational and non-gravitational acceleration.

There are a number of possible ways to solve the first problem. The use of a damped two-axes platform system, such as the LaCoste & Romberg Air-Sea gravimeter, is the most established method for attitude stabilization. The platform is mechanically stabilized by using gyros and accelerometers in a feedback loop. The damping period of the platform is typically chosen at 4 minutes for airborne applications. This means that horizontal accelerations with a longer period, as in long turns, are regarded by the system as changes of the vertical. In theory, the effect of horizontal accelerations is completely eliminated by using a Schuler-tuned platform with a damping period of 84.4 minutes (Schuler period). However, such a long period requires extremely accurate gyros and accelerometers that have virtually no errors or drifts within this time range (Meyer et al., 2003). Example of systems that use a Schuler-tuned three-axes inertial platform are the GT-1A gravimeter, developed by Joint Stock Company Gravimetric Technologies in the Russian Federation and made available for commercial use by Canadian Micro Gravity Pty Ltd (Gabell

et al., 2004) and the Airborne Inertially Referenced Gravimeter (AIRGrav) developed by Sander Geophysics Limited (Sander et al., 2004). An alternative to a stabilized platform system is a Strapdown Inertial Navigation System (SINS) that consists of three orthogonal accelerometers and a set of three gyroscopes. In that case the mechanical stabilization is replaced by computing the rotation matrix between the body frame and the local-level frame. The approaches for attitude stabilization are schematically shown in figure 2.2.

The separation of gravitational and inertial acceleration is possible by computing the difference between the specific force measured by an accelerometer and the output of a system that provides the inertial acceleration. This process is also known as motion compensation. Since the introduction of GPS, all airborne systems use carrier phase DGPS positioning to determine aircraft motion. However, a laser-altimeter or radar-altimeter can also be used if only the vertical aircraft acceleration is required.

Which system concept should be used depends on the quantity to be measured and on the application the measurements are used for. The following classification is generally used for airborne gravimetry (e.g. Schwarz and Li (1997), Wei (1999)):

- Scalar gravimetry

- Vector gravimetry

- Gravity gradiometry

In scalar gravimetry the magnitude of the gravity (disturbance) vector is determined. This can be implemented using a stable platform system or by using a strapdown system. The latter case is often referred to as Strapdown INS Scalar Gravimetry (SISG), in which case only the vertical component of the gravity vector is of interest. An alternative concept is to use a triad of three orthogonal accelerometers to obtain the magnitude of gravity from the difference between the specific force vector and the aircraft acceleration vector. Because the absolute orientation of the accelerometers with respect to the local vertical is not needed in this case, this approach is called Rotation Invariant Scalar Gravimetry (RISG). This approach was first explored by Czompo (1994) and later compared with SISG by Wei and Schwarz (1997).

In vector gravimetry all three components of the gravity vector are determined. This can only be done with systems that make use of inertial technology, i.e. SINS and inertial platform systems. The horizontal components are generally of much poorer accuracy than the vertical component due to attitude errors caused by gyro drifts (Bruton, 2000). Good results for the estimation of the full gravity vector have been obtained by Jekeli and Kwon (1999).

In airborne gravity gradiometry the second derivatives of the gravity potential are observed. In the last decade, several operational gradiometer systems capable of rapidly measuring all components of the gravity gradient tensor have been developed. Examples are the FALCON gravity gradiometer of BHP Billiton (Lee, 2001) and the Air-FTG gradiometer system operated by Bell Geospace (Murphy, 2004). The standard gradiometer concept is based on a design that uses opposing pairs of accelerometers on a rotating
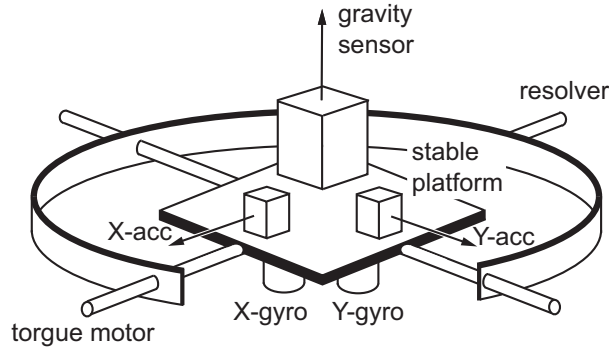
(a) Damped two-axes platform system.
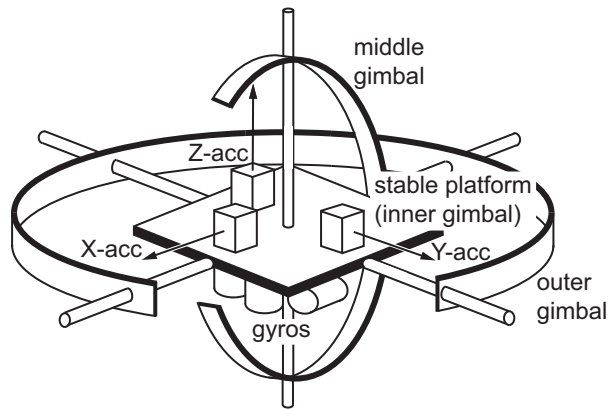
(b) Schuler-tuned platform system.
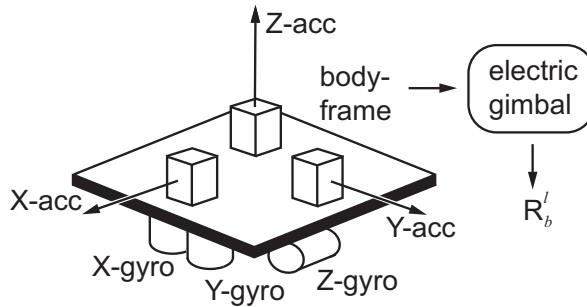
(c) Strapdown INS.

Figure 2.2: Attitude stabilization and sensor orientation for airborne gravimetry (after Schwarz and Li (1997)).

disk. The input axes of the accelerometer pair point in opposite directions so that the common mode acceleration is canceled out when their signals are summed. As a result, gradiometer systems are much less sensitive to GPS positioning errors and results can be obtained with higher accuracy and resolution compared to scalar and vector gravimetry. This technique is therefore particularly interesting for the mining and oil industry. For an overview of the characteristics of gravity gradiometry, see Bell et al. (1997).

2.3 Mathematical models

2.3.1 Measurement model

The principle of airborne gravimetry is based on Newton's second law of motion. Rearranged with respect to gravity it is

$$\mathbf{g}^i = \ddot{\mathbf{x}}^i - \mathbf{f}^i, \tag{2.1}$$

where $\mathbf{g}^i$ is gravity, $\ddot{\mathbf{x}}^i$ is the inertial acceleration and $\mathbf{f}^i$ is the specific force measured by an inertial system, where the superscript i refers to the inertial frame. Usually, airborne gravimetry measurements are expressed in the local-level frame (l), which is a local Cartesian reference frame with the origin on the ellipsoid. The z-axis is aligned with the local ellipsoidal normal, the x-axis points towards the ellipsoidal east and the y-axis towards the ellipsoidal north, thus forming a North-East-Up frame. Equation (2.1) written in the local-level frame is

$$\mathbf{g}^l = \ddot{\mathbf{x}}^l - \mathbf{f}^l + (2\mathbf{\Omega}_{ie}^l + \mathbf{\Omega}_{el}^l)\dot{\mathbf{x}}^l, \tag{2.2}$$

where $\ddot{\mathbf{x}}^l$ is the aircraft acceleration, $\mathbf{f}^l$ is the specific force, $\dot{\mathbf{x}}^l$ is the aircraft velocity, and $\mathbf{\Omega}_{ie}^l$ and $\mathbf{\Omega}_{el}^l$ are skew-symmetric matrices due to the Earth rotation ω_{ie} and aircraft rate, respectively:

$$\mathbf{\Omega}_{ie}^l = \begin{bmatrix} 0 & -\omega_{ie}\sin\varphi & \omega_{ie}\cos\varphi \\ \omega_{ie}\sin\varphi & 0 & 0 \\ \omega_{ie}\cos\varphi & 0 & 0 \end{bmatrix}$$

and

$$\mathbf{\Omega}_{el}^l = \begin{bmatrix} 0 & -\dot{\lambda}\sin\varphi & \dot{\lambda}\cos\varphi \\ \dot{\lambda}\sin\varphi & 0 & \dot{\varphi} \\ \dot{\lambda}\cos\varphi & -\dot{\varphi} & 0 \end{bmatrix},$$

where $\dot{\lambda}$ and $\dot{\varphi}$ denote longitude and latitude rate. The gravity vector can be written as the sum of the normal gravity vector $\boldsymbol{\gamma}$ and the gravity disturbance vector $\boldsymbol{\delta}\mathbf{g}$, e.g.

$$\mathbf{g} = \boldsymbol{\gamma} + \boldsymbol{\delta}\mathbf{g}.$$

The gravity disturbance is the observable that is generally used in airborne gravimetry. The measurement model for airborne gravimetry is given as

$$\boldsymbol{\delta}\mathbf{g}^l = \ddot{\mathbf{x}}^l - \mathbf{f}^l + (2\mathbf{\Omega}_{ie}^l + \mathbf{\Omega}_{el}^l)\dot{\mathbf{x}}^l - \boldsymbol{\gamma}^l. \tag{2.3}$$

In case of strapdown airborne gravimetry, accelerometer and gyro measurements are obtained in the body frame (b). The body frame generally refers to the vehicle to be navigated. The x-axis is defined along the forward direction of the aircraft (longitudinal axis) the y-axis towards the right (lateral axis) and the z-axis points downwards (through-the-floor). For strapdown gravimetry Eq. (2.3) becomes

$$\boldsymbol{\delta}\mathbf{g}^l = \ddot{\mathbf{x}}^l - \mathbf{R}_b^l \mathbf{f}^b + (2\boldsymbol{\Omega}_{ie}^l + \boldsymbol{\Omega}_{el}^l)\dot{\mathbf{x}}^l - \boldsymbol{\gamma}^l, \tag{2.4}$$

where $\mathbf{R}_b^l$ is the transformation matrix which rotates the accelerometer measurements $\mathbf{f}^b$ to the local-level frame. It can be obtained by integrating the measured angular velocities $\boldsymbol{\omega}_{ib}^b$ between the body frame and the inertial frame.

For scalar gravimetry only the third component of Eq. (2.4) is of interest. When written explicitly it is

$$\delta g_U = \ddot{x}_U - f_U - \left(\frac{v_E}{R_1 + h} + 2\omega_{ie}\cos\varphi\right)v_E - \frac{v_N^2}{R_2 + h} - \gamma_U, \tag{2.5}$$

where subscripts E, N, U stand for East, North, Up in a local-level ellipsoidal frame, and R_1 and R_2 are the prime vertical and meridian radii of curvature. The sum of the third and fourth terms is also called the Eötvös correction.

In principle, Eq. (2.5) is also valid for stable-platform gravimetry. However, attitude control and the measurement of the specific force is different. As a result, two additional corrections need to be applied: the cross-coupling correction and the tilt correction. The cross-coupling correction is applied to account for horizontal accelerations experienced by the platform, that cross-couple into the vertical acceleration output whenever the beam is not in the null position. The formula for this correction is given in Valliant (1992) as (see also Eq. (A.4) in appendix A)

$$\epsilon_{cc} = c_1\dot{B}^2 + c_2(f_y B) + c_3(f_x \dot{B}) + c_4(f_y \dot{B}) + c_5(f_x^2 \dot{B}), \tag{2.6}$$

where $c_1, c_2, \ldots, c_5$ are statistically or empirically determined coefficients, $\dot{B}$ is the beam velocity, B is the beam position, and f_x and f_y are the horizontal accelerometer measurements. The tilt correction can be estimated from the horizontal accelerometer output and DGPS-determined horizontal accelerations as (Olesen et al., 1997)

$$\epsilon_{tilt} = \frac{f_x^2 + f_y^2 - a_E^2 - a_N^2}{2g}, \tag{2.7}$$

where a_E and a_N are the kinematic aircraft accelerations in the east and north directions, and g is the magnitude of gravity.

2.3.2   Error model

The general error model of airborne gravimetry can be obtained by linearizing Eq. (2.3) for a stable platform system or Eq. (2.4) for strapdown INS, as shown by Schwarz and

Wei (1995). For strapdown inertial vector gravimetry it is:

$$d\boldsymbol{\delta}\mathbf{g}^l = \mathbf{F}^l\boldsymbol{\epsilon}^l - \mathbf{R}_b^l d\mathbf{f}^b + d\ddot{\mathbf{x}}^l + (2\boldsymbol{\Omega}_{ie}^l + \boldsymbol{\Omega}_{el}^l)d\dot{\mathbf{x}}^l - \mathbf{V}^l(2d\boldsymbol{\omega}_{ie}^l + d\boldsymbol{\omega}_{el}^l)$$
$$- d\boldsymbol{\gamma}^l + (\dot{\mathbf{R}}_b^l\mathbf{f}^b + \mathbf{R}_b^l\dot{\mathbf{f}}^b)dT, \tag{2.8}$$

where $\boldsymbol{\epsilon}^l$ denotes the attitude errors due to initial misalignment and gyro measurement noise, $d\mathbf{f}^b$ represents accelerometer noise, $d\ddot{\mathbf{x}}^l$ and $d\dot{\mathbf{x}}^l$ are aircraft acceleration and velocity errors, $d\boldsymbol{\omega}_{ie}^l$ and $d\boldsymbol{\omega}_{el}^l$ are errors in angular velocity, $d\boldsymbol{\gamma}^l$ denotes the errors in the computation of normal gravity, and $\mathbf{F}^l$ and $\mathbf{V}^l$ are skew-symmetric matrices containing the components of the specific force vector and the velocity vector, i.e.

$$\mathbf{F}^l = \begin{bmatrix} 0 & -f_U & f_N \\ f_U & 0 & -f_E \\ -f_N & f_E & 0 \end{bmatrix}, \quad \mathbf{V}^l = \begin{bmatrix} 0 & -v_U & v_N \\ v_U & 0 & -v_E \\ -v_N & v_E & 0 \end{bmatrix}.$$

The term dT is added to account for the time synchronization error between the two measurement systems, GPS and INS. Assuming that positions and velocities can be obtained using GPS with standard deviations of $\sigma_p = 20\text{cm}$ and $\sigma_v = 5\text{cm/s}$, respectively, the fourth, fifth and sixth terms in Eq. (2.8) can be safely neglected since their contribution to the total error budget is less than $0.5\,\text{mGal}$ (Schwarz and Wei, 1995). Then, the most significant errors affecting the gravity disturbance vector are given by

$$d\boldsymbol{\delta}\mathbf{g}^l = \mathbf{F}^l\boldsymbol{\epsilon}^l - \mathbf{R}_b^l d\mathbf{f}^b + d\ddot{\mathbf{x}}^l + (\dot{\mathbf{R}}_b^l\mathbf{f}^b + \mathbf{R}_b^l\dot{\mathbf{f}}^b)dT. \tag{2.9}$$

For scalar gravimetry using INS the error model reads (Glennie et al., 2000)

$$d\delta g = f_E\epsilon_N - f_N\epsilon_E - \mathbf{A}\mathbf{f}^b - d\ddot{x}_U + (\dot{\mathbf{A}}\mathbf{f}^b + \mathbf{A}\dot{\mathbf{f}}^b)dT, \tag{2.10}$$

where $\mathbf{A}$ and $\dot{\mathbf{A}}$ are row vectors of the form

$$\mathbf{A} = \begin{bmatrix} -\cos\theta\sin\phi & \sin\theta & \cos\theta\cos\phi \end{bmatrix},$$
$$\dot{\mathbf{A}} = \begin{bmatrix} \dot{\theta}\sin\theta\sin\phi - \dot{\phi}\cos\theta\cos\phi & \dot{\theta}\cos\theta & -\dot{\theta}\sin\theta\cos\phi - \dot{\phi}\cos\theta\sin\phi \end{bmatrix}, \tag{2.11}$$

with ϕ and θ the roll and pitch angles of the transformation from the body frame to the local-level frame. Because the roll angle and the quantities $\dot{\theta}$ and $\dot{\phi}$ are generally small values, Eq. (2.10) can be simplified as

$$d\delta g = f_E\epsilon_N - f_N\epsilon_E - df_U + d\ddot{x}_U + \dot{f}_U dT. \tag{2.12}$$

A good understanding of the errors affecting airborne gravimetry is of great importance for system design and filtering. The error characteristics are briefly discussed and compared below for the various approaches to airborne scalar gravimetry.

In order to compare the error sources for stable platform gravimetry and SINS, Glennie et al. (2000) performed a first-order error linearization of Eqs. (2.5), (2.6) and (2.7), resulting in

$$
\begin{aligned}
\mathrm{d}\delta g = {}& \mathrm{d}f_U - \mathrm{d}\ddot{x}_U + \frac{f_x}{g}\mathrm{d}f_x + \frac{f_y}{g}\mathrm{d}f_y - \frac{a_E}{g}\mathrm{d}a_E - \frac{a_N}{g}\mathrm{d}a_N \\
& + (c_3\dot{B} + 2c_5 f_x\dot{B})\mathrm{d}f_x + (c_2 B + c_4\dot{B})\mathrm{d}f_y \\
& + (2c_1\dot{B} + c_3 f_x + c_4 f_y + c_5 f_x^2)\mathrm{d}\dot{B} + (c_2 f_y)\mathrm{d}B \\
& - \dot{B}^2\mathrm{d}c_1 + f_y B\mathrm{d}c_2 + f_x\dot{B}\mathrm{d}c_3 + f_y\dot{B}\mathrm{d}c_4 + f_x^2\dot{B}\mathrm{d}c_5,
\end{aligned}
\tag{2.13}
$$

where $\mathrm{d}c_1, \mathrm{d}c_2, \ldots, \mathrm{d}c_5$ are errors in the cross-coupling coefficients, $\mathrm{d}\dot{B}$ is the beam velocity error, and $\mathrm{d}B$ is the beam position error. From Eq. (2.12) and Eq. (2.13) it is clear that for both cases DGPS vertical acceleration errors $\ddot{x}_U$ have an identical effect on the gravity estimates. The remaining errors in the first line of Eq. (2.13) are similar to those for the RISG approach to airborne gravimetry, of which the error model is given as (Wei and Schwarz, 1998)

$$
\mathrm{d}\delta g = \frac{f_x}{f_U}\mathrm{d}f_x + \frac{f_y}{f_U}\mathrm{d}f_y + \frac{f_z}{f_U}\mathrm{d}f_z - \frac{a_E}{f_U}\mathrm{d}a_E - \frac{a_N}{f_U}\mathrm{d}a_N - \mathrm{d}a_U + \dot{f}_U\mathrm{d}T.
\tag{2.14}
$$

Because the RISG approach does not require attitude determination for the airborne gravity sensor, it can be applied to all airborne gravity systems with an orthogonal accelerometer triad.

When applied to a strapdown INS system, the RISG approach is shown to have a similar error behavior as the SINS approach (SISG) to airborne scalar gravimetry determination. Glennie et al. (2000) therefore state that the first line of Eq. (2.13) will give similar error characteristics as the first four terms of Eq. (2.12). However, the error in the specific force $\mathrm{d}f_U$ or $\mathrm{d}f_x$ depends on the system used. In case of stable platform systems it is derived from beam velocities and spring tension measurements, whereas for strapdown INS systems it is the z-component of the accelerometer output, which may be affected by an unknown bias. Furthermore, the horizontal accelerometers of the platform system are of lower quality than the vertical gravimeter, and therefore the horizontal acceleration errors are a significant error source for stable platform systems such as the LCR gravimeter system. It should be noted that a time synchronization error term has not been included in Eq. (2.13), but this term is identical to the one in the SINS approach.

2.4 Applications and opportunities

Airborne gravity measurements are used for a number of applications in geodesy and geophysics. Although airborne campaigns may serve more than one goal, the survey design largely depends on the application under consideration. The design of a campaign comprises the type of observation and accuracy that is required, the resolution, area coverage, flight path, and choice of platform. Several applications are discussed below. For a

more detailed discussion of airborne gravity applications and related research see Bruton (2000).

Geodetic applications

In geodesy, one of the main applications of airborne gravimetry is local geoid determination. The geoid, defined as the equipotential surface of the gravity field at mean sea level, is used as a reference surface for heights. Geoid determination from airborne gravity data includes the representation of airborne data on a level surface through downward continuation and using these data in combination with other sources of gravity to estimate the geoid. When combined with accurate low-frequency information from satellite gravity models, the geoid can be determined from airborne gravimetry with an accuracy of 2-5 cm at a spatial resolution of 5-10 km (Bruton, 2000). Examples of large-scale campaigns where airborne gravimetry has successfully been applied are the campaigns in Greenland by the Naval Research Laboratory (NRL) (Brozena et al., 1997) and the recent airborne gravity survey over Taiwan by a cooperation of Taiwanese universities and the Danish National Space Center in 2004 and 2005 (Hwang et al., 2007). Another application is the filling of the polar gaps and other remote areas that lack accurate gravity data, for the compilation of high-resolution Earth gravity models, such as the EIGEN-GL04c model (Förste et al., 2008) and the recently published EGM2008 model (Pavlis et al., 2008).

Geodetic airborne campaigns are characterized by a relatively large flight track spacing and relatively high flight velocities to cover large areas, as well as a high flight altitude to minimize effects of turbulence. The instrumentation used in geodetic surveys consists mostly of traditional scalar gravimetry systems such as the LCR spring type air-sea gravimeter combined with DGPS.

Geophysical applications

In the field of geophysics, airborne gravimetry is mainly used for regional geological studies and resource exploration. The requirements for geophysical applications are listed in table 2.1. With the current accuracy and resolution of airborne gravimetry at the level of 1-2 mGal at 3-5 km, scalar airborne gravimetry meets the requirements for regional geological studies, but its use for exploration of mineral deposits is limited (see also Bruton (2000)). This is also shown in figure 2.3, from which it is clear that even a ten-fold improvement in terms of GPS acceleration noise would not be sufficient to recover most of the orebodies (for more details see Van Kann (2004)). In comparison with scalar or vector gravimetry, the application of airborne gravity gradiometry is much more promising because gravity gradiometry anomalies reflect the edges and shapes of sources rather than just mass distributions. Furthermore, it is less sensitive to GPS positioning errors as already mentioned in section 2.2. Figure 2.4 demonstrates that the noise of a gradiometer system should be about 1 Eötvös RMS for wavelengths of 50-100 m. Obtaining such an accuracy and resolution is a challenging problem, but laboratory tests of

Table 2.1: Required gravity accuracy and resolution for solid Earth science (NRC, 1995).

Feature	Accuracy (mGal)	Resolution (km)
Plate boundaries and deformation:		
Large-scale flexure	5	50
Rifts	3	10
Diffuse extension	2	5
Mountains	3	5
Sub-ice topography	2	10
Volcanology:		
Volcano morphology	1	10
Volcano dynamics	0.5	5
Mineral exploration:		
Sedimentary basins	1	3
Salt domes	0.5	1
Mineral prospects	0.1-2.0	1-10

several instruments under development have shown that this may be feasible in the near future (Van Kann, 2004).

Geophysical surveys for mineral exploration are generally flown at speeds as low as possible within small areas, and the track spacing is, as a result, usually much denser than for regional surveys. Air-FTG surveys are for instance typically flown with line spacings from 50 to 2000 m at a terrain clearance as low as 80 m for small survey targets, using a fixed-wing aircraft (Murphy, 2004).

Opportunities

The application of airborne gravimetry for acquiring gravity information routinely is limited due to the availability and costs of the instrumentation (aircraft and gravimeter) and manpower, which add up to the overall costs of airborne gravity campaigns. A large-scale airborne survey for gravity field determination such as the campaign in Taiwan can take more than 200 flight hours to complete. Even though this is still much more efficient than terrestrial measurement techniques, there are several opportunities to reduce the time and costs of airborne gravity surveys.

First of all, there is a renewed interest in the use of strapdown INS for gravity field mapping. These systems are much cheaper than stable platform systems, and with in-
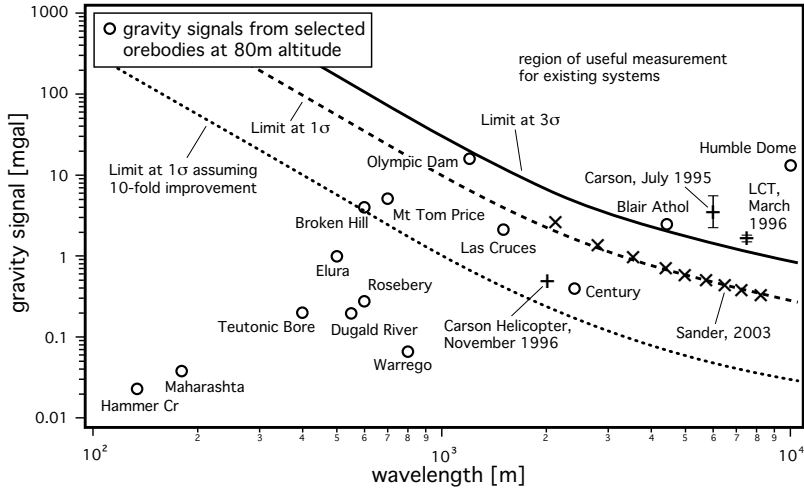
Figure 2.3: Plot of vertical gravity response against wavelength showing signals for selected orebodies. The noise levels for various airborne systems are shown (i.e., Carson helicopter system in November 1996, Carson fixed-wing system in July 1995, LCT fixed-wing system in March 1996, Sander Geophysics fixed-wing system in 2003). Also shown are lines corresponding to GPS-related acceleration noise ('Limit at 1σ', 'Limit at 3σ', and 'Limit at 1σ assuming 10-fold improvement') (modified from Van Kann, 2004).
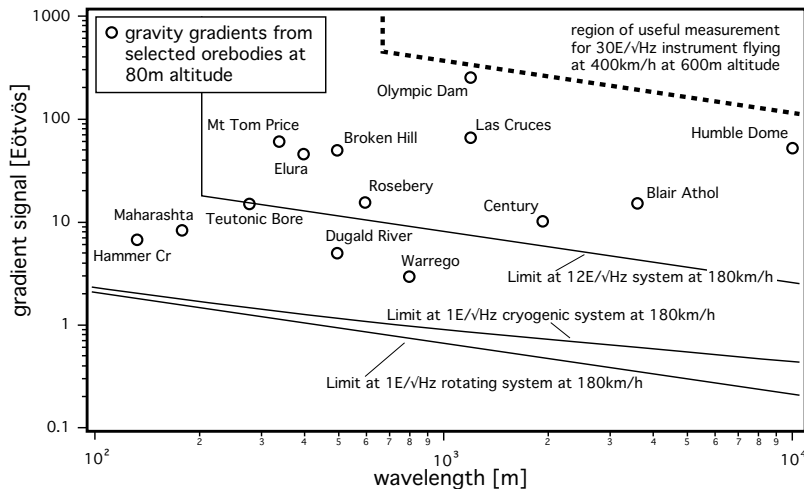
Figure 2.4: Plot of vertical gravity gradient response against wavelength showing signals for selected orebodies. Also shown are lines corresponding to systems with different noise levels (modified from Van Kann, 2004).

19

creased accuracy of accelerometers and gyros, the performance is expected to match that of stable platform systems. Examples of such projects are the Strapdown Airborne Gravimetry System SAGS4 by the Bavarian Academy of Sciences in Munich (Boedecker and Stürze, 2006), the strapdown system being developed for vector gravimetry by the Institute of Geodesy and Navigation in Munich (Kreye et al., 2006), and the Gravimetry using Airborne Inertial Navigation (GAIN) project by the Delft University of Technology (Alberts et al., 2008).

The most promising solution for cost and time reduction is the use of Unmanned Airborne Vehicles (UAV) equipped with a gravimeter or SINS and GPS. UAVs have already been successfully applied in other research fields, such as atmospheric science, remote sensing and hazard monitoring (Clarke, 2002). For accurate airborne gravity measurements a stable platform is required. In case of a UAV, this means that airships are the best option, especially if they are provided with solar panels for power supply. An airborne gravimetry campaign could then consist of one or more UAVs that autonomously map large parts of the Earth, such as oceans or the polar areas.

Processing of airborne gravity data

<div style="text-align: right; font-size: 3em; color: gray;">3</div>

The processing procedure of airborne gravity data can be divided in two steps: pre-processing and inversion. The pre-processing procedure follows the basic equations given in section 2.3.1 and includes a number of steps and corrections that are described in Appendix A. The outcome of data pre-processing is a set of gravity disturbances at flight level, that are downward continued to ground level and used for the computation of other gravity functionals. An important part of the pre-processing is the handling of noise in the data. Usually this includes a low-pass filtering to suppress high-frequency noise and a cross-over adjustment to eliminate bias and drift terms. Both techniques are discussed in section 3.1.

For the inversion of airborne gravity measurements into gravity functionals on the Earth's surface or on the geoid, many methods have been proposed in literature. Among the most popular ones in practical applications are integral methods based on the theory of boundary value problems for the Laplace equation, and least-squares collocation. A different approach that is used in regional gravity field determination makes use of radial base functions for the representation of the disturbing potential. The inversion of airborne gravity data using these methodologies is discussed in section 3.2. The chapter concludes with a comparison of the different approaches.

3.1 Pre-processing

3.1.1 Low-pass filtering

Airborne gravity measurements are made in a very dynamic environment, resulting in extremely large noise in the data. Typically, noise-to-signal ratios of 1000 or more can be observed (Schwarz and Li, 1997). Figure (3.1) shows the 'raw' gravity signal, which varies by about 5000 mGal, and the target gravity signal at flight level, which shows a variation of about 20 mGal. Extracting the gravity signal from measurements contaminated by such strong noise is one of the major challenges in airborne gravimetry.

The largest contribution consists of high frequency noise, caused by the effect of aircraft vibrations on the gravimeter system and the amplification of GPS system noise when computing accelerations. To reduce these effects, a filtering technique can be ap-
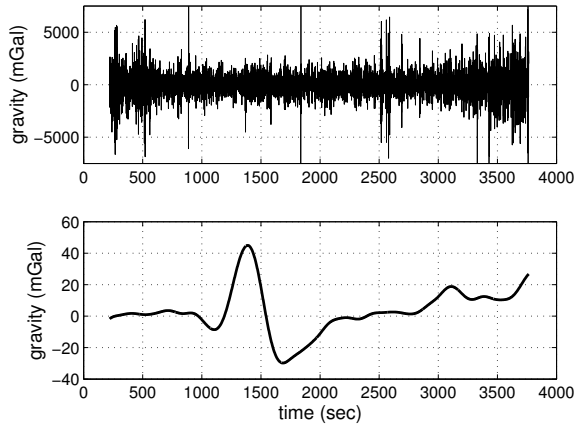
Figure 3.1: 'Raw' gravity measurements (top) and the target gravity signal at flight level (bottom).

plied to the airborne gravity data. Because in the low-frequency part of the spectrum the noise level is below the level of the gravity signal, the most commonly used filters are low-pass filters, although some alternative model-based approaches have been proposed (Hammada and Schwarz, 1997). When a low-pass filter is used, the filter passes low-frequency signals, but attenuates any signal above the cut-off frequency.

In general, there are two classes of low-pass filters: finite impulse response (FIR) and infinite impulse response (IIR) filters. The impulse response of a filter is the output sequence from the filter when a unit impulse is applied as its input. The term IIR, however, is not very accurate, since the actual impulse responses of nearly all IIR filters virtually reduce to zero in a finite time. Therefore, the terms non-recursive and recursive filters are often used instead. Both types of low-pass filters have been used for airborne gravity data processing. The FIR filter for instance has been used by the University of Calgary (Wei and Schwarz, 1998) for the processing of SINS data and by Brozena and Peters (1988), who combined it with a resistor-capacitor (RC) filter to sharpen the frequency roll-off. An example of an IIR filter is the Butterworth filter, which has been used by Forsberg et al. (1999) and Meyer et al. (2003).

An advantage of using a low-pass filter is its easy implementation. However, even though both signal and noise are attenuated in the high-frequency band, some noise will remain in the pass-band, reducing the accuracy of the gravity data. The accuracy may be improved by using a larger filter length, but this reduces the resolution of the data. Instead of low-pass filtering, a few model-based approaches have been used, mainly applied to SINS data. One example is Kalman filtering with a shaping filter as the stochastic model for the gravity disturbance (Eisfeller and Spietz, 1989; Hammada and Schwarz, 1997). Another approach is based on the wave filtering concept, where a deterministic model
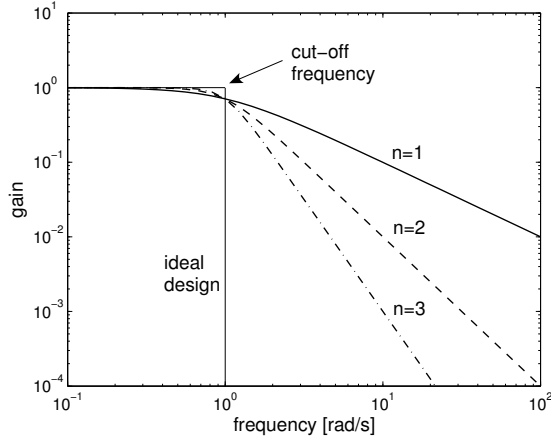
Figure 3.2: The frequency magnitude response of a first-, second-, and third-order Butterworth filter versus an ideal low-pass filter ($H_0 = 1, \omega_c = 1 \, \mathrm{rad/s}$).

filtering is used that approximates the gravity disturbance by a simple function or a ramp (see e.g. Salychev et al., 1994). Hammada and Schwarz (1997) compared the model-based filtering approaches with low-pass filtering, and concluded that a low-pass filter performs systematically better.

The design of a low-pass filter comprises the choice of several parameters, including the order of the filter and the filter length. The latter is chosen according to the flight speed and the minimum wavelength to be resolved. The filter design can be analyzed using the transfer function $H(z)$, which gives the ratio of the output of a filter over the input of the filter

$$H(z) = \frac{Y(z)}{X(z)}, \tag{3.1}$$

where $X(z)$ is the z-transform ($z = e^{j\omega T}$) of the input signal and $Y(z)$ is the z-transform of the filter output signal. From the transfer function the filter's frequency magnitude response $|H(e^{j\omega T})|$ and phase response $\angle H(e^{j\omega T})$ can be computed. One of the most popular recursive filter designs is the Butterworth filter. Figure 3.2 shows the frequency magnitude response of a Butterworth filter for different orders compared to the ideal low-pass filter design. In this thesis a 2nd-order Butterworth filter is used to analyze and compare the performance of the filtering strategy developed in the next chapter. The filter is the same as used by Olesen (2003) and Meyer et al. (2003). Because Butterworth filters introduce a phase shift between the input and output signals (Hamming, 1989), the filter is implemented as a two-way (i.e. forward/backward) filter, which removes the phase shift.

23

3.1.2 Cross-over adjustment

After the computation of gravity disturbances at flight level according to Eq. (2.5) and the application of a low-pass filter, often a cross-over adjustment is applied. This operation aims at minimizing the misfits at locations of crossing flight lines, by estimating biases, and optionally a drift, for each profile.

Assuming that airborne gravity measurements are corrupted by a drift d and a bias b per profile, the observed gravity disturbance $\delta\tilde{g}$ can be written as

$$\delta\tilde{g} = \delta g + d\Delta t + b, \tag{3.2}$$

where δg is the true gravity disturbance. Then, at the cross-over of intersecting lines, the difference between two measurements reads (e.g. Glennie and Schwarz (1997), Hwang et al. (2006))

$$\Delta\delta\tilde{g}_{ij} = d_i\Delta t_i - d_j\Delta t_j + b_i - b_j, \tag{3.3}$$

where d_i, d_j, b_i and b_j are the drifts and biases of lines i and j, respectively, and Δt_i and Δt_j are the time differences between the start of the flight line and the current crossing point. The bias and drift parameters are obtained by applying a least-squares adjustment to the measurement model of Eq. (3.3). Because the model has a rank-defect, at least one survey line must be held fixed in the adjustment by adding constraints to the functional model. It means that the bias and drift parameters are estimated relative to the fixed line.

The cross-over adjustment procedure as described here has several disadvantages. Firstly, the location of the measurements does, in general, not match the exact cross-over point of two lines. This means that interpolation is required to find the position and to obtain gravity values g_i and g_j at the cross-over point. For an accurate interpolation, a constant flight level is needed. Secondly, the misfits at cross-over points may be the result of random noise, for instance caused by turbulence. If that is the case, a cross-over adjustment can in fact degrade the accuracy of the data, as an estimated bias or drift can corrupt other parts of the profile. Furthermore, lines that have only one cross-over point are usually not adjusted as the cross-over difference directly translates into a bias for this line. Finally, the redundancy in a cross-over adjustment is typically small. If only a few crossing lines are available, the number of cross-overs is only slightly more than the number of bias and drift parameters to be estimated.

That the misfits at the cross-over points can be very large has for example been shown by Bell et al. (1999). Because large cross-over misfits indicate data segments of low quality, they removed these parts of the flight tracks, until an RMS of less than 3 mGal was achieved for the cross-over differences. Then, the data were corrected for biases and drifts, which were obtained in a cross-over adjustment. Other examples where a cross-over adjustment has been applied as part of the pre-processing are found in (Glennie and Schwarz, 1997) and (Hwang et al., 2007).

Several authors (e.g. Olesen (2003), Forsberg et al. (2007)) do not apply a cross-over adjustment as such a procedure may be a source of aliasing, and is not required due to the

excellent stability of the LCR gravimeter they use. In such a case, an analysis of cross-over differences may be performed to check the internal consistency of the data. Olesen and Forsberg (2007a) report an RMS cross-over misfit of 2.5-3.0 mGal for a large number of surveys performed with the LCR gravimeter. Assuming that noise is uncorrelated between the profiles, the noise level is estimated as $\sigma_e = \sigma_x/\sqrt{2}$, indicating a noise level of 1.8-2.1 mGal for the airborne data. They claim that a cross-over adjustment would lower the RMS of the misfits, but the derived error estimates would be too optimistic and no longer reflect the real noise level.

3.2 Inversion of airborne gravity data

3.2.1 Remove-restore technique

The goal of this section is to discuss the determination of the disturbing potential or geoid from airborne gravity measurements. The geoid is an equipotential surface of the gravity potential W that (approximately) coincides with the mean ocean surface (see figure 3.3). This equipotential surface is defined as

$$W(x, y, z) = W_0 = \text{constant.} \tag{3.4}$$

The disturbing or anomalous potential T at point P is defined as the difference

$$T(P) = W(P) - U(P), \tag{3.5}$$

where $U(P)$ is the normal potential of the reference ellipsoid at point P. The gravity vector $\mathbf{g}$ is the gradient of W and its magnitude (called gravity), which is a measurable quantity, is denoted by g. Then, analogous to Eq. (3.5) the gravity disturbance is defined as

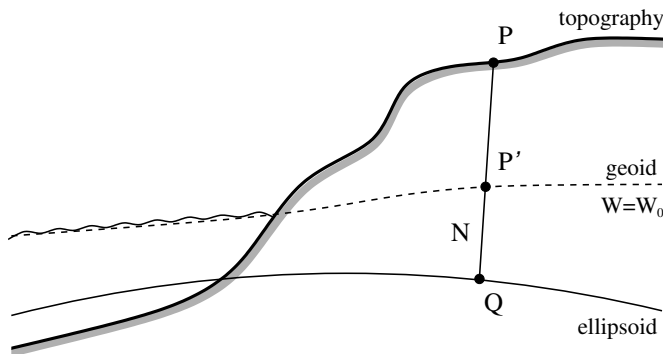$$\delta g(P) = g(P) - \gamma(P), \tag{3.6}$$

Figure 3.3: Geometry of the geoid.

where $\gamma(P)$ is normal gravity. In spherical approximation, the gravity disturbance is related to the disturbing potential by the simple relation

$$\delta g = -\frac{\partial T}{\partial r}, \tag{3.7}$$

where r is the radial distance. The gravity disturbance is the observation that is generally used in airborne gravity field determination. In classical geoid determination, the gravity anomaly is used, which is defined as

$$\Delta g(P) = g(P) - \gamma(Q). \tag{3.8}$$

In spherical approximation, the gravity anomaly is related to T as

$$\Delta g = -\frac{\partial T}{\partial r} - \frac{2}{r}T. \tag{3.9}$$

If δg or Δg is known at the geoid, it is possible to solve the boundary value problem for T and obtain the geoid height N above the reference ellipsoid by means of Bruns' formula (Heiskanen and Moritz, 1967)

$$N = \frac{T}{\gamma}. \tag{3.10}$$

As part of the processing of airborne gravity data, the remove-compute-restore technique (e.g. Rapp and Rummel, 1975) (or remove-restore in short) is usually applied. Because airborne gravimetry provides regional data sets, wavelengths longer than twice the size of the area cannot be resolved, but are modeled using a global geopotential model and removed from the data. Furthermore, the accuracy of downward continuation can be further improved by removing the effect of the terrain, which results in a smoother signal at flight level.

In the remove-restore technique, the geoid height is written as (Forsberg and Tscherning, 1981)

$$N = N_{GGM} + N_{topo} + N_{res}, \tag{3.11}$$

where N_{GGM} is the contribution from the global geopotential model, N_{topo} is the part that describes the terrain effect from topographic masses, and N_{res} is the residual geoid, which is modeled from residual gravity observations. To obtain residual gravity observations, the gravity disturbance (or anomaly) is split into the same contributions as in Eq. (3.11) and the computed quantities δg_{GGM} and δg_{topo} are removed from the observed gravity disturbances. As such, the residual gravity disturbances are given as

$$\delta g_{res} = \delta g - \delta g_{GGM} - \delta g_{topo}. \tag{3.12}$$

When the residual geoid has been computed, the contributions N_{topo} and N_{res} are restored to yield the complete geoid height N. Methods for the inversion of gravity disturbances δg obtained at flight level into the disturbing potential T are discussed in the following sections, where it is assumed that residual quantities are being used.

3.2.2 Integral methods

The downward continuation and geoid computation based on airborne gravity data using integral equations has been discussed by several authors (e.g. Novák and Heck (2002), Alberts and Klees (2004)). Various approaches have been proposed to solve the integral equations based on the theory of boundary value problems. The transformation of gravity disturbances into geoid heights can be performed in two steps; the downward continuation of a harmonic function as the inverse solution of the Dirichlet problem and the integration of gravity disturbances by means of the Hotine integral. These steps may be applied in arbitrary order. Alternatively, the solution can be computed directly from the mathematical model that is obtained by applying the radial derivative to the Poisson integral.

The approximation procedure used in this thesis is based on the Runge-Krarup theorem (Krarup, 1969; Moritz, 1980):

> *Any harmonic function ϕ, regular outside the Earth's surface, may be uniformly approximated by harmonic functions $\bar{\phi}$, regular outside an arbitrarily given sphere inside the Earth, in the sense that for any given $\varepsilon > 0$, the relation $|\phi - \bar{\phi}| < \varepsilon$ holds everywhere outside and on (any closed surface completely surrounding) the Earth's surface.*

The value of ε may be arbitrarily small. Thus, the disturbing potential is approximated by a harmonic function, but for simplicity no distinction is made between this function and the true disturbing potential. The sphere completely embedded inside the Earth is called the Bjerhammar sphere (see figure 3.4) and serves as the boundary surface of the harmonic domain of $\bar{\phi}$. For the determination of the disturbing potential on the Earth's topography S, alternative formulations are given in Alberts and Klees (2004).

Two-step approach

In this section two approaches are formulated for the transformation of airborne gravity measurements into the disturbing potential on the Bjerhammar sphere. In the first approach, denoted as approach A in Novák (2003b) and method A in Alberts and Klees (2004), the disturbing potential is first computed at flight level from the observed gravity disturbances. Subsequently, the obtained disturbing potential is downward continued to the Bjerhammar sphere. Alternatively, these steps may be reversed, i.e. the gravity disturbances are first downward continued to the Bjerhammar sphere and then transformed into the disturbing potential. The latter approach is identical to approach B in Novák (2003b) or method B in Alberts and Klees (2004).

For the first approach (method A), the solution of the first step is obtained by the numerical evaluation of the Hotine integral (Hotine, 1969), which is the space-domain representation of the solution of the Neumann boundary value problem for a spherical
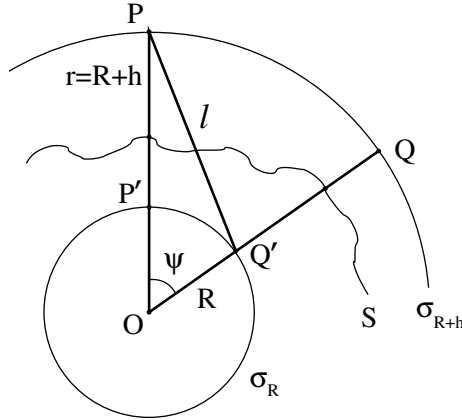
Figure 3.4: Geometry of the downward continuation to the Bjerhammar sphere σ_R.

surface. The Hotine integral is given as

$$T(P) = \frac{1}{4\pi(R+h)} \iint\limits_{\sigma_{R+h}} \delta g(Q)\, \mathcal{H}(\psi_{PQ})\, \mathrm{d}\sigma_{R+h}(Q), \quad P \in \sigma_{R+h}, \tag{3.13}$$

where R is the radius of the Bjerhammar sphere, h is the height above R, and $\mathrm{d}\sigma_{R+h} = (R+h)^2 \cos\varphi \mathrm{d}\varphi \mathrm{d}\lambda$ (cf. figure 3.4). $\mathcal{H}$ is the spherical Hotine function

$$\begin{aligned}
\mathcal{H}(\psi_{PQ}) &= \sum_{n=0}^{\infty} \frac{2n+1}{n+1} P_n(\cos\psi_{PQ}) \\
&= \mathrm{cosec}\frac{\psi_{PQ}}{2} - \ln(1 + \mathrm{cosec}\frac{\psi_{PQ}}{2}),
\end{aligned} \tag{3.14}$$

with ψ_{PQ} the angular distance between P and Q, so that

$$\cos\psi_{PQ} = \sin\varphi_P \sin\varphi_Q + \cos\varphi_P \cos\varphi_P \cos(\lambda_Q - \lambda_P). \tag{3.15}$$

The second step requires the downward continuation of the disturbing potential to the Bjerhammar sphere by inversion of the Poisson integral, which represents the solution of the Dirichlet boundary value problem for a spherical surface. The Poisson integral reads

$$T(P) = \frac{1}{4\pi R^2} \iint\limits_{\sigma_R} T(Q')\, \mathcal{P}(R, \psi_{PQ'}, r_P) \mathrm{d}\sigma_R(Q'), \quad P \in \sigma_{R+h}, \tag{3.16}$$

with $r_P = R + h, r_{Q'} = R$ and $\mathrm{d}\sigma_R = R^2 \cos\varphi \mathrm{d}\varphi \mathrm{d}\lambda$. The values $T(P), \ P \in \sigma_{R+h}$, are

the solution of the first step. $\mathcal{P}$ is the spherical Poisson kernel (Kellogg, 1929)

$$\begin{aligned} \mathcal{P}(R, \psi_{PQ'}, r_P) &= \sum_{n=0}^{\infty} (2n+1) \left(\frac{R}{r_P} \right)^{n+1} P_n(\cos \psi_{PQ'}) \\ &= R \frac{r_P^2 - R^2}{l^3}, \end{aligned} \tag{3.17}$$

where l is the spatial distance between the computation point P and the integration point Q'

$$l = \sqrt{r_P^2 + r_{Q'}^2 - 2 r_P r_{Q'} \cos \psi_{PQ'}}. \tag{3.18}$$

The disturbing potential T on the Bjerhammar sphere is the inverse solution of Eq. (3.16), which can be computed after discretization of the integral formulas and solving the obtained linear system using least-squares techniques.

The two computation steps described above can also be applied in reverse order. In that case, the first step uses the formula for the upward continuation of a harmonic function $r \cdot \delta g$, which is given by the Poisson integral as

$$\begin{aligned} r_P \cdot \delta g(P) &= \frac{1}{4\pi R^2} \iint_{\sigma_R} R \cdot \delta g(Q') \, \mathcal{P}(R, \psi_{PQ'}, r_P) \mathrm{d}\sigma_R(Q') \\ \Leftrightarrow \delta g(P) &= \frac{1}{4\pi R \, r_P} \iint_{\sigma_R} \delta g(Q') \, \mathcal{P}(R, \psi_{PQ'}, r_P) \mathrm{d}\sigma_R(Q'), \end{aligned} \tag{3.19}$$

with $P \in \sigma_{R+h}$. The gravity disturbances are obtained on the Bjerhammar sphere σ_R as the inverse solution of Eq. (3.19). In the second step the disturbing potential is obtained at σ_R from the resulting gravity disturbances by numerical evaluation of the Hotine integral as

$$T(P') = \frac{1}{4\pi R} \iint_{\sigma_R} \delta g(Q') \, \mathcal{H}(\psi_{P'Q'}) \, \mathrm{d}\sigma_R(Q'), \quad P' \in \sigma_R. \tag{3.20}$$

An alternative method, which is similar to the latter approach (method B), is given in Alberts and Klees (2004). It uses a single-layer representation of the disturbing potential. The advantage of this formulation is that it does not require a spherical boundary surface. The results obtained with this approach were almost identical to method B (see Alberts and Klees (2004) for more details).

Single-step approach

Instead of a two-step approach, as discussed in the previous section, the disturbing potential can be computed directly on the sphere σ_R from gravity disturbances at flight level. The functional model is easily found when the radial-derivative operator is applied to the

Poisson integral (3.16). For $P \in \sigma_{R+h}$, the following expression is obtained (Novák, 2003a; Alberts and Klees, 2004)

$$\left.\frac{\partial T}{\partial r}\right|_P = -\delta g(P) = \frac{1}{4\pi R^2} \iint\limits_{\sigma_R} T(Q') \left.\frac{\partial \mathcal{P}(R, \psi_{PQ'}, r_P)}{\partial r}\right|_P \mathrm{d}\sigma_R(Q'),$$

$$\Leftrightarrow \delta g(P) = -\frac{1}{4\pi R^2} \iint\limits_{\sigma_R} T(Q') \left.\frac{\partial \mathcal{P}(R, \psi_{PQ'}, r_P)}{\partial r}\right|_P \mathrm{d}\sigma_R(Q'). \qquad (3.21)$$

The derivative of the Poisson kernel is given as

$$\left.\frac{\partial \mathcal{P}(R, \psi_{PQ'}, r_P)}{\partial r}\right|_P = -\frac{1}{R} \sum_{n=0}^{\infty} (n+1)(2n+1) \left(\frac{R}{r_P}\right)^{n+2} P_n(\cos \psi_{PQ'})$$

$$= R \left[\frac{2\, r_P}{l^3} - \frac{3(r_P^2 - R^2)(2r_P - 2R \cos \psi_{PQ'})}{2l^5}\right]. \qquad (3.22)$$

The disturbing potential at points on σ_R is obtained as the inverse solution of the integral equation (3.21) for $T(Q')$, $Q' \in \sigma_R$. The major advantage of this approach over the two-step approaches is that for the same data coverage at flight altitude, the disturbing potential can be determined in a larger area on the Bjerhammar sphere than for the other methods (see e.g. Novák, 2003a; Alberts and Klees, 2004). As shown by Alberts and Klees (2004), a spherical cap size of 1.5° is sufficient to reduce edge effects, whereas the combination of the Poisson and the Hotine integral requires typically a cap size of 5°, making the single-step approach much more efficient.

Practical considerations

Kernel modification
The integral equations must be integrated over the full spatial angle, but data are generally only available in a local area. Therefore, the integration is limited to a spherical cap centered at the computation point, and the data are combined with a global geopotential model, which largely represents the contribution of the area outside the spherical cap. The truncation error introduced by limiting the integration to a spherical cap centered at the computation point can be reduced by a modification of the kernel function. In literature many modifications have been proposed, see e.g. Molodenskii et al. (1962), Wong and Gore (1969), Meissl (1971b), Heck and Grüninger (1987), Vaníček and Kleusberg (1987), Featherstone et al. (1998). An alternative approach for the computation of gravity functionals when data are only available in a local area is given in Prutkin and Klees (2007).

Integration and interpolation errors
The evaluation of the integral formulas and the solution of the integral equations require

the numerical computation of surface integrals, which is done using numerical integration. The surface σ is usually decomposed into a sum of patches σ_k and the integral is evaluated as a weighted sum of function values at a limited number of points, called the 'nodes' of the integration formula. Mathematically this can be written as

$$\iint\limits_{\sigma_k} g(Q)K(P,Q)\mathrm{d}\sigma_k(Q) \approx \sum_{i=1}^{M} g(Q_i)K(P,Q_i)w_i, \qquad (3.23)$$

where Q_i are the nodes and w_i are the weights. The integral methods discussed in this section involve the evaluation of weakly singular integrals with $O(1/l)(l \rightarrow 0)$ kernel functions at the center of the patch σ_k. Standard integration formulas require a large number of nodes M to reduce the integration error introduced in Eq. (3.23). The accuracy of the integration can be improved when a suitable parameter transformation is applied before numerical integration (Klees, 1996). The Jacobian of such a transformation is zero at the computation point and the product of the Jacobian with the kernel function behaves smoothly.

The nodes Q_i are irregularly distributed over each patch σ_k and usually not identical to the points where the data are given. Therefore, the data have to be interpolated at the nodes of the integral formula, which in turn introduces interpolation errors. As an alternative, the contribution of a patch to the surface integral can be computed using the data at the observation points, often reduced to a block mean value, as the only node, which corresponds to the application of the composed one-point Newton-Cotes integration formula (see e.g. Novák et al., 2000; Novák and Heck, 2002). To minimize integration and interpolation errors, Alberts and Klees (2004) use modified polar coordinates as introduced by Klees (1996) in combination with least-squares prediction to obtain gravity values at the nodes. This approach improved the performance of the integral-based methods considerably.

3.2.3 Least-squares collocation

Least-squares collocation (LSC) is often used for the downward continuation of airborne gravity data and the inversion into gravity functionals at ground level. Examples are given in Forsberg and Kenyon (1994), Marchenko et al. (2001) and Forsberg (2002). LSC is an optimal linear estimation method for gravity modeling. For the derivation, two fundamentally different viewpoints have been derived; the deterministic approach and the probabilistic (or statistical) approach. Both approaches have certain advantages and drawbacks (see e.g. Kotsakis and Sideris (1999) for a discussion). The deterministic viewpoint, first introduced by Krarup (1969), considers the unknown disturbing potential as an individual element in a reproducing kernel Hilbert Space (RKHS) $\mathcal{H}$, which is modeled from observations belonging to a dual Hilbert space $\mathcal{H}^*$ of $\mathcal{H}$ (see appendix C for the definition of a Hilbert space and some of its properties). The optimal solution is

then defined as the smoothest function that satisfies the given observations. This approach suffers from two important problems: the norm choice (or equivalently, the choice of the reproducing kernel) and the lack of efficient measures to evaluate the accuracy of the approximation.

The probabilistic approach models the unknown disturbing potential as a zero-mean stochastic process and the available observations are considered as zero-mean random variables. The optimal solution is then defined as the one with the smallest mean square error (MSE) and should be an unbiased estimator, which is linearly related to the available discrete data. The underlying framework is known as the Wiener-Kolmogorov theory, which was introduced in gravity modeling by Moritz (1962). The main drawback of this viewpoint is that the gravity field is not a stochastic phenomenon, since repetitive gravity measurements should always provide the same result (excluding time-dependent variations and measurement errors).

Both viewpoints provide identical solutions if the reproducing kernel function of the deterministic approach is combined with the covariance function used in the probabilistic approach. This leads to an intermediate viewpoint, which was first proposed by Heiskanen and Moritz (1967) and rigorously worked out by Sansò (1980). This viewpoint uses spatial statistical measures to describe the disturbing potential and its accuracy and the covariance function is defined as a purely deterministic quantity using a spatial averaging operator M. The solution still satisfies the minimum MSE principle. In this way, it can be regarded as a minimum-norm solution in an RKHS with the reproducing kernel equal to the deterministic covariance function.

Pure least-squares collocation

This section describes 'pure' collocation without noise and systematic parameters. The derivation of the expressions within the concept of Hilbert spaces with a reproducing kernel function is discussed in detail in appendix C. The mathematical concept of a Hilbert space is the natural generalization to an infinite number of dimensions of the Euclidean space $\mathbb{R}^n$. A Hilbert space is an inner product space which, as a metric space, is complete. The advantage of working in a Hilbert space is that the norm in the Hilbert space is associated with a quadratic expression, so that the process of minimization leads to linear problems.

Suppose for an unknown function $f \in \mathcal{H}$, n observations $l_i = L_i f$ are available. In gravity field modeling, the unknown function f is often the disturbing potential T and the observations l_i are linear functionals of T, e.g. gravity disturbances. When the dimension of the Hilbert space $\mathcal{H}$ is larger then n, the function f is not uniquely determined. Among all approximate solutions $\bar{f}$ that are compatible with the observations l_i, there is one, $\hat{f}$, for which the norm is minimum (Moritz, 1980):

$$\|\bar{f}\| \geq \|\hat{f}\|. \tag{3.24}$$

The solution $\hat{f}$ is the orthogonal projection of f onto a subspace of $\mathcal{H}$. It is precisely the

solution given by least-squares collocation, which reads (see appendix C)

$$\hat{f} = (\mathbf{L}K)^T (\mathbf{L}(\mathbf{L}K)^T)^{-1} \mathbf{l}, \tag{3.25}$$

where $K = K(P, Q)$ is the reproducing kernel.

With the notation $\mathbf{C}_{fl} := (\mathbf{L}K)^T$ and $\mathbf{C}_{ll} := \mathbf{L}(\mathbf{L}K)^T$ the LSC solution $\hat{f}$ takes the usual Wiener-Kolmogorov form

$$\hat{f} = \mathbf{C}_{fl} \mathbf{C}_{ll}^{-1} \mathbf{l}. \tag{3.26}$$

Instead of least-squares collocation, the method of determining $\hat{f}$ as outlined here is also called least-norm collocation, because the norm $\|\hat{f}\|^2$ is minimized.

Least-squares collocation in the presence of noise

In the previous section it was assumed that the observations l_i were noise-free, but in practice gravity measurements always contain measurement errors. Then the observation model of least-squares collocation becomes

$$l_i = L_i f + e_i, \quad i = 1, \dots, n, \tag{3.27}$$

where e_i is the error in the observation l_i. In matrix notation this is written as

$$\mathbf{l} = \mathbf{L}f + \mathbf{e}.$$

The least-squares estimator of f for this case is given as (Moritz, 1980)

$$\hat{f} = (\mathbf{L}K)^T (\mathbf{L}(\mathbf{L}K)^T + \mathbf{C}_{ee},)^{-1} \mathbf{l}. \tag{3.28}$$

where $\mathbf{C}_{ee}$ is the variance-covariance matrix of the noise. Using again the notation $\mathbf{C}_{fl} := (\mathbf{L}K)^T$ and $\mathbf{C}_{ll} := \mathbf{L}(\mathbf{L}K)^T$, this equation can be written in the well known form for LSC with noise

$$\hat{f} = \mathbf{C}_{fl} (\mathbf{C}_{ll} + \mathbf{C}_{ee})^{-1} \mathbf{l}. \tag{3.29}$$

The latter expression is equivalent to Tikhonov regularization with signal constraint, with the regularization parameter equal to 1, as will be shown in section 4.3.3. As a consequence, LSC provides a stable solution for the generally ill-posed problem of gravity field determination.

The model for least-squares collocation may be further extended to incorporate the estimation of additional parameters, such as datum parameters. For the derivation of the solution in the presence of additional parameters, see Moritz (1980).

The covariance function

The application of LSC requires the determination of the kernel function $K(P,Q)$, which is identified with the covariance function of the disturbing potential. The function $K(P,Q) = K(\psi_{PQ})$ can be expanded in a series of spherical harmonics as (see appendix C)

$$K(\psi_{PQ}) = \sum_{n=2}^{\infty} c_n \left(\frac{R_B^2}{r_P r_Q} \right)^{n+1} P_n(cos\psi_{PQ}), \tag{3.30}$$

where ψ_{PQ} is the spherical distance between P and Q, c_n is the signal degree variance and R_B is the radius of the Bjerhammar sphere. The function $K(P,Q)$ defined this way expresses the spatial covariance function of f, often denoted by $C(\psi_{PQ})$. Similarly, the matrix $\mathbf{C}_{ll}$ defined in Eq. (3.26) is called auto-covariance matrix of the observations l and the matrix $\mathbf{C}_{fl}$ is called the cross-covariance matrix between f and l.

When the remove-restore procedure is applied, a long-wavelength model is subtracted from the observations, as described in section 3.2.1. Then, the covariance-function is given as

$$C(\psi_{PQ}) = \sum_{n=2}^{N} \epsilon_n \left(\frac{R_E^2}{r_P r_Q} \right)^{n+1} P_n(cos\psi_{PQ})$$
$$+ \sum_{n=N+1}^{\infty} c_n \left(\frac{R_B^2}{r_P r_Q} \right)^{n+1} P_n(cos\psi_{PQ}). \tag{3.31}$$

where N is the maximum degree of the global gravity field model (GGM) that has been subtracted and ϵ_n is the error degree variance related to the GGM.

The degree variances are expressed by Eq. (C.21) in terms of spherical harmonic coefficients, which are generally not available for $n \geq N$. In practice, an analytical model is often fitted to an empirically derived covariance function. A degree variance model that has been used in many applications is the Tscherning and Rapp model (Tscherning and Rapp, 1974), which is given in terms of degree variances of the disturbing potential as

$$c_n(T,T) = \frac{A}{(n-1)(n-2)(n+B)}, \tag{3.32}$$

where A is a constant in units of $(m/s)^4$ and the integer B is typically put equal to a small number (e.g. $B = 4$) if a gravity model has been subtracted from the data. To fit the covariance function to the empirically derived function, both A and R_B need to be estimated.

For local and regional gravity field modeling, a covariance function is determined using available gravity functionals within the area of interest. For airborne gravimetry this means that the covariance function is computed from gravity disturbances, and in a second step related to the disturbing potential using the law of covariance propagation. The

relation between the degree variances of the disturbing potential and the degree variance models associated with the auto- and cross-covariance functions of gravity disturbances are given as

$$c_n(\delta g, \delta g) = \frac{(l+1)^2}{r_P r_Q} c_n(T, T) \tag{3.33}$$

$$c_n(T, \delta g) = \frac{(l+1)}{r_Q} c_n(T, T). \tag{3.34}$$

For other functionals, the relations are easily obtained by applying the corresponding linear operators to the degree variances of the disturbing potential (see e.g. (Meissl, 1971a) for the functional relations).

An alternative analytical covariance function for airborne gravimetry was derived by (Forsberg, 1987), who uses a planar approximation of the Earth's surface. The derived planar attenuated logarithmic covariance model for gravity disturbances at flight level is

$$C(x_P - x_Q, y_P - y_Q, z_P + z_Q) = \frac{C_h \sum_{i=0}^{3} \alpha_i \log(z_i + r_i)}{\sum_{i=0}^{3} \alpha_i \log(2D_i + 4h)}, \tag{3.35}$$

where C_h is the variance of gravity disturbances at flight level h. The parameters α_i, z_i and r_i are given as

$$\alpha_0 = 1, \quad \alpha_1 = -3, \quad \alpha_2 = 3, \quad \alpha_3 = -1,$$

$$z_i = z_P + z_Q + D_i,$$

$$r_i = \sqrt{(x_P - x_Q)^2 + (y_P - y_Q)^2 + z_i^2},$$

with

$$D_i = D + iT,$$

where D is the high-frequency attenuation parameter and T the low-frequency attenuation parameter. See (Forsberg, 1987) for more details. The model represents the planar equivalent of the Tscherning-Rapp model and is especially suitable for local and regional applications such as airborne gravimetry and airborne gradiometry.

3.2.4 Sequential multipole analysis

The representation of the disturbing potential by potentials of radial multipoles was developed by Marchenko (1998). This method has been applied to airborne gravity data acquired during the AGMASCO campaign by Marchenko et al. (2001) for the Skagerrak area and by Marchenko et al. (2004) for the Azores region. A multipole represents a point

object at a point P_i inside the Bjerhammar sphere (cf. fig. 3.5). The potential of a radial multipole is characterized by the degree n_i and its coordinates $d_i, \varphi_i, \lambda_i$ for geocentric distance, latitude and longitude, respectively.

The disturbing potential can be represented at any point P outside the Bjerhammar sphere by a convergent series of K non-orthogonal harmonic functions as

$$T(P) = \frac{GM}{R} \sum_{i=1}^{K} \mu_i^n \left(\frac{R}{r} \right)^{n+1} v_n^i(P) \tag{3.36}$$

where μ_i^n are the dimensionless multipole moments (or coefficients) and v_n^i is the dimensionless potential function of the radial multipole of degree n. The function v_n^i is defined as

$$v_n^i(P) = \frac{1}{n!} \frac{\partial^n}{\partial s_i^n} \left(\frac{1}{q_i} \right), \tag{3.37}$$

with $s_i = d_i/r$ and $q_i = r_i/r$, where r_i is the distance between the radial multipole and point P,

$$r_i = \sqrt{r^2 + d_i^2 - 2rd_i \cos \psi_i}, \tag{3.38}$$

where $\psi_i = \psi_{PP_i}$ is the spherical distance between P and P_i, computed from Eq. (3.15). Following the derivation in Marchenko et al. (2001) the potential of radial multipoles can be expressed in terms of Legendre polynomials as

$$v_n^i = \left(\frac{r}{r_i} \right)^{n+1} P_n(\cos \theta_i), \tag{3.39}$$

with

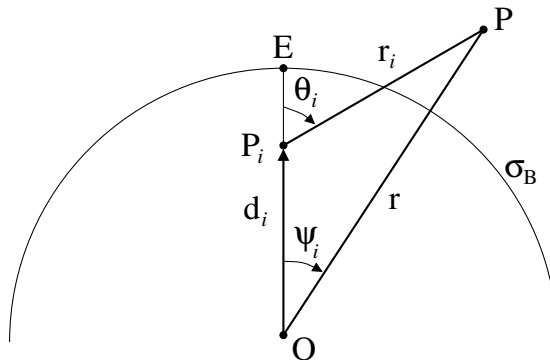$$\cos \theta_i = (r cos \psi_i - d_i)/r_i. \tag{3.40}$$

Figure 3.5: Location of a radial multipole (P_i) inside the Bjerhammar sphere.

It can be shown that the recursion formula for Legendre polynomials (Heiskanen and Moritz, 1967) can be used for the straightforward computation of the functions v_n^i as well, resulting in the recursion formula (Marchenko, 1998)

$$
\begin{aligned}
v_0^i &= \frac{1}{q_i} \\
v_1^i &= \frac{\cos\psi_i - s_i}{q_i^3} \\
nq_i^2 v_n^i &= (2n-1)(\cos\psi_i - s_i)v_{n-1}^i - (n-1)v_{n-2}^i.
\end{aligned}
\tag{3.41}
$$

The expression for the gravity disturbance in terms of the potential of radial multipoles can be found by applying the radial derivative operator to Eq. (3.36) as

$$
\begin{aligned}
\delta g(P) = -\frac{\partial T}{\partial r} &= \frac{GM}{R}\sum_{i=1}^{K}\mu_i^n\frac{\partial}{\partial r}\left(\left(\frac{R}{r}\right)^{n+1}v_n^i(P)\right) \\
&= \frac{GM}{R^2}\sum_{i=1}^{K}\mu_i^n\left(\frac{R}{r}\right)^{n+2}g_n^i(P),
\end{aligned}
\tag{3.42}
$$

where the functions $g_n^i(P)$ are given as (Marchenko et al., 2004)

$$
g_n^i(P) = -(n+1)(v_n^i(P) + s_i\, v_{n+1}^i(P)).
\tag{3.43}
$$

For the gravity anomaly a similar expression can be found using the fundamental equation of physical geodesy. Denoting the potential functions by $\tilde{g}_n^i$, they read (Marchenko et al., 2001)

$$
\tilde{g}_n^i(P) = (n+1)s_i\, v_n^i(P) + (n-1)v_n^i(P).
\tag{3.44}
$$

A practical application of the expressions derived above requires the solution of the inverse problem. That is, based on the observations, an appropriate finite set of radial multipoles, i.e. values of the moments (coefficients), locations and degrees, must be determined to approximate the disturbing potential. Within the sequential multipole analysis (SMA) algorithm the solution is obtained in several steps, which may be summarized as (Marchenko et al., 2001)

1. Input of the initial data set;

2. Find the largest absolute value of the gravity data; postulate this extremum as the epicenter E of the i-th radial multipole with coordinates (φ_i, λ_i); estimate the empirical isotropic function;

3. Determine the multipole parameters s_i, n and μ_i^n;

4. Compute the transformed data by removing the contribution of the potential of the i-th multipole from the data;

5. Return to step 2 if the desired accuracy is not achieved.

The determination of the relative distance s_i, the degree n and the moment μ_i^n, in step 3, is done on the basis of the empirical isotropic function (EIF) determined in step 2. The EIF is characterized by three parameters: the magnitude of v_n^i at the epicenter, the decreasing length and the curvature. The definition of these parameters is identical to the definition of those that describe the signal auto-covariance function (i.e. the variance, the correlation length and the curvature) used in LSC. The optimal degree n, the parameters s_i and μ_i^n, and the location of the radial multipole can be determined by a non-linear fitting of the EIF to the analytical isotropic function given by the function $g_n^i(\psi_i)$, or from the closest approximation of the gravity data locally. See Marchenko et al. (2001) for more details. After all radial multipoles have been selected, the multipole moments μ_i^n are re-adjusted by a least-squares estimation.

3.3 Discussion

This chapter gives an overview of the procedures used for the processing of airborne gravity data, which consists of pre-processing and inversion. The pre-processing consists of several independent steps, such as low-pass filtering, an adjustment of cross-over misfits, and gridding or interpolation. Each of these steps may introduce errors that accumulate in the course of processing or limit the resolution of the resulting gravity field. Therefore, in the next chapter several alternative strategies will be proposed, that replace the steps of filtering and cross-over adjustment by combining them with the estimation of gravity field parameters.

For the inversion of airborne gravity data into gravity functionals at ground level, a number of methods that are used in practice have been outlined, namely integral methods, least-squares collocation and sequential multipole analysis. Several authors have compared the performance of the approaches, especially in terms of geoid height errors. Alberts and Klees (2004) investigated the accuracy of the integral methods and compared them with LSC. They found that least-squares collocation performed slightly better, but differences between the outcomes were small. A study by Marchenko et al. (2001) showed that the SMA approach and LSC yield comparable results, which was confirmed by Klees et al. (2005) who used a simulated data set for the comparison between the methods.

From these studies it can be concluded that if a proper comparison is made between the approaches, they yield similar results in terms of geoid height and gravity disturbance errors at ground level. However, the methods may differ significantly with respect to the numerical complexity, stability and the extend to which they can be applied in practice. For instance, the integral methods require the computation of block mean values or interpolation of the data to the integration nodes. Furthermore, the data must be provided in an area that is much larger than the region for which the gravity functionals are computed. This is especially the case for the two-step integral approaches due to the large

integration cap size of the Hotine kernel, for which typically a value of 5 degrees is chosen to reduce the far-zone effect. The single-step integral approach is more efficient, but still a cap size of 1.5-2 degrees is required to obtain accurate results.

The inversion methods differ with respect to the number of base functions that are required to represent the data and determine the disturbing potential. For LSC the number of base functions equals the number of observations, which means that the signal-covariance matrix is generally very large and not easy to invert. In practice, LSC is often applied block-wise, or data are left out or gridded. When spherical base functions are used in combination with the application of a data-adaptive algorithm such as the SMA approach, the number of base functions can be reduced significantly without corrupting the quality of the solution. The SMA approach depends, however, on a pre-defined level of accuracy in the iteration scheme. Both LSC and the SMA algorithm do not require regularization, but the actual noise level may be underestimated.

In the following chapter a different representation of the disturbing potential will be used. It is based on a linear combination of harmonic functions that are the fundamental solutions of Laplace's equation in Cartesian coordinates. The advantages of this approach are the simple implementation and the fact that the number of base functions only depends on the resolution that is required. Furthermore, techniques to handle colored noise that have been developed for satellite gravimetry can be applied directly.

Combined data processing and inversion

4

This chapter gives the theoretical outline of the developed methodology that is applied to simulated and real data in the following chapters. The approach was first introduced by Alberts et al. (2005) and further investigated in Alberts et al. (2007a,b). It combines the processing steps that were discussed in the previous chapter with the estimation of gravity field parameters in one algorithm. The main advantage of the developed methodology is that it requires a minimum of pre-processing. The traditional low-pass filtering is replaced by a frequency-dependent data weighting; frequencies where the noise is high get a lower weight and vice versa. Furthermore, bias and drift parameters are included in the functional model, and the data are not gridded but used at the locations where they have been acquired.

In the first section a suitable gravity field representation is introduced. The disturbing potential is parameterized as a linear combination of harmonic functions that are the fundamental solutions of Laplace's equation in Cartesian coordinates. The parameters of this representation are estimated using least-squares techniques, which are discussed in section 4.2. Because the inversion of airborne gravity data is an ill-posed problem, a regularization is applied, which is the topic of section 4.3. Here, Tikhonov regularization is used, which requires two choices to be made; the choice of the regularization matrix and the choice of the regularization parameter which determines the weight of the regularization matrix. Section 4.4 describes the frequency-dependent data weighting scheme to properly take colored noise into account. The approach uses an ARMA model of the colored noise within a pre-conditioned conjugate gradients (PCCG) scheme. The advantage of this approach is that the variance-covariance matrix of the observations does not need to be inverted. Other error types such as biases and drifts are treated in section 4.5. Bias and drift parameters, but also other parameters such as instrument scale factors can be estimated by including them in the functional model. The chosen representation of the disturbing potential, described in the first section, implicitly assumes periodicity of the gravity signal, which results in strong oscillations at the borders of the area. Several methods are discussed in section 4.6 for the reduction of these edge effects. Finally, section 4.7 shows how errors at low frequencies can be reduced by adding prior information or constraints to the functional model.

4.1 Gravity field representation

In global gravity field modeling the most frequently used functions to represent the gravitational potential are spherical harmonics, because they are orthogonal on a sphere, which is an advantage for global gravity field modeling. These functions are obtained as general solutions of Laplace's equation in spherical coordinates, using the technique of separation of variables (see e.g. Heiskanen and Moritz, 1967). However, spherical harmonics are not convenient for regional applications. Firstly because the number of base functions would be very large to obtain a high-resolution gravity field solution and, more important, because it would require data to be available over the whole sphere, which is obviously not the case for airborne gravimetry.

A more suitable choice of a coordinate system for regional applications is a local Cartesian reference frame. For Cartesian coordinates the expression of the gravitational potential is obtained in the same way as for spherical harmonics, by solving Laplace's equation. Laplace's equation in Cartesian coordinates is given as

$$\Delta V(x, y, z) = \frac{\partial^2 V}{\partial x^2} + \frac{\partial^2 V}{\partial y^2} + \frac{\partial^2 V}{\partial z^2} = 0. \tag{4.1}$$

The transformation from traditionally used ellipsoidal coordinates $\{\varphi, \lambda, h\}$ to local Cartesian coordinates $\{x, y, z\}$ is given in appendix B. After separating the variables x, y, z by writing the potential as

$$V(x, y, z) = f(x)g(y)h(z), \tag{4.2}$$

and inserting this expression in Eq. (4.1), the following solution for Laplace's equation in Cartesian coordinates is obtained

$$V(x, y, z) = \sum_{l=-\infty}^{\infty} \sum_{m=-\infty}^{\infty} C_{lm}\, \varphi_l(x)\, \varphi_m(y)\, e^{-\gamma_{lm} z}, \tag{4.3}$$

where C_{lm} are coefficients of degree l and order m, and $\varphi_l(x)$ and $\varphi_m(y)$ are harmonic base functions defined as

$$\varphi_l(x) = \begin{cases} \cos \alpha_l x, & l \geq 0 \\ \sin \alpha_l x, & l < 0 \end{cases} \qquad \varphi_m(y) = \begin{cases} \cos \beta_m y, & m \geq 0 \\ \sin \beta_m y, & m < 0 \end{cases} \tag{4.4}$$

with

$$\alpha_l = \frac{2\pi|l|}{D_x}, \quad \beta_m = \frac{2\pi|m|}{D_y}. \tag{4.5}$$

To fulfill the condition of harmonicity ($\Delta V = 0$), γ_{lm} is given by definition as

$$\gamma_{lm} := \sqrt{\alpha_l^2 + \beta_m^2} = 2\pi \sqrt{\left(\frac{l}{D_x}\right)^2 + \left(\frac{m}{D_y}\right)^2}. \tag{4.6}$$
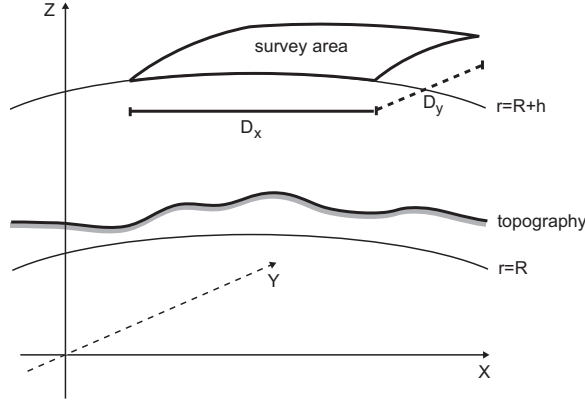
Figure 4.1: Geometry of the representation in a local Cartesian reference frame.

The parameters D_x and D_y denote the size of the computation domain in the x and y directions (see figure 4.1). The gravitational potential is thus expressed as a linear combination of harmonic functions, that are the fundamental solutions of Laplace's equation in Cartesian coordinates. The same representation was already used by Tsuboi and Fuchida (1938) to transform gravity field data from one elevation to another. Note that this representation of the disturbing potential is not a planar approximation. Data are used at the locations where they are observed and their coordinates are transformed to a local Cartesian coordinate frame, as shown in appendix B for ellipsoidal coordinates.

The longest wavelength that can be represented by Eq. (4.3) is equal to the size of the area, fixed by D_x and D_y. This requires the application of the remove-restore technique as described in section 3.2.1, where a long-wavelength model (for instance a GGM) is subtracted and only the residual field is expressed using Eq. (4.3). Furthermore, for practical applications the series Eq. (4.3) is truncated at a maximum degree L and order M. Then, the disturbing potential is represented by a series of harmonic functions, expressed in Cartesian coordinates, as

$$T(x, y, z) = \sum_{l=-L}^{L} \sum_{m=-M}^{M} C_{lm} \, \varphi_l(x) \, \varphi_m(y) \, e^{-\gamma_{lm} z}. \tag{4.7}$$

The minimum wavelength that is represented by this series can be computed from L and M as

$$\lambda_x = \frac{D_x}{L}, \quad \lambda_y = \frac{D_y}{M}, \tag{4.8}$$

with λ_x and λ_y the wavelength in the x and y directions. Instead of minimum wavelength, the term spatial resolution is often used, which is characterized in terms of the half-wavelength that can be resolved. The resolution in x and y direction is $\lambda_x/2$ and $\lambda_y/2$, respectively.

The coefficients C_{lm} are unknown, i.e. they must be determined from measured gravity functionals. As mentioned in section 2.3.1, the commonly used observables in airborne gravimetry are gravity disturbances, which are related to the disturbing potential as $\delta g = -\partial T/\partial r$. Approximating the radial derivative by the derivative in the vertical direction, $\partial T/\partial r \approx \partial T/\partial z$, the relation between observed gravity disturbances, denoted by T_z, and the unknown coefficients is found by applying the z-derivative operator to Eq. (4.7). The error introduced by this approximation can be written as

$$\varepsilon_{\delta g} \approx \delta g - \delta g \cos \frac{d}{R}, \tag{4.9}$$

where d is the distance from the middle of the area to the location of δg. For $d =$500 km and δg is 100 mGal, this error is only 0.3 mGal, which is below the noise level of airborne gravimetry. The expression for T_z reads

$$T_z(x,y,z) = \frac{\partial T}{\partial z} = -\sum_{l=-L}^{L} \sum_{m=-M}^{M} \gamma_{lm} C_{lm} \, \varphi_l(x) \, \varphi_m(y) \, e^{-\gamma_{lm}z}. \tag{4.10}$$

Note that $\gamma_{00} = 0$. Hence, the coefficient C_{00}, which represents the constant part of the potential, cannot be determined in regional gravity field modeling from airborne gravimetry measurements. Furthermore, it means that the constant part of the gravity disturbances T_z is not modeled. Therefore, an extra term κz is added to Eq. (4.7), where κ represents the constant part of the gravity disturbances. Note that the function κz is also harmonic.

Instead of gravity disturbances, gravity anomalies are also used as observables in many applications in geodesy or geophysics. The relation between the gravity anomaly and the disturbing potential was given in section 3.2.1 as

$$\Delta g = -\frac{\partial T}{\partial r} - \frac{2}{r}T \approx -\frac{T}{z} - \frac{2}{r}T. \tag{4.11}$$

Inserting the expressions for the disturbing potential (Eq. (4.7)) and the gravity disturbance T_z (Eq. (4.10)) into this equation gives the (approximate) expression for the gravity anomalies in terms of fundamental solutions of Laplace's equation in Cartesian coordinates:

$$\Delta g(x,y,z) = \sum_{l=-L}^{L} \sum_{m=-M}^{M} \left(\gamma_{lm} - \frac{2}{r} \right) C_{lm} \, \varphi_l(x) \, \varphi_m(y) \, e^{-\gamma_{lm}z}. \tag{4.12}$$

4.2 Inversion methodology

4.2.1 Least-squares estimation

The functional model for gravity field recovery from airborne gravity data (Eq. (4.10)) may be written as a standard Gauss-Markov model. The functional model reads

$$\mathbf{y} = \mathbf{A}\mathbf{x} + \mathbf{e}, \tag{4.13}$$

where $\mathbf{y}$ is the $n \times 1$ observation vector containing the gravity disturbances T_z, $\mathbf{e}$ is the $n \times 1$ vector of residuals, and $\mathbf{x}$ is the $u \times 1$ vector of unknown coefficients C_{lm}. The $n \times u$ design matrix $\mathbf{A}$ describes the functional relations between $\mathbf{y}$ and $\mathbf{x}$.

The stochastic properties of the residuals are described by the stochastic model

$$E\{\mathbf{e}\} = 0, \quad E\{\mathbf{e}\mathbf{e}^T\} = D\{\mathbf{e}\} = \mathbf{Q_y}, \tag{4.14}$$

where $E\{\cdot\}$ denotes the expectation operator, and $D\{\cdot\}$ the dispersion operator. The noise in the observations is described by the variance-covariance matrix of $\mathbf{e}$, which is denoted $\mathbf{Q_y}$.

In the absence of prior information the optimal gravity field solution is obtained by minimizing the quadratic functional

$$\Phi(\mathbf{x}) = (\mathbf{y} - \mathbf{A}\mathbf{x})^T \mathbf{Q_y}^{-1} (\mathbf{y} - \mathbf{A}\mathbf{x}), \tag{4.15}$$

which is equivalent to solving the system of normal equations

$$(\mathbf{A}^T \mathbf{Q_y}^{-1} \mathbf{A})\hat{\mathbf{x}} = \mathbf{A}^T \mathbf{Q_y}^{-1} \mathbf{y}, \tag{4.16}$$

where $\hat{\mathbf{x}}$ is the best linear unbiased estimate (BLUE). The product of matrices on the left-hand side of Eq. (4.16) is called the normal matrix and is denoted by $\mathbf{N}$, i.e

$$\mathbf{N} = \mathbf{A}^T \mathbf{Q_y}^{-1} \mathbf{A}. \tag{4.17}$$

The least-squares estimators of the observation vector and the vector of residuals are given as

$$\hat{\mathbf{y}} = \mathbf{A}\hat{\mathbf{x}}, \tag{4.18}$$

$$\hat{\mathbf{e}} = \mathbf{y} - \hat{\mathbf{y}}. \tag{4.19}$$

4.2.2 Solution strategies

The solution $\hat{\mathbf{x}}$ is obtained by solving the normal equations of Eq. (4.16). If the number of unknown parameters is huge, the numerical costs to compute $\mathbf{N}$ and it inverse are very large. This section discusses two strategies that can be used to reduce the numerical costs.

Conjugate gradients

The system of equations can be solved effectively using the conjugate gradients (CG) method (Hestenes and Stiefel, 1952). Its performance (convergence rate) can be improved by implementing a suitable pre-conditioner $\mathbf{P}$, resulting in the so-called pre-conditioned conjugate gradients (PCCG) method. The PCCG iterations can be performed according to the following scheme (e.g Ditmar and Klees, 2002):

1. $\mathbf{x}_0 = \tilde{\mathbf{x}}_0, \ \mathbf{r}_0 = \tilde{\mathbf{r}}_0 = \mathbf{A}^T \mathbf{Q_y}^{-1} \mathbf{y}, \ \mathbf{p}_0 = \tilde{\mathbf{p}}_0 = \mathbf{P}^{-1} \mathbf{r}_0, \ k = 0;$

2. $\mathbf{a}_k = \mathbf{N} \mathbf{p}_k;$

3. $\alpha_k = \frac{\mathbf{r}_k^T \mathbf{p}_k}{\mathbf{a}_k^T \mathbf{p}_k};$

4. $\mathbf{x}_{k+1} = \mathbf{x}_k + \alpha_k \mathbf{p}_k;$

5. $\mathbf{r}_{k+1} = \mathbf{r}_k - \alpha_k \mathbf{a}_k;$

6. $\mathbf{e}_k = \tilde{\mathbf{r}}_k - \mathbf{r}_{k+1};$

7. $\gamma_k = -\frac{\mathbf{r}_{k+1}^T \mathbf{e}_k}{\tilde{\mathbf{r}}_k - \mathbf{r}_{k+1}^T \mathbf{e}_k};$

8. $\tilde{\mathbf{x}}_{k+1} = \mathbf{x}_{k+1} + \gamma_k (\tilde{\mathbf{x}} - \mathbf{x}_{k+1};$

9. $\tilde{\mathbf{r}}_{k+1} = \mathbf{r}_{k+1} + \gamma_k (\tilde{\mathbf{r}} - \mathbf{r}_{k+1};$

10. If $\frac{\|\mathbf{r}_{k+1}\|}{\|\mathbf{r}_0\|} < \epsilon$ set $\mathbf{x} = \tilde{\mathbf{x}}_{k+1}$, stop;

11. $\tilde{\mathbf{p}}_{k+1} = \mathbf{P}^{-1} \mathbf{r}_{k+1};$

12. $\beta_{k+1} = \frac{\mathbf{r}_{k+1}^T \tilde{\mathbf{p}}_{k+1}}{\mathbf{r}_k^T \tilde{\mathbf{p}}_k};$

13. $\mathbf{p}_{k+1} = \tilde{\mathbf{p}}_{k+1} + \beta_{k+1} \mathbf{p}_k;$

14. $k = k + 1$, go to item (2).

The advantage of the conjugate gradients method is that the normal matrix does not have to be computed explicitly. Instead, the application of the normal matrix to a vector $\mathbf{p}$ (step 2) is performed, which can be decomposed into a sequence of three matrix-vector multiplications:

1. $\mathbf{u} = \mathbf{A}\mathbf{p};$

2. $\mathbf{v} = \mathbf{Q_y}^{-1} \mathbf{u};$

3. $\mathbf{q} = \mathbf{A}^T \mathbf{v}.$

The first step, the application of the design matrix $\mathbf{A}$ to a vector, is nothing but a synthesis as expressed in Eq. (4.10). The multiplication of the matrix $\mathbf{Q_y}^{-1}$ to the resulting vector can be interpreted as filtering. The final step, the application of the transposed design matrix $\mathbf{A}^T$ to the filtered vector is called co-synthesis. The co-synthesis is given as

$$q_{lm} = -\gamma_{lm} \sum_{i=1}^{n} \varphi_l(x_i) \varphi_m(y_i) e^{-\gamma_{lm} z_i} v_i \qquad (4.20)$$

for $-L \leq l \leq L$ and $-M \leq m \leq M$, with n the number of observations T_z, the set $\{x_i, y_i, z_i\}$ describes the position of observation i, and v_i the i-th entry of $\mathbf{v}$.

Cholesky factorization

Since the normal matrix $\mathbf{N}$ is a symmetric positive definite matrix with real entries, it can be decomposed as (e.g. Golub and Van Loan, 1996)

$$\mathbf{N} = \mathbf{G}\mathbf{G}^*, \tag{4.21}$$

where $\mathbf{G}$ is a lower triangular matrix with positive diagonal entries, and $\mathbf{G}^*$ denotes the conjugate transpose of $\mathbf{G}$. The decomposition in Eq. (4.21) is called Cholesky factorization. It can be used for the numerical solution of a linear system of equations $\mathbf{N}\mathbf{x} = \mathbf{b}$ by first computing the Cholesky decomposition, then solving the system $\mathbf{G}\mathbf{p} = \mathbf{b}$ for $\mathbf{p}$, and finally solving $\mathbf{G}^T\mathbf{x} = \mathbf{p}$ to obtain the solution $\mathbf{x}$.

4.3 Regularization and parameter choice rule

The inversion of airborne gravity data is an ill-posed problem. A problem

$$\mathbf{y} = \mathbf{A}\mathbf{x} \tag{4.22}$$

is called ill-posed if at least one of the following conditions is not satisfied (e.g. Schwarz, 1979):

1. The solution of Eq. (4.22) exists for any $\mathbf{y}$;

2. The solution of Eq. (4.22) is unique;

3. The solution of Eq. (4.22) depends continuously on $\mathbf{y}$.

For airborne gravimetry it is the third condition that is not satisfied. Difficulties arise because a comparatively smooth function (e.g. gravity disturbances at flight level) is used to compute a more detailed, and thus less smooth, function (e.g. gravity disturbances at ground level). As a result the LS solution strongly oscillates, because data errors and unmodeled signal get strongly amplified due to the ill-conditioning of the normal matrix. In practical applications the stability of the problem not only depends on observational errors, but also on the number of observations and their distribution.

4.3.1 Regularization method

Several methods exist to solve the problem of ill-posedness of inverse problems. Among the most often used in geodesy are Tikhonov-Phillips regularization and truncated singular value decomposition. For the methodology derived in this chapter the method of Tikhonov-Phillips regularization (often just called Tikhonov regularization) is used. The regularized solution is obtained as

$$\hat{\mathbf{x}}_\alpha = (\mathbf{A}^T\mathbf{Q_y}^{-1}\mathbf{A} + \alpha\mathbf{R})^{-1}\mathbf{A}^T\mathbf{Q_y}^{-1}\mathbf{y} \tag{4.23}$$

with the regularization parameter α and a symmetric positive (semi-)definite regularization matrix $\mathbf{R}$. This estimate minimizes the penalized LS functional

$$\Phi_\alpha(\mathbf{x}) = (\mathbf{y} - \mathbf{A}\mathbf{x})^T \mathbf{Q_y}^{-1}(\mathbf{y} - \mathbf{A}\mathbf{x}) + \alpha \mathbf{x}^T \mathbf{R}\mathbf{x}. \tag{4.24}$$

It can be shown that the solution $\hat{\mathbf{x}}_\alpha$ depends continuously on the data $\mathbf{y}$ (e.g. Kress (1989)).

From Eq. (4.23) it is clear that both the choice of regularization matrix and regularization parameter play an important role in obtaining an optimal solution. Bouman (1998) compared signal constraint with first- and second-derivative constraints for the downward continuation of airborne gravity data. The results for the first- and second-derivative constraints were comparable and slightly better than the signal constraint. In Bouman (2000), however, it was found that for global gravity field modeling the signal constraint was slightly preferable, but differences were small. The choice of the regularization matrix $\mathbf{R}$ thus seems to depend on the application and more than one should be considered. In this thesis, the regularization with signal constraint, also called zero-order Tikhonov regularization (ZOT), will be compared with the first-derivative constraint, called first-order Tikhonov regularization (FOT), and least-squares collocation.

Zero-order Tikhonov regularization (ZOT)

For spherical harmonics, zero-order Tikhonov (ZOT) regularization is equivalent to minimizing the L_2-norm of the disturbing potential on a sphere with radius R, which results in a regularization matrix equal to unity. For the base functions used here, defined by Eq. (4.7), it means that the L_2-norm of the disturbing potential is minimized at $z = 0$. The derivation of the ZOT matrix, which is given in appendix D, is done in the same way as in Ditmar et al. (2003) for spherical harmonics. The regularization term in the objective function of Eq. (4.24) is defined as

$$\Phi^{\text{ZOT}} = \iint_D T^2(x, y, z)\mathrm{d}x\,\mathrm{d}y, \tag{4.25}$$

where the integration domain D is the computation area. Inserting the expression of Eq. (4.7) into the regularization condition of Eq. (4.25) and changing the order of integration and summation yields

$$\Phi^{\text{ZOT}} = \frac{D_x D_y}{4}\, \mathbf{x}^T \mathbf{R}^{\text{ZOT}}\mathbf{x}, \tag{4.26}$$

where the entries of $\mathbf{R}^{\text{ZOT}}$ are given as (see appendix D)

$$\mathbf{R}_{ij}^{\text{ZOT}} = \begin{cases} 4\,\delta_{ij}\, e^{-2\gamma_{l_i m_i}z}, & \text{if } l_i = m_i = 0 \\ 2\,\delta_{ij}\, e^{-2\gamma_{l_i m_i}z}, & \text{if } l_i = 0 \text{ or } m_i = 0 \\ \delta_{ij}\, e^{-2\gamma_{l_i m_i}z}, & \text{otherwise.} \end{cases} \tag{4.27}$$

Note that the ZOT regularization matrix would also be equal to the unity for this case, if the base functions were normalized. Furthermore, the constant term $D_x D_y/4$ in Eq. (4.26) can be ignored since the regularization matrix has to be scaled by the regularization parameter α. Then, in case of orthonormal base functions, ZOT regularization is equivalent to adding $\alpha \mathbf{I}$ to the normal matrix.

First-order Tikhonov regularization (FOT)

Analogous to the derivation of ZOT regularization, the expression for first-order regularization can be derived. Instead of the gravity potential itself, the horizontal gradient of the gravity potential at $z = 0$ is minimized, i.e.

$$\Phi^{\text{FOT}} = \iint\limits_{D} (\nabla_H T(x, y, z))^2 \mathrm{d}x \, \mathrm{d}y, \tag{4.28}$$

where ∇_H is the surface gradient operator

$$\nabla_H = \begin{pmatrix} \frac{\partial}{\partial x} \\ \frac{\partial}{\partial y} \\ 0 \end{pmatrix}.$$

Inserting the expression for the disturbing potential Eq. (4.7) into the regularization condition above and using the orthogonality properties of the sine and cosine functions, the following expression is obtained

$$\Phi^{\text{FOT}} = \frac{D_x D_y}{4} \, \mathbf{x}^T \mathbf{R}^{\text{FOT}} \mathbf{x}, \tag{4.29}$$

where D_x and D_y denote the size of the area. The elements of the regularization matrix $\mathbf{R}^{\text{FOT}}$ are given as

$$\mathbf{R}_{ij}^{\text{FOT}} = \begin{cases} 0 & \text{if } l_i = m_i = 0 \\ 2\,\delta_{ij}(\alpha_{l_i}^2 + \beta_{m_i}^2)\,e^{-2\gamma_{l_i m_i} z}, & \text{if } l_i = 0 \text{ or } m_i = 0 \\ \delta_{ij}(\alpha_{l_i}^2 + \beta_{m_i}^2)\,e^{-2\gamma_{l_i m_i} z}, & \text{otherwise.} \end{cases} \tag{4.30}$$

with α_l, β_m and γ_{lm} being defined by Eq. (4.5).

4.3.2 Regularization error

Although regularization stabilizes the solution of Eq. (4.16), it is not obtained without a penalty. Regularization namely introduces a bias into the solution. Furthermore, instead of obtaining the solution $\hat{\mathbf{x}}$ from error-free data, the regularized solution $\hat{\mathbf{x}}_\alpha^\varepsilon$ is obtained from erroneous data $\mathbf{y}^\varepsilon$. The total error in the solution is given as (Bouman, 1998)

$$\delta\hat{\mathbf{x}} = \hat{\mathbf{x}}_\alpha^\varepsilon - \hat{\mathbf{x}} = \mathbf{N}_\alpha^{-1} \mathbf{A}^T \mathbf{Q}_y^{-1}(\mathbf{y}^\varepsilon - \mathbf{y}) + (\mathbf{N}_\alpha^{-1} - \mathbf{N}^{-1})\mathbf{A}^T \mathbf{Q}_y^{-1}\mathbf{y}, \tag{4.31}$$

where $\mathbf{N}_\alpha = (\mathbf{A}^T\mathbf{Q}_y^{-1}\mathbf{A} + \alpha\mathbf{R})$. The first term on the right-hand side is called the data error, the second one is the regularization error. Bouman (1998) shows that the latter term is equal to the bias as studied in Xu (1992a,b). Because $E\{(\mathbf{y}^\varepsilon - \mathbf{y})\} = 0$, the expectation of the total error $\delta\hat{\mathbf{x}}$ yields

$$
\begin{aligned}
E\{\delta\hat{\mathbf{x}}\} = \Delta x &= \left((\mathbf{A}^T\mathbf{Q}_y^{-1}\mathbf{A} + \alpha\mathbf{R})^{-1} - (\mathbf{A}^T\mathbf{Q}_y^{-1}\mathbf{A})^{-1}\right)\mathbf{A}^T\mathbf{Q}_y^{-1}\mathbf{A}\mathbf{x} \\
&= (\mathbf{A}^T\mathbf{Q}_y^{-1}\mathbf{A} + \alpha\mathbf{R})^{-1}(\mathbf{A}^T\mathbf{Q}_y^{-1}\mathbf{A} + \alpha\mathbf{R} - \alpha\mathbf{R})\mathbf{x} - \mathbf{I}\mathbf{x} \\
&= -(\mathbf{A}^T\mathbf{Q}_y^{-1}\mathbf{A} + \alpha\mathbf{R})^{-1}\alpha\mathbf{R}\mathbf{x},
\end{aligned}
\tag{4.32}
$$

which is only equal to zero if $\alpha = 0$.

4.3.3 Relation to least-squares collocation

The least-squares collocation formula for data with observation noise $\mathbf{y}^\varepsilon = \mathbf{y} + \varepsilon$, given in section 3.2.3, may be written as

$$
\mathbf{x}^\varepsilon = \mathbf{C}_{xy}(\mathbf{C}_{yy} + \mathbf{C}_{\varepsilon\varepsilon})^{-1}\mathbf{y}^\varepsilon,
\tag{4.33}
$$

where $\mathbf{x}$ is the signal to be recovered, $\mathbf{C}_{yy}$ is the signal auto-covariance matrix of $\mathbf{y}$, $\mathbf{C}_{xy}$ is the cross-covariance matrix between $\mathbf{x}$ and $\mathbf{y}$ and $\mathbf{C}_{\varepsilon\varepsilon}$ is the noise covariance matrix. The signal and noise are here assumed to be uncorrelated. Using the relations

$$
\begin{aligned}
\mathbf{C}_{xy} &= \mathbf{C}_{xx}\mathbf{A}^T \\
\mathbf{C}_{yy} &= \mathbf{A}\mathbf{C}_{xx}\mathbf{A}^T,
\end{aligned}
$$

and setting $\mathbf{C}_{\varepsilon\varepsilon} = \sigma^2\mathbf{I}$, Eq. (4.33) can be written as (Rummel et al., 1979; Bouman, 1998)

$$
\begin{aligned}
\mathbf{x}^\varepsilon &= \mathbf{C}_{xx}\mathbf{A}^T(\mathbf{A}\mathbf{C}_{xx}\mathbf{A}^T + \sigma^2\mathbf{I})^{-1}\mathbf{y}^\varepsilon \\
&= (\sigma^{-2}\mathbf{A}^T\mathbf{A} + \mathbf{C}_{xx}^{-1})^{-1}\mathbf{A}^T\mathbf{y}^\varepsilon \\
&= (\mathbf{A}^T\mathbf{A} + \sigma^2\mathbf{C}_{xx}^{-1})^{-1}\mathbf{A}^T\mathbf{y}^\varepsilon.
\end{aligned}
\tag{4.34}
$$

which is the minimization of

$$
\Phi_{\alpha=1}(\mathbf{x}) = \|\mathbf{A}\mathbf{x} - \mathbf{y}\|_{\mathbf{C}_{\varepsilon\varepsilon}}^2 + \|\mathbf{x}\|_{\mathbf{C}_{xx}^{-1}}^2.
\tag{4.35}
$$

Comparing Eq. (4.34) with Eq. (4.23) it is clear that, with $\mathbf{R} = \sigma^2\mathbf{C}_{xx}^{-1}$, Tikhonov regularization and least-squares collocation are formally equivalent. The only difference is a factor α, which is usually set equal to one in least-squares collocation. Naturally, this factor is implicitly used if σ^2 is set to a different value than the actual observation noise. The obtained relation shows that LSC is a special kind of regularization method which provides a statistical motivation to a particular choice of regularization matrix.

4.3.4 Parameter choice rule

The crucial point in obtaining a stable solution when using a regularization method such as Tikhonov regularization is the selection of the regularization parameter α. This parameter controls the trade-off between the accuracy and the degree of smoothness of the solution. In this thesis two approaches will be used: Generalized cross-validation (GCV) and Variance Components Estimation (VCE). Both methods are heuristic a posteriori methods, which means that the methods do not depend on prior assumptions concerning the unknown solution, but are based on the actual data, and that exact knowledge of the variance factor is not required.

Generalized cross-validation (GCV)

The method of generalized cross-validation for finding the optimal regularization parameter was first proposed by Golub et al. (1979). The idea of cross-validation is that if an arbitrary element of the observation vector is left out, the corresponding regularized solution should predict this observation well. The regularization parameter that gives the optimal solution is the one for which the cross-validation function is minimal, which is denoted by *arg min*. Assuming uncorrelated observations of equal weight, the ordinary cross-validation parameter α_{cv} is given as

$$
\alpha_{cv} = \arg\min \frac{1}{n} \sum_{k=1}^{n} \left((\mathbf{A}\hat{\mathbf{x}}_{\alpha}^{[k]})_k - y_k \right)^2
$$

$$
= \arg\min \frac{1}{n} \sum_{k=1}^{n} \frac{((\mathbf{A}\hat{\mathbf{x}}_{\alpha})_k - y_k)^2}{(1 - Q_{kk}^{\alpha})^2}, \tag{4.36}
$$

where n is the number of observations, $\hat{\mathbf{x}}^{[k]}$ is the leave-out-one solution, and Q_{kk}^{α} are the main diagonal elements of the influence matrix $\mathbf{Q}^{\alpha}$, defined as

$$
\mathbf{Q}^{\alpha} = \mathbf{A}(\mathbf{A}^T\mathbf{A} + \alpha\mathbf{R})^{-1}\mathbf{A}^T. \tag{4.37}
$$

For the derivation of the second expression in Eq. (4.36) see Golub and Van Loan (1996). For the computation of the generalized cross-validation parameter α_{gcv}, the weights $(1 - Q_{kk}^{\alpha})$ are replaced by their average, which is trace$(\mathbf{I} - \mathbf{Q}^{\alpha})/n$, resulting in

$$
\alpha_{gcv} = \arg\min \frac{n\|\mathbf{A}\hat{\mathbf{x}}_{\alpha} - \mathbf{y}\|^2}{(\text{trace}(\mathbf{I} - \mathbf{Q}^{\alpha}))^2}. \tag{4.38}
$$

In the presence of colored noise, which is the case for unfiltered airborne gravity measurements, Eq. (4.38) has to be de-correlated using the inverse covariance matrix $\mathbf{Q_y}^{-1}$. Furthermore, the denominator may be rewritten using the relation trace$(\mathbf{AB}) = \text{trace}(\mathbf{BA})$. Then, the expression for the GCV parameter becomes

$$
\alpha_{gcv} = \arg\min \frac{n\|\mathbf{A}\hat{\mathbf{x}}_{\alpha} - \mathbf{y}\|_{\mathbf{Q_y}^{-1}}^2}{(n - u + \alpha\mathcal{T}_{\alpha})^2}, \tag{4.39}
$$

with

$$\mathcal{T}_\alpha = \text{trace}(\mathbf{L}(\mathbf{A}^T\mathbf{Q_y}^{-1}\mathbf{A} + \alpha\mathbf{R})^{-1}\mathbf{L}^T), \tag{4.40}$$

where the regularization matrix is decomposed as $\mathbf{R} = \mathbf{L}^T\mathbf{L}$. For large scale problems, the computation of the trace term, which includes the computation of the inverse normal matrix, may become time consuming or even impossible. The numerical efficiency can be improved by using stochastic trace estimation (STE) (Girard, 1989). The use of STE in GCV was discussed in the context of global gravity field modeling by Kusche and Klees (2002). An unbiased estimation of the trace term can be obtained as

$$\hat{\mathcal{T}}_\alpha = \mathbf{z}^T\mathbf{L}(\mathbf{A}^T\mathbf{Q_y}^{-1}\mathbf{A} + \alpha\mathbf{R})^{-1}\mathbf{L}^T\mathbf{z}, \tag{4.41}$$

where $\mathbf{z}$ is a random vector with

$$E\{\mathbf{z}\} = 0, \qquad D\{\mathbf{z}\} = \mathbf{I}. \tag{4.42}$$

Following (Hutchinson, 1990), the vector $\mathbf{z}$ contains independent samples of the values $+1$ and -1 with equal probability. The computation of the estimator $\hat{\mathcal{T}}_\alpha$ is done in three steps:

1. Generate a random vector $\mathbf{z}$,

2. solve the system $(\mathbf{A}^T\mathbf{Q_y}^{-1}\mathbf{A} + \alpha\mathbf{R})\mathbf{q}_\alpha = \mathbf{L}^T\mathbf{z}$ for $\mathbf{q}_\alpha$, and

3. compute $\hat{\mathcal{T}}_\alpha = \mathbf{z}^T\mathbf{L}\mathbf{q}_\alpha$.

In order to find the minimum of the GCV function, golden section search (Kiefer, 1953) can be applied.

Variance component estimation (VCE)

The regularization of the system Eq. (4.16) can also be interpreted as adding prior information. Then, the regularization parameter can be obtained as the ratio of two variance components, as proposed by Arsenin and Krianev (1992). It is a special case of a scenario with heterogeneous data divided in p observation groups, for which the observation model of each group can be written as (see e.g. Koch and Kusche (2002))

$$\mathbf{y}_i = \mathbf{A}_i\mathbf{x} + \mathbf{e}_i, \quad E\{\mathbf{e}_i\} = \mathbf{0}, \quad D\{\mathbf{y_i}|\sigma_i^2\} = \sigma_i^2\mathbf{Q}_i, \quad i = 1,\ldots,p \tag{4.43}$$

where σ_i^2 is a variance component that determines the relative weight of observation group i. If the observations are combined with prior information $\boldsymbol{\mu}$, an additional observation group is introduced for which the observation model reads

$$\boldsymbol{\mu} = \mathbf{x} + \mathbf{e}_\mu, \quad D\{\boldsymbol{\mu}|\sigma_\mu^2\} = \sigma_\mu^2\mathbf{Q}_\mu, \tag{4.44}$$

where $\boldsymbol{\mu}$ is a $u \times 1$ vector containing the prior information and $\mathbf{Q}_\mu$ is the cofactor matrix. The variance components σ_i^2 are unknown random parameters as the optimal weighting of

different observations or observations groups is generally not known. The variance component σ_μ^2 is also assumed unknown. Combining equations Eq. (4.43) and (4.44) gives the observation model with unknown variance components (Koch and Kusche, 2002)

$$
\begin{bmatrix} \mathbf{y}_1 \\ \vdots \\ \mathbf{y}_p \\ \boldsymbol{\mu} \end{bmatrix} = \begin{bmatrix} \mathbf{A}_1 \\ \vdots \\ \mathbf{A}_p \\ \mathbf{I} \end{bmatrix} \mathbf{x} + \begin{bmatrix} \mathbf{e}_1 \\ \vdots \\ \mathbf{e}_p \\ \mathbf{e}_\mu \end{bmatrix}, \quad E\left\{ \begin{bmatrix} \mathbf{e}_1 \\ \vdots \\ \mathbf{e}_p \\ \mathbf{e}_\mu \end{bmatrix} \right\} = \mathbf{0},
$$

$$
D\left\{ \begin{bmatrix} \mathbf{y}_1 \\ \vdots \\ \mathbf{y}_p \\ \boldsymbol{\mu} \end{bmatrix} \right\} = \sigma_1^2 \mathbf{P}_1 + \cdots + \sigma_p^2 \mathbf{P}_p + \sigma_\mu^2 \mathbf{P}_\mu, \tag{4.45}
$$

where

$$
\mathbf{P}_1 = \begin{bmatrix} \mathbf{Q}_1 & \cdots & \mathbf{0} & \mathbf{0} \\ \vdots & \ddots & \vdots & \vdots \\ \mathbf{0} & \cdots & \mathbf{0} & \mathbf{0} \\ \mathbf{0} & \cdots & \mathbf{0} & \mathbf{0} \end{bmatrix}, \cdots, \quad \mathbf{P}_p = \begin{bmatrix} \mathbf{0} & \cdots & \mathbf{0} & \mathbf{0} \\ \vdots & \ddots & \vdots & \vdots \\ \mathbf{0} & \cdots & \mathbf{Q}_p & \mathbf{0} \\ \mathbf{0} & \cdots & \mathbf{0} & \mathbf{0} \end{bmatrix},
$$

$$
\mathbf{P}_\mu = \begin{bmatrix} \mathbf{0} & \cdots & \mathbf{0} & \mathbf{0} \\ \vdots & \ddots & \vdots & \vdots \\ \mathbf{0} & \cdots & \mathbf{0} & \mathbf{0} \\ \mathbf{0} & \cdots & \mathbf{0} & \mathbf{Q}_\mu \end{bmatrix}.
$$

The least-squares estimate $\hat{\mathbf{x}}$ of the unknown parameters $\mathbf{x}$ follows from the normal equations

$$
\mathbf{N}\hat{\mathbf{x}} = \mathbf{b}, \tag{4.46}
$$

with

$$
\mathbf{N} = \frac{1}{\sigma_1^2}\mathbf{A}_1^T\mathbf{Q}_1^{-1}\mathbf{A}_1 + \cdots + \frac{1}{\sigma_p^2}\mathbf{A}_p^T\mathbf{Q}_p^{-1}\mathbf{A}_p + \frac{1}{\sigma_\mu^2}\mathbf{Q}_\mu^{-1}, \tag{4.47}
$$

$$
\mathbf{b} = \frac{1}{\sigma_1^2}\mathbf{A}_1^T\mathbf{Q}_1^{-1}\mathbf{y}_1 + \cdots + \frac{1}{\sigma_p^2}\mathbf{A}_p^T\mathbf{Q}_p^{-1}\mathbf{y}_p + \frac{1}{\sigma_\mu^2}\mathbf{Q}_\mu^{-1}\boldsymbol{\mu}. \tag{4.48}
$$

For the processing of airborne gravity data each flight track can be considered as a separate observation group. In that case a variance component has to be estimated for each flight track according to the equations above. If the set of airborne gravity measurements is considered as one observation group $\mathbf{y}_1$ that is combined with the prior information $\boldsymbol{\mu}$, the normal equations are given as

$$
(\frac{1}{\sigma_1^2}\mathbf{A}_1^T\mathbf{Q}_1^{-1}\mathbf{A}_1 + \frac{1}{\sigma_\mu^2}\mathbf{Q}_\mu^{-1})\hat{\mathbf{x}} = \frac{1}{\sigma_1^2}\mathbf{A}_1^T\mathbf{Q}_1^{-1}\mathbf{y}_1 + \frac{1}{\sigma_\mu^2}\mathbf{Q}_\mu^{-1}\boldsymbol{\mu}. \tag{4.49}
$$

Introducing the regularization parameter α as the ratio of the two variance components

$$\alpha = \frac{\sigma_1^2}{\sigma_\mu^2}, \tag{4.50}$$

this can be rewritten as

$$(\mathbf{A}_1^T\mathbf{Q}_1^{-1}\mathbf{A}_1 + \alpha\mathbf{Q}_\mu^{-1})\hat{\mathbf{x}} = \mathbf{A}_1^T\mathbf{Q}_1^{-1}\mathbf{y}_1 + \alpha\mathbf{Q}_\mu^{-1}\boldsymbol{\mu}. \tag{4.51}$$

For $\boldsymbol{\mu} = \mathbf{0}$ the last term on the right-hand side of Eq. (4.51) is zero and the solution for Tikhonov regularization is obtained with $\mathbf{R} = \mathbf{Q}_\mu^{-1}$.

Starting from approximate values, the unknown variance components σ_1^2 and σ_μ^2 are computed iteratively until convergence is reached. For the estimation of the components several approaches have been proposed (see e.g. Crocetto et al. (2000); Van Loon (2008)). When the iterative maximum-likelihood method is used, the estimates are obtained as

$$\hat{\sigma}_1^2 = \frac{\hat{\mathbf{e}}_1^T\mathbf{Q}_1^{-1}\hat{\mathbf{e}}_1}{r_1} \quad \text{and} \quad \hat{\sigma}_\mu^2 = \frac{\hat{\mathbf{e}}_\mu^T\mathbf{Q}_\mu^{-1}\hat{\mathbf{e}}_\mu}{r_\mu}, \tag{4.52}$$

where $\hat{\mathbf{e}}_1$ and $\hat{\mathbf{e}}_\mu$ denote the vectors of residuals

$$\hat{\mathbf{e}}_1 = \mathbf{A}_1\hat{\mathbf{x}} - \mathbf{y}_1 \quad \text{and} \quad \hat{\mathbf{e}}_\mu = \hat{\mathbf{x}} - \boldsymbol{\mu}, \tag{4.53}$$

and r_1 and r_μ the partial redundancies, i.e. the contributions of, respectively, the observations $\mathbf{y}_1$ and the prior information $\boldsymbol{\mu}$ to the overall redundancy $(n + u) - u = n$. The partial redundancies are computed as (Koch and Kusche, 2002)

$$r_1 = n_1 - \text{tr}(\frac{1}{\sigma_1^2}\mathbf{A}_1^T\mathbf{Q}_1^{-1}\mathbf{A}_1\mathbf{N}^{-1}), \quad n_1 = n$$

$$r_\mu = u - \text{tr}(\frac{1}{\sigma_\mu^2}\mathbf{Q}_\mu^{-1}\mathbf{N}^{-1}), \tag{4.54}$$

with

$$\mathbf{N} = \frac{1}{\sigma_1^2}\mathbf{A}_1^T\mathbf{Q}_1^{-1}\mathbf{A}_1 + \frac{1}{\sigma_\mu^2}\mathbf{Q}_\mu^{-1}. \tag{4.55}$$

The computation of the trace term to obtain the partial redundancies in Eq. (4.54) requires the inversion of the normal matrix $\mathbf{N}$, which may not be possible or too time consuming for a large number of gravity field parameters. Similar to the problem of generalized cross-validation, discussed in the previous section, the numerical efficiency can be improved using stochastic trace estimation.

4.4 Frequency-dependent data weighting

The standard approach to deal with the extremely large noise in airborne gravity measurements is to apply an aggressive low-pass filtering to the data, which was discussed

in section 3.1.1. However, low-pass filtering also deteriorates (part of) the signal. Generally, a larger filter length leads to less noise in the obtained signal, but the signal gets attenuated as well, which limits the resolution of the gravity signal. Furthermore, noise in the filtered signal is often assumed to be white in the frequency band of interest, which is generally not the case.

Unfiltered airborne gravity measurements are contaminated by colored noise, i.e. the noise is non-uniformly distributed over the frequencies. For a proper handling of colored noise in the estimation of gravity field modeling, an adequate noise model must be used. Such a model may include a dependence of noise on frequency. Then, the concept of (low-pass) filtering is replaced by the concept of frequency-dependent data weighting. Frequencies at which the noise is large get a lower weight than frequencies at which the noise is small. If the noise statistics are known a maximum of the signal is preserved.

The handling of colored noise in satellite gravimetry data has been discussed by several authors. Schuh (1996) proposed to de-correlate observations and the functional model by autoregressive moving-average (ARMA) filters. This idea was used by Schuh (2003) and Klees et al. (2003) to develop efficient computational algorithms to handle stationary colored noise in solving large systems of equations. The question how to obtain such an ARMA model was discussed in Klees and Broersen (2002). A problem of using de-correlation by filtering is edge effects, that show up at the beginning and at the end of a data segment, thus also when data gaps are present. Klees and Ditmar (2004) proposed a methodology using a PCCG algorithm based on ARMA filters, which does not introduce approximations when applying the inverse covariance matrix, even when there are data gaps. Ditmar and van Eck van der Sluijs (2004) also used the PCCG scheme, but they approximated the noise dependence on frequency by an analytic relationship. Furthermore, Ditmar et al. (2004) showed how this procedure can take non-stationary noise into account.

A generalization of the frequency-dependent data weighting approach was given by Ditmar et al. (2007), who showed that any dependence of noise on frequency can be combined with non-stationary noise. Furthermore, they discussed how a dependence of noise on frequency can be derived from the data. They successfully applied the developed methodology to the processing of CHAMP (CHAllenging Minisatellite Payload) satellite (Reigber et al., 1996) data.

Here, a review of the developed approach will be given with application to the handling of colored noise in unfiltered airborne gravimetry data.

4.4.1   ARMA filters and Toeplitz systems

When dealing with colored noise, the covariance matrix of the observations will be non-diagonal. Therefore, the inverse Q_y^{-1} cannot be easily computed when the number of observations is large. However, the product $Q_y^{-1}A$ can be considered as the application of Q_y^{-1} to the columns of A. Then, the problem is reduced to solving a system of linear equations with equation matrix Q_y.

If it is assumed that the noise is stationary and if there are no data gaps in the time series of measurements, the covariance matrix is Toeplitz. An efficient method to solve Toeplitz systems has been proposed by Klees et al. (2003), which has a numerical complexity of $O(n)$. The approach uses an ARMA model of the colored noise:

$$\xi_n = \varepsilon_n - \sum_{k=1}^{p} a_{p,k}\xi_{n-k} + \sum_{i=1}^{q} b_{q,i}\varepsilon_{n-i}, \quad n \in \mathcal{Z}, \tag{4.56}$$

where ξ_n is the colored noise process, ε_n is a white noise process with zero mean and variance σ_ε^2, and $\mathcal{Z}$ denotes the set of integer values (for more details see e.g. Brockwell and Davis, 1991). The coefficients $a_{p,k} : k = 1, \ldots, p$ and $b_{q,i} : i = 1, \ldots, q$ are the model parameters and the pair (p, q) defines the order of the ARMA model. There are two special cases: if $p = 0$, the process is a moving-average process of order q (MA(q)), and if $q = 0$, the process is purely autoregressive of order p (AR(p)). Eq. (4.56) can be written in a compact form as

$$A_p(z)\xi_n = B_q(z)\varepsilon_n, \quad n \in \mathcal{Z}, \tag{4.57}$$

or as

$$\xi_n = \frac{B_q(z)}{A_p(z)}\varepsilon_n, \tag{4.58}$$

where $A_p(z)$ and $B_q(z)$ are the polynomials

$$A_p(z) = 1 + \sum_{k=1}^{p} a_{p,k}z^k, \tag{4.59}$$

$$B_q(z) = 1 + \sum_{i=1}^{q} b_{q,i}z^i. \tag{4.60}$$

The z term in the equations above must be interpreted as a shift operator, defined by $z^j\xi_n = \xi_{n-j}$ for arbitrary $j \in \mathcal{Z}$. The sequence ξ_n can be seen as the output of a rational filter with transfer function

$$H(z) = \frac{B_q(z)}{A_p(z)}, \quad |z| \leq 1, \tag{4.61}$$

where the input is a white noise sequence with variance σ_ε^2, i.e. the covariance matrix of a vector $\boldsymbol{\varepsilon} = [\varepsilon_1, \ldots, \varepsilon_N]^T$, is $\sigma_\varepsilon^2\mathbf{I}$. Then, the covariance matrix of the vector $\boldsymbol{\xi} = [\xi_1, \ldots, \xi_N]^T$ is $\tilde{\mathbf{Q}}_\mathbf{y} = \sigma_\varepsilon^2\mathbf{G}\mathbf{G}^T$, where $\mathbf{G}$ is a matrix that relates the output $\mathbf{s}$ of the filter with transfer function $H(z)$ of Eq. (4.61) to the input $\mathbf{t}$ as $\mathbf{s} = \mathbf{G}\mathbf{t}$.

In general, the matrix $\tilde{\mathbf{Q}}_\mathbf{y}$ is only an approximation to the Toeplitz covariance matrix $\mathbf{Q}_\mathbf{y}$ of the colored noise, due to initialization of the filter. However, only a few elements in the upper-left part of the matrix $\tilde{\mathbf{Q}}_\mathbf{y}$ differ significantly from their corresponding elements in $\mathbf{Q}_\mathbf{y}$.

Since the matrix $\mathbf{G}$ is a lower triangular Toeplitz matrix (see e.g. Hayes, 1996), and every Toeplitz matrix is per-symmetric (symmetric about the anti-diagonal), it holds that $\mathbf{G}^T = \mathbf{XGX}$, where $\mathbf{X}$ is the exchange matrix, which has ones on the anti-diagonal and all other elements are zero. Therefore, the matrix $\tilde{\mathbf{Q}}_\mathbf{y}$ can be written as

$$\tilde{\mathbf{Q}}_\mathbf{y} = \sigma_\varepsilon^2 \mathbf{GXGX}. \tag{4.62}$$

Because $\mathbf{X}^{-1} = \mathbf{X}$, the approximate solution of the system $\mathbf{Q}_\mathbf{y}\mathbf{v} = \mathbf{u}$ can now be obtained as

$$\tilde{\mathbf{v}} = \frac{1}{\sigma_\varepsilon^2}\mathbf{X}\,\mathbf{G}^{-1}\,\mathbf{X}\,\mathbf{G}^{-1}\,\mathbf{u}, \tag{4.63}$$

which is schematically shown in figure 4.2. Thus, the approximation $\tilde{\mathbf{v}}$ of $\mathbf{v}$ can be obtained in the following way (Klees et al., 2003; Klees and Ditmar, 2004):

1. Filter $\mathbf{u}$ (filter with transfer function $H(z)^{-1}$);

2. Flip result of step 1 (apply exchange matrix);

3. Filter result of step 2 (filter with transfer function $H(z)^{-1}$);

4. Flip result of step 3 (apply exchange matrix);
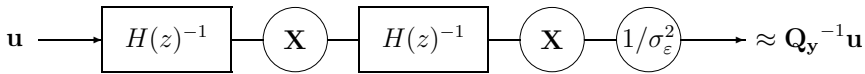
5. Scale result of step 4 with $1/\sigma_\varepsilon^2$.

Figure 4.2: Approximate computation of $\mathbf{Q_y}^{-1}\mathbf{u}$ using ARMA filtering. $H(z)^{-1}$ is the transfer function of the ARMA filter and $\mathbf{X}$ is the exchange matrix. After Klees et al. (2003).

In the presence of data gaps, this approach corrupts the data series before and after each data gap, even if gaps are ignored, or filled with zeroes or interpolated observations, or if data segments separated by data gaps are treated as uncorrelated. The most simple solution is to remove the corrupted segments after filtering from the solution, but this approach has two drawbacks. First, this may lead to significant reduction of redundancy if many gaps are present in the data. For airborne gravimetry each profile is considered a new segment, which means that for each profile the begin and end of the profile would be discarded. Secondly, the symmetry of the covariance matrix is violated and, therefore, the symmetry of the normal matrix, which makes the LS inversion more difficult. The next section discusses an alternative approach, proposed by Klees and Ditmar (2004), that properly handles colored noise in the presence of data gaps.

4.4.2 ARMA filtering in the presence of data gaps

The approach presented in Klees and Ditmar (2004) aims at obtaining the exact solution of $\mathbf{Q}_y\mathbf{v} = \mathbf{u}$ and has the same numerical complexity as the ARMA filtering approach, discussed in the previous section. Furthermore, the approach does not produce any edge effects at the beginning of the data series and in the vicinity of data gaps, and does not rely on discarding data in the course of processing.

The basic idea is to solve the system $\mathbf{Q}_y\mathbf{v} = \mathbf{u}$ iteratively, using a PCCG procedure. Within each iteration this requires the exact multiplication of the variance-covariance matrix with a vector and an approximate multiplication of the inverse covariance matrix with a vector. The second step serves as a pre-conditioning for which the procedure outlined in the previous section offers a fast and efficient way to perform this operation.

The first step, i.e. the multiplication of the covariance matrix to a vector, is a straight-forward series of operations, see Eq. (4.62). However, as mentioned in the previous section, this operation only provides an approximation due to the initialization of the filter. Therefore, the idea of infinite extension of the data, as presented in Klees and Ditmar (2004) and Ditmar and van Eck van der Sluijs (2004), is used. First, it is assumed that the data set contains no data gaps and is infinite in time, i.e. the infinite extensions of $\mathbf{y}$ and $\mathbf{Q_y}$ are denoted by $\mathbf{y}^\infty$ and $\mathbf{Q_y^\infty}$, respectively.

The actual data set can then be obtained from the infinite one by extracting the selected measurements. Such an extraction can be performed by applying a mask matrix $\mathbf{M}$, which can be obtained from the infinite unit matrix by keeping only the rows that correspond to the actual measurements. Thus, the relation between the actual arrays and their infinite counterparts can be written as

$$\mathbf{y} = \mathbf{M}\mathbf{y}^\infty, \tag{4.64}$$

$$\mathbf{Q_y} = \mathbf{M}\mathbf{Q_y^\infty}\mathbf{M}^T. \tag{4.65}$$

Using the latter expression with Eq. (4.62), the covariance matrix can be rewritten as

$$\mathbf{Q_y} = \sigma_\varepsilon^2 \mathbf{M}\mathbf{G}^\infty\mathbf{X}^\infty\mathbf{G}^\infty\mathbf{X}^\infty\mathbf{M}^T. \tag{4.66}$$

Then the computation of $\mathbf{Q_y}\mathbf{d}$ within the PCCG procedure can be obtained by applying the following steps (Klees and Ditmar, 2004):

1. Extend $\mathbf{d}$ with zeroes (apply transposed mask matrix);

2. Flip extended vector $\mathbf{d}_e$ (apply exchange matrix);

3. Filter result of step 2 (filter with transfer function $H(z)$);

4. Flip result of step 3 (apply exchange matrix);

5. Filter result of step 4 (filter with transfer function $H(z)$);

6. Extract required entries from step 5 (apply mask matrix);

7. Scale result of step 6 with σ_ε^2.

The exact computation of $\mathbf{Q_y d}$, which is shown schematically in figure 4.3, would require to extend the vector with infinitely many zeros. However, when the ARMA model is causal and invertible (cf. Brockwell and Davis, 1991), the filter coefficients decay quickly. In practice, the number of zeroes to be added depends on the desirable accuracy of the computation.
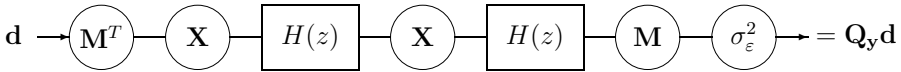
$$\mathbf{d} \rightarrow \mathbf{M}^T - \mathbf{X} - \boxed{H(z)} - \mathbf{X} - \boxed{H(z)} - \mathbf{M} - \sigma_\varepsilon^2 \rightarrow = \mathbf{Q_y d}$$

Figure 4.3: Exact computation of $\mathbf{Q_y d}$ using ARMA filtering. After Klees and Ditmar (2004).

With the described algorithms, the solution of $\mathbf{Q_y v} = \mathbf{u}$ can be computed with the following pre-conditioned conjugate gradient procedure (see also Klees and Ditmar, 2004):

1. $\mathbf{v}_0 = 0$, $\mathbf{r}_0 = \mathbf{u}$, $\tilde{\mathbf{p}}_0 = \mathbf{p}_0 = \mathbf{Q}_y^{-1}\mathbf{v}_0$, $k = 0$;

2. $\mathbf{b}_k = \tilde{\mathbf{p}}_k^T \mathbf{r}_k$;

3. Extend $\mathbf{p}_k$ by adding zeroes for missing data;

4. $\mathbf{a}_k = \mathbf{Q}_y \mathbf{p}_k$ (cf. figure 4.3);

5. Replace elements of $\mathbf{a}_k$ at the locations where data were missing by zeroes;

6. $\gamma_k = \frac{\mathbf{r}_k^T \mathbf{p}_k}{\mathbf{a}_k^T \mathbf{p}_k}$;

7. $\mathbf{v}_{k+1} = \mathbf{v}_k + \gamma_k \mathbf{p}_k$;

8. $\mathbf{r}_{k+1} = \mathbf{r}_k - \gamma_k \mathbf{a}_k$;

9. If $\|\mathbf{r}_{k+1}\| < \epsilon_1$ and difference $(\mathbf{v}_k, \mathbf{v}_{k+1}) < \epsilon_2$, stop;

10. $\tilde{\mathbf{p}}_{k+1} = \mathbf{Q}_y^{-1}\mathbf{r}_{k+1}$ (cf. figure 4.2);

11. $\beta_{k+1} = \frac{\mathbf{r}_{k+1}^T \tilde{\mathbf{p}}_{k+1}}{\mathbf{r}_k^T \tilde{\mathbf{p}}_k}$;

12. $\mathbf{p}_{k+1} = \tilde{\mathbf{p}}_{k+1} + \beta_{k+1}\mathbf{p}_k$;

13. $k = k + 1$, go to item (2).

Note that this PCCG procedure may either be applied in each iteration step of the PCCG procedure for the estimation of the gravity field parameters as described in section 4.2.2, or in the explicit computation of the normal matrix when the Cholesky decomposition is used. In the latter case the filtering operation is applied to the columns of the design matrix $\mathbf{A}$.

4.4.3   Description of the noise model

The procedure described in the previous subsection uses an ARMA model of the colored noise to solve the system $\mathbf{Q_y v} = \mathbf{u}$. This section describes how such an ARMA model can be obtained. First it is assumed that a noise realization or noise power spectral density (PSD) function is given, from which an ARMA model can be estimated. In practice, however, this information is usually not available and must be obtained prior to ARMA model estimation. Two strategies to obtain a noise model are discussed. The first strategy uses an analytically derived filter that can either be used directly in the filtering scheme or it can be used to obtain a PSD that serves as input to ARMA model estimation. Alternatively, a noise model may be obtained from a-posteriori LS residuals, that are used as a first approximation of the colored noise.

ARMA model identification

Usually an ARMA representation is obtained from a noise realization. The corresponding estimation procedure is known as model identification, which is a standard problem in time-series analysis (see e.g. Kay and Marple, 1981; Brockwell and Davis, 1991). There are many situations where, instead of a noise realization, only a noise PSD is available. For example, the expected performance of the gradiometer on board the Gravity Field and Ocean Circulation Explorer (GOCE) satellite (ESA, 1999), is provided by the manufacturer in terms of an estimated noise PSD function. A procedure for ARMA model identification from a PSD function was developed by Klees et al. (2003) and discussed in more detail in Klees and Broersen (2002). Furthermore, Klees and Broersen (2002) presented a modified approach for model identification from a noise realization, which has a better performance when applied to short time-series (few hundred samples). It combines known techniques for model parameter estimation with finite-sample order selection criteria.

The first step in the determination of an ARMA model to represent an observed stationary time series, is the computation of AR, MA, and ARMA models up to a predefined maximum order (p, q). For each model type, the best-fitting model is selected according to a statistical selection criterion. When the best-fitting AR, MA, ARMA models have been identified, the final step is to make a selection among these three, using the minimum prediction error. A detailed discussion is given in Broersen (2000).

When the noise sequence contains gaps or if only a PSD function is available, a slightly different procedure has to be used. The starting point is the computation of the

auto-covariance sequence. From a noise series it can be computed directly, if a PSD is used it is obtained by an inverse Fourier transform. The auto-covariance sequence can be transformed into a very long AR model, which serves as the basis model to estimate and select AR, MA, and ARMA models. After the order of the models is selected, the AR, MA, and ARMA models are estimated as outlined in Klees and Broersen (2002) and Klees et al. (2003). Once the best-fitting AR, MA, and ARMA models are identified, the final step comprises the selection among these three best-fitting models according to a statistical selection criterion.

Note that a noise PSD function contains much less information than a noise realization. Therefore, the method of model identification from a PSD should only be used if a noise realization is not available. In the following it is discussed how a realistic noise PSD function or noise realization can be obtained for airborne gravity measurements.

Analytical filtering

The largest contribution to the noise in airborne gravity measurements comes from the double differentiation of GPS positions, to obtain aircraft accelerations. If the three-point rule is used for the numerical differentiation of vertical aircraft positions h, i.e.

$$f(t) = \frac{\partial^2 h(t)}{\partial t^2} \doteq \frac{h(t - \Delta t) - 2h(t) + h(t + \Delta t)}{\Delta t^2}, \tag{4.67}$$

the noise in the gravity observations due to positioning errors can, according to the law of variance-covariance propagation, be represented as

$$\mathbf{Q_y} = \mathbf{D}\mathbf{Q_h}\mathbf{D}^T, \tag{4.68}$$

where $\mathbf{D}$ is the matrix of double differentiation

$$\mathbf{D} = \frac{1}{\Delta t^2} \begin{bmatrix} 1 & -2 & 1 & & \\ & \ddots & \ddots & \ddots & \\ & & 1 & -2 & 1 \end{bmatrix}, \tag{4.69}$$

and $\mathbf{Q_h}$ describes the noise in the vertical GPS positions. Assuming white noise in the GPS positions, the matrix $\mathbf{Q_h}$ is given as $\sigma_h^2 \mathbf{I}$, with σ_h the standard deviation of the GPS noise.

The inverse variance-covariance matrix $\mathbf{Q_y}^{-1}$ could be obtained if $\mathbf{D}$ would be invertible. Obviously this is not the case; foremost because the matrix $\mathbf{D}$ is not square. Ditmar and van Eck van der Sluijs (2004) apply several steps to make $\mathbf{D}$ invertible: 1) the first and last columns are removed to obtain a square matrix; 2) the top-right and bottom-left corners are filled with value 1; 3) the matrix is made positive-definite by changing the sign; and 4) the matrix is regularized by adding a small value ϵ^2 to the diagonal elements.

The resulting circulant approximation of $\mathbf{D}$ is then given as

$$\tilde{\mathbf{D}} = \frac{1}{\Delta t^2} \begin{bmatrix} 2+\epsilon^2 & -1 & & & & -1 \\ -1 & 2+\epsilon^2 & -1 & & & \\ & \ddots & \ddots & \ddots & & \\ & & -1 & 2+\epsilon^2 & -1 & \\ -1 & & & -1 & -2+\epsilon^2 \end{bmatrix}. \tag{4.70}$$

A circulant matrix is a special kind of Toeplitz matrix where each row vector is rotated one element to the right relative to the preceding row vector. Its inverse, which is also circulant, can be obtained by means of the discrete Fourier transform (Davis, 1979). Following the derivation in Ditmar and van Eck van der Sluijs (2004), the matrix $\tilde{\mathbf{D}}$ is written as

$$\tilde{\mathbf{D}} = \mathbf{F}^* \mathbf{S_D} \mathbf{F}, \tag{4.71}$$

where $\mathbf{F}$ is the matrix of the discrete Fourier transform

$$\{\mathbf{F}\}_{j,k} = e^{i\frac{2\pi(j-1)(k-1)}{N}}, \quad j,k = 1,\ldots,N, \tag{4.72}$$

with N the number of rows/columns of $\tilde{\mathbf{D}}$; $\mathbf{F}^*$ is its transposed complex-conjugate and $\mathbf{S_D}$ is a diagonal matrix, obtained by distributing the discrete Fourier spectrum of the first row of $\tilde{\mathbf{D}}$ along the main diagonal, i.e.

$$\mathbf{S_D} = \text{diag}\left(\frac{1}{N}\mathbf{F}\left\{\tilde{\mathbf{D}}\right\}_1\right). \tag{4.73}$$

Then, the inverse of $\tilde{\mathbf{D}}$ is obtained as

$$\tilde{\mathbf{D}}^{-1} = \frac{1}{N^2}\mathbf{F}^* \mathbf{S_D}^{-1}\mathbf{F}. \tag{4.74}$$

Using Eqs. (4.70), (4.72) and (4.73) the elements of $\mathbf{S_D}$ can be computed analytically as (Ditmar and van Eck van der Sluijs, 2004)

$$\{\mathbf{S_D}\}_{kk} = \frac{1}{N(\Delta t)^2}\left[2(1-\cos(\omega_k \Delta t)) + \left(\frac{\Delta t}{\tau}\right)^2\right], \tag{4.75}$$

where ω_k is the angular frequency (corresponding to the k-th spectral line): $\omega_k = 2\pi k/(N\Delta t)$, and $\tau = \Delta t/\epsilon$ is the filter half-width. The latter determines the noise level of the PSD at low frequencies (Ditmar et al., 2007). The expression of Eq. (4.75) can be used to compute the approximate noise PSD function. The unknown parameters τ and σ_h of the noise representation have to be determined. This can be done using ground truth data, or using the strategy that is discussed in the next subsection.

The computation of the function given in Eq. (4.75) allows a direct analytical implementation of the corresponding noise covariance matrix (see e.g. Liu, 2008). Alternatively, the PSD function can be used to derive an ARMA model as discussed in the previous subsection, which is used in the low-level PCCG scheme as outlined in section 4.4.2. This way, the part of the colored noise, which is the result of double differentiation of vertical GPS positions can be taken into account. A similar approach could be used to model gravimeter noise, of which the largest contributors are spring tension noise and beam velocity noise. The latter is derived from beam positions by numerical differentiation.

Noise estimation from least-squares residuals

In practice, the noise characteristics may be different for each flight due to the sensor used and the flight conditions. Therefore, an approach similar to the one proposed by Liu et al. (2007) and Ditmar et al. (2007) can be used to obtain a noise model of airborne gravity data. It uses the residuals of a preliminary least-squares solution to estimate a noise model, which is used as input to the frequency-dependent data weighting scheme.

The first five steps are equivalent to the procedure presented in Liu (2008).

1. Compute a posteriori residuals $\hat{\mathbf{e}} = \mathbf{y} - \mathbf{A}\hat{\mathbf{x}}$ with $\mathbf{Q}_y = \mathbf{I}$. The residuals are considered as an approximation of the data noise;

2. Estimate the noise auto-covariance function from the a posteriori residuals as

$$c_k = \frac{1}{N_k} \sum_{j=1}^{N_k} e_j e_{j+k} \quad k = 0, \ldots, N_a, \tag{4.76}$$

where e_j and e_{j+k} are LS residuals separated by lag k, N_k is the number of pairs that are used to estimate the k-th auto-covariance element, and N_a is the maximum lag for which the auto-covariance is estimated. In practice, it is advisable to choose $N_a \leq N/10$, where N is the total number of residuals used for the estimation (Klees and Broersen, 2002);

3. Order the auto-covariance elements such that the element with index zero is the first one: $\mathbf{c} = (c_0, c_1, \ldots, c_{N_a-1}, c_{N_a}, c_{N_a-1}, \ldots, c_1)$;

4. Truncate the auto-covariance elements to ensure that the estimated PSD (step 5) is positive for all frequencies. The auto-covariances are multiplied by a truncation function that rapidly decreases in time:

$$\tilde{c}_k := c_k w_k, \quad k = 0, \ldots, N_a, \tag{4.77}$$

with

$$w_k = e^{-\frac{(k\Delta t)^2}{2Q^2}}, \tag{4.78}$$

where Q is the maximum possible half-width of the truncation function, which can be determined empirically.

5. Estimate the noise PSD $u(f)$. The noise PSD can be estimated from the auto-covariance sequence trough a discrete Fourier transformation (Kay and Marple, 1981):

$$\mathbf{u} \approx \Delta t \mathbf{F}^* \mathbf{c}, \tag{4.79}$$

where $\mathbf{F}^*$ is the conjugate transpose of the matrix of the discrete Fourier transform $\mathbf{F}$ (Eq. (4.72)), and Δt is the sampling interval.

6. Estimate the ARMA model from the PSD as outlined in the first part of this sub-section (ARMA model identification) (see also Klees and Broersen, 2002).

When analytical filtering is used instead of an ARMA model, the steps described above can directly be used to obtain the noise covariance matrix.

The derived noise model can be used in a second iteration to compute a new set of a posteriori residuals from which an improved noise model can be derived. Ditmar et al. (2007) argued that for highly redundant computational problems, such as global gravity field modeling, two iterations are sufficient. The developed methodology was tested by Liu et al. (2007) for simulated CHAMP data. They showed that the procedure works best in case of purely stationary noise. In chapters 5 and 6 it will be investigated how many iterations are required to obtain a model of the colored noise in airborne gravity data and how accurately the actual noise model can be derived.

4.5 Estimation of non-gravitational parameters

4.5.1 Bias and drift handling

As discussed in section 3.1.2, the traditional processing of gravity data includes a cross-over adjustment to deal with remaining low-frequency errors in the data. This is done by minimizing gravity differences at cross-over locations between crossing flight lines. This method of adjustment of cross-over misfits has several disadvantages such as the requirement of a close coincidence of measurement points at crossing lines, which means that observations must be acquired at about the same altitude, and the limited number of cross-overs that are available for the estimation of bias and drift parameters.

Within the methodology described in this chapter, the handling of bias and drift parameters is combined with the estimation of the gravity field parameters. The bias and drift parameters can be included in the functional model, Eq. (4.13), and estimated jointly with the potential coefficients. The advantage of this approach is that it does not require the computation of cross-overs, which means that a close coincidence of flight lines at cross-over points is not required. Furthermore, the redundancy for estimating the parameters is much higher as all observations are used in the estimation. Although the com-

putation of cross-overs is not required, connecting control lines are still needed, because otherwise the estimated bias parameters would absorb the mean value of each profile.

Alternatively, the bias and drift parameters can be removed from the data, by setting up a covariance matrix that filters out the low-frequency noise. It can easily be shown that both methods, estimation and filtering, lead to exactly the same results.

When the bias and drift parameters are estimated explicitly, the functional model changes to

$$\mathbf{y} = \mathbf{A}\mathbf{x} + \mathbf{B}\mathbf{q} + \mathbf{e}, \tag{4.80}$$

where the vector $\mathbf{q} = [d^1, b^1, \ldots, d^p, b^p]^T$ contains the drift and bias parameters d^i and b^i for each profile $i = 1, \ldots, p$, respectively. The matrix $\mathbf{B}$ reads

$$\mathbf{B} = \begin{bmatrix} 0 & \Delta t_2^1 & \ldots & \Delta t_{n_1}^1 & & & & & & & \\ 1 & 1 & \ldots & 1 & & & & & & & \\ & & & & 0 & \Delta t_2^2 & \ldots & \Delta t_{n_2}^2 & & & \\ & & & & 1 & 1 & \ldots & 1 & & & \\ & & & & & & & & \ddots & & \\ & & & & & & & & & 0 & \Delta t_2^p & \ldots & \Delta t_{n_p}^p \\ & & & & & & & & & 1 & 1 & \ldots & 1 \end{bmatrix}^T . \tag{4.81}$$

where Δt_j^i is the time difference between the start of the i-th flight line and the current observation point j, and n_i is the number of observations along line i.

Alternatively, a filter matrix can be constructed that removes the bias and drift parameters from the data. Consider a linear filter matrix $\mathbf{F}$ with the property $\mathbf{F}\mathbf{B} = 0$. Then, applying this matrix to Eq. (4.80) gives

$$\mathbf{F}\mathbf{y} = \mathbf{F}\mathbf{A}\mathbf{x} + \mathbf{F}\mathbf{B}\mathbf{q} + \mathbf{F}\mathbf{e} = \mathbf{F}\mathbf{A}\mathbf{x} + \mathbf{F}\mathbf{e}, \tag{4.82}$$

i.e. the parameters $\mathbf{q}$ are eliminated from the functional model. The filter matrix is obtained as follows. Let $\mathbf{F}_1$ be the projection matrix onto the column space of $\mathbf{B}$, defined as

$$\mathbf{F}_1 = \mathbf{B}(\mathbf{B}^T\mathbf{Q_y}^{-1}\mathbf{B})^{-1}\mathbf{B}^T\mathbf{Q_y}^{-1}. \tag{4.83}$$

Then $\mathbf{F} := \mathbf{I} - \mathbf{F}_1$ satisfies $\mathbf{F}\mathbf{B} = 0$. Furthermore, the matrix $\mathbf{F}\mathbf{Q_y}$ is symmetric, i.e. $\mathbf{F}\mathbf{Q_y} = \mathbf{Q_y}\mathbf{F}^T$. Because $\mathbf{F}\mathbf{F} = \mathbf{F}$ holds, the matrix $\mathbf{F}\mathbf{Q_y}\mathbf{F}^T$ can be written as $\mathbf{F}\mathbf{Q_y}$. The filter matrix $\mathbf{F}$ has rank $n - q$ (with q the number of parameters to be eliminated). Therefore, the matrix $\mathbf{F}\mathbf{Q_y}\mathbf{F}^T$ is singular with rank defect q, and its Caley inverse does not exist. A generalized inverse of $\mathbf{F}\mathbf{Q_y}\mathbf{F}^T$ is obtained as

$$(\mathbf{F}\mathbf{Q_y}\mathbf{F}^T)^- = \mathbf{Q_y}^{-1}\mathbf{B}(\mathbf{B}^T\mathbf{Q_y}^{-1}\mathbf{B})^{-1}\mathbf{B}^T\mathbf{Q_y}^{-1} = \mathbf{Q_y}^{-1}\mathbf{F}. \tag{4.84}$$

Using this expression, the least-squares solution $\hat{\mathbf{x}}$ after elimination of the parameters $\mathbf{q}$, becomes

$$\hat{\mathbf{x}} = (\mathbf{A}^T\tilde{\mathbf{Q}}_\mathbf{y}^{-1}\mathbf{A})^{-1}\mathbf{A}^T\tilde{\mathbf{Q}}_\mathbf{y}^{-1}\mathbf{y}, \tag{4.85}$$

65

with

$$\tilde{\mathbf{Q}}_\mathbf{y}^{-1} = \mathbf{F}^T \mathbf{Q_y}^{-1} \mathbf{F} = \mathbf{Q_y}^{-1} \mathbf{F}. \tag{4.86}$$

The same result can be obtained in a straightforward way using the least-squares solution of the Gauss Markov model (Eq. (4.80)):

$$\begin{bmatrix} \mathbf{A}^T \mathbf{Q_y}^{-1} \mathbf{A} & \mathbf{A}^T \mathbf{Q_y}^{-1} \mathbf{B} \\ \mathbf{B}^T \mathbf{Q_y}^{-1} \mathbf{A} & \mathbf{B}^T \mathbf{Q_y}^{-1} \mathbf{B} \end{bmatrix} \begin{bmatrix} \hat{\mathbf{x}} \\ \hat{\mathbf{q}} \end{bmatrix} = \begin{bmatrix} \mathbf{A}^T \mathbf{Q_y}^{-1} \mathbf{y} \\ \mathbf{B}^T \mathbf{Q_y}^{-1} \mathbf{y} \end{bmatrix}. \tag{4.87}$$

The parameters $\hat{\mathbf{q}}$ can be eliminated using the second equation

$$\hat{\mathbf{q}} = -(\mathbf{B}^T \mathbf{Q_y}^{-1} \mathbf{B})^{-1} \mathbf{B}^T \mathbf{Q_y}^{-1} \mathbf{A} \hat{\mathbf{x}} + (\mathbf{B}^T \mathbf{Q_y}^{-1} \mathbf{B})^{-1} \mathbf{B}^T \mathbf{Q_y}^{-1} \mathbf{y}. \tag{4.88}$$

Inserting the expression into the first equation of Eq. (4.87), and using the definition of the filter matrix $\mathbf{F}$, the LS solution of Eq. (4.85) is obtained.

Note that it is not necessary to compute the new covariance matrix $\tilde{\mathbf{Q}}_\mathbf{y}^{-1}$ explicitly as it can be considered as a series of matrix multiplications which are solved in the same manner as discussed in section 4.4.2.

For the most simple case, when n observations contain only a bias and are contaminated by white noise ($\mathbf{Q_y} = \mathbf{I}$), the matrix $\mathbf{B}$ becomes $\mathbf{B} = [\,1\ 1\ \ldots\ 1\,]^T$ and the filter matrix simplifies to

$$\mathbf{F} = \begin{bmatrix} 1 - 1/n & -1/n & \ldots & -1/n \\ \vdots & \vdots & & \vdots \\ -1/n & -1/n & \ldots & 1 - 1/n \end{bmatrix}. \tag{4.89}$$

In case both a bias and drift are to be eliminated, the entries of the projection matrix $\mathbf{F}_1$ are obtained as

$$\{\mathbf{F}_1\}_{lk} = \frac{1}{\det} \left[\sum t_i^2 - (t_l + t_k) \sum t_i + t_l t_k n \right], \quad l, k = 1, \ldots, n, \tag{4.90}$$

with

$$\det = n \sum t_i^2 - \left(\sum t_i \right)^2. \tag{4.91}$$

Both cases can be easily extended for the elimination of bias and drift from each profile, resulting in a block diagonal matrix, with the blocks build up either by Eq. (4.89) or by Eq. (4.90). In case of colored noise, the entries of $\mathbf{F}_1$ are obtained by a series of matrix computations described in Eq. (4.83).

4.5.2 Estimation of scale factors

Airborne gravimeter measurements, such as spring tension and beam velocities, are related to actual gravity observations by applying several scale factors. The LaCoste and Romberg air/sea gravimeter, used for the acquisition of the data sets described in sections

6.1 and 6.2, consists of a highly damped, spring-type gravity sensor mounted on a gyro-stabilized platform. Because of the high damping, the motion of the gravity meter beam can be described by the following differential equation (Valliant, 1992)

$$g + \ddot{z} + k\dot{B} - cS = 0, \tag{4.92}$$

where g denotes gravity, $\ddot{z}$ is the vertical acceleration with z positive in the upward direction, $\dot{B}$ is the beam velocity, S is the spring tension and k and c are scaling factors. This equation is just an approximation and correction terms, known as cross-coupling, have to be applied. The scaling factor k, generally referred to as the k-factor, and the scaling factor c (or spring tension calibration factor) may be determined by laboratory calibration. An alternative method to determine the k-factor is given in Olesen et al. (1997).

In this thesis the scaling factors are estimated simultaneously with the gravity parameters, by incorporating beam velocities and/or spring tension values in the functional model. The functional model for estimating one k-factor for the whole data set then becomes

$$\tilde{\mathbf{y}} = \mathbf{A}\mathbf{x} - \mathbf{K}\delta k + \mathbf{e}; \quad D\{\mathbf{e}\} = \mathbf{Q_y}, \tag{4.93}$$

where $\mathbf{K} = [\dot{B}_1 \ \dot{B}_2 \cdots \dot{B}_m]^T$ and δk is the correction to the k-factor k_p that was initially used in the pre-processing, i.e. the estimated k-factor is obtained as $\hat{k} = k_p + \delta\hat{k}$. The model can easily be extended for the estimation of one k-factor per profile, in the same way as for the estimation of bias and drift parameters (see previous subsection). The same holds for the estimation of the spring tension calibration factor.

4.5.3   Testing of non-gravitational parameters

By including additional parameters, the fit of the data to the model can be improved. However, adding more parameters is not necessarily an improvement of the gravity model since they may absorb part of the gravity signal. Furthermore, the parameters may be highly correlated, which means that they should not be estimated simultaneously. It is therefore necessary to test whether the parameters are statistically significant and compute the statistical correlation.

The statistical correlation coefficient $\rho_{\hat{x}\hat{y}}$ between to estimated variables $\hat{x}$ and $\hat{y}$ is computed as

$$\rho_{\hat{x}\hat{y}} = \frac{\sigma_{\hat{x}\hat{y}}}{\sigma_{\hat{x}}\sigma_{\hat{y}}}, \tag{4.94}$$

where the covariance $\sigma_{\hat{x}\hat{y}}$ between $\hat{x}$ and $\hat{y}$, and the standard deviations $\sigma_{\hat{x}}$ and $\sigma_{\hat{y}}$ can be obtained from $\mathbf{Q_{\hat{x}}} = (\mathbf{A}^T\mathbf{Q_y}^{-1}\mathbf{A})^{-1}$. When Cholesky decomposition is used to solve the system of normal equations, it can easily be computed by inverting the normal matrix. If the correlation coefficient ρ is close to one, the estimated parameters are highly correlated.

To test if an estimated parameter $\hat{x}_i$ deviates significantly from a given value x_{0i}, the following two hypotheses are formulated (e.g. Koch, 1999):

$$H_0 : x_i = x_{0i}, \text{for a given } i \in 1, \ldots, u; \quad H_A : x_i \neq x_{0i}, \tag{4.95}$$

67

where H_0 is called the null hypothesis and H_A the alternative hypothesis. These hypotheses are tested against each other with the test statistic

$$T = \frac{(\hat{x}_i - x_{0i})^2}{\hat{\sigma}_i^2}, \tag{4.96}$$

where

$$\hat{\sigma}_i^2 = \hat{\sigma}^2 \sigma_{x_i}. \tag{4.97}$$

The estimator $\hat{\sigma}^2$ of the variance factor of unit weight (or a posterior variance factor) reads

$$\hat{\sigma}^2 = \frac{\hat{\mathbf{e}}^T \mathbf{Q_y}^{-1} \hat{\mathbf{e}}}{n - u}. \tag{4.98}$$

The distribution of T under H_0 and H_A is given as (e.g. Koch, 1999)

$$H_0 : \hat{\sigma}^2 \sim F(1, n - u); \quad H_A : \hat{\sigma}^2 \sim F(1, n - u, \lambda), \tag{4.99}$$

where the non-centrality parameter λ is computed as

$$\lambda = \frac{1}{\sigma^2}(\mathbf{Hx} - x_{0i})(\mathbf{HN}^{-1}\mathbf{H}^T)^{-1}(\mathbf{Hx} - x_{0i}). \tag{4.100}$$

Here, $\mathbf{H}$ is a vector with zeros and the value 1 on the i-th position: $\mathbf{H} = [\,0\,\ldots\,1\,\ldots\,0\,]^T$. Rejecting the H_0-hypothesis implies accepting H_A, which justifies the addition of non-gravitational parameters to the functional model.

4.6 Edge effect reduction

When fundamental solutions of Laplace's equation in Cartesian coordinates are used, the model implicitly assumes that the signal is periodic on the computation domain. For regional gravity field observation this is obviously not the case. The series of Eq. (4.3) only converges to the true signal at points of continuity, but at points of discontinuity to the average of the two limits. As a result, near points of discontinuity, a "ringing" known as the Gibbs phenomenon occurs (see e.g. Bracewell, 2000). Notice that different function values at the opposite borders are also considered discontinuities; it is especially this type of discontinuity that occurs in case of regional gravity field modeling when periodic base functions are used. The Gibbs effect is illustrated in figure 4.4 for a straight line.

In this section, several approaches are discussed that aim at the reduction of the Gibbs effect at the edges. Although edge effects are also caused by neglecting gravity data outside the computation area or as the result of the intrinsic non-uniqueness of the problem (see Prutkin and Klees, 2007), the methods described in this section do not aim at the reduction of this type of errors. The reduction of edge effects may be done in two ways: either by extension of the computation area where the signal is assumed periodic; or by modification of the base functions, such that the requirement of periodicity is circumvented.

4.6.1 Extension of the computation area

Four approaches are introduced that use an extension of the computation area; they are zero padding, cosine taper, least-squares prediction, and controlled area extension, which are schematically shown in figure 4.5. Note that when the area is extended, D_x and D_y become larger and L and M have to be changed accordingly to obtain the same resolution as without extension. The first three approaches were tested by Alberts et al. (2007a), controlled area extension was introduced by Alberts et al. (2007b).

Zero padding

The most simple approach to reduce edge effects is to extend the computation area with zero-observations, i.e. zero-padding, which is a common procedure in discrete Fourier techniques. This way the signal becomes periodic on the larger domain. However, the discontinuity at the (former) edge of the area remains, resulting again in high oscillations. The estimated value at this point equals the average of the two limits at the discontinuity, which is now half the gravity value at the former edge. Therefore, the result of zero-padding can even be worse than if the area is not extended by zero-observations.

Cosine taper

A different way to make the signal periodic is to use a cosine taper. Values $\delta \tilde{g}$ outside the computation area are computed as

$$\delta \tilde{g} = \delta g_e \left(\tfrac{1}{2} \cos \frac{\pi d}{\Delta} + \tfrac{1}{2} \right), \tag{4.101}$$
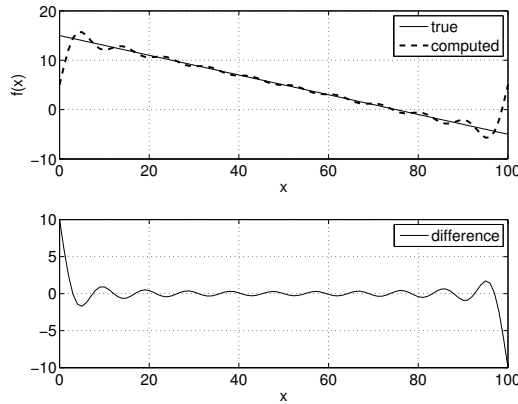
Figure 4.4: The Gibbs effect caused by discontinuities at the edges in 1D, illustrated for maximum degree $L = 10$.
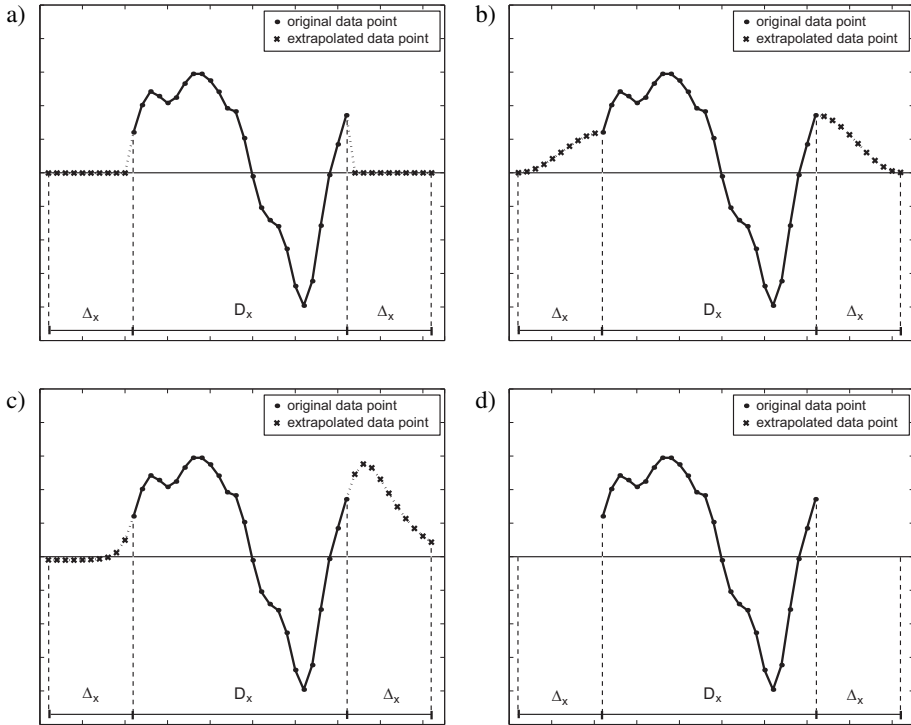
Figure 4.5: Approaches to reduce edge effects using different techniques of extending the computation area; a) Zero padding, b) Cosine taper, c) Least-squares prediction, and d) Controlled area extension.

where δg_e is the observed gravity disturbance value at the (former) edge, Δ defines how far the area is extended and d is the distance between the point where the value is computed and the nearest point at the edge. The transition between the observed signal and the computed values may, however, not be very smooth (see figure 4.5b). Oscillations can therefore still occur near the former edges.

Least-squares prediction

The third approach to reduce edge effects is to estimate gravity disturbances outside the computation area from the observed signal using interpolation by LSC (see section 3.2.3), which is also called least-squares prediction. This way the transition of the observed signal to the values outside the computation area is smooth and due to the nature of LS prediction the signal gradually approaches zero for distances much larger than the correlation length. However, when processing observations contaminated by colored noise,

70
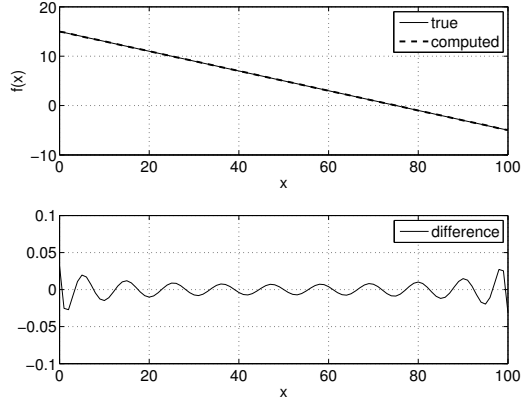
Figure 4.6: The estimation of a straight line using controlled area extension in 1D, illustrated for maximum degree $L = 10$.

the noise will propagate into the predicted values, which may cause large errors. Furthermore, the resulting error-covariance matrix that is used in the frequency-dependent weighting scheme will no longer be Toeplitz and the numerical costs to obtain the optimal solution may become too large.

Controlled area extension

As mentioned above, the size of the area is defined by the parameters D_t (with t being either x or y). Increasing the parameter D_t by Δ_t, makes the estimated signal periodic on the interval $D_t + \Delta_t$, whereas data are only available on the interval D_t. This implicit extension of the computation area reduces edge effects significantly, especially for larger Δ_t. However, an increase of Δ_t also results in an increase of the condition number, i.e. the system of normal equations becomes unstable. For the example shown in figure 4.6, where the parameter Δ_x was set to 20, the condition number increases three orders of magnitude, but the errors have been reduced significantly. Thus, the optimal value of the parameter Δ_t has to be found, which is a trade off between edge effects and instability of the normal equations. For larger values of Δ_t, the system of normal equations can be stabilized using a regularization method.

4.6.2 Modification of the base functions

Representation in terms of cosine functions

Alternatively to the representation of the disturbing potential in Eq. (4.7), the potential can also be represented as a series of cosine functions only, with a repeat interval of

71
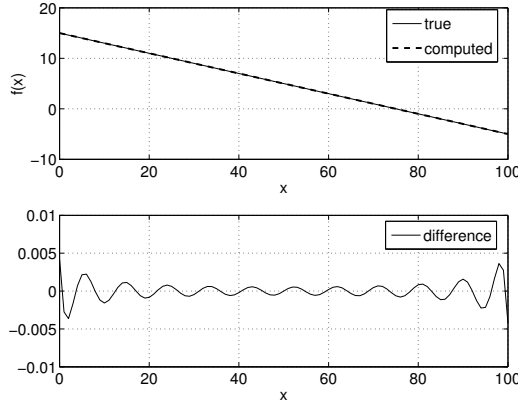
Figure 4.7: The estimation of a straight line using the additional base functions in 1D, illustrated for maximum degree $L = 10$.

$2D_x$ and $2D_y$ along the x-axis and y-axis, respectively. Then, the representation of the disturbing potential becomes

$$T(x, y, z) = \sum_{l=0}^{2L} \sum_{m=0}^{2M} C_{lm} \cos \frac{\pi lx}{D_x} \cos \frac{\pi my}{D_y} e^{-\gamma_{lm} z}, \tag{4.102}$$

with

$$\gamma_{lm} := \pi \sqrt{\left(\frac{l}{D_x}\right)^2 + \left(\frac{m}{D_y}\right)^2}. \tag{4.103}$$

Although the requirement of periodicity is now evaded, the solution will only be free of edge effects when the derivative of the signal is zero at the boundary of the computation area. Similarly, only the sine functions can be used in the expansion. Then, the requirement is that the signal is zero at the boundary to prevent edge effects.

Additional base functions

Instead of using only cosine functions as base functions, a set of functions, that are not periodic on the computation domain, can be added to the original set of base functions:

$$T(x, y, z) = \sum_{l=-L-1}^{L+1} \sum_{m=-M-1}^{M+1} C_{lm} \, \varphi_l(x) \, \varphi_m(y) \, e^{-\gamma_{lm} z} \tag{4.104}$$

where $\varphi_l(x)$, $\varphi_m(y)$ are the same as defined in Eq. (4.4), except for $l = \pm(L + 1)$ and $m = \pm(M + 1)$:

$$
\varphi_l(x) = \begin{cases} \cos \dfrac{\pi x}{D_x}, & l = L + 1 \\[2mm] \sin \dfrac{\pi x}{D_x}, & l = -L - 1 \end{cases} \quad , \quad \varphi_m(y) = \begin{cases} \cos \dfrac{\pi y}{D_y}, & m = M + 1 \\[2mm] \sin \dfrac{\pi y}{D_y}, & m = -M - 1 \end{cases} \quad (4.105)
$$

and the expression for γ_{lm} becomes (see appendix E)

$$
\gamma_{lm} := \begin{cases} 2\pi \sqrt{\left(\dfrac{l}{D_x}\right)^2 + \left(\dfrac{m}{D_y}\right)^2}, & -L \le l \le L; \quad -M \le m \le M \\[4mm] \pi \sqrt{\left(\dfrac{1}{D_x}\right)^2 + \left(\dfrac{2m}{D_y}\right)^2}, & l = \pm(L + 1); \quad -M \le m \le M \\[4mm] \pi \sqrt{\left(\dfrac{2l}{D_x}\right)^2 + \left(\dfrac{1}{D_y}\right)^2}, & -L \le l \le L; \quad m = \pm(M + 1) \\[4mm] \pi \sqrt{\left(\dfrac{1}{D_x}\right)^2 + \left(\dfrac{1}{D_y}\right)^2}, & l = \pm(L + 1); \quad m = \pm(M + 1) \end{cases} \quad (4.106)
$$

The same test as shown in figure 4.4, the estimation of a straight line, was also done using the additional base functions. The result in figure 4.7 clearly shows a large improvement (the errors are reduced by a factor 1000), which means that the additional base functions are well suitable for signal representation.

4.7 Combination with prior information

Regional gravity field solutions are generally affected by long-wavelength errors. This is particularly the case for the computation of geoid heights. These errors can be caused by the propagation of edge effects, the absence of observations outside the computation area and imperfections in the reference GPM when using the remove-restore technique. Furthermore, they may be the result of the intrinsic non-uniqueness of the inversion problem, that is, solving a boundary value problem without having data at all the boundaries. To remove long-wavelength effects, two approaches are discussed, both of which make use of prior information added to the functional model. This prior information is that the disturbing potential at low spatial frequencies is zero. Both approaches are discussed in Alberts et al. (2007a).

4.7.1 Addition of pseudo-observations

To obtain a solution without low-frequency errors, pseudo-observations $T = 0$ are added to the functional model. The model of Eq. (4.13) then becomes

$$\left[\begin{array}{c} \mathbf{y} \\ \mathbf{y_p} \end{array}\right] = \left[\begin{array}{c} \mathbf{A} \\ \mathbf{B} \end{array}\right] \mathbf{x_p} + \left[\begin{array}{c} \mathbf{e} \\ \mathbf{e_p} \end{array}\right] \quad ;$$

$$D\{ \left[\begin{array}{c} \mathbf{e} \\ \mathbf{e_p} \end{array}\right] \} = \left[\begin{array}{cc} \mathbf{Q_y} & \mathbf{0} \\ \mathbf{0} & \mathbf{Q_p} \end{array}\right], \tag{4.107}$$

where $\mathbf{y_p}$ are the pseudo-observations $T = 0$, $\mathbf{e_p}$ is the vector of residuals with expectation $E\{\mathbf{e_p}\} = 0$, and $\mathbf{B}$ is the design matrix which describes the relation between the disturbing potential and the coefficients (Eq. (4.7)). The entries of the covariance matrix $\mathbf{Q_p}$ are computed using the covariance function

$$C(\psi) = \sum_{n=2}^{N_1} \varepsilon_n P_n(\cos \psi) + \sum_{n=N_1+1}^{N_2} \sigma_n P_n(\cos \psi), \tag{4.108}$$

where ψ is the spherical distance, ε_n are the error degree variances of the geopotential model that was subtracted from the gravity signal up to degree N_1 and σ_n are signal degree variances which may be computed using Kaula's rule (Kaula, 1966) up to degree N_2. The optimal solution is found by solving the following system of normal equations:

$$(\mathbf{A}^T \mathbf{Q_y}^{-1} \mathbf{A} + \mathbf{B}^T \mathbf{Q_p}^{-1} \mathbf{B}) \hat{\mathbf{x}}_\mathbf{p} = \mathbf{A}^T \mathbf{Q_y}^{-1} \mathbf{y}. \tag{4.109}$$

4.7.2 Addition of fixed constraints

A different approach to reduce long-wavelength errors is to add integral constraints to the functional model. Because the goal is to compute only the high-frequency part of the disturbing potential, the following constraints are added

$$\iint_\Omega T(P) \overline{Y}_{l'm'}(P) \, \mathrm{d}\Omega = 0, \tag{4.110}$$

where $\overline{Y}_{l'm'}(P)$ are the spherical harmonics up to a pre-defined maximum degree and order, expressed by l' and m', and the integration domain Ω equals the computation area. The choice of the maximum degree and order depends on the maximum wavelength that is solved for in the determination of the gravity field, but in practice this would result in a very large number of constraints. Therefore, only a small number of l' and m' should be used. In discretized form Eq. (4.110) becomes

$$\sum_{i=1}^{N} T(P_i) \overline{Y}_{l'm'}(P_i) = 0, \tag{4.111}$$

where N is the number of points P_i. Inserting the representation of the disturbing potential T in Cartesian coordinates, given by Eq. (4.7), results in

$$\sum_{l,m} C_{lm} \sum_{i=1}^{N} \varphi_l(x_i)\varphi_m(y_i)e^{-\gamma_{lm}z_i}\overline{Y}_{l'm'}(P_i) = 0. \qquad (4.112)$$

The constraint equation may symbolically be written as

$$\mathbf{Kx} = \mathbf{c}, \qquad (4.113)$$

where $\mathbf{K}$ is the design matrix relating the coefficients to be estimated to the constraint observations, Eq. (4.112), and $\mathbf{c}$ is a vector of zero-observations. Adding the constraints to the functional model of Eq. (4.13), results in the Gauss-Markov model with fixed constraints, which is given as (see e.g. Koch, 1999)

$$\begin{bmatrix} \mathbf{y} \\ \mathbf{c} \end{bmatrix} = \begin{bmatrix} \mathbf{A} \\ \mathbf{K} \end{bmatrix} \mathbf{x_f} + \begin{bmatrix} \mathbf{e} \\ \mathbf{0} \end{bmatrix}; \quad D\{\mathbf{e}\} = \mathbf{Q_y}. \qquad (4.114)$$

The optimal solution $\hat{\mathbf{x}}_\mathbf{f}$ is found by minimizing the Lagrange function

$$\Phi(\mathbf{x}, \boldsymbol{\lambda}) = (\mathbf{y} - \mathbf{Ax})^T \mathbf{Q_y}^{-1}(\mathbf{y} - \mathbf{Ax}) - 2\boldsymbol{\lambda}(\mathbf{c} - \mathbf{Kx}), \qquad (4.115)$$

yielding the normal equations

$$\begin{bmatrix} \mathbf{N} & \mathbf{K}^T \\ \mathbf{K} & \mathbf{0} \end{bmatrix} \begin{bmatrix} \hat{\mathbf{x}}_\mathbf{f} \\ \hat{\boldsymbol{\lambda}} \end{bmatrix} = \begin{bmatrix} \mathbf{A}^T\mathbf{Q_y}^{-1}\mathbf{y} \\ \mathbf{c} \end{bmatrix}. \qquad (4.116)$$

The constrained parameter vector is obtained by eliminating the Lagrange multiplier $\hat{\boldsymbol{\lambda}}$ from Eq. (4.116), resulting in

$$\hat{\mathbf{x}}_\mathbf{f} = \hat{\mathbf{x}} + \mathbf{N}^{-1}\mathbf{K}^T(\mathbf{K}\mathbf{N}^{-1}\mathbf{K}^T)^{-1}(\mathbf{c} - \mathbf{K}\hat{\mathbf{x}}) \qquad (4.117)$$

The solution can thus be computed as an update to the unconstrained solution $\hat{\mathbf{x}}$.

If too many constraints are added, the constrained solution cannot be obtained since the matrix $\mathbf{K}\mathbf{N}^{-1}\mathbf{K}^T$ is in that case not invertible. In practice the maximum degree l' and order m' of the spherical harmonic representation in Eq. (4.110) should be limited to a small number as discussed above.

Application to simulated data

5

This chapter is devoted to testing the theory presented in chapter 4 using simulated data. The purpose of the simulations is to ensure that the developed methodology performs as expected under controlled circumstances. Furthermore, the simulations are used to choose the optimal strategy in case more than one option is available and to compare the results with more traditional approaches. In this context, "optimal" means that the selected approach should yield the best results in terms of RMS errors. This can only be assessed in simulations since the estimated gravity field functions can be compared with their true values. In case of real data true values are often not available, or not known with sufficient accuracy and resolution to allow for a good comparison.

The performance of the developed methodology is investigated using two data sets which are described in section 5.1. The first data set is used in section 5.2 for the computations with noise-free data, to test the performance of the chosen gravity field representation and investigate the approaches for edge effect reduction. The second data set is used for the computations with white noise and colored noise, presented in sections 5.3 and 5.4 respectively. The aim of the computations is to select the optimal regularization method and investigate the performance of the frequency-dependent data weighting scheme. The second data set is also used for the investigation of bias and drift handling, which is discussed in section 5.5. Finally, a summary of the optimal strategy is given in section 5.6.

5.1   Description of the data

The simulated observations used for the numerical experiments described in this chapter are computed from the global geopotential model GPM98b (Wenzel, 1998), which is complete to spherical harmonic degree 1800. On the equator, this corresponds to a half-wavelength resolution of approximately 10 km. Two data sets have been created: for the first data set the points are distributed on a regular grid, for the other data set the points are located along simulated airborne profiles. To avoid artifacts from long-wavelength signals, the frequency content of both data sets is limited to spherical harmonic degrees 361-1800, i.e. the data do not contain wavelengths longer than approximately 110 km. Details of the data sets are described below.
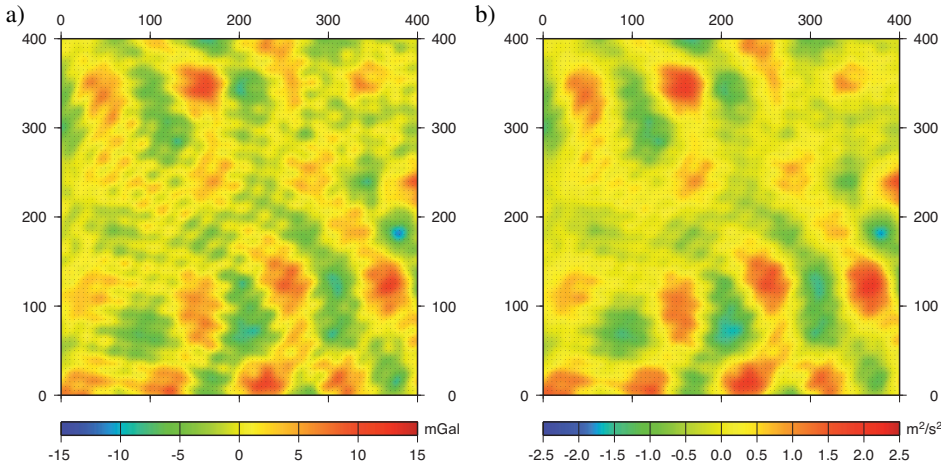
Figure 5.1: Simulated gravity field functionals over the 400×400 km test area (data set 1); a) gravity disturbances at flight level; b) disturbing potential at ground level.

Data set 1

The first data set is the same data set as used in Alberts et al. (2007a) and Alberts et al. (2007b). It consists of 6561 gravity disturbances computed on a regular grid with a spacing of 5 km at an altitude of 4000 m. The area is located in the Canadian Rocky Mountains, with the coordinate center of the Cartesian reference frame (φ_c, λ_c) at 51.7° Northern latitude and 241.0° Eastern longitude. The size of the area is 400×400 km. The statistics for this data set are: min=-12.78; max=10.68; mean=-0.12; RMS=3.12 mGal. The simulated gravity field functionals are shown in figure 5.1.

Data set 2

The second data set is the same as used in Klees et al. (2005). The area is located in the United States, north of the gulf of Mexico, with the coordinate center (φ_c, λ_c) at 33.25° Northern latitude and 260.0° Eastern longitude. The size of the area is 6.5×6.5 degrees (630×730 km). To simulate an airborne gravity data set distribution, observations are computed at a flight level of 2000 m along 66 East-West oriented profiles, with a distance of 0.1° between the lines, and at 5 North-South oriented profiles at a distance of 1.4° from each other. The spacing of the points along-track is 1 arc-minute, resulting in 27761 observations. The statistics for this data set are: min=-30.92; max=46.60; mean=0.01; RMS=5.99 mGal. The simulated gravity signal and the flight pattern are shown in figure 5.2a. The disturbing potential at ground level and the distribution of the control points that are used to compute error statistics, are shown in figure 5.2b.
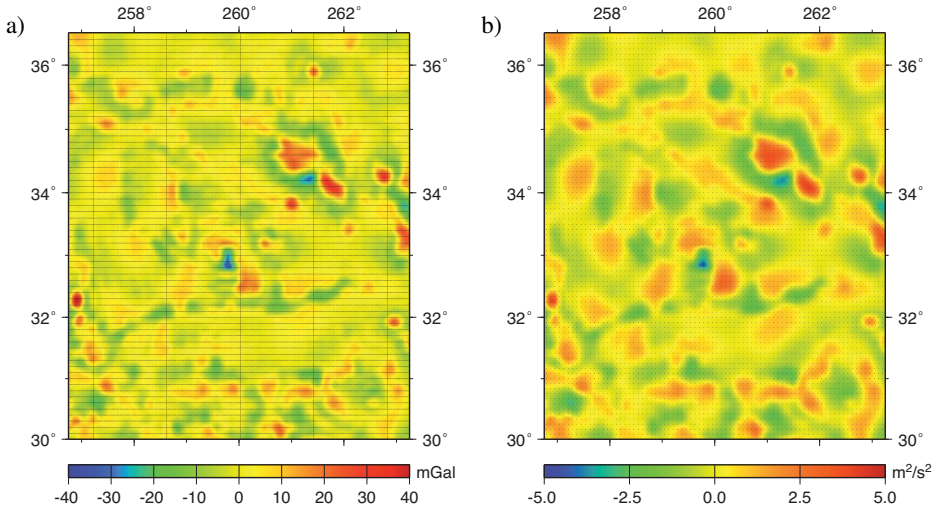
Figure 5.2: Simulated gravity field functionals and their distribution for data set 2; a) gravity disturbances at flight level; b) disturbing potential at ground level.

5.2 Computations with noise-free data

5.2.1 Gravity field representation and downward continuation

Fundamental solutions of Laplace's equation

The performance of the approach using fundamental solutions of Laplace's equation is first tested using the noise-free observations of data set 1, and the results are compared to the ones obtained with LSC. The maximum degree L and order M of the representation are set to $L = M = 32$, which corresponds to a resolution of 6 km. Coefficients C_{lm} are estimated by a LS adjustment as described in section 4.2; the normal equations are solved using Cholesky decomposition. No regularization has been applied. From the estimated coefficients, gravity disturbances and disturbance potential values are computed at ground level ($h = 0$ m). Note that in terms of z, the z-coordinates vary at ground level.

Errors are computed at ground level with control data, which are also computed from GPM98b. The results are shown in figures 5.3a and 5.3b, for gravity disturbance errors and geoid height errors, respectively. The latter are computed from disturbing potential errors using Bruns' formula (Eq. (3.10)). The error pattern for the gravity disturbances (cf. figure 5.3a) is the result of the Gibbs effect discussed in section 4.6: the base functions are periodic, but the data are not, which results in large errors at the edges that propagate into the area. Figure 5.3b shows that for the computed geoid heights, this results in large long-wavelength errors. The error statistics of the solutions are given in tables 5.1 and 5.2.

Least-squares collocation

A gravity field solution has also been computed using LSC. From the observations at flight level an empirical auto-covariance function (ACF) is estimated, which is shown in figure 5.4. Two analytical models are fitted to this function: the Tscherning-Rapp degree-variance model (Eq. (3.32)) and the planar logarithmic covariance function (Eq. (3.35)). An analytical model is used to set up the signal-covariance matrix of the gravity disturbances at flight level and the cross-covariance matrix between gravity disturbances and the disturbing potential at flight level and ground level, respectively. For the planar model, the attenuation parameters D and T that define the function were found empirically such that the variance and correlation length are the same as for the empirical auto-covariance function. This yields values of $D = 6$ and $T = 28$. For the fitting of the Tscherning-Rapp model the program COVFIT, which is part of the GRAVSOFT package (Tscherning et al., 1994) has been used. The program estimates the model parameter A and the depth to the Bjerhammar sphere iteratively as described by Knudsen (1987). From figure 5.4 it is clear that the Tscherning-Rapp model provides the best fit to the empirical auto-covariance function. The parameters of this model can directly be used in the GRAVSOFT module GEOCOL, which is used her for the downward continuation of gravity disturbances, and for the determination of the disturbing potential at ground level.

Errors are computed by computing differences with the control data at ground level. The results are shown in figures 5.3c and 5.3d for gravity disturbance errors and geoid height errors, respectively; their statistics are given in tables 5.1 and 5.2. From the figures and the tables it is clear LSC performs much better than the representation using the fundamental solutions of Laplace equation in Cartesian coordinates. The latter suffers from large edge effects that propagate into the computation area. When disturbing potential values are computed, the solution is dominated by long-wavelength errors. These errors are the result of periodicity of the base functions whereas the data are non-periodic, and of missing data outside of the computation area. The second effect is common to all types of parameterizations and estimation techniques, but LSC may perform better than

Table 5.1: Statistics of gravity disturbance errors [mGal] at ground level.

Method	Min	Max	Mean	RMS
Laplace solutions	-10.24	15.94	0.078	1.12
Least-squares collocation	-1.88	1.69	0.005	0.15

Table 5.2: Statistics of geoid errors [m] at ground level.

Method	Min	Max	Mean	RMS
Laplace solutions	-0.119	0.115	0.003	0.017
Least-squares collocation	-0.072	0.040	-0.005	0.015
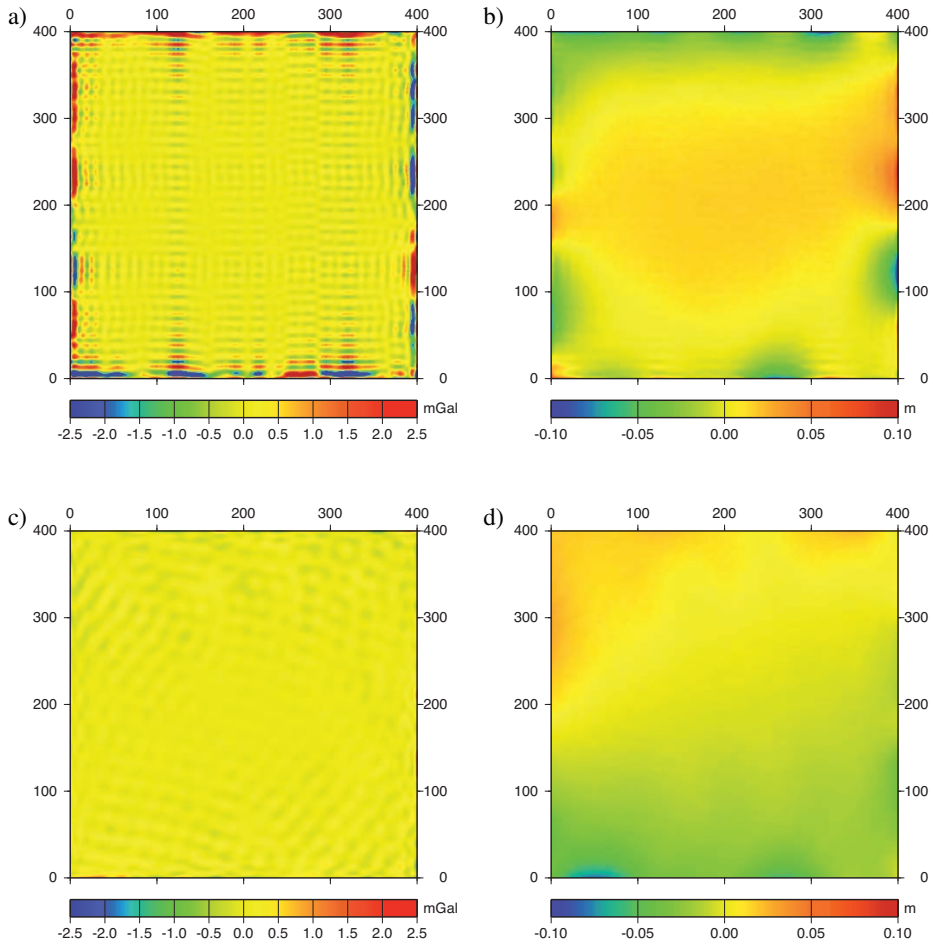
Figure 5.3: Errors at ground level for the solutions of Laplace's equation (a and b), and for LSC solutions (c and d). Figures a) and c) show gravity disturbance errors; figures b) and d) show geoid height errors.

other methods if the auto-covariance function also provides a good representation of the data outside the area. However, if the ACF is not representative for these data (e.g. because the signal is anisotropic there) LSC will also suffer from edge effects. The problem of periodicity is typical for using fundamental solutions of Laplace's equation in Cartesian coordinates. Therefore, in the next section the approaches for edge effect reduction, discussed in section 4.6, are tested and the results are compared with the LSC solution.
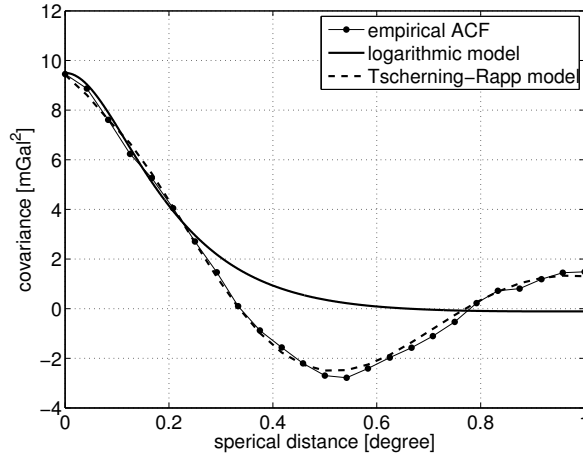
Figure 5.4: The empirical auto-covariance function of the gravity disturbances of data set 1 and the fitted analytical models. Two models are fitted; the logarithmic model and the Tscherning-Rapp model.

5.2.2 Reduction of edge effects

Extension of the area

In section 4.6.1 four approaches were proposed to reduce edge effects that use an extension of the computation area, namely zero-padding, cosine taper, LS prediction and controlled area extension. The performance of the approaches is tested with data set 1. For the first three methods the area is extended by 50 km in the x and y directions, resulting in an area size of $D_x = D_y = 500$ km. The spacing of the extrapolated data points is the same as the spacing of the original data points, which means that the number of observations is increased to 10201. To obtain the same resolution as in the previous subsection, the coefficients C_{lm} were estimated up to $L = 40$, $M = 40$.

For controlled area extension, the parameter Δ_t was set to 50 km, resulting in values of $D_x = D_y = 450$ km and coefficients are solved up to $L = M = 36$. Because the normal equations become unstable with this approach, Tikhonov regularization is applied with the regularization parameter set empirically to the smallest value for which a stable solution could be obtained. The optimal value of Δ_t was empirically derived by computing the RMS gravity disturbance error and the condition number of the normal matrix for various values of Δ_t. The results are given in table 5.3. The table shows an increasing ill-conditionedness for larger values of Δ_t, but the gravity disturbance error does not become smaller for an area extension larger than the chosen value of 50 km.

For all approaches, gravity field solutions are computed for the original area of 400 by 400 km at ground level. The errors are shown in figures 5.5 and 5.6, and their statistics are given in tables 5.4 and 5.5 for the computed gravity disturbances and geoid heights,

Table 5.3: RMS gravity disturbance errors [mGal] and the condition number c of the normal matrix for varying Δ_t for a controlled area extension.

Δ_t [km]	0	12.5	25	37.5	50	75	100
RMS	1.12	0.65	0.15	0.07	0.07	0.07	0.07
c	2.3e+04	7.7e+04	9.4e+08	2.7e+14	5.7e+18	5.2e+19	1.3e+20

respectively.

Comparing the results of table 5.4 with table 5.1 shows that with zero-padding and with the cosine taper, the errors can be even larger than without a reduction method applied. This is because there are still discontinuities at the former edges. Nevertheless, the resulting RMS geoid height errors are somewhat smaller, indicating that the long-wavelength errors are smaller inside the computation area compared to the case that no reduction method is used. For LS-prediction, the results are much better than for zero-padding and cosine tapering. The solution is almost free of edge effects due to the smooth transition between original and predicted data points at the former edge of the computation area. The explanation is that the correlation length for this data set was about 20 km, resulting in predicted values that are nearly zero at the edge of the extended area. As such, the signal can be considered periodic over the larger domain without discontinuities. A larger area extension (e.g. four times the correlation length) may further reduce the edge effects when LS prediction is used.

Among the methods that use an extension of the computation area, the best results are obtained with controlled area extension. Both figures 5.5b and 5.6b, and statistics show a large improvement with respect to the results presented in the previous subsection. Especially the geoid height errors at ground level show that the results are no longer affected by long-wavelength errors in the whole area. At a distance of 10 km from the boundaries of the area the errors are below 2.5 cm

Modified base functions

Instead of an extension of the area, edge effects may also be reduced by modifying the base functions as shown in section 4.6.2. For the computations with the cosine functions and the additional base functions, the test setup is the same as for the computations with the original base functions described in the previous subsection. The results are shown in figures 5.5 and 5.6, the error statistics are given in tables 5.4 and 5.5. Both approaches show an improvement in terms of gravity disturbance errors with respect to the original base functions. However, the results are worse for the computation of the disturbing potential at ground level. Especially the additional base function solution gets completely distorted by large long-wavelength errors.

The results obtained in this section show that controlled area extension is the optimal method for the reduction of edge effects. It is much more efficient than the other three methods that use an extension of the area and outperforms all the investigated approaches,
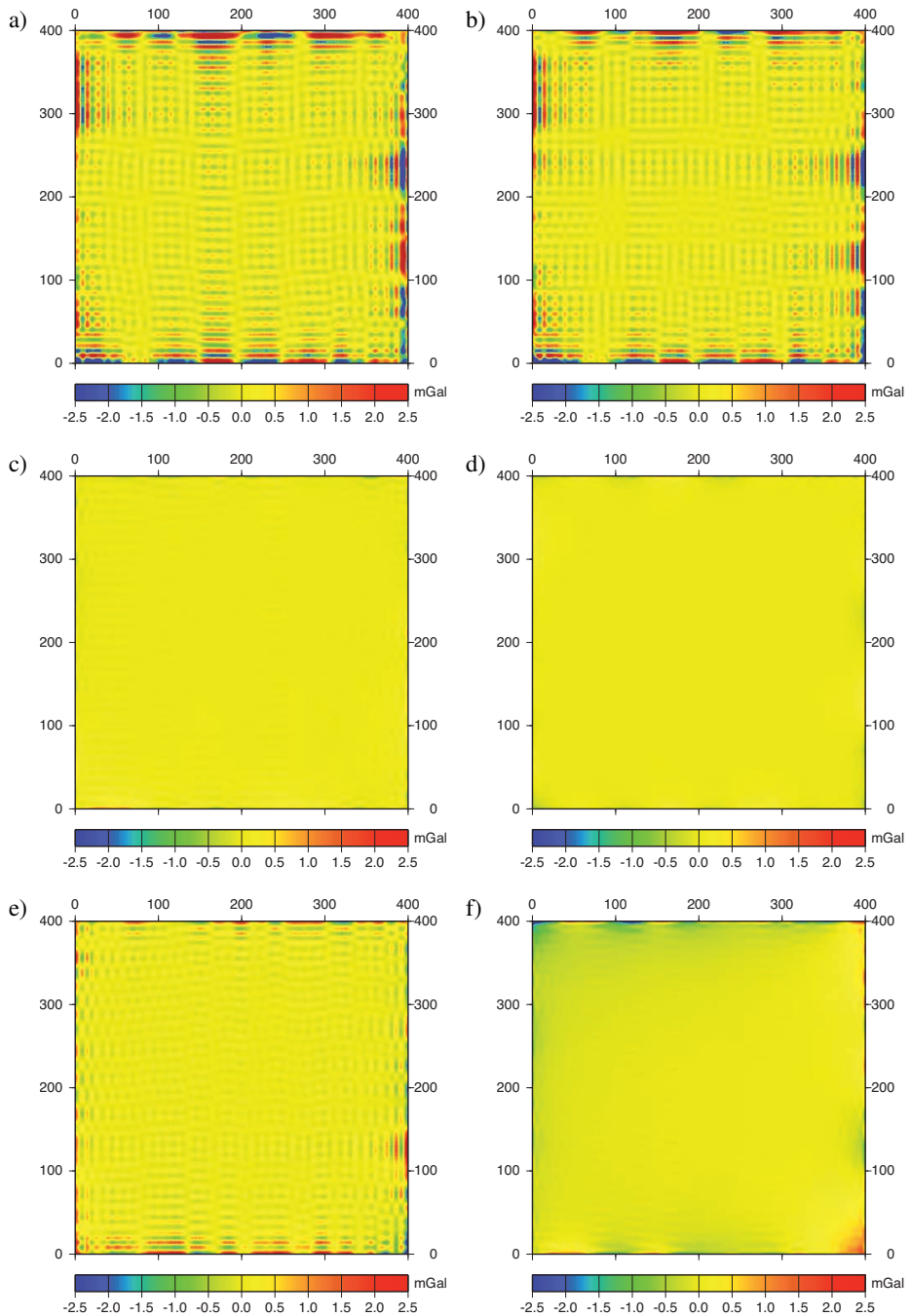
Figure 5.5: Gravity disturbance errors for the various approaches for edge effect reduction: a) zero padding; b) cosine taper; c) LS prediction; d) controlled area extension; e) cosine functions; and f) additional base functions.
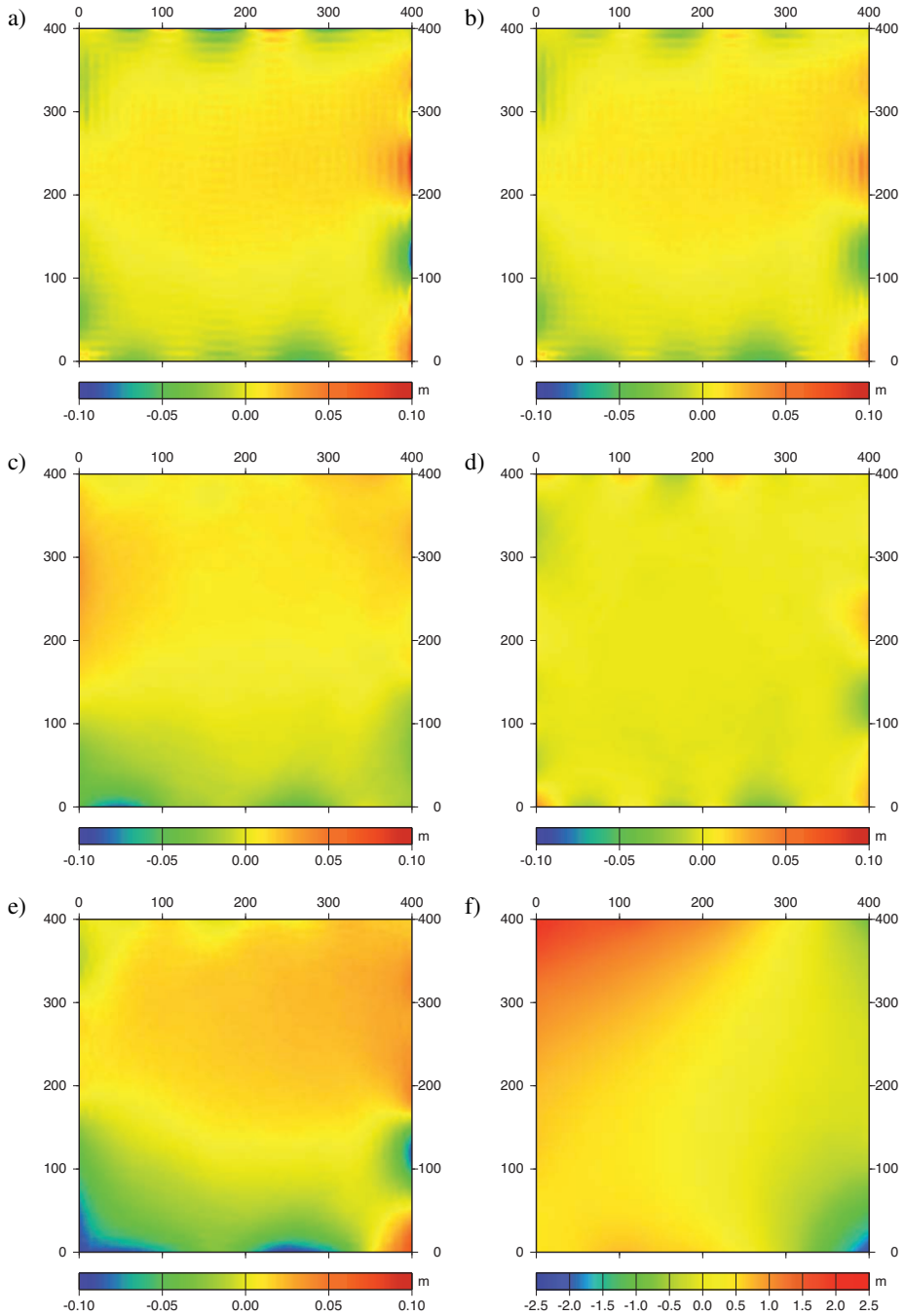
Figure 5.6: Geoid height errors for the various approaches for edge effect reduction: a) zero padding; b) cosine taper; c) LS prediction; d) controlled area extension; e) cosine functions; and f) additional base functions (note the different color scale).

Table 5.4: Statistics of gravity disturbance errors [mGal] at ground level.

Method	Min	Max	Mean	STD	RMS
a) Zero-padding	-17.03	21.63	0.02	1.34	1.34
b) Cosine taper	-6.85	18.63	0.03	0.88	0.88
c) Least-squares prediction	-1.23	1.95	0.01	0.11	0.11
d) Controlled area extension	-0.85	0.75	0.00	0.07	0.07
e) Cosine functions	-6.68	7.73	0.06	0.56	0.57
f) Additional base functions	-4.45	2.91	-0.09	0.31	0.32

Table 5.5: Statistics of geoid height errors [m] at ground level.

Method	Min	Max	Mean	STD	RMS
a) Zero-padding	-0.130	0.158	0.003	0.014	0.014
b) Cosine taper	-0.066	0.092	0.003	0.013	0.013
c) Least-squares prediction	-0.085	0.036	0.003	0.011	0.011
d) Controlled area extension	-0.035	0.045	0.003	0.004	0.005
e) Cosine functions	-0.103	0.074	0.003	0.024	0.024
f) Additional base functions	-2.218	2.240	0.390	0.456	0.600

including LSC, in terms of RMS gravity disturbance and geoid height errors. The only drawback of controlled area extension may be the decrease of numerical stability, which requires regularization. However, regularization is a standard procedure in processing of noisy data (the issue of regularization is studied in the next section). It is therefore recommend to use a sufficiently large value of $D_t + \Delta_t$, when fundamental solutions of Laplace's equation in Cartesian coordinates are used for airborne gravity data processing.

5.3   Computations with data corrupted by white noise

In this section a numerical study is conducted to find the optimal regularization method and parameter choice rule. For this study, the simulated airborne gravity data set (data set 2, section 5.1) is corrupted by random white noise with an RMS of 2 mGal. The data are used to estimate coefficients C_{lm} complete to degree $L = 36$ and order, $M = 36$, resulting in 5328 parameters, from which gravity functionals are computed at the control points at ground level (cf. figure 5.2). To reduce edge effects, controlled area extension is used with $\Delta_t = 50 \,\mathrm{km}$, as described in the previous section. The quality of the solutions is quantified in terms of the RMS deviation from the true noise-free data computed from the GPM98b model at the control points.
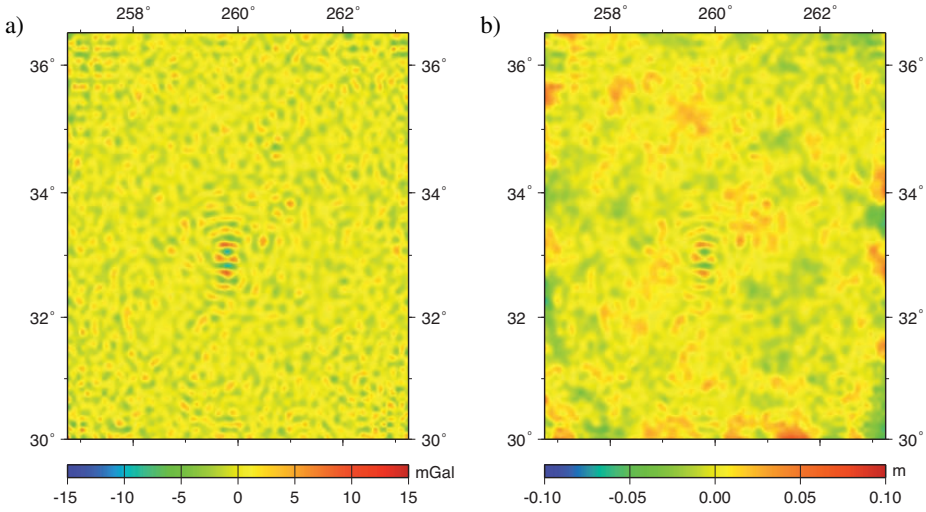
Figure 5.7: Errors at ground level for ZOT regularization with the optimal regularization parameter derived empirically. a) Gravity disturbance errors; b) geoid height errors.

5.3.1 Choice of regularization matrix

The first goal of the numerical study is to compare the two regularization techniques presented in section 4.3.1: zero-order Tikhonov (ZOT) and first-order Tikhonov (FOT) regularization. The regularized solutions are first computed with the optimal regularization parameter, which is determined empirically. The parameter choice rules are studied in the next subsection.

The errors for the solutions obtained with ZOT regularization are shown in figure 5.7. The results for FOT regularization are omitted because they look very similar to the ones obtained with ZOT. The errors observed in figure 5.7 are due to two reasons. The first reason is the propagated data noise, which shows up as the homogeneous high-frequency pattern in both plots. The second reason is the high-frequency spatial variations of the gravity field that get smoothed by applying regularization. In the figure this is especially clear in the middle of the plots. Choosing a larger regularization parameter leads to a stronger smoothing of gravity field features, whereas a smaller regularization parameter causes stronger noise in the solution.

The optimal regularization parameter is here defined as the one that gives the smallest RMS gravity disturbance error. The dependence of the accuracy on the regularization parameter is shown in figures 5.8a and 5.8b, for ZOT and FOT respectively. With ZOT regularization the minimum RMS gravity disturbance error is obtained for $\alpha = 2.5 \cdot 10^2$, yielding an RMS of 1.5 mGal. Thus, the effect of white noise of $\sigma = 2$mGal is largely reduced.

87

For FOT regularization the optimal regularization parameter is $\alpha = 3.5 \cdot 10^9$, which gives slightly better results than ZOT regularization with an RMS of 1.4 mGal. However, the RMS geoid height error is much better for ZOT regularization than for FOT regularization: the RMS errors are 1.2 cm and 2.1 cm, respectively (see also tables 5.6 and 5.7). Note that choosing the optimal regularization parameter on the basis of RMS gravity disturbance error does not necessarily lead to the smallest maximum error or RMS geoid height error. Especially in case of FOT regularization, smaller RMS geoid height errors are obtained for larger α's; for $\alpha = 5 \cdot 10^{10}$ the RMS is 1.6 cm, but the RMS gravity disturbance error has increased to 1.7 mGal. In case of ZOT regularization the geoid height errors are less sensitive to the choice of α; between $\alpha = 1 \cdot 10^2$ and $\alpha = 1 \cdot 10^3$ the RMS geoid error remains 1.2 cm. This can be explained by the fact that, in case of ZOT regularization, all coefficients (except for $l = 0$ and/or $m = 0$) are regularized in the same way, whereas for FOT regularization the higher degrees and orders are more regularized. This means that for larger values of α the higher frequencies get smoothed more than the lower frequencies. Therefore, the results for gravity functionals such as gravity disturbances or anomalies that are relatively less smooth than geoid heights, are more accurate for a smaller regularization parameter, but a larger α gives a better geoid solution when FOT regularization is applied.

From the results in this section it can be concluded that ZOT regularization yields the better overall results. Although the RMS and maximum gravity disturbance errors are slightly larger than for FOT regularization, the geoid height errors are considerably smaller. However, the choice of regularization depends on the spectrum of the signal. For the simulated data the spectral content is limited due to the maximum degree of 1800 of the GPM98 model. If the observations contain more high-frequency signal, FOT regularization may provide better results. This is tested for the computations with real data in chapter 6.

Optimal regularization does not only depend on the choice of the regularization matrix. The performance of ZOT or FOT regularization in combination with the parameter choice rule should be analyzed together, which is done in the next subsection.

5.3.2 Parameter choice rules

In practical applications the regularization parameter cannot be determined on the basis of RMS gravity disturbance or geoid height errors. Instead, a parameter choice rule must be applied. Here, two heuristic methods are tested: the generalized cross-validation method (GCV) and the variance component estimation technique (VCE).

GCV

The estimated regularization parameter is located at the minimum of the GCV function (Eq. (4.38)), which is found using the golden section search (Kiefer, 1953). For ZOT regularization the search interval was set to $[1.0; 1.0 \times 10^6]$ and the minimum was obtained
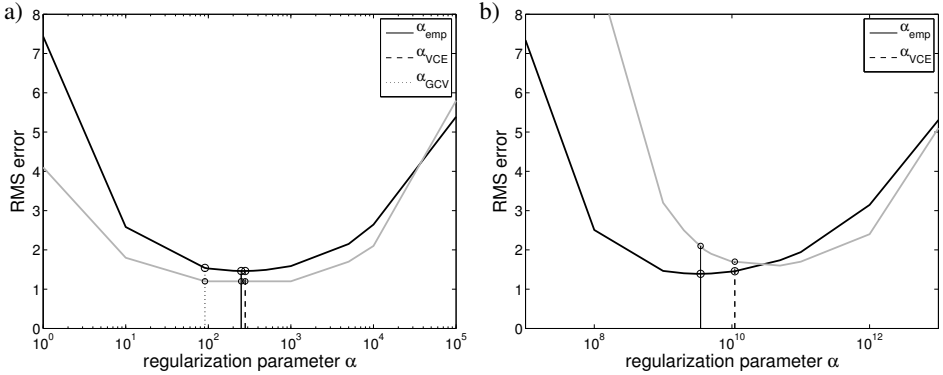
Figure 5.8: Dependence of the RMS error on the regularization parameter. Black lines denote the RMS gravity disturbance error (mGal); grey lines correspond to the RMS geoid height error (cm). a) ZOT regularization; b) FOT regularization. The circles show the RMS errors obtained with the estimated regularization parameters using GCV and VCE, and for the empirical value of α. For FOT regularization GCV did not yield an absolute minimum.

after 8 iterations. Figure 5.9a shows on a semi-logarithmic scale the computed GCV function for a wide range of regularization parameters. The minimum of the function is determined at $\alpha = 0.91 \times 10^2$. The result is also shown in figure 5.8a, from which it is clear that the obtained regularization parameter is too small compared to the empirically determined optimal value. Nevertheless, the results are only slightly worse; the resulting RMS gravity disturbance error is larger (1.5 mGal), but the RMS geoid error is the same as for the empirically found α.

Remarkably, the GCV function does not yield an absolute minimum within the search interval (set to $[1.0 \times 10^7; 1.0 \times 10^{13}]$) when FOT regularization is applied. After 10 iterations the value converged to the upper limit of the interval (cf. figure 5.9b), which already yields a regularization parameter that is much larger than the optimal value, and the resulting gravity disturbances are close to zero. A larger search interval has been tried as well, but again GCV did not provide an estimate of the regularization parameter.

Droge (1996) proposed an alternative variant of cross-validation, called full cross-validation. He showed that under certain conditions, such as linear estimates and normally distributed observations, the cross-validation criterion is outperformed by the full cross-validation criterion. The same holds for the generalized variant, which is used in this thesis. The GCV function of Eq. (4.38) may be written as

$$GCV(\alpha) = \frac{1/n \|\mathbf{A}\mathbf{x}_\alpha - \mathbf{y}\|^2}{(1 - 1/n \, \text{trace}(\mathbf{Q}^\alpha))^2}. \tag{5.1}$$

Its modified version, the generalized full cross-validation function (GFCV), is given as
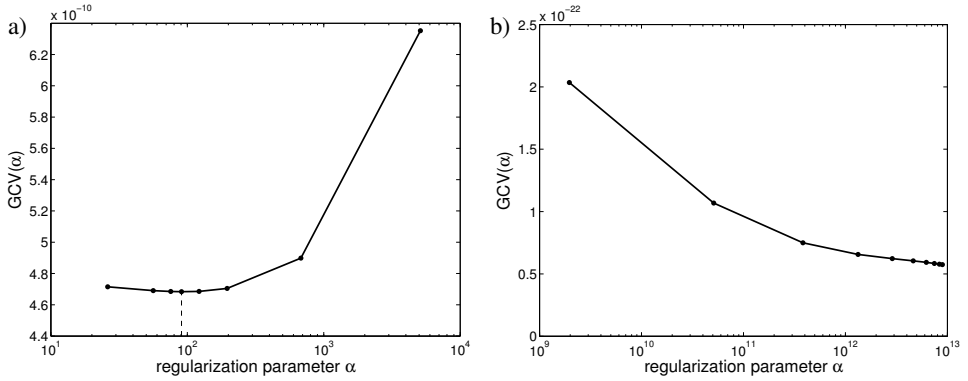
Figure 5.9: Determination of the regularization parameter with generalized cross-validation using golden section search. a) ZOT regularization; b) FOT regularization.

(see Droge (1996) for details)

$$GFCV(\alpha) = 1/n\|\mathbf{A}\mathbf{x}_\alpha - \mathbf{y}\|^2(1 + 1/n \text{ trace}(\mathbf{Q}^\alpha)^2). \qquad (5.2)$$

However, applying this function with ZOT regularization, does not improve upon the results obtained with GCV. The minimum of the GFCV function is again obtained with golden section search, yielding a regularization parameter that is even smaller than the one derived with GCV: $\alpha_{GFCV} = 0.6 \cdot 10^2$. The resulting RMS gravity disturbance error is 1.6 mGal. For FOT regularization, GFCV also does not improve the estimation of the regularization parameter. The GFCV function does not have an absolute minimum within the search interval and the golden section search algorithm converges to the lower bound of the interval at $1.0 \cdot 10^7$.

VCE

With VCE, the regularization parameter is obtained as the ratio of two variance components, σ_1^2 and σ_μ^2, according to Eq. (4.50). As shown in section 4.3.4, the estimation of the variance components requires the computation of the partial redundancies. Because their sum equals the overall redundancy, only one of the partial redundancies needs to be computed; here r_μ is computed as

$$r_\mu = u - tr(\frac{1}{\sigma_\mu^2}(\mathbf{R}\mathbf{N}^{-1}), \qquad (5.3)$$

with $\mathbf{R}$ being either the ZOT or FOT regularization matrix, and u is the number of unknowns. The trace term in this equation is computed explicitly, using the Cholesky decomposition of the normal matrix. For larger problems stochastic trace estimation, as
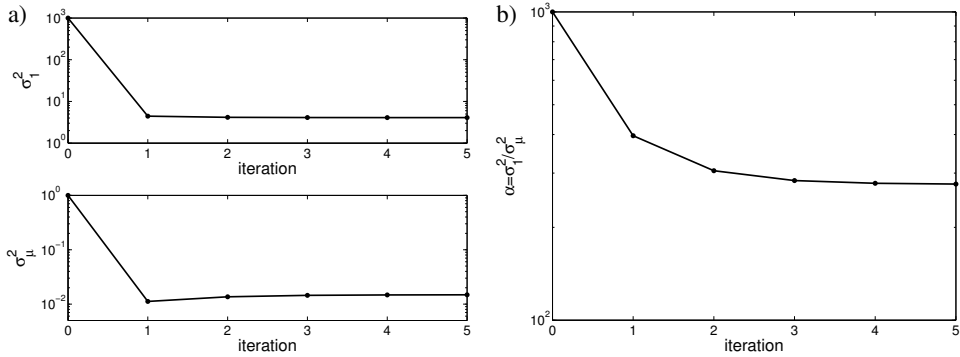
Figure 5.10: Change of the estimated variance components $\hat{\sigma}_1$ and $\hat{\sigma}_\mu$ (a); and b) change of the regularization parameter α during the iteration process.

described in section 4.3.4, can be used instead. Tests with the noisy data set showed that the trace can be estimated very accurately in this way, yielding the same variance components as when the trace is computed explicitly.

With ZOT regularization, the variance component σ_1^2 of the covariance matrix $\mathbf{Q}_1$ is estimated as $\hat{\sigma}_1^2 = 4.1$. Because the matrix $\mathbf{Q}_1$ was set equal to the unity scaled by the input unit (mGal^2), the total variance of the observations is estimated at $4.1\,\mathrm{mGal}^2$, which closely corresponds to the variance of the added noise ($\sigma^2 = 4.0\,\mathrm{mGal}^2$). Convergence of the variance components is obtained after 5 iterations (see figure 5.10). The obtained regularization parameter of $\alpha = 2.8 \cdot 10^{10}$ is very close the one that was determined empirically (cf. figure 5.8).

Unlike GCV, VCE does provide a good estimate of the regularization parameter in case of FOT regularization. The variance component σ_1^2 is estimated as $\hat{\sigma}_1^2 = 4.3$, which means that the noise in the observations is slightly overestimated. This leads to a larger regularization parameter ($\alpha = 0.11 \cdot 10^{11}$) than the empirically determined optimal parameter (cf. figure 5.8b). Again, convergence of the variance components was obtained after 5 iterations. Tables 5.6 and 5.7 show that the gravity disturbances at ground level obtained with FOT regularization with VCE have the same accuracy as the results of ZOT/VCE , but the geoid height errors are somewhat larger. However, if the empirically optimal α would be determined according to the minimum RMS geoid height error criterion, the FOT regularization parameter found with VCE would be very close to that one.

5.3.3 Comparison with LSC

To assess the quality of the results obtained in this section, a comparison is made with LSC. The solution of LSC with noise is obtained by adding $\mathbf{D} = \sigma^2 \mathbf{I}$ to the signal
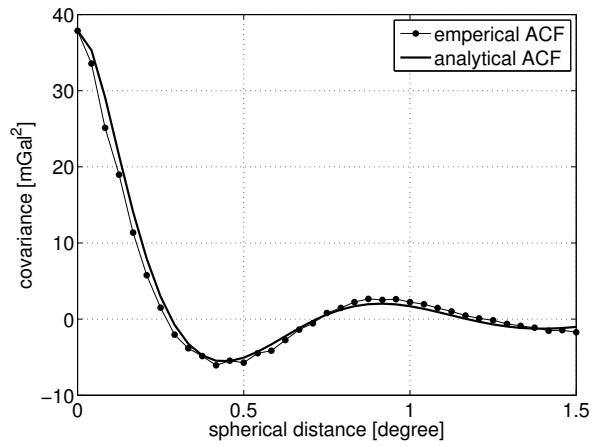
Figure 5.11: The empirical auto-covariance function of the gravity disturbances of data set 2 and the fitted analytical Tscherning-Rapp model.
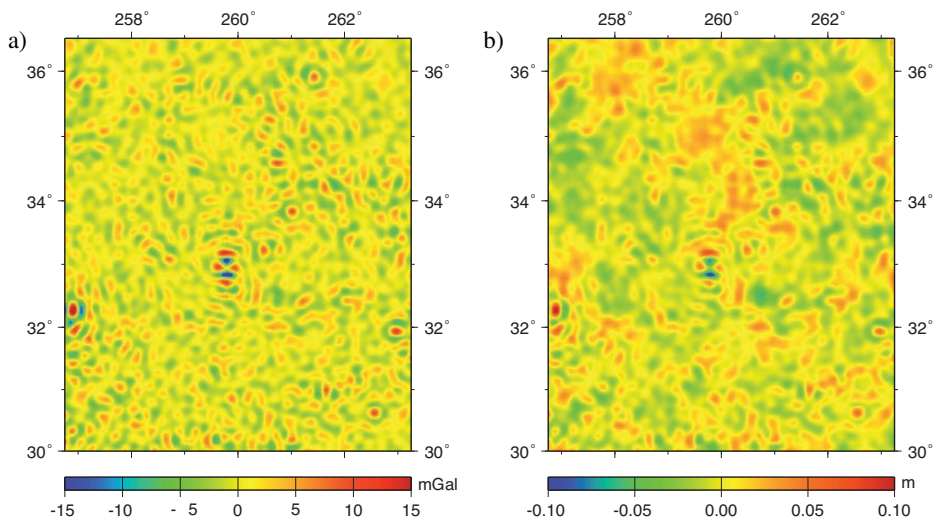
Figure 5.12: Errors at ground level for LSC; a) Gravity disturbance errors; b) geoid height errors.

Table 5.6: Statistics of gravity disturbance errors [mGal] at ground level for the regularized solutions.

Method	Min	Max	Mean	RMS
ZOT: empirical	-10.35	15.85	-0.01	1.46
ZOT: VCE	-10.84	15.30	-0.01	1.46
ZOT: GCV	-11.73	23.94	-0.01	1.54
FOT: empirical	-9.21	11.79	-0.01	1.39
FOT: VCE	-14.20	10.91	-0.01	1.46
LSC	-19.30	13.41	-0.01	2.18

Table 5.7: Statistics of geoid height errors [m] at ground level for the regularized solutions.

Method	Min	Max	Mean	RMS
ZOT: empirical	-0.068	0.073	0.001	0.012
ZOT: VCE	-0.068	0.073	0.001	0.012
ZOT: GCV	-0.072	0.094	0.001	0.012
FOT: empirical	-0.085	0.133	0.001	0.021
FOT: VCE	-0.096	0.113	0.001	0.017
LSC	-0.098	0.103	0.000	0.016

auto-covariance matrix with $\sigma = 2$ mGal (see Eq. (3.29)). For the computation of the gravity disturbances and disturbing potential at ground level, the GRAVSOFT package (Tscherning et al., 1994) for gravity field modeling has been used. As described in section 5.2, the package uses the Tscherning-Rapp degree-variance model, which was fitted to the empirical covariance function using the program COVFIT. As shown in figure 5.11 this model matches the empirical function very well. The resulting errors at ground level are shown in figure 5.12 and the error statistics are again given in tables 5.6 and 5.7. The error pattern is similar to the results computed with ZOT regularization (cf. figure 5.7), but the RMS errors are slightly larger, especially for the computed gravity disturbances. As mentioned in section 4.3.3, the amount of smoothing is defined by the noise-covariance matrix. The results could be improved by applying an additional regularization as for instance presented in Marchenko et al. (2001).

5.4 Computations with data corrupted by colored noise

5.4.1 Simulation of colored noise

The largest contribution to the noise spectrum of airborne gravity observations comes from the double differentiation of GPS positions. The double differentiation changes the noise behavior, so that even if noise in the positions is white, it turns into colored noise in the accelerations, which has especially a lot of power in the high-frequency band. In this
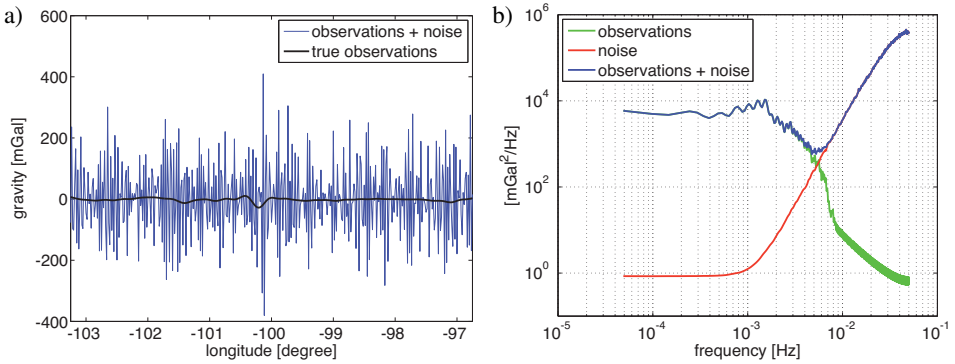
Figure 5.13: Simulated noise and the gravity signal at flight level along one profile a); and b) the corresponding PSDs estimated for the whole data set.

section the frequency-dependent data weighting scheme is tested, using a colored noise sequence obtained by double differentiation of random white noise. Note that the noise level in the low-frequency band may be too optimistic in this test. Tests with a more realistic noise spectra are presented in chapter 6.

The spacing of the observations of data set 2 is 1 arc-minute. Assuming a flight speed of 150 m/s, the data spacing corresponds to a sampling rate of 10 seconds. For an RMS error of the vertical GPS positions equal to 5 cm, this results in a total variance of the airborne gravity noise of $15000 \ \mathrm{mGal}^2$. The simulated noise and the noise-free observations are shown for one profile in figure 5.13a. The corresponding PSD of the resulting colored noise time series is shown together with the PSDs of the simulated observations in figure 5.13b, for the whole data set. The figure shows that the (noise-free) gravity signal contains almost no power above $8 \cdot 10^{-3}$ Hz, which is due to the maximum degree and order of 1800 of the GPM98b model. However, for frequencies larger than approximately $5 \cdot 10^{-3}$ Hz the colored noise has more power than the gravity signal. This means that this part of the spectrum cannot be recovered accurately.

5.4.2 Data weighting using the exact noise model

The PSD of the colored noise sequence is used to derive ARMA model coefficients, as described in section 4.4.3. For a more detailed description of the algorithms see (Klees and Broersen, 2002). The estimated ARMA model is a MA(2) model, which is used for the application of the inverse covariance matrix $\mathbf{Q_y}^{-1}$ in the LS adjustment. From the data corrupted by colored noise, a gravity field solution is computed using ZOT regularization and VCE to estimate the regularization matrix.

The estimated variance factor $\hat{\sigma}_1^2$ of the covariance matrix is close to one, which shows that the MA(2) model correctly describes the noise in the observations. Errors at ground

level are shown in figure 5.14 and the statistics are given in table 5.8 for the whole area and for the inner $4.5° \times 4.5°$ area. The latter are given because the errors are much larger at the edges of the area. This is the result of remaining noise in the high-frequency part of the spectrum, where the noise has more power then the signal to be recovered (see figure 5.13b). Because the solution is solved for frequencies higher than $5 \cdot 10^{-3}$ Hz, part of the noise is modeled. For the inner area this noise gets largely smoothed by the applied regularization.

A solution was also computed with FOT regularization applied in combination with VCE, but the results were slightly worse, confirming the results presented in the previous section.

5.4.3 Comparison with low-pass filtering

A gravity field solution was also computed from low-pass filtered data. The observations are filtered using a forward-backward 2nd-order Butterworth filter, as described in appendix A. The optimal length of the filter was determined empirically as the one that yields the smallest RMS gravity disturbance error at flight level, resulting in a filter length of 200 seconds. The RMS difference between the low-pass filtered and the true observations is 1.2 mGal. To prevent filter artifacts at the beginning and at the end of the profiles, a cosine taper is applied prior to filtering the data. Nevertheless, the results computed from the filtered observations, shown in figure 5.15, are still affected by edge effects. Also for the inner area the gravity disturbance errors and geoid errors are larger than for the solutions computed with frequency-dependent data weighting. The error statistics are given in table 5.9.

Table 5.8: Statistics for the results computed with frequency-dependent data weighting. The results in brackets denote the statistics for the inner area of $4.5° \times 4.5°$.

	δg [mGal]		N [m]	
Min	-50.39	(-8.42)	-0.260	(-0.037)
Max	39.26	(6.65)	0.165	(0.032)
Mean	-0.03	(0.00)	0.000	(0.000)
RMS	3.28	(1.42)	0.019	(0.007)

Table 5.9: Statistics for the results computed from the low-pass filtered data. The results in brackets denote the statistics for the inner area of $4.5° \times 4.5°$.

	δg [mGal]		N [m]	
Min	-48.44	(-7.70)	-0.226	(-0.039)
Max	116.80	(8.25)	0.427	(0.048)
Mean	0.02	(-0.01)	0.000	(0.000)
RMS	3.45	(1.56)	0.022	(0.008)
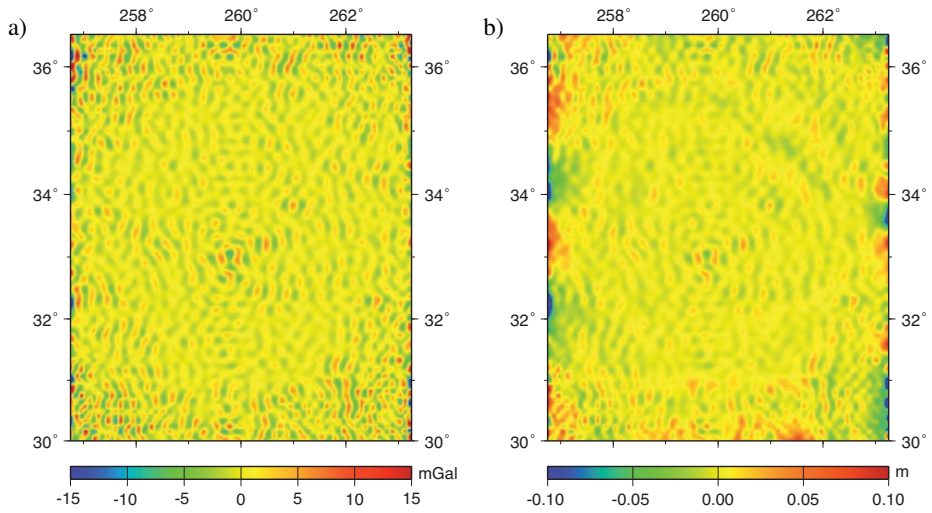
Figure 5.14: Errors at ground level for the solution computed with frequency-dependent data weighting using the exact noise model. a) Gravity disturbance errors; b) geoid height errors.
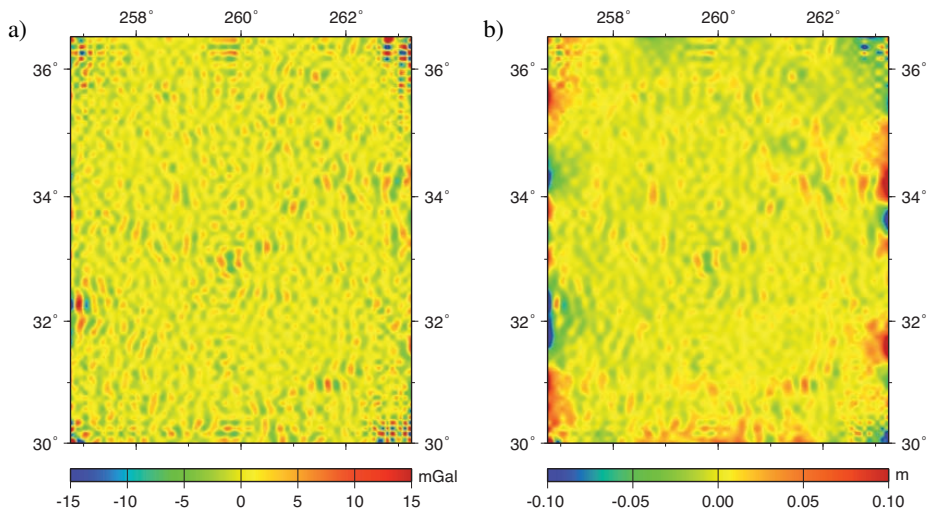
Figure 5.15: Errors at ground level for the solution computed from low-pass filtered data. a) Gravity disturbance errors; b) geoid height errors.
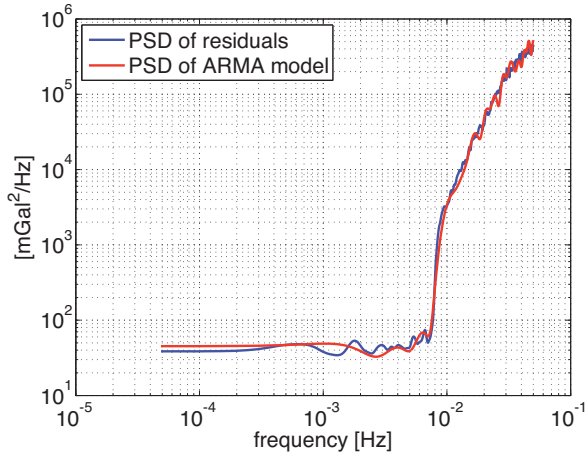
Figure 5.16: PSDs estimated from a posteriori LS residuals ($\alpha = 1$) and the resulting ARMA model.

5.4.4 Noise model estimation from residuals

In section 5.4.2, the true noise sequence is used to derive the noise model. In practice this information is usually not available. Therefore, the strategy discussed in section 4.4.3 is applied. It uses the a posteriori residuals of a preliminary LS solution, from which the noise model is derived iteratively.

To ensure that the computed PSD is positive, the covariance function is truncated by multiplying it with the Gaussian function of Eq. (4.77), with $Q = 360$ seconds. This value is determined by trial and error, starting from a large Q and gradually decreasing it until the PSD becomes positive at all frequencies. To make it easier to approximate the PSD by an ARMA model a more drastic smoothing is applied with $Q = 100$ seconds. This way the order (p, q) of the ARMA-filter is smaller, which makes the algorithm more efficient.

The first model is estimated from residuals $\hat{\mathbf{e}} = \hat{\mathbf{y}} - \mathbf{y}$ computed using $\mathbf{Q_y} = \sigma_y^2 \mathbf{I}$, with $\sigma_y = 1$ mGal. In this case both VCE and GCV fail to determine the regularization parameter. The computation of the partial redundancies for VCE and the nominator of the GCV function requires the de-correlation of the residuals using the (unknown) covariance matrix. Therefore, the regularization parameter is first set equal to one. This choice is arbitrary; below it will be investigated whether the final noise model is sensitive to the initial choice of the regularization parameter.

The PSDs estimated from the residuals and the resulting ARMA model are shown in figure 5.16. The model estimated from the residuals is a MA(29) model, which is used in the subsequent LS adjustment. The results from this estimation already show a large improvement: the RMS gravity disturbance error is 4.2 mGal and the PSD of the noise
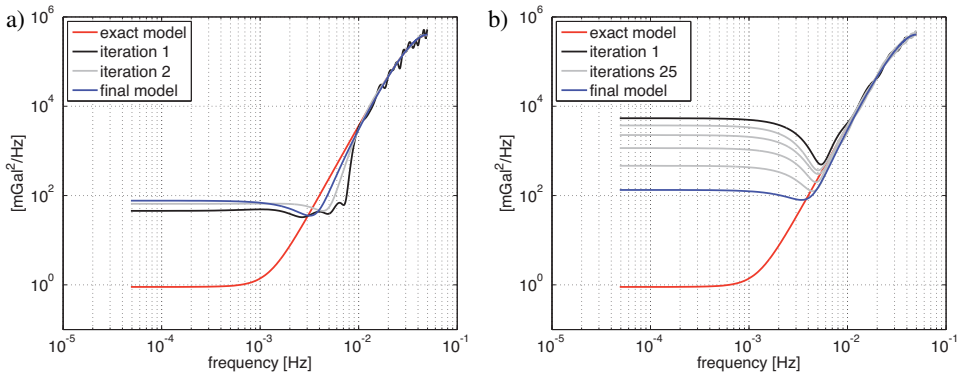
Figure 5.17: PSDs computed from the estimated noise models for each iteration compared to the exact model. a) The initial regularization parameter was is equal to one and the final model is obtained after three iterations; b) the initial regularization parameter is set to $\alpha = 1 \cdot 10^6$ and the final model is obtained after 6 iterations.

model is close to PSD of the exact model, especially in the high-frequency band. The procedure of model estimation is repeated until convergence is obtained. The stopping criterion of the iteration process is that the RMS difference between two iterations should be smaller than a pre-defined value. Here, a value of 0.5 mGal is used. In this study convergence is obtained after three iterations. The model of the second iteration is a MA(8) model, which gives an RMS error of 3.4 mGal. This RMS error is very close to the RMS error computed with the exact noise model. The final model is a MA(3) model, which yields an RMS error of 3.2 mGal. The PSDs of the models are shown for each iteration in figure 5.17a.

For the test described above, the regularization parameter was set equal to one. To test the dependence of the procedure on the initial choice of the regularization parameter, the estimation of the noise model is repeated for a much larger α. For $\alpha = 1 \cdot 10^6$ the resulting gravity disturbances are close to zero, and the residuals contain most of the signal. Nevertheless, an accurate model of the colored noise can still be obtained, but more iterations are required. Convergence is now obtained after 6 iterations. The PSD of the ARMA model for each iteration is shown in figure 5.17b. The initial model has much power at the low frequencies, since most of the signal is absorbed, but with every iteration step the power decreases until convergence is reached. The results computed with the final model, which is a MA(2) model, show an RMS gravity disturbance error of 3.2 mGal. Although this test indicates that the estimation procedure is robust against the initial choice of regularization parameter, it is recommend to start from a smaller α so most of the signal is preserved when computing residuals. Furthermore, in this case only a few iterations are required to obtain the noise model. The procedure for noise model estimation in airborne gravity data processing is shown schematically in figure 5.18.
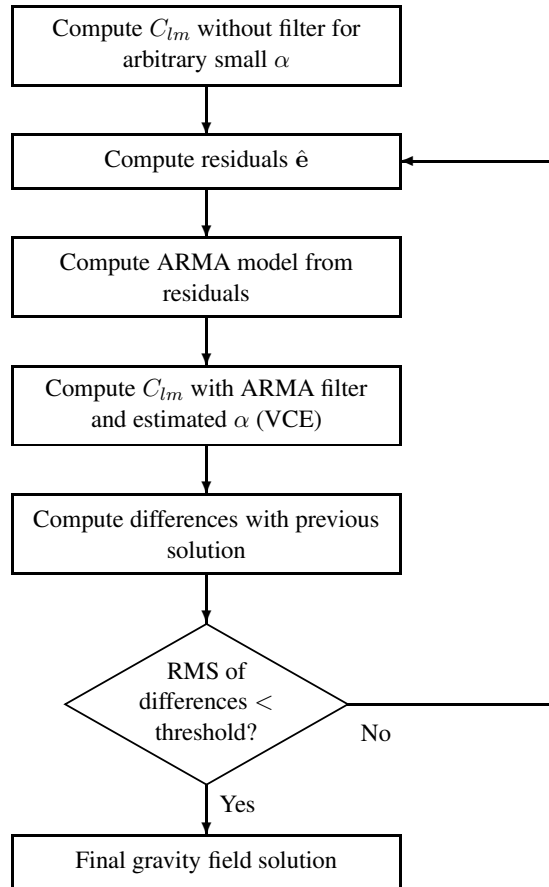
Figure 5.18: Noise estimation from a posteriori LS residuals in the frequency-dependent data weighting scheme.

5.5 Bias and drift handling

5.5.1 Estimation and filtering of bias parameters

In this section the proposed methods for bias and drift handling are tested and compared with a cross-over adjustment. For the first test, random biases with an RMS of 4.0 mGal and zero-mean are added to the flight profiles of data set 2. Figure 5.19a shows the histogram for the cross-over differences computed at the 330 cross-overs. Their standard deviation is $\sigma_x = 5.1$ mGal, which indicates an overall accuracy of the observations of $\sigma_e = \sigma_x/\sqrt{2} = 3.6$ mGal, instead of the actual noise level of 4.0 mGal.

99
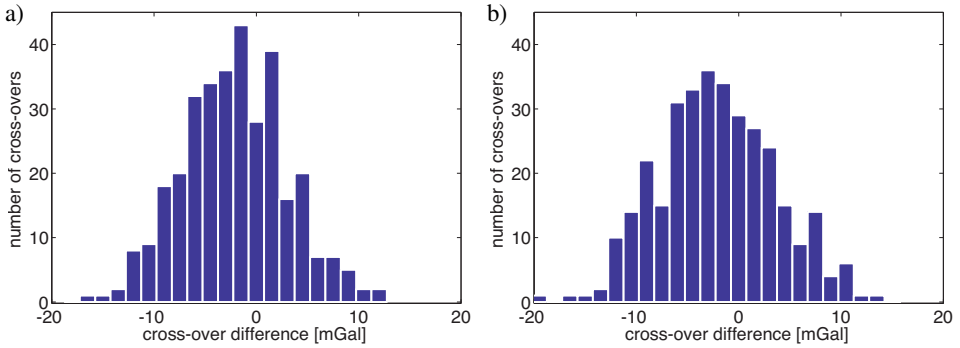
Figure 5.19: Histogram of cross-over differences, where a random bias was added to each profile. a) Noise-free observations; b) observations corrupted by white noise.

When bias are estimated jointly with the gravity field parameters (according to Eq. (4.80)) from noise-free data contaminated by biases, the estimation results in maximum differences between the true (added) biases and estimated biases of less than 0.001 mGal, disregarding a mean difference of 0.009 mGal. The mean difference is equal to the mean value of the input data, which is absorbed by the estimated biases. The explanation is that when bias parameters are added to the functional model, it is not possible to distinguish between a common bias in the data and the constant part of the gravity signal. The same holds for each individual line if there would be no crossing lines. In that case the estimated bias would include the mean value of each flight line. To make sure the mean value of the data is not absorbed by the estimated biases, a constraint can be added to the functional model. Here, a fixed constraint that the sum of the estimated biases is equal to zero is applied.

Bias estimation is also performed for the data corrupted with white noise (RMS=2 mGal). A cross-over analysis performed for this case yields a standard deviation of $\sigma_x = 5.6$ mGal for the cross-over differences. See figure 5.19b for the histogram of the computed cross-over differences. The standard deviation of the cross-over errors indicates an estimated noise level of $\sigma_e = 4.0$ mGal, which again underestimates the true noise level of 4.6 mGal.

The result of the estimation is given in figure 5.20a. It shows for each flight line the true bias and the estimated bias, where the lines 67–71 denote the N-S profiles. The statistics of the estimation are given in table 5.10. Both table and figure show that the biases are estimated very well; the maximum error in the estimated biases is 1.1 mGal, whereas the RMS difference is only 0.4 mGal, which is below the noise level of the data.

Instead of estimating bias parameters as additional parameters, they may also be filtered out by applying a filter matrix to the functional model (Eq. (4.83)). In this case the results for the computed gravity field solutions are nearly the same. Small differences may occur due to the slightly larger overall redundancy in case of filtering. The numerical
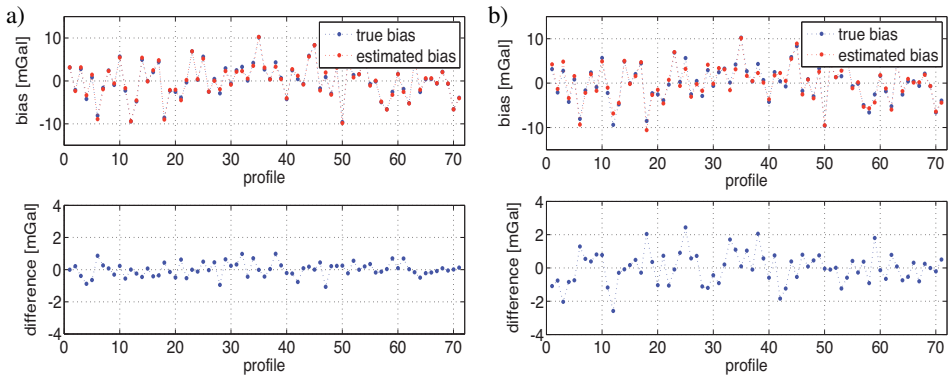
Figure 5.20: Results of bias estimation where a random bias is added to each profile and observations are corrupted with white noise. a) Biases are estimated as additional parameters in the functional model; b) biases are estimated by a cross-over adjustment (the estimated biases are corrected for a mean difference of -1.7 mGal). The bottom part of the figures shows the differences between the true and the estimated bias parameters.

costs to compute the filter matrix are however much higher, especially in case of colored noise. Therefore, bias and drift estimation is preferred over bias and drift filtering.

5.5.2 Cross-over adjustment

Bias parameters are also computed by means of a cross-over adjustment, for which the software AGX (Hwang et al., 2006) is used. In the adjustment, the line with the smallest added bias is fixed, and biases are estimated from the 330 cross-over differences. When the data are only corrupted by a bias, the RMS difference between true and estimated biases is 0.009 mGal, with a maximum error of 0.022 mGal. These differences are the result of interpolation errors at the cross-over points.

In case of random white noise the results of the cross-over adjustment are worse then when biases are estimated as additional parameters in the functional model (see table 5.10). Because in many points the simulated noise is larger than the true bias, the computation of cross-over differences is corrupted and therefore the estimated biases get corrupted as well. The differences between true biases and estimated biases show a mean error of 1.7 mGal, resulting in an RMS error of 1.9 mGal. The results for the estimated bias parameters computed by the cross-over adjustment are shown in figure 5.20b.

5.5.3 Simultaneous estimation of bias and drift parameters

Besides a bias, data obtained from gravity sensors generally contain a drift, although the drift may be very small. For LaCoste and Romberg gravimeters, excellent drift characteristics of less than 1 mGal/day have been reported (Forsberg and Olesen, 2006). In

Table 5.10: Statistics of the differences between true and estimated biases ($\mathbf{b} - \hat{\mathbf{b}}$) [mGal] for bias estimation and cross-over adjustment.

Method	Min	Max	Mean	STD	RMS
Bias estimation	-1.08	0.98	0.00	0.00	0.43
Cross-over adjustment	-4.35	0.82	-1.70	0.91	1.95

such a case drift estimation is not required since the error is well below the noise level of the data. For INS systems the drift can be as large as 15 mGal/h (Glennie and Schwarz, 1999), in which case drifts should be estimated.

To test whether drift parameters can be estimated simultaneously with bias and gravity parameters, the data are corrupted by a random drift with a standard deviation of 2.0 mGal/hr. Figure 5.21 shows the surface described by the estimated drift and bias parameters per profile for the noise-free data set, if no constraint for the drift parameters is added to the functional model. In fact, any surface that can be described by the function $f(x, y) = a + bx + cy + dxy$ gets absorbed by the estimated bias and drift parameters. This case is similar to the mean gravity value absorbed by estimated bias parameters per profile, but in practice the latter can be restored by tying the data set to ground values.

The results for the estimated drift parameters per profile are given in figure 5.22, which shows the differences between true and estimated drift parameters in a LS adjustment with data corrupted with white noise. The RMS difference between true and estimated drifts is 1.1 mGal/hr. The RMS difference between the estimated and added bias parameters is in this case 0.7 mGal and the overall RMS gravity disturbance error at ground level is 1.7 mGal, which is only slightly worse than if data are only corrupted with white noise (see section 5.3).

Nevertheless, the estimation of a drift per profile is only recommend if the sensors
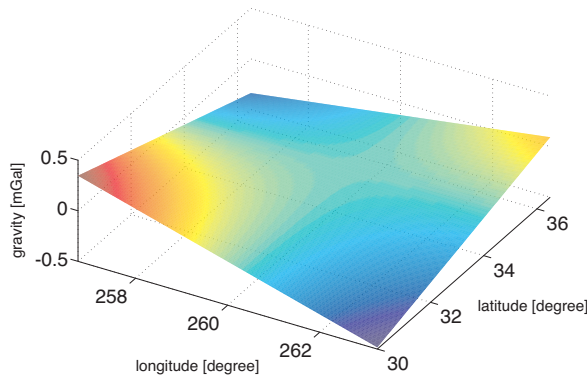
Figure 5.21: Surface described by the estimated drift and bias parameters for the uncorrupted noise-free data if no constraints are added to the functional model.
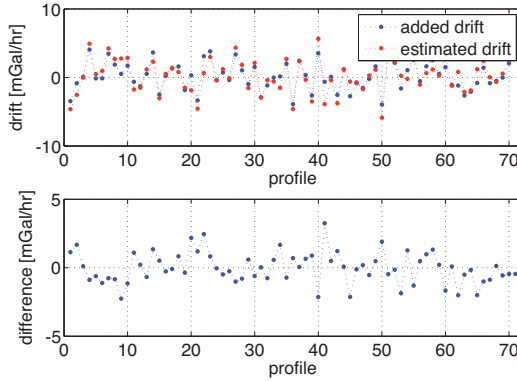
Figure 5.22: Results for the estimated drift parameters where a bias and a drift are added to each profile and observations are corrupted with white noise. Bias and drift parameters are estimated per profile as additional parameters in the functional model.

used to measure gravity are known to drift, such as the case for INS systems. The sensors that are used for the acquisition of the gravity data described in the next chapter generally show very small drifts. Therefore, only biases will be estimated as additional parameters in the functional model.

5.6 Summary of the optimal solution strategy

The developed methodology provides accurate results when applied to simulated data sets. For the numerical studies presented in this chapter the methodology outperforms the more traditional approaches of airborne gravity data processing. Based on the simulations, several conclusions can be drawn and choices among various proposed methods can be made. This leads to an optimal strategy, summarized below, that will be applied to real data in chapter 6.

Gravity field representation

The fundamental solutions of Laplace's equation in Cartesian coordinates are a suitable representation of the disturbing potential, if a method for edge effect reduction is applied. The controlled area extension method is the optimal choice to reduce these edge effects. It was found that an extension of the area, fixed by the parameters Δx and Δy, by a tenth of the area size already improve the results significantly. The obtained results are more accurate than for LSC in terms of gravity disturbance and geoid height errors.

Regularization and parameter choice rule

To overcome the instability of the downward continuation problem, a regularization method must be applied. For the base functions used in this thesis, VCE should be used to estimate the regularization parameter, but the choice of regularization matrix depends on the signal spectrum. In case of the simulated data ZOT regularization yields good results for both high-frequency solutions (e.g. gravity disturbances) and smooth solutions (e.g. the disturbing potential), but in practice FOT regularization may perform better. This is investigated with real data in chapter 6.

Frequency-dependent data weighting

To handle colored noise in airborne gravity data frequency-dependent data weighting is applied. The noise is efficiently modeled by employing ARMA filters to compute the application of the (inverse) covariance matrix to a vector. It was shown that a noise model can be estimated from a posteriori LS residuals in an iterative manner. Starting with a (scaled) identity matrix as covariance matrix and a relatively small regularization parameters, an accurate noise model can be obtained after a few iterations. The results are slightly more accurate than for low-pass filtered data. The developed method is fully data-driven, and provides a more formalized approach to filtering of airborne gravity data.

Bias and drift handling

Data acquired from gravity sensors often contain a bias and/or a drift. The optimal approach to account for these long wavelength effects is to estimate them as additional parameters in the functional model. This way all data are used in the estimation, which leads to much better results than a cross-over adjustment, especially if the noise level of the data is high.

Application to airborne gravimetric survey data $\qquad$ 6

In this chapter the developed methodology for airborne gravity data processing as derived in the previous chapters, is applied to real gravimetric survey data. Three data sets are used for the computations.

The first data set, described in section 6.1, consists of airborne gravity measurements obtained in 1996 over the Skagerrak area between Norway and Denmark. The survey was performed as part of the AGMASCO campaign, by a cooperation between several European institutes. Because the survey provided accurate airborne gravity data and because good ground surface data is available for this region, this data set is very useful to demonstrate and optimize the performance of the developed methodology. First a noise model is derived to handle colored noise in a frequency-dependent data weighting and the results are compared to the ones obtained from low-pass filtered data. Furthermore, a method for outlier detection is investigated and bias parameters are estimated jointly with gravity field parameters. Finally, a local geoid is computed using the developed methodology and with LSC, and the results are compared to the geoid for the Nordic countries (NKG-2004).

In section 6.2, tests conducted with airborne gravity data measured by the Geo-ForschungsZentrum (GFZ) during the CHICAGO campaign are presented and analyzed. The area covered by this survey is situated near the coast of Chile, and shows strong gravity gradients due to the Peru-Chile subduction zone. The overall accuracy of the data is lower than that of the first data set. Therefore, it is used to investigate whether the estimation and testing of non-gravitational parameters can improve upon the obtained results. Furthermore, the results obtained with the developed methodology are compared to the more traditional approach for airborne gravity data processing.

The third data set consists of data acquired during an airborne gravity evaluation survey performed by Sander Geophysics Limited (SGL). The goal of this survey was to demonstrate the application of airborne gravimetry for mineral exploration. The area is located just north of Timmins, Ontario, and is much smaller than the survey areas of the other two data sets. The reported accuracy of this data set is very good; a comparison with upward continued ground data produced a standard deviation of 0.6 mGal, after low-pass filtering. It is therefore a very challenging data set to test the frequency-dependent data weighting scheme and apply downward continuation of the data to the location of

the control points at ground level. The results for this data set are presented in section 6.3.

A discussion of the results obtained from the computations with the three data sets is given in section 6.4.

6.1 Skagerrak data set

The Skagerrak campaign was flown at the end of 1996 as part of AGMASCO (Development of an Airborne Geoid Mapping System for Coastal Oceanography), an international project funded by the European Commission within the framework of the MAST-III program (e.g. Forsberg et al. (1997), Hehl et al. (1997), Timmen et al. (1998)). The goal of this project was to setup a hard- and software system for a combined airborne gravity and airborne altimetry application in near coastal regions. The Skagerrak area, a strait running between the Jutland peninsula of Denmark and southern Norway, was chosen as a first test of the system, because good ground truth data were available for comparisons. Furthermore, strong localized gravity anomalies are present in the area, which are associated with a buried volcano just south of the Norwegian coast and salt domes at the Danish side of the Skagerrak. The availability of good surface gravity data and the fact that the survey was flown at a relatively low flight level (400 m), make the data very suitable for developing new processing strategies and comparison studies.

6.1.1 Description of the data

Airborne gravity data

For the computations described in this section, all gravity data were pre-processed anew using the Airborne Gravity Software (AGS) (Meyer, 2004). After pre-processing, low-pass filtered and unfiltered data sets have been obtained in the original observation points. The sampling of the data is 1 second, which results in 70000 observations, divided over 26 tracks. The processing steps performed within AGS are described in Appendix A. The filtered set of observations is obtained with the 2nd-order Butterworth filter and is used to compare the results of the computations with those obtained with frequency-dependent data weighting.

The processing of the GPS data has been performed with the Kinematic/Static GPS Software KSGSoft (Xu et al., 1998). The track pattern of the processed profiles is shown in figure 6.1. Because all computations are done in a local Cartesian reference frame, the ellipsoidal coordinates were transformed to Cartesian coordinates according to Eqs. (B.1) and (B.2). The local x-axis is aligned with the direction of profiles (cf. figure 6.1).

Ground truth data

There is a good surface data coverage in the Skagerrak area to assess the quality of the airborne gravity data. During the AGMASCO project new shipborne reference gravity
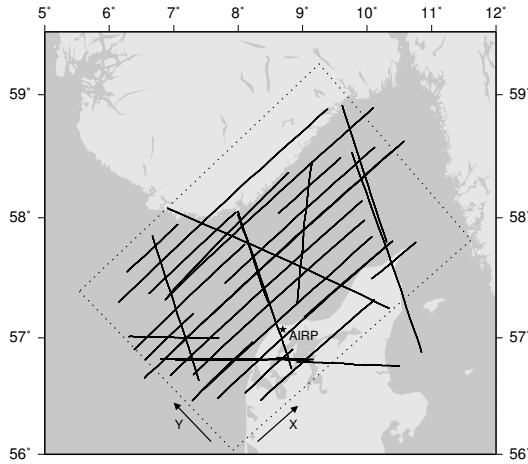
Figure 6.1: The flight tracks of the Skagerrak campaign. The star marks the location of the GPS reference station at the airport in Thisted. The dotted lines denote the area of the airborne gravimetry survey.

data were acquired along some of the flight lines. The surface data used for the comparisons comprises both gridded land and shipborne data as described by Olesen et al. (1997). The gravity anomalies are shown in figure 6.2. The data have been upward continued to flight level using the fundamental solutions of Laplace's equation in Cartesian coordinates. Two solutions are computed. The first solution is solved up to a very high degree and order of $L = 70$ and $M = 50$, which corresponds to a resolution of 2.5 km. From the estimated coefficients C_{lm}, gravity disturbances are computed in the locations of the airborne gravity observations. The resulting gravity field solution is used to derive a noise model to be applied in the frequency-dependent data weighting scheme.

The second solution is solved up to degree and order $L = 14$ and $M = 10$, which is based on the spacing of approximately 15 km of the flight tracks of the airborne gravity data. Again, gravity disturbances are computed at the locations of the airborne gravity observations from the estimated coefficients C_{lm}. This solution, which has the same resolution as the solutions computed in the following section, is used to validate the results of the developed methodology at flight level. This way the quality of the data can be assessed and a good comparison of filter techniques can be made since the solutions are free of downward continuation effects. The solutions at flight level obtained from the surface gravity data are shown in figure 6.3.
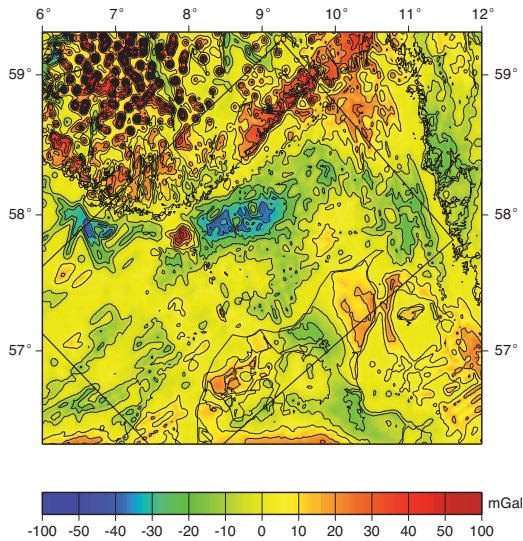
Figure 6.2: Surface gravity anomalies in the Skagerrak area. The black rectangle denotes the area of the airborne gravimetry survey.
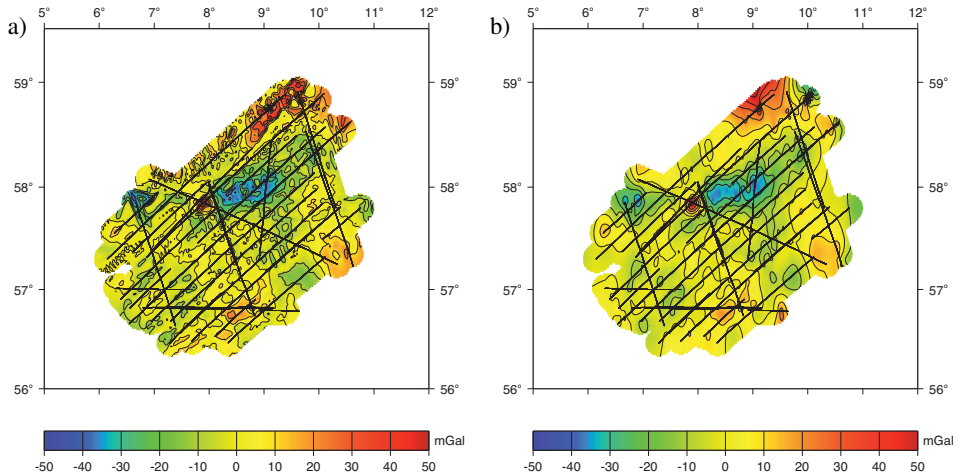

Figure 6.3: Upward continued ground truth data at flight level; a) High resolution, solved for $L = 70, \ M = 50$; b) Low resolution, solved for ($L = 14, \ M = 10$).
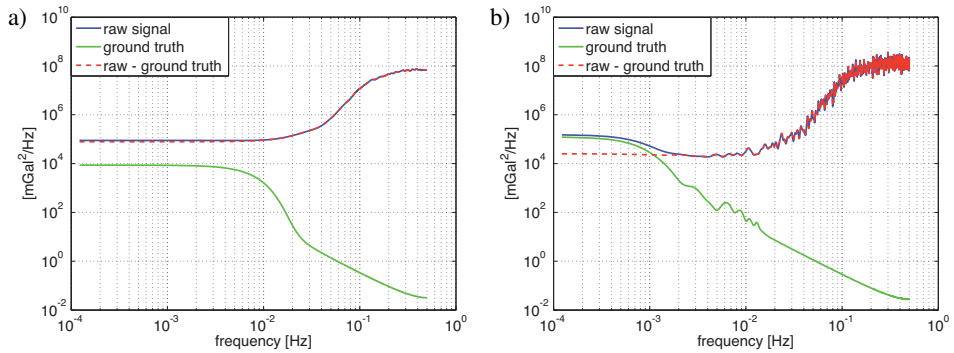
Figure 6.4: PSDs computed from the difference between upward continued surface gravity data and unfiltered airborne gravity data. a) Estimated using all profiles; b) estimated using only one profile.

6.1.2 Frequency-dependent data weighting

Noise model from ground truth data

The performance of the developed methodology is first assessed for the determination of gravity disturbances at flight level. To obtain a noise model, the high resolution gravity model computed from the surface gravity data (cf. figure 6.3a) is used. The difference between upward continued gravity and the unfiltered airborne gravity data is in this case considered as noise. From these differences a covariance function is computed, which is transformed into a power spectral density function using the inverse Fourier transform. To ensure that the PSD is positive for all frequencies, the covariances are multiplied by a truncation function as described in section 4.4.3. The resulting noise PSD is shown in figure 6.4a, together with the signal PSDs computed from the upward continued ground data and the airborne gravity data. Obviously, the noise is larger than the gravity signal for all frequencies, which would mean that the signal cannot be resolved. This is not true. The airborne gravity data are acquired in multiple flights over several days, during which the noise characteristics change. It means that noise in the data is non-stationary, which results in an inaccurate estimation of the low-frequency part of the spectrum. Therefore, the noise PSD is estimated on the basis of one long flight track that was not affected by large turbulence. A longer profile allows for the estimation of longer lags in the computation of the covariance function, and the absence of turbulence leads to a more accurate estimation of the PSD due to less non-stationary noise. The resulting noise and signal PSDs are shown in figure 6.4b.

From this noise PSD an ARMA model is estimated using the approach described in (Klees and Broersen, 2002). The resulting model, which is a MA(33) model, is shown in figure 6.5. It is used to derive a proper noise covariance matrix applied in the estimation
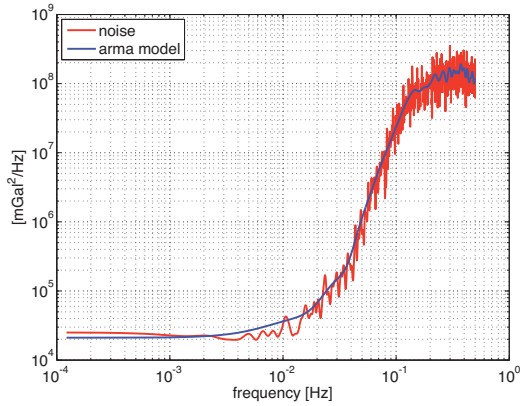
Figure 6.5: PSDs computed from the difference between observations and upward continued ground truth data (red), and the best-fitting ARMA model (blue).

of gravity field parameters. Whether it is justified to apply an ARMA model obtained on the basis of only one profile is addressed at the end of this section.

From the estimated coefficients C_{lm}, gravity disturbances are computed at flight level with the same resolution as for the upward continued gravity (i.e $L = 14$, $M = 10$, cf. figure 6.3b). To stabilize the solution, regularization must be applied. Because the spectrum of the signal is different than for the simulations, solutions are computed for both ZOT and FOT regularization applied. The regularization parameter is estimated using VCE. Furthermore, controlled area extension of 50 km is applied to reduce edge effects. Here, a solution is obtained without the estimation of bias parameters; the joint estimation of bias parameters and gravity field parameters is investigated in section 6.1.4.

Differences are computed at the observations points between the ground truth solution (cf. figure 6.3b) and the airborne gravimetry solution, which yields an RMS difference of 4.5 mGal for ZOT regularization and 3.1 mGal for FOT regularization (see table 6.2). The gravity field solution at flight level obtained with FOT regularization and the difference with the upward continued surface gravity are shown in figure 6.6. The application of FOT regularization provides more accurate results than ZOT regularization, even though the latter performed better in case of the simulations in chapter 5. Real airborne gravity observations contain more power in the high-frequency spectrum, which means that the structure of the FOT regularization matrix gives a better description of the covariance matrix of the prior information. This supports the statement in chapter 5 that the choice of the regularization matrix should be made on the basis of the spectrum of the data. In the following sections FOT regularization is used to obtain a stable solution.
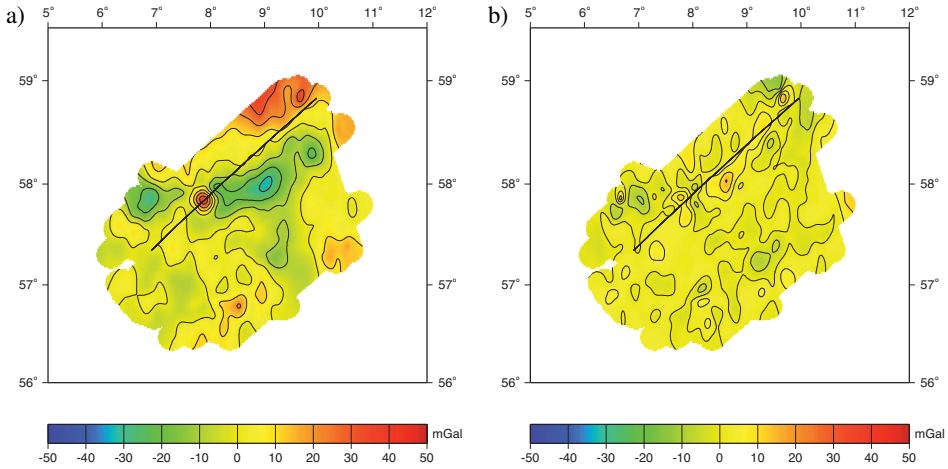
Figure 6.6: a) Gravity field solution computed with frequency-dependent data weighting; and b) differences with upward continued ground truth data. The results along the profile denoted by the black line are shown in figure 6.8.
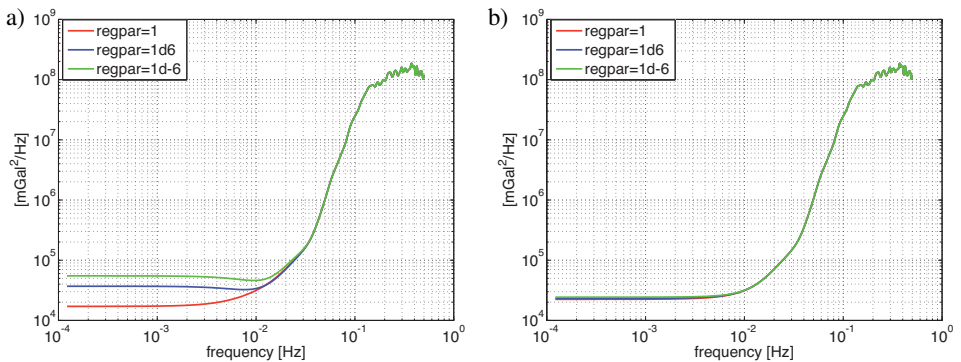

Figure 6.7: Noise PSDs for varying initial regularization parameters. a) PSDs estimated from residuals of the initial solutions; a) PSDs of residuals computed after one iteration.

Noise model estimation

In many occasions, good ground surface data may not be available and the noise model has to be obtained in a different way. In chapter 5 it was shown that if the noise is large in the high-frequency part of the spectrum, a noise model can be estimated from a-posteriori residuals of a preliminary LS adjustment without using a noise model. The estimation of the variance components for determining the regularization parameter does not converge

because the residuals are not de-correlated. In chapter 5 it was shown that the estimation of the noise model is robust against the initial choice of the regularization parameter. To test whether this is also the case for real data, the estimation of the noise model is repeated for three different initial regularization parameters ($\alpha = 1 \cdot 10^{-6}$, $\alpha = 1$, $\alpha = 1 \cdot 10^{6}$). The noise PSDs computed from residuals of the initial solutions are shown for each choice of regularization parameter in figure 6.7a. For each initial choice of regularization parameter, only two iterations are required and the final noise PSDs, shown in figure 6.7b, are nearly identical. As a result, the differences between the solutions are very small. They are at the level of the uncertainty in estimating different ARMA models from one noise realization. The RMS difference between the three solutions and the ground truth solution is given in table 6.1 for each iteration step.

The results confirm that an accurate noise model can be estimated from residuals of a preliminary LS solution. Furthermore, the procedure is not sensitive to the initial choice of the regularization parameter. Although the simulations in chapter 5 showed that more iterations may be required for a large initial regularization parameter, it is not the case for this data set. This can be explained by the fact that the power of the noise in the high frequency band is much larger here, due to the higher sampling rate of this data set.

Table 6.1: RMS difference [mGal] between the upward continued ground truth solution and the solutions computed with the estimated noise models for different initial choices of the regularization parameters.

initial solution		1st iteration		2nd iteration
$\alpha_{init} = 1 \cdot 10^{-6}$	57.33 $\Rightarrow$	3.58	$\Rightarrow$	3.03
$\alpha_{init} = 1$	19.08 $\Rightarrow$	3.26	$\Rightarrow$	3.04
$\alpha_{init} = 1 \cdot 10^{6}$	9.81 $\Rightarrow$	3.08	$\Rightarrow$	3.07

Table 6.2: Statistics of differences [mGal] between the upward continued ground truth data and the airborne gravimetry solutions computed with frequency-dependent data weighting (FDW) and low-pass filtering.

Method	Min	Max	Mean	RMS
FDW: noise model from ground truth	-9.71	15.24	0.58	3.12
FDW: estimated noise model	-9.89	15.94	0.69	3.03
Low-pass filtering	-10.38	15.87	0.74	3.03

Comparison to low-pass filtering

A solution was also computed from the low-pass filtered data. Again FOT regularization is applied, but the regularization parameter could not be obtained by VCE or GCV. This may indicate that the assumption of white noise in the frequency band of interest is not
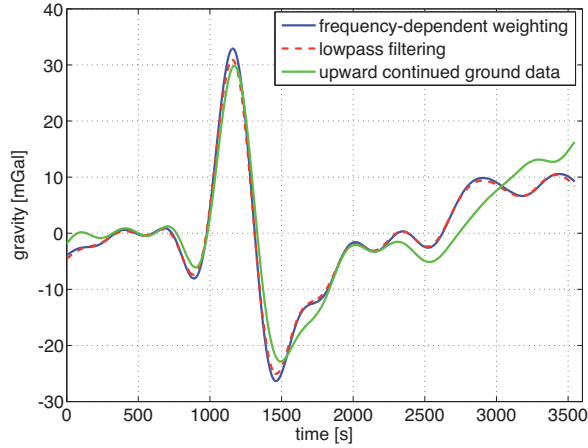
Figure 6.8: Results at flight level for LPF and FDW compared to the upward continued ground truth data along one profile.

valid. Instead, the regularization parameter was chosen as the one that yields the smallest RMS difference with the upward continued ground data. Note that this gives a too optimistic solution. The resulting RMS difference is $3.03 \, \mathrm{mGal}$, which is equal to the RMS difference obtained with frequency-dependent data weighting with the estimated noise model. The statistics of the difference between the computed solutions and the ground data are summarized in table 6.2. The resulting gravity solutions along the profile over the buried volcano are shown in figure 6.8.
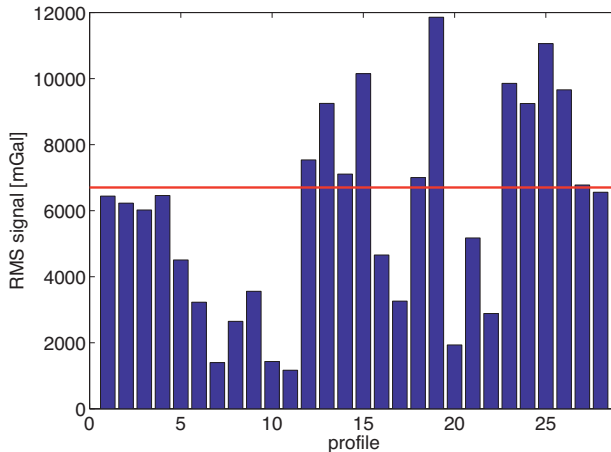
Figure 6.9: Signal variance for each profile, used to rescale the ARMA model.

113

Improvement of the noise model

The development of the filter is based on ground truth data or a posteriori residuals computed for a single track, and the obtained model is used for the filtering of all profiles. However, the noise variance and the noise characteristics are different for each track, due to changing flight circumstances. Figure 6.9 shows the signal RMS of the unfiltered observations for each profile. Because the variance of the noise is several orders of magnitude larger than the variance of the gravity signal, the signal variance can directly be used as a measure of the noise level of each track. The obtained noise variances are used to re-scale the noise model per track and the structure of the noise model is described by the ARMA model estimated in the previous subsection. If a gravity field solution is computed with frequency-dependent data weighting with the scaled model, the results show however no improvement. The RMS difference with upward continued ground data is 3.78 mGal, which is larger than the RMS difference obtained without scaling of the noise model. This can be explained by the fact that the total variance of the signal is the result of high-frequency noise. If these variances are used to re-scale the noise model, the noise level of the low-frequency part of the spectrum also changes, which may result in a wrong weighting of the gravity signal per profile.

Instead of re-scaling the ARMA model of one profile, a separate ARMA model is computed for each track. The ARMA models are estimated from noise PSDs computed from the difference between the high resolution gravity field model computed from the ground truth data (cf. figure 6.3a) and the unfiltered observations. The obtained ARMA models are used for the application of the (inverse) covariance matrices, belonging to the observations of those profiles, in the LS adjustment. In this case, the RMS difference with the ground truth is also larger than for the results computed with one ARMA model: the RMS difference is 4.47 mGal. This indicates that for some profiles a less accurate noise model was estimated due to gaps and non-stationary noise, or because the length of some profiles is too short to get a good estimate for the low-frequency part of the spectrum.

An improvement on the noise modeling presented in this section may be provided by variance component estimation, as discussed in section 4.3.4. Each profile is considered as a separate observation group that gets a different weighting. This is similar to the scaling of one ARMA model, but the relative weights of the co-factor matrices are estimated in an iterated LS estimation. Such an estimation was implemented using the iterative maximum-likelihood method and tested with the ARMA model estimated for one profile, but convergence of the variance components could not be obtained. Since the convergence of VCE depends on the correctness of the noise model, this can indicate that the structure of the applied ARMA model is not representative for the noise structure of all tracks. Further research on obtaining an improved noise model using VCE is recommended. In the following sections, the noise model estimated from a posteriori residuals of one profile is used in the frequency-dependent data weighting scheme.
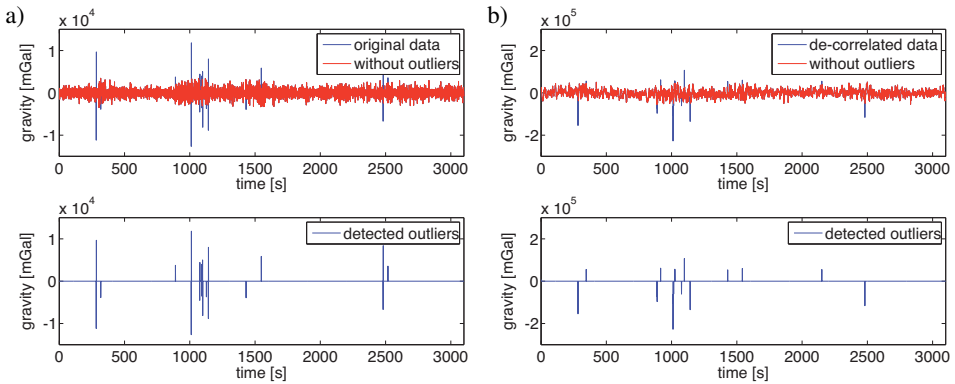
Figure 6.10: Outlier detection using the 3-sigma rule shown for one profile of the Skagerrak data set. a) Applied to the original observations, resulting in 20 detected outliers out of 3151 observations; b) applied to de-correlated observations. In this case 19 observations are identified as outliers.

6.1.3 Outlier detection

With the application of an accurate noise model an accurate gravity field solution can be obtained. However, observations are generally not only contaminated by (colored) noise, but also by outliers and/or systematic errors. It is necessary to detect and remove these errors prior to the computation of gravity field parameters because undetected outliers may lead to erroneous results. For the detection of outliers a vast number of methods can be applied. A conventional approach in geodesy is to test the observations for blunders using the w-test statistic and remove the observation with the highest test-statistic (see e.g. Teunissen, 2000). This procedure of data snooping is however not convenient for large data sets, since a new adjustment must be performed after the removal of each erroneous observation.

A much more simple approach is the application of the 3-sigma rule, which is often used as a quick tool to remove gross errors from the data. Assuming a normal distribution almost all of the observations lie within three standard deviations of the mean. Observations that are not within this range are discarded. Since the removal of these observations reduces the standard deviation, it can be applied in an iterative manner until all observations are within the 3σ range. The noise level of the observations is different for each profile as shown in previous section (cf. figure 6.9), which means that the application of the 3-sigma rule results in the removal of most of the observations located in profiles with a high noise level, whereas for some profiles no outliers are found. Therefore, the method is applied to each profile separately, in which case 1200 outliers are found (2% of the data). Figure 6.10a shows as an example the observations that are identified as outliers within one profile.

An outlier is an observation that does not follow the stochastic properties of the noise

model. As such, some of the detected outliers may be observations contaminated by strong noise, which is removed in the frequency-dependent data weighting. Therefore, the procedure is applied to de-correlated observations, resulting in the 1150 detected outliers in the whole data set. Figure 6.10b shows for the same profile as figure 6.10a the de-correlated observations and the detected outliers for this case. The figures shows that especially the large outliers are detected from the original data as well as from the de-correlated data.

If a solution is computed with the data from which the outliers detected from the de-correlated data are removed, the RMS difference with the upward continued ground data is 4.83 mGal. This is much larger than the RMS difference obtained without outlier detection (cf. table 6.2). This is remarkable because even if the discarded observations are falsely identified as outliers, the redundancy of the data set is large enough to compute an accurate solution when 2% of the observations is removed.

Therefore, the procedure is repeated by removing only the observations that show a specific pattern. Figure 6.10a shows several occasions where the signal jumps from a large negative value to a large positive value (or vice versa), such as for instance the outlier located around 1000 seconds. These outliers occur as large spikes in the de-correlated data shown in figure 6.10b. As discussed by Olesen (2003), these large errors may be caused by GPS cycle slips. For the whole data set 50 occurrences of such jumps were detected and removed. In that case, the RMS difference with the ground truth data is 3.22 mGal, which is still larger than the solution without outlier detection (cf. table 6.2).

It can be argued that a larger RMS difference with the ground truth data does not necessarily mean a less accurate solution. However, as mentioned above, removing only a few observations should not have such a large negative effect due to the large redundancy of the data. The reason for the larger RMS in this case is that removing data introduces a lot of data gaps. Although the PCCG approach for the application of the covariance matrix to a vector, as presented in section 4.4, is not affected by edge effects in the presence of data gaps, the removal of outliers decreases the accuracy of the solution. Even when the outliers are replaced by 'true' values computed from the ground truth, the fit with the upward continued ground data is worse than for the case that no outliers are removed. The reason is that because the data are correlated, removing a single observation affects a number of observations before and after the detected outlier. Therefore, a different strategy should be employed in this case to detect and remove outliers from the data.

A possible method to treat outliers in case of colored noise would be to apply a robust estimation approach, such as M-estimation (Huber, 1981). In that case no observations are discarded, but observations for which the residuals are large get a smaller weight in the estimation. This topic requires further research; in the following sections outlier detection is therefore not applied.
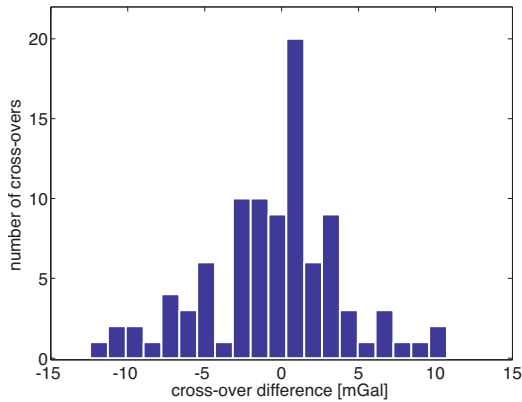
Figure 6.11: Histogram of cross-over errors computed from low-pass filtered observations.

6.1.4 Estimation of bias parameters

A cross-over analysis is performed with the low-pass filtered data to test the internal consistency of the data. The standard deviation computed from 95 cross-overs is 4.48 mGal, which corresponds to an estimated accuracy of 3.17 mGal. The histogram of the computed cross-over misfits is shown in figure 6.11. As discussed in section 3.1.2 these misfits may be the result of local errors, and biases estimated in a cross-over adjustment can reduce the accuracy of the gravity field solution.

Here, biases are estimated jointly with gravity field parameters in a LS adjustment. A solution is computed with frequency-dependent data weighting as well as from the low-pass filtered observations (i.e. without FDW). The estimated bias parameters are shown for both solutions in figure 6.12. For most of the profiles, the difference between the bias parameters estimated from low-pass filtered data and the parameters estimated using frequency-dependent data weighting is very small, except for profiles that contain large data gaps due to the removal of data in segments with large turbulence. Again, this shows that the removal of data distorts the correlated data sequence, which may introduce errors. On the other hand, the error that is introduced is largely absorbed by the estimated bias parameters, and the results for the estimated gravity field solutions obtained with low-pass filtering and frequency-dependent data weighting are nearly the same. The RMS difference with upward continued surface gravity is 3.8 and 4.0 mGal for low-pass filtering and FDW, respectively. These differences are significantly larger than for the solutions obtained without bias estimation (see table 6.2). The reason is that the estimated bias parameter of a profile represents a mean value of the observations within that profile, which is not consistent with mean values of the other profiles. If a part of such a profile is affected by errors, for instance caused by turbulence, this can have a large effect on the mean value of the whole profile. In that case an estimated bias can degrade the accuracy of parts that are not affected by errors. Therefore, bias estimation
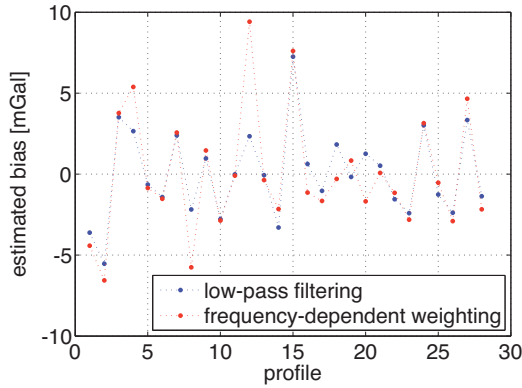
Figure 6.12: Bias parameters estimated from a) low-pass filtered data; b) unfiltered data using frequency-dependent data weighting

is not applied for computations with this data set in the following section.

6.1.5 Geoid determination

In geodesy, the main application of airborne gravimetry is the downward continuation of gravity to be combined with terrestrial data, and the determination of a local geoid. For the computation of the geoid the remove-restore technique is applied. The long-wavelength part of the gravity field is modeled by the EGM96 model (Lemoine et al., 1998) and removed from the observations. As discussed in section 3.2, a terrain correction is often applied in practice to make the signal at flight level more smooth. Here, this correction is not computed because the influence of the topography in the area is very small.

Gravity field solutions are computed on a grid for the area covered by the observations using two approaches. One solution is computed from the unfiltered airborne gravity measurements using frequency-dependent data weighting with the ARMA model estimated from residuals as described in the previous subsection. Coefficients are again estimated for $L = 14$, $M = 10$, which means that the disturbing potential is represented by 608 base functions. The coefficients are estimated in a LS adjustment with FOT regularization applied and the regularization parameter is estimated with VCE. The second solution is computed from the low-pass filtered airborne gravity data set using LSC. The resulting geoid solutions are compared to the NKG-2004 geoid model, which is the gravimetric quasi-geoid for the Nordic countries computed by Forsberg et al. (2004). The NKG-2004 geoid is computed for the area bounded by Northern latitudes of 53-73 degrees and Eastern longitudes of 1-33 degrees, using FFT techniques to evaluate the Stokes kernel function.

Before comparing the solutions, the long-wavelength part computed from EGM96 is

also subtracted from the NKG-2004 geoid. Because the mean value of the disturbing potential within the computation area cannot be determined from the airborne gravity measurements, this mean value of 0.83 meter is removed from the residual NKG-2004 geoid. The resulting residual NKG-2004 model is shown in figure 6.13a.

The residual geoid computed using frequency-dependent data weighting and FOT regularization yields a solution that is too smooth if VCE is used to estimate the regularization parameter. The regularization parameter is estimated as $\alpha_{VCE} = 0.6 \cdot 10^{10}$. A better fit is obtained with $\alpha = 0.7 \cdot 10^9$, for which the differences with the residual NKG-2004 geoid are shown in figure 6.13b. The RMS difference is 9.5 cm and the maximum difference is 36 cm (see also table 6.3). To justify the choice of the regularization matrix, the computation is repeated for ZOT regularization combined with VCE, but again the solution is too smooth. The RMS difference with the NKG geoid is 12 cm, and the maximum difference is 49 cm, which is significantly larger than for FOT regularization. If a solution is computed from low-pass filtered data with the same number of base functions and the regularization parameter of the FOT regularization matrix is determined empirically, the results are almost the same as for the solution computed with frequency-dependent data weighting. The statistics of the differences between the solutions and the residual NKG-2004 geoid are given in table 6.3.

A solution is also computed from the low-pass filtered observations at flight level using LSC. Not all observations have been used for the computation, because it would require the inversion of a 70000 by 70000 signal covariance matrix. Instead 3500 gravity disturbances were selected at a spacing of 2' in latitude direction and 1' in longitude direction. The empirical auto-covariance function is computed using all data and approximated by the Tscherning-Rapp degree-variance model, which is used in the software package GRAVSOFT to obtain a geoid solution. Before applying LSC, the mean value has been subtracted from the observations. The difference with the residual NKG-2004 geoid solution is shown in 6.13c and the statistics are given in table 6.3. For this solution the RMS difference is 8.4 cm, which is slightly better than the solution computed with frequency-dependent data weighting, and the maximum difference is 35 cm.

The solutions computed using fundamental solutions of Laplace's equation suffer more from edge effects than the LSC solution. As discussed in chapter 5, these edge effects are the result of periodicity of the base functions and of missing data outside of the survey area. The first type of edge effects is reduced by using controlled area extension. The second effect is common to all types of parameterizations and estimation techniques, but LSC may perform better than other methods under certain conditions. If the auto-covariance function is also representative for the area outside the survey area edge effects due to missing data will be relatively small. On the other hand, if the auto-covariance function is not representative for data outside the area, LSC will also suffer from significant edge effects.

To investigate how large the effect is of data outside the area covered by the airborne gravity data, two solutions were computed from the ground surface data. One solution is computed from all the available surface gravity data (shown in figure 6.2) and the other
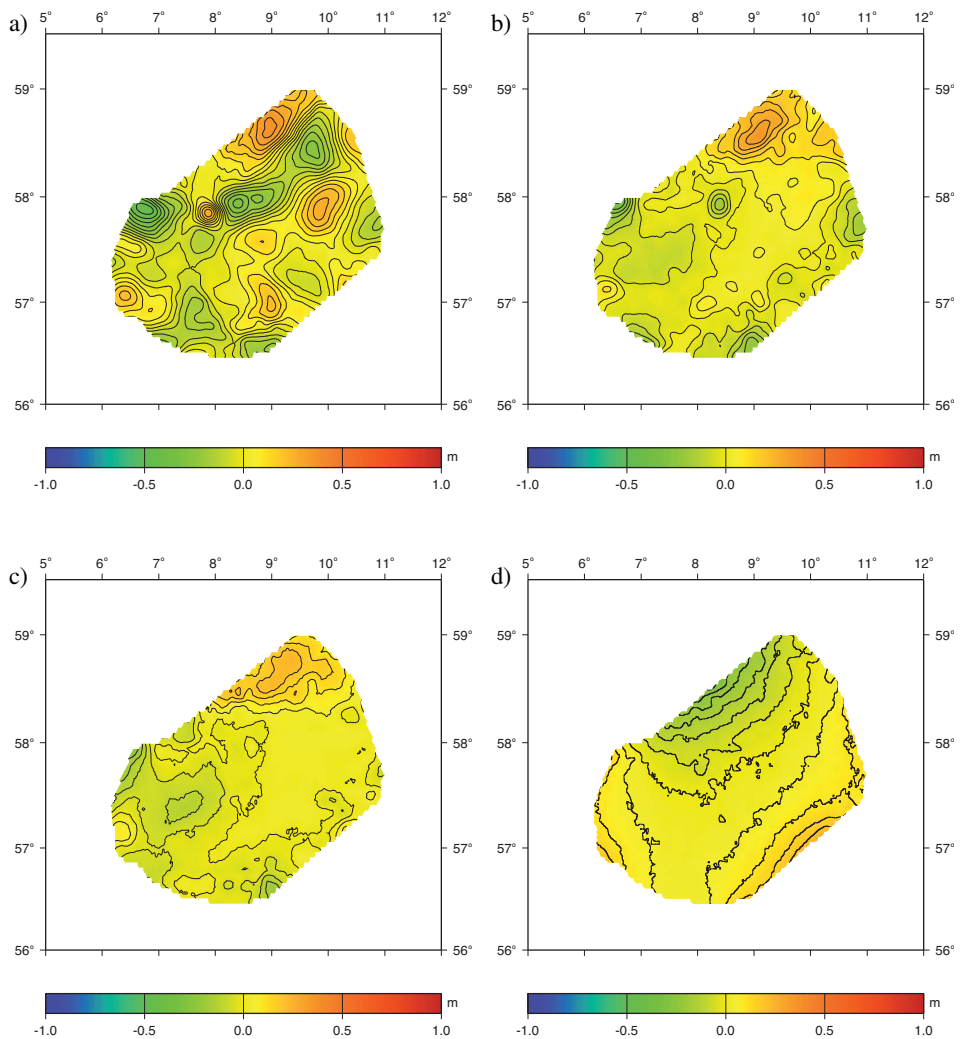
Figure 6.13: Geoid solutions for the Skagerrak area compared to the NKG-2004 geoid. a) The residual NKG-2004 geoid with respect to EGM96; b) differences with NKG-2004 for the solution obtained from unfiltered airborne gravity observations using FDW; c) differences with NKG-2004 for the solution computed from filtered airborne gravity observations using LSC; d) differences between the LSC solution computed from all available ground surface data and the LSC solution computed from data in the area covered by the airborne gravity survey, showing the effect from observations outside the survey area.

solution is computed from ground surface data within the area covered by the airborne survey. The difference between the two solutions is shown in figure 6.13d, from which it is clear that the errors can be very large. In the north-western part and in the south-eastern part the differences are as large as 50 cm, whereas in the middle of the area differences between the two solution are close to zero.

6.1.6 Conclusions

Frequency-dependent data weighting applied to the Skagerrak data set provides gravity field estimates that have the same accuracy as the results obtained with low-pass filtering. The solutions show a good agreement with upward continued surface data and the estimated accuracy is at the level of 3 mGal. A noise model estimated from residuals provides the same results as one derived using upward continued gravity, which shows that the developed methodology is suitable for practical applications and prior knowledge of the gravity field is not required.

As regularization matrix FOT regularization is preferred over ZOT regularization, even though the latter provided more accurate results for simulated data. Real airborne data contains more power in the high-frequency part of the spectrum, which means that the FOT regularization matrix gives a better description of the covariance matrix of the prior information. If FDW is used the regularization parameter can be accurately estimated with VCE, whereas for low-pass filtering convergence of the variance components could not be obtained. This indicates that correlations in the low-pass filtered signal are not correctly described by the scaled unity covariance matrix.

The performance of frequency-dependent data weighting gets worse if detected outliers are removed from the data due to interruption of the correlated data sequence. This can be a problem in practical applications since undetected outliers can have a large influence on the estimated gravity field. The negative effect of introducing data gaps due to the removal of outliers is however larger than the effect of remaining blunders in the data. Therefore, the removal of outliers from the observations is therefore not recommended within frequency-dependent data weighting scheme.

The estimation of bias parameters does not improve the results obtained with this data

Table 6.3: Statistics of differences [m] between the residual NKG-2004 geoid and the airborne gravimetry solutions computed with frequency-dependent data weighting (FDW) and low-pass filtering (LPF).

Method	Min	Max	Mean	STD	RMS
FDW: FOT (α_{VCE})	-0.387	0.347	0.006	0.102	0.102
FDW: FOT (α_{emp})	-0.362	0.349	0.010	0.094	0.095
LPF: FOT (α_{emp})	-0.332	0.344	0.001	0.094	0.094
LPF: LSC	-0.284	0.351	0.009	0.084	0.084

set. Because all observations are used in the estimation of bias parameters, a bias represents a mean error within a profile that is not consistent with other profiles. This means that if short-period errors affect this mean, these errors may leak into longer wavelengths. In this section it is therefore not applied for the computation of a local geoid from the airborne data. Nevertheless, bias estimation can provide valuable information on the instrument stability.

A local geoid is computed using frequency-dependent data weighting as well as using LSC, and compared to the geoid of the Nordic countries NKG-2004. The LSC solution is less affected by edge effects, which indicates that the auto-covariance function provides a good representation of data outside the survey area too. Furthermore, LSC is not affected by errors due to non-periodicity of the data. Local features, such as a buried volcano, are well recovered in both solutions, which shows that airborne gravimetry is a valuable technique for regional gravity field determination.

6.2 Chile data set

6.2.1 Description of the data

The data for which the performance of the developed methodology is tested in this section was acquired in 2002 by GeoForschungsZentrum Potsdam (GFZ) during the CHICAGO campaign in Chile (Meyer and Pflug, 2003). The area is of particular interest due to the presence of the Peru-Chile trench; a subduction zone west of the South American continent. As a result, strong gravity gradients are observed. The survey consisted of 13 off-shore flights near the coast of Chile and 4 flights above the Chilean mainland, resulting in 27 off-shore profiles and 12 on-shore profiles. All off-shore flights, except one because of an island, were performed at about 300 meters altitude, whereas the flights above the mainland were flown at an altitude of 2100 - 3000 meters. To minimize the effect of downward continuation, only data from the off-shore profiles are used for this study. The flight tracks and the main bathymetric features of the area are shown in figure 6.14, the low-pass filtered observations at flight level are shown in figure 6.15. From the 27 off-shore profiles, 24 are used in the computations. The total number of observations after pre-processing with the AGS software (see appendix A) is 85000. The results of the computations presented in this section are compared with gravity anomalies from the DNSC08 ocean-wide gravity model (Andersen et al., 2008), which was derived from satellite altimetry measurements. This model is shown for the Chile region in figure 6.16.

6.2.2 Gravity field determination

A gravity field solution is computed at ground level from low-pass filtered data and using frequency-dependent data weighting (FDW). Based on the spacing of the profiles, coefficients are estimated up to degree and order $L = M = 13$, which means that the disturbing potential is parameterized by 728 base functions. Gravity disturbances are
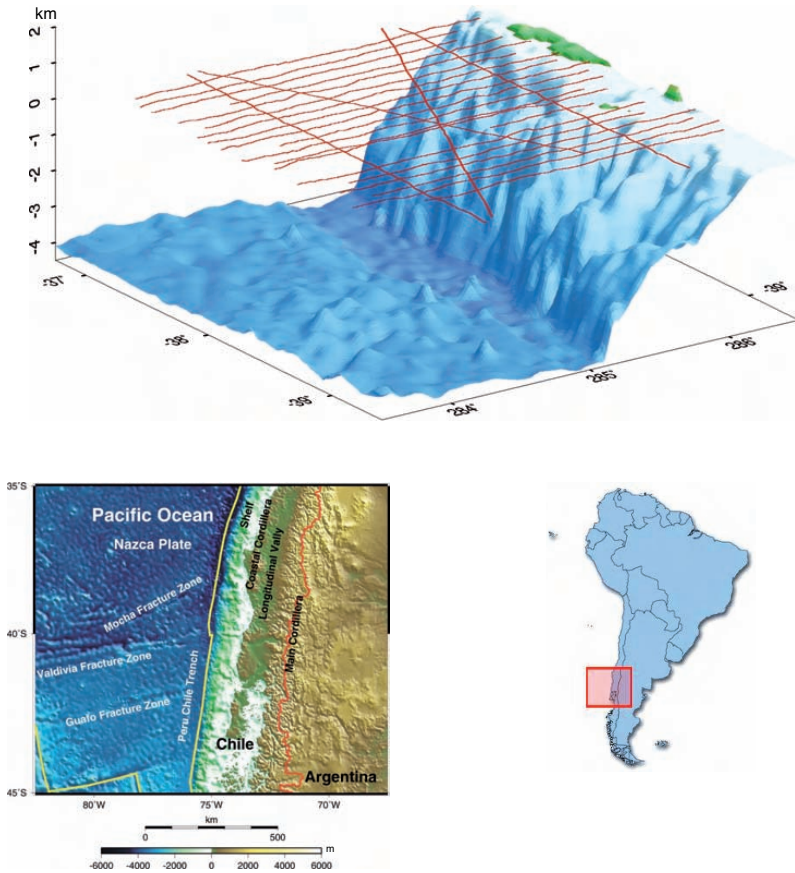
Figure 6.14: The off-shore flight tracks of the CHICAGO survey and the main bathymetric features in the area (top) and an overview of the region of interest (taken from (Meyer and Pflug, 2003)) showing the southern part of the Nazca plate and the Peru-Chile trench (bottom).

computed from the estimated coefficients on a grid defined by the DNSC08 model for a slightly smaller area than for which the airborne data is available.

To obtain a gravity field solution with frequency-dependent data weighting, a noise model must be computed. As shown for the Skagerrak data set it can be estimated from the residuals of a preliminary LS adjustment. To stabilize the normal equations, FOT regularization is applied. Because VCE fails to estimate the regularization parameter if the wrong noise model is used, the regularization parameter is set equal to the smallest value that allows for a stable inversion of the normal equations. As discussed in chapter 5 and in the previous section the initial choice of the regularization parameter does not have a significant influence on the estimation of the noise model. Indeed, convergence of
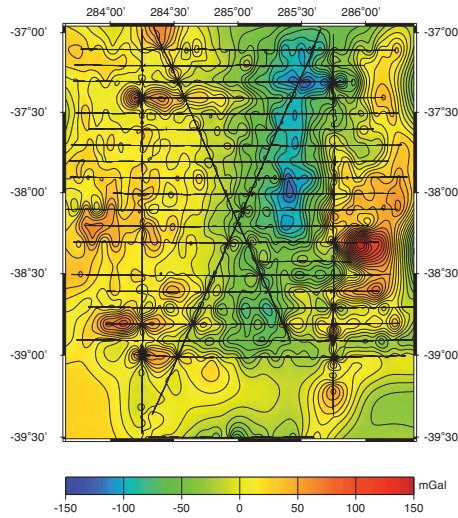
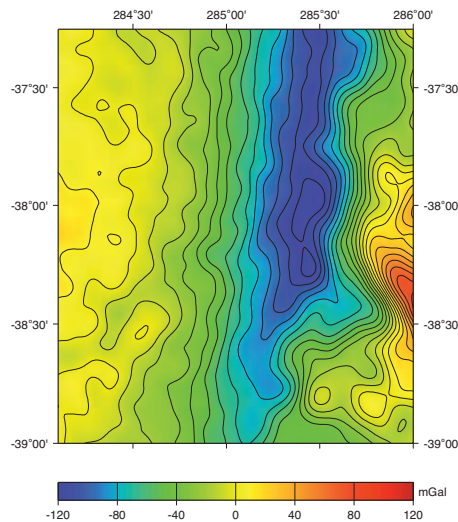Figure 6.15: Low-pass filtered observations at flight level.

Figure 6.16: Gravity anomalies from the DNSC08 satellite altimetry derived gravity model (Andersen et al., 2008) in the survey area.

the noise model is obtained within 3 iterations. The RMS difference between the first and second iterated solution is only 0.6 mGal and the RMS difference between the second and the third solution is 0.4 mGal. The noise PSDs estimated from the residuals for the preliminary LS adjustment and the first two iterated solutions are shown in figure 6.17a.
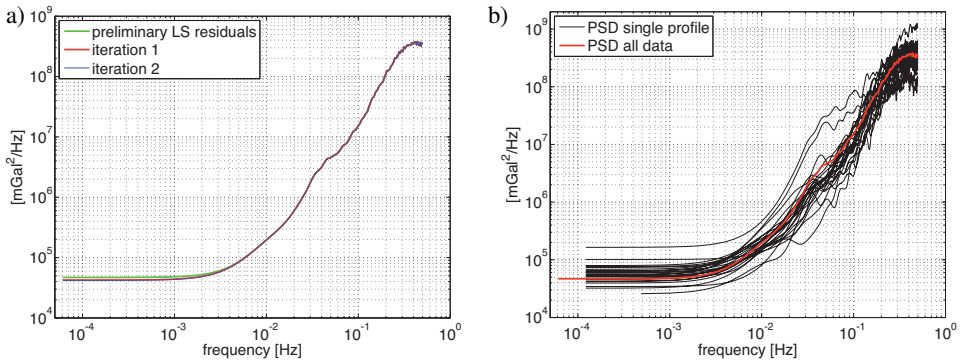
Figure 6.17: Noise PSDs estimated from residuals of the iterated LS adjustments. a) Using all data; b) using data of one profile (first iteration only).

If a proper noise model is applied in the frequency-dependent data weighting, the regularization parameter can be determined by VCE. The variance factor of the covariance matrix of the observations is equal to 0.98 for the first iterated solution and 0.99 for the second and the third. This indicates that the noise in the observations is correctly described by the ARMA model. The resulting gravity field solution computed with the final noise model is shown in figure 6.18a.

The noise model is estimated using the residuals of the whole data set, whereas for the Skagerrak area only one (long) profile was used because gaps and non-stationary noise led to a bias in the estimation of the low-frequency part of the spectrum (see section 6.1.2). Figure 6.17b shows the PSDs estimated from the preliminary a posteriori residuals for each profile separately. It is clear that the PSD estimated from all residuals represents the average noise characteristics of this data set very well.

The quality of the frequency-dependent data weighting solution is assessed using the DNSC08 model. Differences are computed at the locations where the gravity anomalies of DNSC08 are available, which yields a standard deviation of 12.8 mGal. Furthermore, a mean difference of 20 mGal is observed between the model and the FDW solution. The differences are shown in figure 6.18b, and their statistics are given in table 6.4. Figures 6.16 and 6.18 show that the main features, such as the large anomalies in the Eastern part and in the middle of the area at the location of the trench, are well recovered, but locally there are large differences. A solution is also computed using the low-pass filtered observations, but in that case the estimation of the regularization parameter with VCE does not converge. This indicates that the assumption that the noise in the low-pass filtered data is white is not correct. In the following subsection, solutions are computed using frequency-dependent data weighting.
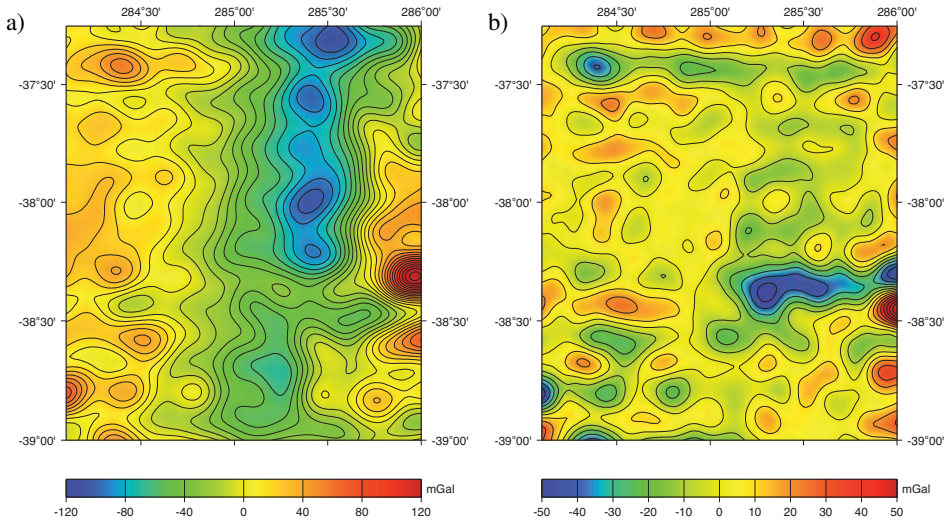
Figure 6.18: a) Gravity disturbances at ground level estimated using frequency-dependent data weighting; b) differences between the FDW solution and the DNSC08 model. For the computation of gravity field parameters the laboratory values of the k-factor and calibration factor have been used.

6.2.3 Estimation of non-gravitational parameters

The solution shown in figure 6.18a is obtained without estimating biases or other non-gravitational parameters, such as scaling factors. However, figure 6.15 shows that especially at intersections of the flight lines misfits can be identified. A cross-over analysis is performed to assess the internal consistency and estimate the accuracy of the data set. The total number of cross-overs is 76, and the standard deviation of the cross-over misfits is $\sigma_x = 18.3$ mGal, which indicates a noise level of the filtered observations of $\sigma_e = \sigma_x/sqrt2 = 12.9$ mGal. The misfits at cross-over points, which at some locations are as large as 40 mGal, can be the result of biases, which in turn may be caused by changing flight conditions that affect the performance of the instrument.

Instrument readings are related to gravity by applying several scaling factors such as the beam velocity scaling factor (called k-factor) and the spring tension calibration factor. These values may be determined by laboratory calibration, but conditions may differ for each flight. Therefore, they are estimated here simultaneously with the gravity field parameters and tested as described in section 4.5. In this section it will be investigated how accurate the scaling factors can be estimated and whether the parameters correlate. If the correlation is high they should not be estimated simultaneously, because in that case their effect on the gravity field parameters is the same. Furthermore, it will be shown what the effect is of the estimated non-gravitational parameters on the gravity field solution.

Table 6.4: Statistics of differences [mGal] between the DNSC08 model and the solutions for the joint estimation of non-gravitational and gravity field parameters.

Method	Min	Max	Mean	STD	RMS
laboratory values of k and c	-75.59	63.25	-20.69	12.79	24.32
estimated k and c	-80.13	54.10	-26.93	12.23	29.58
estimated k and c per profile	-65.21	50.87	-26.10	10.53	28.14
estimated k and bias per profile	-65.19	50.99	-26.13	10.54	28.17

In the pre-processing of the data the laboratory values of the k-factor ($k = 39.0$) and spring tension calibration factor ($c = 1.014$) were used. If they are determined together with the gravity field parameters, the k-factor is estimated as $\hat{k} = 38.909 \pm 1 \cdot 10^{-3}$ and for the calibration factor a value of $\hat{c} = 1.01460 \pm 1 \cdot 10^{-5}$ is obtained. Although the estimated k-factor differs only slightly from the laboratory value, the deviation is statistically significant. The effect of this difference is on the gravity solution is, however, small: the maximum effect is only 1.1 mGal. The difference in c is also small, but a mean value of 6 mGal is absorbed. The reason is that because spring tension values are always positive (values range from 9000 to 12000 cu), a change in c leads to a change of the mean value of the estimated gravity field. Compared to the DNSC08 model, the estimation of a k-factor and calibration factor leads to minor improvement. The standard deviation of the differences between the estimated gravity field at ground level and DNSC08 is 12.23 mGal (see table 6.4), but the mean difference with the model increases from 20.7 mGal to 26.9 mGal.

The joint estimation of one k-factor and one calibration factor per profile with the estimation of gravity field parameters, leads to an improvement of the solution when compared to the DNSC08 gravity anomalies at ground level. The gravity field solution and the differences with DNSC08 are shown in figure 6.20. The standard deviation of the differences of 10.5 mGal is significantly smaller than for the solution without estimating non-gravitational parameters. The estimated k-factors and calibration factors per profile deviate much more from the laboratory values of k and c, than when only one k-factor and calibration factor is estimated for the whole data set, which is demonstrated in figures 6.19a and 6.19b. For some profiles, the variation of the k-factors results in a change in gravity with respect to the original solution of about ± 15 mGal, which is shown in figure 6.21a, and the estimation of a calibration factor per profile has an effect on the solution of ± 30 mGal (see figure 6.21b).

When the estimation of calibration factors is combined with the estimation of bias parameters, it is found that these parameters are highly correlated (the correlation coefficient is almost equal to -1), which means that they have the same effect on the parameter estimation. Indeed, when bias parameters are estimated instead of spring tension calibration factors, nearly the same gravity field solution is obtained (see table 6.4). Differences between both solutions are smaller than 0.3 mGal for the whole area. The estimated bias parameters (cf. figure 6.19) show the same pattern as the calibration factors in fig-
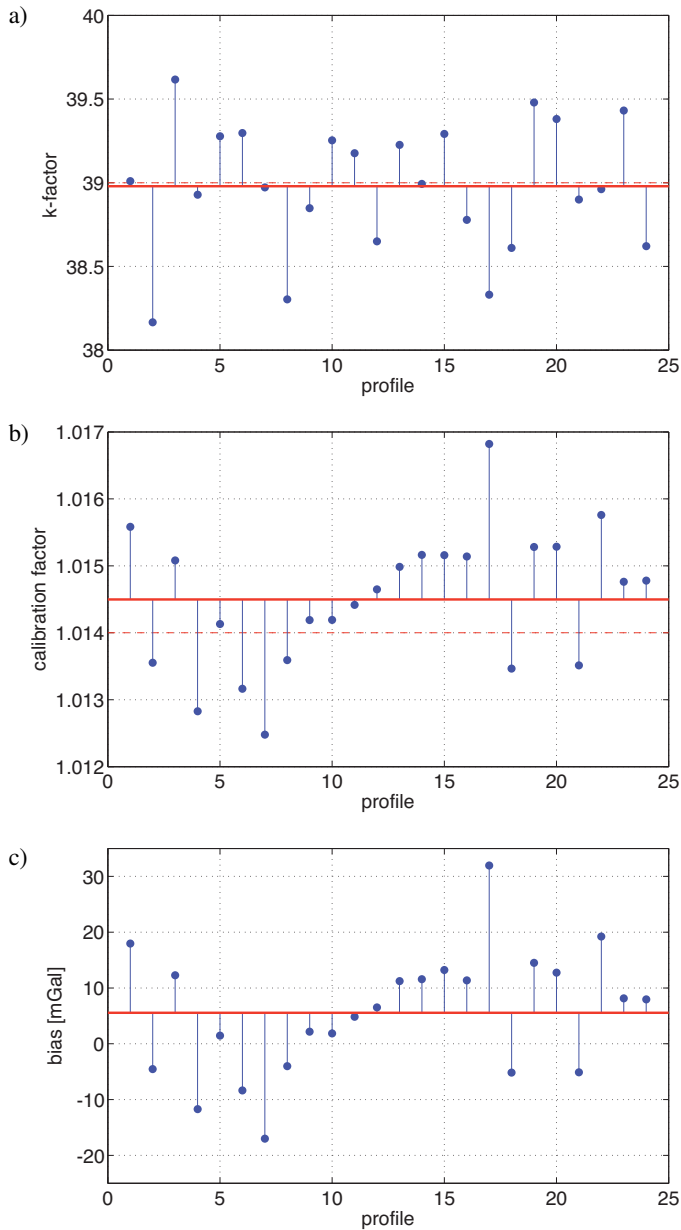
Figure 6.19: Results of the estimation of non-gravitational parameters. The dashed lines denote the laboratory values, the solid denote the mean value of the estimated parameters. a) Estimated k-factors per profile; b) estimated spring tension scaling factors per profile. c) estimated biases per profile, multiplied by -1 to show the similarity to the estimated spring tension scaling factors.
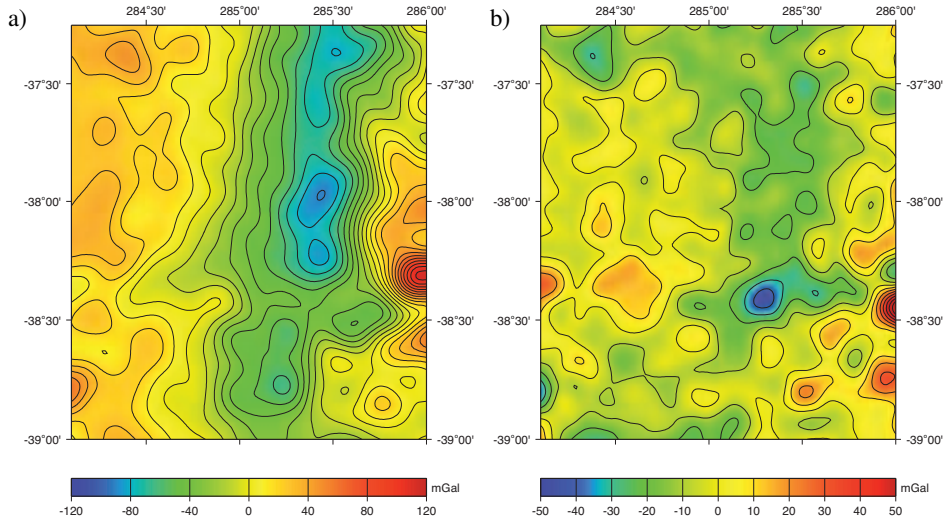
Figure 6.20: Gravity field solution at ground level corrected for a k-factor and a calibration factor estimated for each profile (a); b) differences with the DNSC08 model.
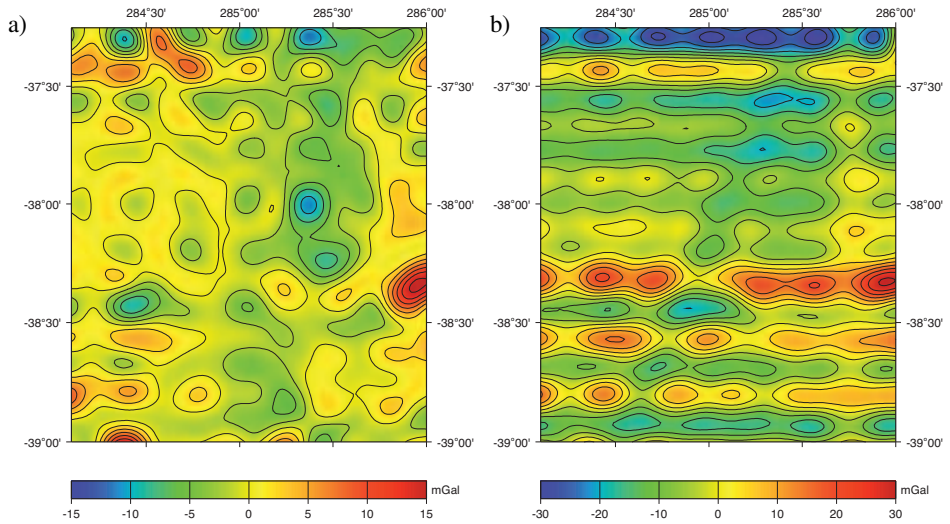

Figure 6.21: Effect of the estimation of non-gravitational parameters of the gravity field solution. a) Differences between the solution obtained without estimating scaling factors (cf. figure 6.18) and the solution where one k-factor is estimated per profile; b) same as for (a) but for the solution where one calibration factor is estimated per profile.

ure 6.19. Correlations computed between k-factors and bias parameters, and between k-factors and calibration factors are smaller then 0.5. From the results presented in figure 6.20 and table 6.4 it is clear that the final solution for which k-factors and calibration factors (or bias parameters) are estimated per profile gives the best results when compared to the DNSC08 model.

6.2.4 Conclusions

A gravity field solution computed using frequency-dependent data weighting to handle colored noise, without the estimation of non-gravitational parameters yields an RMS difference of 12.8 mGal with the satellite altimetry derived gravity model DNSC08. The proper noise model is estimated using the LS residuals of all observations, instead of a single long profile as was done in case of the Skagerrak data set. A noise PSD could be estimated from all data because the data contain no gaps and the profiles have the same length. In practice, the choice of which strategy should be used, can be made by computing noise PSDs for all profiles and compare their spectra with the one computed for the whole data set. If they match, the noise PSD of all data can be used as the input for ARMA model estimation. Otherwise, a long profile which is less affected by turbulence and has no data gaps could be used instead.

The gravity field solution is improved significantly if non-gravitational parameters are jointly estimated with the gravity field parameters. The RMS difference between the final gravity field model and DNSC08 is 10.5 mGal, which is significantly smaller than the RMS difference of 12.8 mGal, obtained if no additional parameters are estimated. Instrument scale factors, such as the k-factor and spring tension calibration factors, can be accurately estimated. For the Chile data set, they significantly deviate form the laboratory values, especially if they are estimated per profile. Estimated bias parameters and spring tension parameters are highly correlated, which means that biases in the data are predominantly caused by deviations in the spring tension data. In practice there is however no physical justification for the deviations of the spring tension calibration factor, due to the excellent drift stability of the LCR gravimeter. Therefore, it is recommend to apply bias estimation combined with the estimation of k-factors for each profile, to improve the gravity field solution.

6.3 Timmins, Ontario data set

6.3.1 Description of the data

In 2003 Sander Geophysics Limited (SGL) conducted a high-resolution gravimetric survey north of Timmins, Ontario, Canada. The survey was flown with the AIRGrav (Airborne Inertially Referenced Gravimeter) system (Sander et al., 2004), which uses a Schuler-tuned inertial platform supporting three orthogonal accelerometers. The survey flight lines were flown with a dense line spacing of 500 m at a constant GPS height of 458 m,
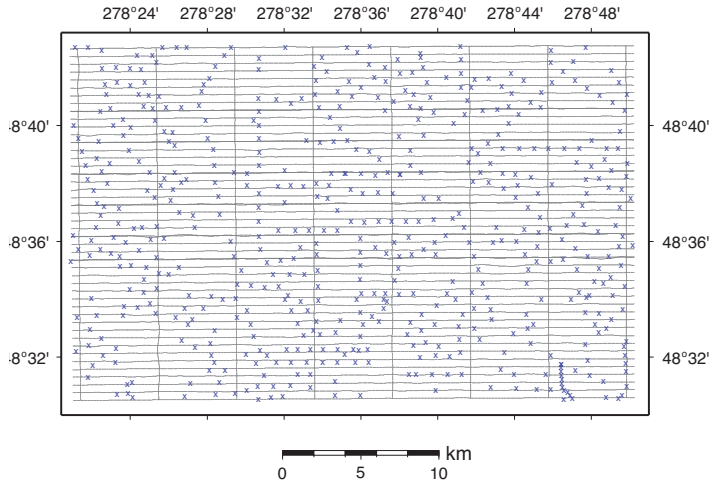
Figure 6.22: Gravity data coverage in the Timmins area. The blue crosses denote the locations of ground data points, the black lines denote the airborne gravity profiles.

chosen to safely clear the highest terrain in the area (terrain elevations vary between 250 m and 400 m). The total area size is 36 by 24 km. Several control lines were flown at a spacing of 5000 m. A detailed description of the survey is given in Elieff (2003); Elieff and Sander (2004). Within the survey area, 573 ground Bouguer gravity anomalies, acquired in a large ground survey performed in 2001, are available for evaluation of the AIRgrav data. A map showing the locations of the ground Bouguer gravity anomalies and the AIRGrav flight lines is shown in figure 6.22.

The pre-processing of this data set was performed by Elieff (2003), resulting in a set of filtered Bouguer gravity anomalies at flight level which are shown in figure 6.23. These values are computed by applying several corrections such as Eötvös effect, free-air and Bouguer corrections, and a correction for the Earth curvature. Furthermore, a static correction and a level correction are applied to account for instrument variations. The static connection is based on ground readings, i.e it is applied to tie the data to surface data, and the level correction is computed from control line intersection misfits to adjust individual lines with a constant shift. The latter is used in section 6.3.3 to compare the results of the estimation of bias parameters. Finally, the gravity anomalies are low-pass filtered to remove high-frequency noise and averaged using a spatial filter with a mid point of 2.85 km (for more details see Elieff, 2003).

6.3.2 Estimation of the noise model

To test how well the filtered AIRGrav data can be recovered from unfiltered observations using frequency-dependent data weighting, a noise model is first computed from the
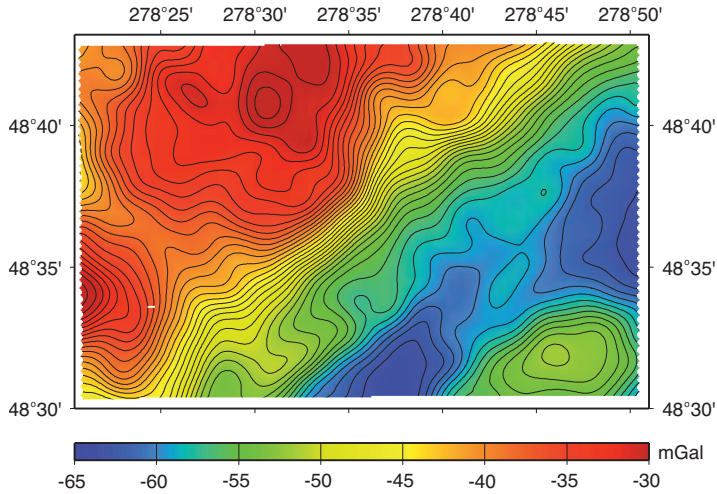
Figure 6.23: Filtered AIRgrav Bouguer gravity anomalies at flight level as computed by Elieff (2003) for the Timmins survey.

difference between the filtered data (cf. figure 6.23) and the unfiltered observations. A PSD of this difference, which is the part removed by the low-pass filter and considered as noise, is computed for the whole data set. The resulting PSD is shown in figure 6.24. The noise increases for higher frequencies, but rapidly decreases above 0.25 Hz. This indicates that some pre-filtering may have been applied to the data. Nevertheless, an ARMA model is estimated from the smooth noise PSD of figure 6.24a, which results in an ARMA(22,21) model. This ARMA model is used in the frequency-dependent data weighting to handle the strong colored noise.

In the LS estimation, coefficients C_{lm} are estimated from 77000 observations up to degree $L = 11$ and $M = 8$, which means that the disturbing potential is represented by 390 base functions. The area size is 36 by 24 km and the parameters D_x and D_y were set to 44 and 32 km, respectively, to reduce edge effects. That is, controlled area extension is applied with $\Delta_t = 8$ km. The resulting resolution of the estimated gravity field is 2 km. To obtain a stable solution, FOT regularization was applied with VCE as parameter choice rule. The resulting gravity anomalies at flight level are shown in figure 6.25. It can be seen that the solution is affected by edge effects, but at 1 km from the borders of the area the gravity signal is well recovered. The RMS difference with the low-pass filtered data is 1.08 mGal, with a maximum error of 16.5 mGal at the edge, but for the inner area (1 km from the edges) the RMS is only 0.65 mGal and the maximum difference is 3.5 mGal.

The edge effects are not the result of filtering, since the application of the (inverse) covariance matrix to a vector is not affected by data gaps, but due to the use of periodic base functions to represent the non-periodic gravity signal. The application of controlled
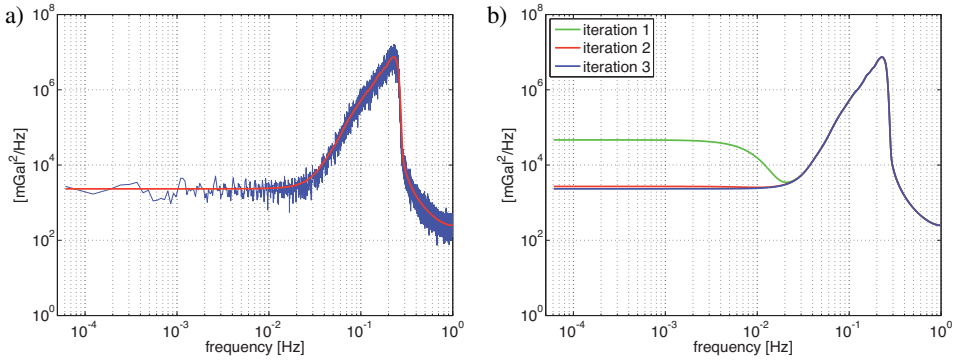
Figure 6.24: Estimated noise PSDs for the Timmins survey. a) PSD computed from the difference between unfiltered and filtered observations. To ensure positiveness of the PSD, the covariance function was smoothed with $Q = 5000$ seconds (blue) and $Q = 50$ seconds (red). b) Noise PSDs estimated from residuals for the three iterations.

area extension with $\Delta_t = 8$ km to reduce edge effects does not completely remove them, but does prevent propagation of the errors into the area. If larger values of D_x and D_y are used and more base functions are estimated to obtain the same resolution, the edge effects are smaller. For example, using $D_x = 88$, $D_y = 64$ km and increasing the degree and order to $L = 22$, $M = 16$ reduces the maximum error to 12.3 mGal and the RMS difference to 0.75 mGal for the whole area, and 2.9 mGal (max) and 0.57 mGal (RMS) for the inner area.

Next, a noise model is estimated from residuals of a preliminary LS adjustment without applying a model of the colored noise. For the initial solution, the regularization parameter was set to a small value ($\alpha = 1 \cdot 10^{-6}$) and the resulting LS residuals are used to estimate an ARMA model. This ARMA model is used in a following adjustment and the process of noise model estimation is repeated. Convergence was already obtained after 3 iterations, resulting in an ARMA(15,14) model. The PSD functions for each iteration are shown in figure 6.24b. When compared with the noise PSD in figure 6.24a it is clear that the final model is nearly the same as the one obtained from the difference between low-pass filtered and unfiltered observations. The resulting gravity field solution is therefore also the same; the RMS difference with solution computed with ARMA(22,21) (cf. figure 6.25) is only 0.07 mGal for the whole area and 0.03 mGal for the inner area.

6.3.3 Bias estimation

Elieff (2003) gives an detailed analysis on the system resolution and accuracy. The internal consistency was measured by a cross-over analysis, which yielded an estimated accuracy of 0.45 mGal (the RMS of the cross-over errors was 0.64 mGal). Based on the
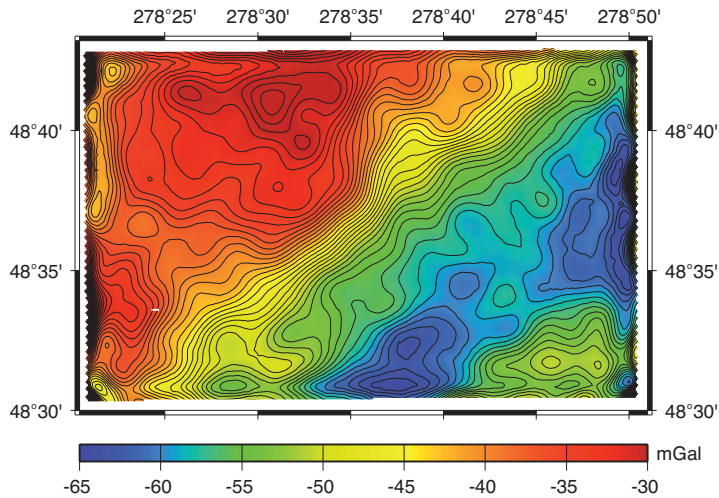
Figure 6.25: Bouguer gravity anomalies estimated from unfiltered observations using frequency-dependent data weighting.

misfits at the line intersections Elieff (2003) applied a cross-over adjustment to account for biases in the data. For the comparison of this adjustment with the results in this section, only the filtered values of this correction, called level correction by Elieff (2003), are available. These values are shown figure 6.26. Therefore, the mean value of this correction of each track is considered a bias that is removed from the data.

In the developed methodology these biases can be estimated as additional parameters in the functional model. This is tested here for frequency-dependent data weighting and for the low-pass filtered data (i.e without FDW). The estimated parameters are compared with the mean values of the level correction of each line, which is shown in figure 6.27a for the filtered observations. The RMS difference between the bias parameters and the level correction values is only 0.19 mGal. The difference between the adjusted gravity anomalies and the low-pass filtered data (cf. figure 6.23) yields an RMS of 0.26 mGal (min=-1.04; max=0.90 mGal), which shows that the anomalies are accurately represented by the base functions. The solution is not corrupted by edge effects, unlike the solution computed from the unfiltered observations in the previous subsection.

Note that when a low-pass filter is applied, the beginning and end of the profile are corrupted by filter artifacts and discarded. It means that the original data area is larger than the provided data set as it is used in this thesis. A more fair comparison between low-pass filtering and frequency-dependent data weighting, needs the data in the larger area.

When biases are estimated from the unfiltered observations, the edge effects corrupt the bias parameters. Figure 6.27b shows that especially the biases estimated for the profiles located near the edge of the area are very large. Furthermore, a clear trend can
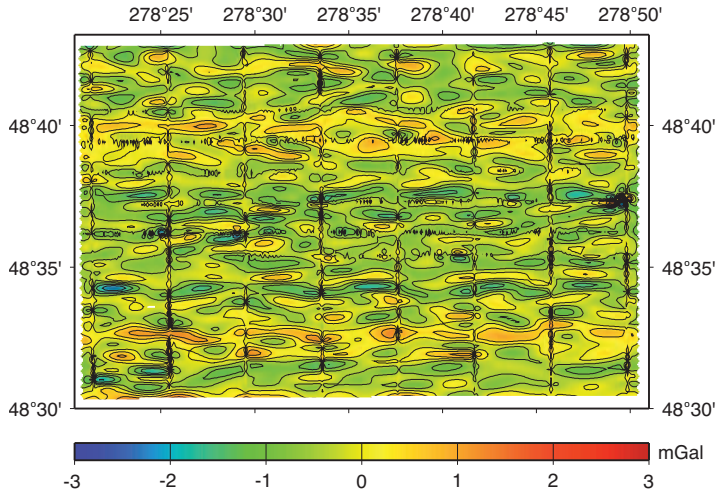
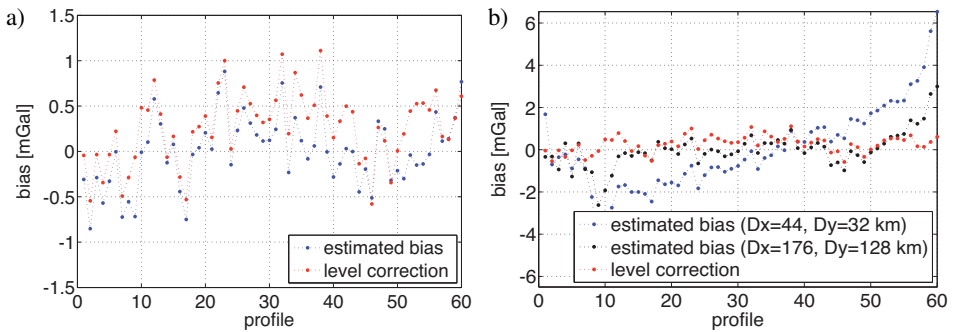Figure 6.26: Level correction computed by Elieff (2003).

Figure 6.27: Estimated bias parameters compared to the mean value of the level correction computed for each line. a) Estimated from low-pass filtered observations; b) estimated from unfiltered observations using frequency-dependent data weighting.

be seen in the estimated bias parameters of the East-West oriented tracks (lines 9–60). The consequence of the estimated trend absorbed by the bias parameters is that the RMS difference of the gravity solution with the low-pass filtered observations is much larger than without bias estimation: 1.76 mGal.

If a solution is computed with a much larger controlled area extension (D_x =176 km, D_y =128 km), the estimated bias parameters for the profiles near the edges are still large, but there is no trend in the estimated parameters. The resulting gravity field solution corrected for these biases is shown in figure 6.28. The RMS difference between

the solution and the low-pass filtered data is 1.03 mGal for the whole area and 0.62 mGal for the inner area.

For the estimation of the bias parameters no constraint was added to the functional model, which means that the mean value of the data had to be added back to the solution. If the constraint that the sum of the estimated biases must be equal to zero is added, the edge effects corrupt all estimated bias parameters in order to fulfill the constraint. This results in a less accurate gravity field solution than for the unconstrained solution.

6.3.4 Downward continuation

Within the Timmins area good surface is data is available to assess the quality of the solutions. Elieff (2003) made a comparison with upward continued ground data, using the 573 measurements within the area and an additional 213 ground readings, which gave a standard deviation of 0.62 mGal at flight level between air gravity and the ground readings. Furthermore, a constant off-set of 1.4 mGal was found between the air and ground data.

An advantage of the developed approach is that when a solution is obtained, gravity field functionals can be computed at any point within the computation area. This means that a comparison with ground truth values can be done at the locations of the available surface data. Gridding and upward continuation to average flight level of these observations is thus not required. For the Timmins area, 564 of the ground Bouguer gravity anomalies, shown in figure 6.29, are located within the area covered by the flight tracks.

If the low-pass filtered gravity anomalies are downward continued to the locations of the surface measurements, a mean difference of 2.4 mGal is observed. The standard deviation of the difference between the computed gravity anomalies and the surface data is 1.25 mGal. Edge effects up to 11.6 mGal occur, even though controlled area extension with $\Delta_t = 8$ km is applied. However, edge effects may still be expected due to lack of data outside the area. For 409 values that are located 2 km away from the edges the results are much better: the standard deviation of the differences is 0.81 mGal and the mean value is 2.0 mGal. The mean value for the inner area is larger than the off-set of 1.4 mGal found by Elieff (2003) between the grids of airborne gravity and upward continued ground data at flight level. The differences corrected for the mean value are shown in figure 6.30 and the statistics are given in table 6.5.

A solution at the ground data locations is also obtained from the unfiltered observations using frequency-dependent data weighting with the noise model estimated from the residuals. The differences computed at these locations (again corrected for the mean difference) are shown in figure 6.31 and their statistics are given in table 6.5. For this solution the edge effects are larger (max=17.3 mGal), but for the inner area (2 km from the edges) the results are almost the same as for the low-pass filtered data. The standard deviation of the difference between the two data sets in the inner area is 0.86 mGal.
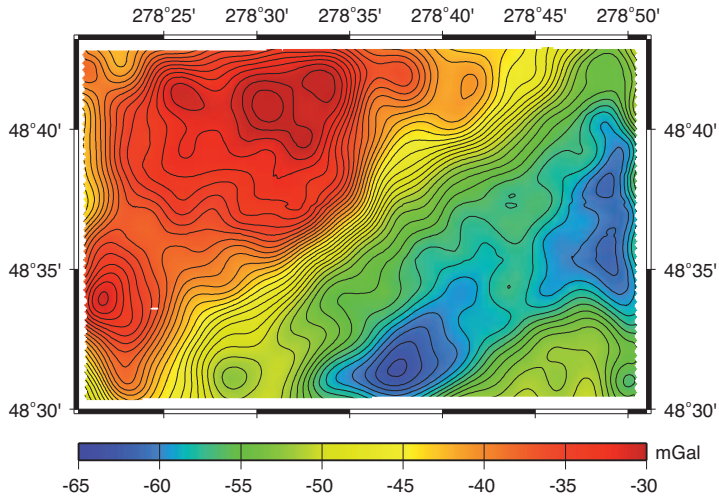
Figure 6.28: Bouguer gravity anomalies estimated from unfiltered observations using frequency-dependent data weighting and bias estimation.

Figure 6.29: Ground Bouguer gravity anomalies within the area covered by the airborne gravimetry survey.

Figure 6.30: Difference between ground Bouguer gravity anomalies and downward continued AIRGrav Bouguer gravity using low-pass filtering.

Figure 6.31: Difference between ground Bouguer gravity anomalies and downward continued AIRGrav Bouguer gravity using frequency-dependent data weighting.

Table 6.5: Statistics for the difference between ground Bouguer gravity anomalies and downward continued AIRGrav Bouguer gravity computed [mGal] using low-pass filtering (LPF) and f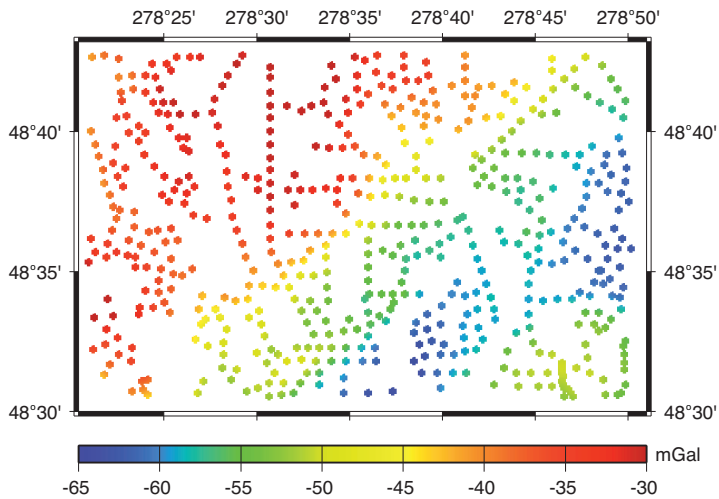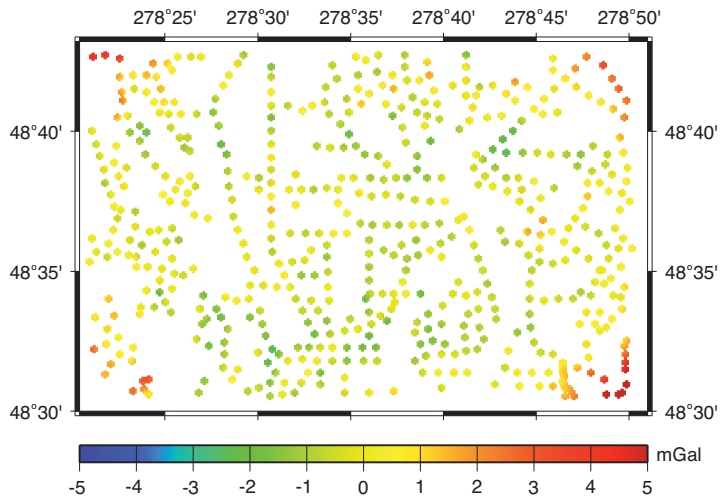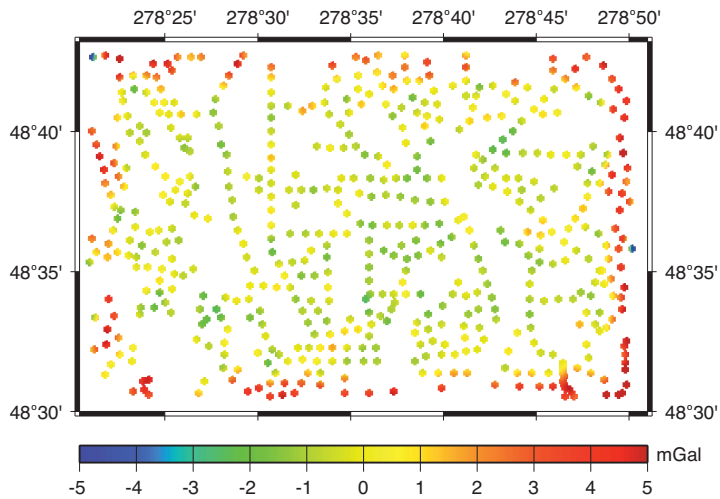requency-dependent data weighting (FDW). Bias estimation is not applied. The results in brackets denote the statistics for the inner area.

	LPF		FDW	
Min	0.06	(0.06)	-3.108	(-0.25)
Max	11.63	(4.57)	17.391	(4.93)
Mean	2.37	(2.04)	2.850	(1.97)
STD	1.25	(0.81)	2.016	(0.87)
RMS	2.68	(2.20)	3.491	(2.15)

6.3.5 Conclusions

The area used in this section is considerably smaller than the Skagerrak and Chile regions. Furthermore, the gravity field is determined with a much higher resolution, which is possible due to line spacing of 500 m. Similar to the Chile data set, a noise model could be estimated using the whole data set. The approach of noise model estimation from a posteriori LS residuals is validated by comparing the obtained model to a model estimated from signal removed by the low-pass filter. Differences between the solutions obtained with both noise models are smaller than 0.1 mGal.

Contrary to the computations for the Skagerrak and Chile data sets, the small size of the area shows some limitations of the developed methodology. The periodicity of the base functions causes edge effects when frequency-dependent data weighting is applied instead of low-pass filtering, even when controlled area extension is applied. The latter does prevent the propagation of these effects into the area, but extremely large extensions are needed which increases the ill-conditioning of the normal equations. Furthermore, edge effects corrupt the estimated bias parameters, especially for profiles near the edges of the area. Nevertheless, the estimated accuracy of the gravity field solution after downward continuation is at the level of 1 mGal, when compared to ground truth data.

6.4 Summary and discussion

The developed methodology is successfully applied to real airborne gravimetric survey data. The gravity field solutions obtained with frequency-dependent data weighting are comparable to those obtained with low-pass filtering. The resolution of the estimated gravity field solutions, defined by L and M, was based on the track spacing of the airborne data and at these frequencies the noise is well below the frequency where the noise dominates the signal. As such, a low-pass filter does not attenuate much of the signal in the frequency band of interest. However, the advantage of the frequency-dependent data weighting scheme is that it is completely data-driven and as such does not depend on pre-defined parameters such as the filter length in case of low-pass filtering.

For each data set an accurate noise model could be estimated from a posteriori residuals of a preliminary LS adjustment. No more than three iterations were required for the Skagerrak and Timmins data set and only two for the Chile data set. The results obtained with the estimated noise models were at the same accuracy level as those obtained with a noise model from ground truth data or using low-pass filtered data.

To stabilize the computation and reduce the influence of remaining noise in the data, regularization is applied. Based on a comparison with available ground truth data, FOT regularization provided more accurate results than ZOT regularization. In case of the application of frequency-dependent data weighting, the regularization parameter could be estimated using VCE, but for the computations with low-pass filtered data this was not the case. The assumption that noise is white in the filtered data is not correct, since correlations in the remaining noise result in divergence of the estimated variance components. For the computations, described within this chapter, using low-pass filtered data the regularization parameter was chosen as the one that provides the best RMS fit with ground truth data. However, this gives a very optimistic choice, which makes the comparison with FDW less fair.

For the Skagerrak region the computed gravity anomaly solution using FDW shows a good agreement with the surface gravity anomalies. The estimated accuracy is at the level of 3 mGal. From the airborne gravity data a local geoid solution has been computed for both FDW and LSC. Although the most important features of the gravity field are well recovered, the result shows that the accuracy of a geoid obtained from airborne gravity data is limited due to lack of data outside the computation area. Nevertheless, the geoid can be determined at decimeter level for a small area such as the Skagerrak. A comparison between the approaches shows that LSC seems less affected by edge effects resulting from missing data outside the area, and the results were slightly better than the ones obtained with FDW. However, for the computation of the LSC solution much more base functions were used to represent the gravity field.

For the Chile data set, the internal consistency of the data was lower than for the other data sets. To improve the gravity solution, scale factors and bias parameters were estimated simultaneously with the gravity field parameters. It was found that the correlation between bias parameters and the spring tension scale factors was very high, which implies that the biases in the data are purely driven by variations in the spring tension observations. A comparison with satellite altimetry derived gravity anomalies yields an estimated accuracy of 10 mGal for this data set.

The results obtained from the Timmins data set in the last section confirm the excellent quality of the gravity data and the AIRGrav system. Furthermore, the results demonstrate the feasibility of applying the developed methodology to a small geophysical airborne gravity survey. An accurate noise model can be obtained and, although the area is small, the fundamental solutions of Laplace's equation form a suitable representation of the gravity field. The errors after downward continuation of the observations are below 1 mGal.

Conclusions and recommendations 7

7.1 Conclusions

A new strategy for the processing airborne gravity data has been developed. The approach combines several independent steps, such as low-pass filtering and cross-over adjustment, with the estimation of gravity field parameters. The concept of low-pass filtering is replaced by a frequency-dependent data weighting and non-gravitational parameters are estimated by adding them to the functional model. The performance of the developed methodology is at the same level as traditional methods in terms of gravity field errors, but provides a more flexible and powerful approach to airborne gravity data processing. It requires a minimum of pre-processing and all observations are used for the determination of the gravity field.

The conclusions are presented below by addressing the items listed in section 1.2:

Representation of the gravity field
The fundamental solutions of Laplace's equation form a valid and suitable set of base functions to represent the disturbing potential. Coefficients of the representation can be estimated with LS techniques and be used to compute gravity functionals on or near the Earth's surface at any location in the computation area. Edge effects related to the periodicity of the base functions can effectively be reduced by applying controlled area extension, which is a simple modification to the base functions. In practical applications only few base functions are required to obtain an accurate gravity field solution from airborne gravity measurements.

The drawback of this representation is that edge effects due to periodicity of the base functions can still be significantly large, even when controlled are extension is applied. Especially if the area is small (e.g. less than 50 km wide) the processing of data contaminated with colored noise can lead to less accurate results than when low-pass filtering is applied. Furthermore, the representation is not very suitable if the measurements are

irregularly distributed, because the resolution of the estimated gravity field depends on the average spacing of the observations in the x and y directions.

Regularization

Among the investigated regularization methods, first-order Tikhonov regularization generally provides the best results to obtain a stable solution. Especially for the downward continuation of gravity disturbances the method performs better than zero-order Tikhonov regularization. Nevertheless, the choice of the regularization matrix depends on the signal spectrum. For a narrow spectrum ZOT regularization can provide more accurate results as was shown for the simulated data.

An advantage of using frequency-dependent data weighting over low-pass filtering is that the use of proper covariance matrix in the LS adjustment allows an optimal estimation of the regularization parameter with VCE. The estimated regularization parameters are close to the empirically derived ones. For low-pass filtering the variance components do not converge because correlations in the low-pass filtered signal are not correctly described by the scaled unity covariance matrix. VCE does not provide an estimate of the regularization parameter in case of low-pass filtering instead of frequency-dependent data weighting. Since the noise covariance matrix in that case is a scaled unity matrix, remaining correlated noise in the signal is not correctly described which leads to divergence of the variance components.

Frequency-dependent data weighting

Frequency-dependent data weighting provides a good alternative to low-pass filtering. A statistically optimal solution is obtained and it provides a formalized approach for the handling of colored noise. The procedure depends, unlike low-pass filtering, purely on the input data and not on previous experience of the user. A posteriori residuals, obtained from a preliminary LS estimation, can be used to derive the noise model, for which only few iterations are required. The procedure of noise model estimation is robust against the initial choice of the regularization parameter used for computing the preliminary LS solution. Furthermore, the use of a proper noise model allows the estimation of the regularization parameter with VCE.

The limitation of frequency-dependent data weighting is the lower performance in case of data gaps introduced by outlier detection. The removal of a single outlier affects a number of observations before and after the detected outlier, which has a negative effect on the accuracy of the gravity field solution. This effect is larger than the accuracy gained from removing a large error from the data. Therefore, other techniques for the treatment of outliers should be used.

Bias and drift handling

Non-gravitational parameters, such as biases, drifts and scale factors, can be estimated simultaneously with gravity field parameters. Because the estimated bias parameters absorb the mean value of the local gravity field, a constraint that the sum of the biases is

zero should be added to the functional model. In that case bias parameters can be determined accurately, since all measurements are used for the estimations. The developed methodology outperforms the method of cross-over adjustment for the estimation of bias parameters, but short-period errors such as edge effects or errors due to turbulence, may still be distributed into along-track corrections. The estimation of instrument related scaling factors can significantly improve the gravity field solution and provide information on the performance of the gravimeter system. However, a testing procedure should be applied to avoid statistically insignificant estimations as the estimated parameters can be highly correlated with each other.

Comparison and validation
Tests with simulated gravity data showed that the developed methodology performs better than traditional methods in terms of RMS gravity disturbance and disturbing potential errors. Furthermore, the simulation study led to an optimized strategy for the application of the developed approach to real airborne gravimetric survey data. From the real data sets accurate gravity field solutions were computed, which were validated using available surface gravity data. The downward continuation error was small for all data sets, partially due to the low flight altitudes. Furthermore, the tests described in chapter 6 demonstrate the potential of employing airborne gravimetry data to obtain accurate gravity data which can be used in geodetic and geophysical applications.

7.2   Recommendations

To improve upon the developed methodology a number of recommendations are given for further research.

- In this thesis the disturbing potential is represented using fundamental solutions of Laplace's equation in Cartesian coordinates. This method is especially suitable for areas of rectangular shape and evenly distributed observations. For areas which contain irregularly distributed observations or large areas, other representations should be considered. A good alternative is to make use of spherical radial base functions to represent of the disturbing potential, especially if use is made of data-adaptive algorithms as described by Klees and Wittwer (2007). In that case the locations of the base functions are derived from the data, which leads to a smaller number of functions needed to determine the gravity field. Besides, these functions do not suffer from the Gibbs effect at the edges as the Laplace's solutions due to periodicity of the base functions. Furthermore, spherical radial base functions are suited for global and local gravity field modeling and they allow for local refinements of spherical harmonic representation of the gravity field. As such, it is recommended to apply these functions as part of the developed methodology for airborne gravity data processing.

- The developed approach provides opportunities for the joint processing of airborne gravity data with other data types, such as terrestrial, marine or satellite gravity data.

Because the quality and the spectral content of the various data types can be very different, the development of such an approach is a challenging task that deserves further investigation. The goal of the joint processing could be to obtain a united high-resolution representation of the regional gravity field, for instance using spherical radial base functions, or in case of global gravity field modeling, in terms of spherical harmonics. Alternatively, the airborne gravity data can be processed separately into a gridded set of gravity anomalies at ground level and then combined with other data types. In that case the optimal combination of the airborne gravity solution with other solutions should be derived, especially for the combination with long wavelength satellite models.

- To improve upon the application of the noise model in the frequency-dependent data weighting, several strategies have been explored. One method uses VCE for the weighting of the profiles as different data groups using one ARMA model to describe the covariance matrix, but convergence of the variance components could not be obtained. In principle, if the structure of the covariance matrix can be determined more accurately, its weight in the adjustment can be determined by VCE. ARMA models, for instance derived from estimated noise PSDs for each profile separately, can provide such a description of the noise covariance matrix. However, for some profiles it may not be possible to obtain an accurate noise PSD due to the presence of gaps, non-stationary noise or the relatively short length of some profiles. In that case other strategies should be explored to improve the estimation of the noise model.

- The developed approach for frequency-dependent data weighting should be tested for strapdown INS data processing. The data sets used in this thesis were all acquired using a stabilized platform and are less affected by low-frequency noise. The noise characteristics of SINS data may be the same in the high-frequency part of the spectrum but drifts in the accelerometers and gyroscopes can result in large low-frequency errors. It should be tested whether the procedure of noise model estimation based on residuals also works for such a noise spectrum. More information on the spectrum of SINS observations is found in Bruton (2000). The derived spectra therein may be useful for the determination of ARMA models to be used for the processing of SINS airborne gravity data processing.

- In this thesis gravitational effects of the topography and bathymetry, that are the main source for local gravity variations have not been considered. The application of terrain corrections to the airborne gravity data can result in a smoother residual signal at flight level. Generally, a smoother signal can be represented more accurately by a small number of base functions, which can improve the result of the inversion into gravity functionals on or near the Earth's surface. Not only for mountainous areas, but also for areas with large bathymetric features, such as the Chile data set described in chapter 6, such a correction should be considered.

- Finally a general recommendation on airborne gravimetry research is made. First of all, the use of SINS/GPS gravimeter systems should be further explored, since these systems have several advantages when compared to stable platform gravimeters such as power consumption and costs. Improvement in accuracy can be made by optimizing the design of SINS/GPS systems and by developing new processing strategies. Furthermore, with the development of improved gravimeter systems for airborne gravimetry, the main limitation to the accuracy of airborne gravity measurements is the determination of accelerations from GPS positions. Optimization of the derivation of accelerations from GPS positions or Doppler-derived velocities is therefore recommended.

A

A.1   GPS processing

For the surveys described in chapter 6, the processing of the GPS data was performed with KSGSoft (Kinematic/Static GPS Software) (Xu et al., 1998). This software was developed in 1994 to fulfill the needs of precise GPS navigation for airborne gravimetry. Some results of GPS kinematic processing with KSGSoft are described in Xu et al. (1994) and Xu et al. (1997). The main characteristics of the software are that KSGSoft can perform a combined adjustment of data of multiple kinematic/static stations. Furthermore, the software can provide carrier phase independent velocity solutions from instantaneous Doppler shift observations, provided the latter are available.

A.2   Gravity processing

The gravity processing has been performed with AGS (Airborne Gravity Software) version 4.5 (Meyer, 2004). The software is based on the initial software written for the AGMASCO project (Olesen et al., 1997), which was modified to fit the requirements of the ANGEL (Airborne Navigation and Gravimetry Ensemble & Laboratory) equipment of GFZ Potsdam (Meyer et al., 2003). The main steps applied with this software to process raw in-flight gravity sensor measurements to gravity disturbances of gravity anomalies, are described below.

Stable platform airborne gravimetry

The expression for the determination of gravity disturbances at flight level using a stabilized platform system is given in chapter 2 as

$$\delta g = g_m - \ddot{z} + \epsilon_{Eot} + \epsilon_{tilt} - g_{m_0} + g_a - \gamma_h, \tag{A.1}$$

where g_m is the vertical acceleration of the gravimeter, which is also called the specific force, $\ddot{z}$ is the vertical aircraft acceleration, ϵ^{Eot} is th Eötvös correction, ϵ^{tilt} is the tilt correction, g_{m_0} is the gravimeter still reading, g_a is the absolute gravity value, and γ_h is the normal gravity.
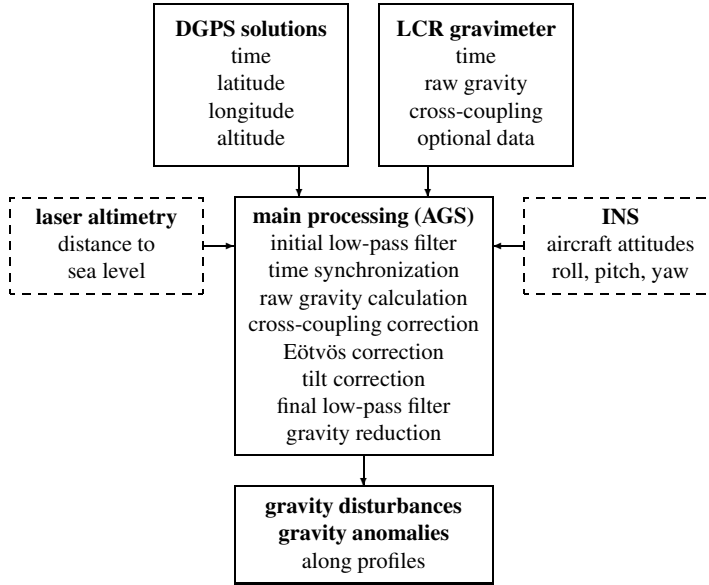
147

Figure A.1: Overview of input data, processing steps and output data of the AGS software, modified from Meyer (2004). Input from laser altimetry and INS is optional.

Vertical acceleration of the gravity sensor

The gravimeter acceleration g_m is modeled as

$$g_m = s(S + k\dot{B} + \epsilon_{cc}), \tag{A.2}$$

where s is a scale factor to convert counter units of the gravimeter to units of mGal, S is the spring tension, k is the beam scale factor (often referred to as k-factor), $\dot{B}$ is the beam velocity, obtained by numerical differentiation of the beam positions, and ϵ_{cc} is the cross-coupling correction. The latter is defined as

$$\epsilon_{cc} = a_1\ddot{x}^2 + a_2\ddot{y}^2 + a_3\ddot{z}^2 + a_8\ddot{y}\dot{z} + a_9\ddot{x}\dot{z} + a_{10}\ddot{y}\dot{z} + \ldots + a_n\ddot{x}^2\ddot{z} + \ldots \tag{A.3}$$

The first two terms are platform leveling errors and are not included in the cross-coupling correction.

In Valliant (1992) the following expression is given for the cross-coupling correction

$$\epsilon_{cc} = c_1\dot{B}^2 + c_2(f_y B) + c_3(f_x\dot{B}) + c_4(f_y\dot{B}) + c_5(f_x^2\dot{B}), \tag{A.4}$$

where $c1, c2, \ldots, c5$ are the cross-coupling coefficients, $\dot{B}$ is the beam velocity, B is the beam position, and f_x and f_y are the horizontal accelerometer measurements.

Time synchronization

The time synchronization between GPS and gravimeter data (or data from additional sensors) is established by computing the correlation coefficient between the two data series. The correlation coefficient for two series x and y is defined as

$$r_{xy} = \frac{\sum_{i=1}^{n}(x_i - \bar{x})(y_i - \bar{y})}{\sqrt{\sum_{i=1}^{n}(x_i - \bar{x})^2}\sqrt{\sum_{i=1}^{n}(y_i - \bar{y})^2}}. \tag{A.5}$$

The time series are synchronized when the correlation coefficient is maximum.

Eötvös correction

The Eötvös effect is caused by the motion of a moving platform over a curved rotating Earth, which results in a centripetal acceleration. A correction for this motion, simply called Eötvös correction, was derived by Harlan (1968) and is given as

$$E = \frac{v^2}{a}\left(1 - \frac{h}{a} - \varepsilon\left(1 - \cos^2\varphi\left(3 - 2\sin^2\alpha\right)\right)\right) + 2v\omega_e\cos\varphi\sin\alpha, \tag{A.6}$$

with

$$\varepsilon = \frac{v^2}{a}\sin^2\varphi + 4v\omega_e$$

and $v = v_E + v_N$, where v_E and v_N are the easterly and northerly components of the speed of the aircraft. In Eq. (A.6) the parameter a is the semi-major axis of the Earth, h is the altitude of the aircraft, ω_e is the angular velocity, and φ and α are the latitude and azimuth of the aircraft. From Eq. (A.6) it can be seen that navigation errors have a large impact on the computation of the Eötvös correction.

Tilt correction

Exact correction
A misalignment of the platform results in errors due to horizontal accelerations. To account for this effect a tilt correction is applied. It is computed as

$$\epsilon_g^{tilt} = \sqrt{g_m^2 + A^2 - a^2} - g_m, \tag{A.7}$$

with $A^2 = (A_X^2 + A_L^2)$, where A_X and A_L are the accelerometer outputs along the cross and long axis and with $a^2 = (a_E^2 + a_N^2)$, where a_E and a_N are horizontal kinematic accelerations in the east and north directions derived from navigational data, and g_m is the gravity meter reading as defined in Eq. (A.2).

Approximate correction

In Valliant (1992) an approximation to Eq. (A.7) is given. Observing that A^2 and a^2 are small compared to g_m^2. The tilt correction is then:

$$\epsilon_g^{tilt} = \frac{A^2 - a^2}{2g_m} \approx \epsilon_g^{tilt} = \frac{A^2 - a^2}{2g}. \tag{A.8}$$

Tilt angle modeling

The tilt correction as derived above is computed by squaring of two noisy signals, which means that zero-mean noise in A or a may introduces a bias in the gravity estimates. Olesen (2003) derived an alternative expression for the tilt correction which is free of such a bias. For small tilt angles the following approximations hold for one axis

$$f_x = q_x \sin \phi_x f_z \approx q_x + \phi_x f_z \approx q_x + \phi_x g, \tag{A.9}$$

which can be rewritten with respect to the angle ϕ_x as

$$\phi_x \approx \frac{f_x - q_x}{g} \tag{A.10}$$

In that case the tilt correction is computed as a linear combination of three acceleration components:

$$\epsilon_g^{tilt} = \sin \phi_x f_x + \cos \phi_x \sin \phi_y f_y + (1 - \cos \phi_x \cos \phi_y) f_z. \tag{A.11}$$

This method for correcting platform tilts is not implemented in AGS 4.5.

Swain correction

(Swain, 1996) proposed an alternative correction for the tilt by applying a filter that removes the error caused by a tilt. This error is given in LaCoste (1967) as

$$e_g = -\ddot{x}\theta - g\theta^2/2 \tag{A.12}$$

where $\ddot{x}$ is the x-component of horizontal acceleration and θ is the off-level error (tilt), or

$$e_g = -\ddot{x}\alpha - \ddot{y}\beta - g(\alpha^2 + \beta^2)/2, \tag{A.13}$$

when the tilt is composed of angles α and β in the x-z and x-y planes. The tilt is estimated from horizontal accelerations using a filter with input p (accelerations) and output q (tilt) (Swain, 1996):

$$q_j = c_0 p_j + c_1 p_{j-1} + c_2 p_{j-2} + d_1 q_{j-1} + d_2 q_{j-2} \tag{A.14}$$

with

$$c_0 = (a + b)/(4 + a + b)$$
$$c_1 = 2b/(4 + a + b)$$
$$c_2 = (b - 1)/(4 + a + b)$$
$$d_1 = (8 - 2b)/(4 + a + b)$$
$$d_2 = (a - b - 4)/(4 + a + b)$$

where $a = 4f\omega_0\Delta t$ and $b = (\omega_0\Delta t)^2$.

Lever arm effect

A horizontal offset in between the locations of the GPS antenna and the gravimeter causes a so-called lever arm effect, i.e. the vertical acceleration experienced by the GPS antenna differs from accelerations observed by the gravimeter due to aircraft attitude variations. The effect can be modeled if aircraft attitude information is available from INS or may be neglected if the offset between the GPS antenna and gravimeter is small. According to Olesen (2003), the effect can be safely neglected for offsets less than 1 meter, in case of scalar gravimetry. For vector gravimetry the lever arm effect should be modeled more accurately, as was shown by De Saint-Jean et al. (2007). Similar to the lever arms of the GPS antennas, the AGS software adjusts for lever arms of the INS and altimeter instruments, if present. All adjustments are made to the location of the gravimeter, which should be located close to the center of gravity of the aircraft.

Low-pass filtering

The final step in gravity pre-processing consists usually of applying a low-pas filter to reduce the extreme high noise level of the airborne gravity data. In the AGS software two filters are implemented; a 1st-order RC-filter and a 2nd-order Butterworth filter. Both filters are implemented as a forward-backward filter to remove the phase shift. For the pre-processing of the data sets used in sections 6.1 and 6.2, the Butterworth filter was used with a filter length of 180 seconds.

Processing example

An example of the output of AGS 4.5 is shown for a profile of the Skagerrak data set (see section 6.1) in figure A.2.
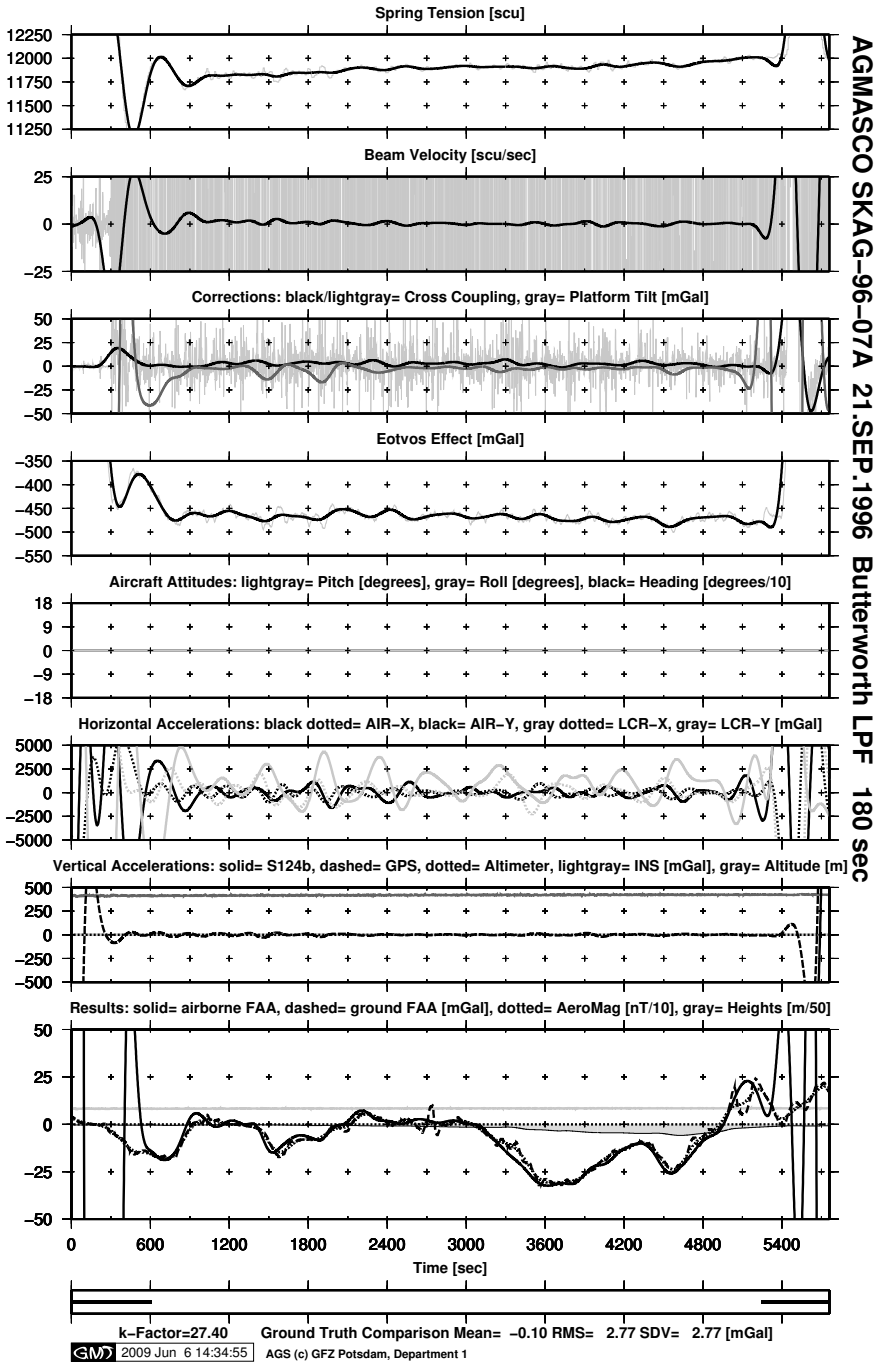
Figure A.2: AGS processing example for an airborne gravity profile from the Skagerrak survey.

Coordinate transformation

The base functions used in this thesis (Eq. (4.3)) require the coordinates to be given in a local Cartesian reference frame. This appendix gives the definitions of the considered coordinate systems and the transformations that were applied.
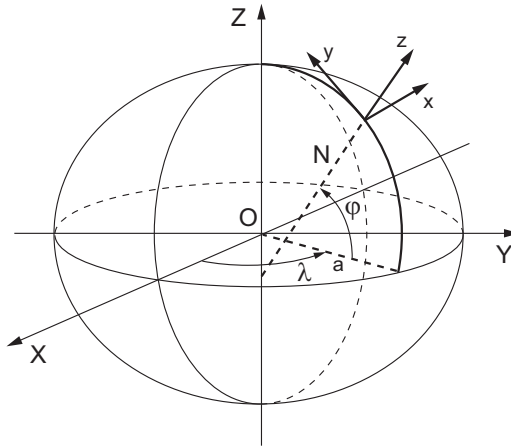
Figure B.1: Graphical representation of the coordinate systems.

The transformation from ellipsoidal coordinates $\{\varphi, \lambda, h\}$ to geocentric coordinates $\{X, Y, Z\}$ is given as

$$
\begin{aligned}
X &= (N + h) \cos \varphi \cos \lambda \\
Y &= (N + h) \cos \varphi \sin \lambda \\
Z &= (N(1 - e^2) + h) \sin \varphi,
\end{aligned}
\tag{B.1}
$$

with N the normal radius of curvature: $N = a/W$, where a is the semi-major axis and W is the latitude function defined as

$$
W = \sqrt{1 - e^2 \sin^2 \varphi}.
$$

In Eq. (B.1) e is the first eccentricity of the ellipsoid used for the definition of the ellipsoidal coordinate system. For spherical coordinates the same transformation formulas

can be used, setting $e^2 = 0$.

The transformation from geocentric coordinates $\{X, Y, Z\}$ to local Cartesian coordinates $\{x, y, z\}$ is given as

$$
\begin{bmatrix} x \\ y \\ z \end{bmatrix} = \begin{bmatrix} -\sin \lambda_c & \cos \lambda_c & 0 \\ -\sin \varphi_c \cos \lambda_c & -\sin \varphi_c \sin \lambda_c & \cos \varphi_c \\ \cos \varphi_c \cos \lambda_c & \cos \varphi_c \sin \lambda_c & \sin \varphi_c \end{bmatrix} \begin{bmatrix} X \\ Y \\ Z \end{bmatrix} + \begin{bmatrix} t_x \\ t_y \\ t_z \end{bmatrix}, \quad \text{(B.2)}
$$

with $\{\varphi_c, \lambda_c\}$ the coordinate center of the area considered and $\{t_x, t_y, t_z\}$ are translations in the corresponding directions. If the general direction of the area is not north-south, the x,y-plane may be rotated about the z-axis by multiplying the obtained coordinates $[x, y, z]^T$ with the rotation matrix

$$
R_z = \begin{bmatrix} \cos \alpha & \sin \alpha & 0 \\ -\sin \alpha & \cos \alpha & 0 \\ 0 & 0 & 1 \end{bmatrix}, \quad \text{(B.3)}
$$

where α is a clockwise rotation about the z-axis.

Least-squares collocation and Hilbert spaces

<div align="right">C</div>

This appendix gives a derivation of LSC as minimum norm solution in a reproducing kernel Hilbert space (RKHS). The first part is a summary of an article on Hilbert spaces by Meissl (1976). Hilbert spaces are an important type of function spaces in functional analysis. They represent the logical generalization to functions of n-dimensional vector spaces. The section describing LSC is based on (Moritz, 1980).

C.1   Definition of a Hilbert space and some properties

Linear space: a set of elements such that for any finite subset $f_1, f_2, \ldots, f_n$, the linear combination $\alpha_1 f_1 + \alpha_2 f_2 + \ldots + \alpha_n f_n$ is also a member of the linear space. The constants $\alpha_1, \alpha_2, \ldots, \alpha_n$ are real numbers. The elements $f_1, f_2, \ldots, f_n$ are linearly independent if there exist no set of $\alpha_1, \alpha_2, \ldots, \alpha_n$ (not all of them being zero) such that $\alpha_1 f_1 + \alpha_2 f_2 + \ldots + \alpha_n f_n = 0$.

Normed linear space: A linear space that assigns to any of its elements f a non-negative number $\|f\|$, called the norm of f, with

$$\|f\| > 0 \quad \text{for } f \neq 0$$
$$\|\alpha f\| = |\alpha| \|f\|$$
$$\|f + g\| \leq \|f\| + \|g\|.$$

The norm can be used to define a distance between two elements f and g: $|f - g\|$, which can be used to define convergence:

1. *Convergence to a limit element*: A sequence $f_1, f_2, \ldots$ converges to the limit element f if

$$\lim_{n \to \infty} \|f - f_n\| = 0.$$

   This type of convergence is called norm convergence.

2. *Convergence in the sense of Cauchy*: A sequence $f_1, f_2, \ldots$ is called a Cauchy convergent if

$$\lim_{n,m \to \infty} \|f_n - f_m\| = 0.$$

The sequence is then called a Cauchy sequence.

Complete normed linear space: A normed linear space is complete if any Cauchy sequence automatically possesses a limit element. They are also called Banach spaces.

Inner product space: A linear space with an inner product $\langle f, g \rangle$ with the properties:

$$\langle f, g \rangle = \langle g, f \rangle$$
$$\langle \alpha f, g \rangle = \alpha \langle f, g \rangle$$
$$\langle f_1 + f_2, g \rangle = \langle f_1, g \rangle + \langle f_2, g \rangle$$
$$\langle f, f \rangle > 0 \quad \text{for } f \neq 0$$

Hilbert space: An inner product space that is complete. For examples of Hilbert spaces see e.g. Meissl (1976).

Linear operators in Hilbert spaces: An operator A is a mapping which assigns to any element f out of the operators domain space $\mathcal{D}$ an image element $A(f)$ out of the operators range space $\mathcal{R}$. An operator is linear if it maps a linear combination onto the linear combination of the individual image elements with the same coefficients:

$$A(\alpha_1 f_1 + \ldots + \alpha_n f_n) = \alpha_1 A(f_1) + \ldots + \alpha_n A(f_n).$$

For linear operators often the notation Af is used instead of $A(f)$.

An operator is continuous if it maps a sequence converging to a limit element onto an image sequence converging to the image of the limit element. A is called bounded if there exists a non-negative number β such that $\|A(f)\| \leq \beta \|f\|$. The smallest β for which this relation holds is called the norm of A.

Linear functionals: An important special case of a linear operator is a linear functional. Its domain is a Hilbert space $\mathcal{H}$, its range is $\mathbb{R}$. Hence, a linear functional L assigns a real number Lf to any element of $\mathcal{H}$. A bounded linear functional fulfills

$$|Lf| \leq \|L\| \|f\|,$$

with $\|L\|$ the norm of the linear functional.

The Riesz-representation theorem states that any linear functional L operating on a Hilbert space can be represented by an inner product with suitable element g_L:

$$Lf = \langle f, g_L \rangle, \quad \|L\| = \|g_L\|.$$

The element $g_L \in \mathcal{H}$ is called the representer of L. A special linear functional is the evaluation functional, $Lf = f(Q)$. Hilbert spaces where the evaluation functional is continuous (i.e. bounded) for all locations, posses a reproducing kernel. They are called reproducing kernel Hilbert spaces.

C.2 Reproducing kernel Hilbert spaces

A function $K(P, Q)$ is called a reproducing kernel belonging to a Hilbert space $\mathcal{H}$ if:

   a. $K(P, Q) \in \mathcal{H}$ for Q fixed,

   b. $f(Q) = \langle f(P), K(P, Q) \rangle_P$ for any $f \in \mathcal{H}$.

The second relation is called the reproducing property. The notation $\langle\,,\,\rangle_P$ indicates that both functions in the inner product are functions of P and that Q is held fixed.

Other properties may be deduced from the properties listed above:

   c. $K(P, P) \geq 0$,

   d. $K(P, Q) = K(Q, P)$, i.e. the reproducing kernel is a symmetric function,

   e. For arbitrary constants λ_j and n fixed points P_j the following relation holds:

$$\sum_{j=1}^{n} \sum_{k=1}^{n} \lambda_j \lambda_k K(P_j, P_k) \geq 0,$$

   f. $K(P, Q)$ is unique,

   g. For any pair of points P, Q the function $K(P, Q)$ is finite.

Properties (c) to (e) state that the kernel function is symmetric and positive definite.

C.3 Least-squares collocation

Pure least-squares collocation

Suppose for an unknown function $f \in \mathcal{H}$, n observations $l_i = L_i f$ are available. If $r_i \in \mathcal{H}$ is the representer of L_i in $\mathcal{H}$, the observations l_i can be written as

$$l_i = L_i f = \langle f, r_i \rangle. \tag{C.1}$$

When the dimension of $\mathcal{H}$ is larger then n, the function f is not uniquely determined. Among all approximate solutions $\bar{f}$ that are compatible with the observations l_i (and therefore satisfy the system (C.1)), there is one, $\hat{f}$, for which the norm is minimum (Moritz, 1980):

$$\|\bar{f}\| \geq \|\hat{f}\|. \tag{C.2}$$

The solution $\hat{f}$ is the orthogonal projection of f onto a subspace of $\mathcal{H}$ spanned by r_i. It is precisely the solution given by least-squares collocation, which is shown below.

The approximation $\hat{f}$ can be expressed as a linear combination of the base functions r_i as

$$\hat{f} = \sum_{i=1}^{n} b_i r_i, \tag{C.3}$$

where b_i are unknown coefficients to be determined from the data. Substituting Eq. (C.3) into Eq. (C.1) gives the observation equations as

$$l_i = L_i f = L_i \hat{f} = \sum_{j=1}^{n} b_j L_i r_j = \sum_{j=1}^{n} b_j \langle r_j, r_i \rangle, \quad i = 1, \ldots, n, \tag{C.4}$$

or in matrix-vector notation

$$\mathbf{l} = \mathbf{R}\mathbf{b},$$

with matrix

$$\mathbf{R} = \begin{bmatrix} \langle r_1, r_1 \rangle & \langle r_1, r_2 \rangle & \cdots & \langle r_1, r_n \rangle \\ \langle r_2, r_1 \rangle & \langle r_2, r_2 \rangle & \cdots & \langle r_2, r_n \rangle \\ \vdots & \vdots & \ddots & \vdots \\ \langle r_n, r_1 \rangle & \langle r_n, r_2 \rangle & \cdots & \langle r_n, r_n \rangle \end{bmatrix}.$$

If the set of representers r_i is linearly independent, the approximation $\hat{f}$ is obtained numerically from the coefficients $\mathbf{b}$

$$\mathbf{b} = \mathbf{R}^{-1}\mathbf{l} \tag{C.5}$$

as

$$\hat{f} = \mathbf{r}^T \mathbf{b} = \mathbf{r}^T \mathbf{R}^{-1}\mathbf{l}. \tag{C.6}$$

In a reproducing kernel Hilbert space $\mathcal{H}$, the representers r_i are simply given as

$$r_i = L_i^Q K(P, Q) = K(P, L_i), \tag{C.7}$$

where $K(P, Q)$ is the reproducing kernel evaluated at the data points $Q = Q_i$. Then, with the following expressions

$$\mathbf{r} = \mathbf{L}K, \quad \mathbf{R} = \mathbf{L}(\mathbf{L}K)^T, \tag{C.8}$$

where

$$\mathbf{L} = \begin{bmatrix} L_1 & L_2 & \cdots & L_n \end{bmatrix}^T \tag{C.9}$$

and

$$\mathbf{L}K = \begin{bmatrix} K(P, L_1) \\ K(P, L_2) \\ \vdots \\ K(P, L_n) \end{bmatrix} = \begin{bmatrix} L_1^Q K(P, Q) \\ L_2^Q K(P, Q) \\ \vdots \\ L_n^Q K(P, Q) \end{bmatrix}, \tag{C.10}$$

the least-squares collocation solution of Eq. (C.6) can be written as

$$\hat{f} = (\mathbf{L}K)^T (\mathbf{L}(\mathbf{L}K)^T)^{-1}\mathbf{l}. \tag{C.11}$$

For the norm of the LSC solution $\hat{f}$, the following expression is obtained (Moritz, 1980)

$$
\begin{aligned}
\|\hat{f}\|^2 = \langle \hat{f}, \hat{f} \rangle &= \langle \hat{f}(P), \sum_{i=1}^{n} b_i L_i^Q k(P,Q) \rangle_P \\
&= \sum_{i=1}^{n} b_i L_i^Q \langle \hat{f}(P), K(P,Q) \rangle_P \\
&= \sum_{i=1}^{n} b_i L_i^Q \hat{f}(Q) = \sum_{i=1}^{n} b_i L_i^Q \sum_{j=1}^{n} b_j L_j^R K(Q,R) \\
&= \sum_{i=1}^{n} \sum_{j=1}^{n} b_i b_j L_i^Q L_j^R K(Q,R) = \mathbf{b}^T (\mathbf{L}(\mathbf{L}K)^T) \mathbf{b}.
\end{aligned}
\tag{C.12}
$$

Using expression (C.5), this can be written in terms of observations l_i as

$$
\|\hat{f}\|^2 = \mathbf{l}^T (\mathbf{L}(\mathbf{L}K)^T)^{-1} \mathbf{l} = \mathbf{l}^T \mathbf{C}_{ll}^{-1} \mathbf{l}.
\tag{C.13}
$$

Instead of least-squares collocation, the method of determining $\hat{f}$ as outlined here is also called least-norm collocation, because the norm $\|\hat{f}\|^2$ is minimized.

LSC in the presence of noise

The observation model of least-squares collocation in the presence of noise is given as

$$
l_i = L_i f + e_i, \quad i = 1, \ldots, n,
\tag{C.14}
$$

where e_i is the error in the observation l_i. In matrix notation this is written as

$$
\mathbf{l} = \mathbf{L}f + \mathbf{e}.
$$

The noise $\mathbf{e}$ is a genuine random (stochastic) quantity with expectation $E\{\mathbf{e}\} = 0$. Denoting the variance-covariance matrix of the noise by $\mathbf{C}_{ee}$, the error norm reads

$$
\|\mathbf{e}\|^2 = \mathbf{e}^T \mathbf{C}_{ee}^{-1} \mathbf{e}.
\tag{C.15}
$$

With the norm for f, which is a norm in a Hilbert space with reproducing kernel $K(P,Q)$, i.e. $\|f\|^2 = \langle f, f \rangle$, the quadratic functional to be minimized is

$$
\Phi = \|f\|^2 + \|\mathbf{e}\|^2 = \langle f, f \rangle + \mathbf{e}^T \mathbf{C}_{ee}^{-1} \mathbf{e}.
\tag{C.16}
$$

Then, the least-squares estimator of f is given as (Moritz, 1980)

$$
\hat{f} = (\mathbf{L}K)^T (\mathbf{L}(\mathbf{L}K)^T + \mathbf{C}_{ee})^{-1} \mathbf{l}.
\tag{C.17}
$$

Definition of the reproducing kernel

Let $f(P)$ be a function harmonic outside the Bjerhammar sphere and regular at infinity, i.e. $f(x) \to 0$, $|x| \to \infty$. Then, the reproducing kernel $K(P, Q)$ is defined as

$$K(P, Q) = M\{f(P), f(Q)\}, \tag{C.18}$$

where $M\{\cdot\}$ is a suitable averaging operator. Following the definition in Heiskanen and Moritz (1967), the mean M is the average over the whole sphere and over all azimuths. Since the operator M is homogeneous and isotropic (i.e. independent of the absolute location and azimuth), the function $K(P, Q)$ is a function only of the spherical distance ψ_{PQ} between P and Q:

$$K(P, Q) = K(\psi_{PQ}) = M\{f(P), f(Q)\}$$
$$= \frac{1}{8\pi^2 R^2} \iint\limits_{\sigma_R} \int\limits_{\alpha_{PQ}=0}^{2\pi} f(P)f(Q) \mathrm{d}\alpha_{PQ} \mathrm{d}\sigma_R(P), \tag{C.19}$$

with ψ_{PQ} given by Eq. (3.15).

The function $K(P, Q)$ can be expanded in a series of spherical harmonics. For K restricted to σ_R the expansion is given as

$$K(\psi_{PQ}) = \sum_{n=2}^{\infty} c_n P_n(\cos \psi_{PQ}), \tag{C.20}$$

where $P_n(\cos \psi)$ are the Legendre polynomials. The coefficients c_n can be expressed in terms of fully normalized spherical harmonic coefficients $\bar{a}_{nm}$ and $\bar{b}_{nm}$ by

$$c_n = \sum_{m=0}^{n} (\bar{a}_{nm}^2 + \bar{b}_{nm}^2). \tag{C.21}$$

The reproducing kernel in the Hilbert space of regular functions in the exterior of σ_R reads

$$K(\psi_{PQ}) = \sum_{n=2}^{\infty} c_n \left(\frac{R_B^2}{r_P r_Q} \right)^{n+1} P_n(cos\psi_{PQ}), \tag{C.22}$$

where R_B is the radius of the Bjerhammar sphere.

Derivation of the ZOT regularization matrix

D

The zero-order Tikhonov regularization functional is given as

$$\Phi^{\text{ZOT}} = \iint\limits_{D} T^2(x, y, z)\mathrm{d}x\,\mathrm{d}y, \tag{D.1}$$

where the disturbing potential T is defined by Eq (4.7). Inserting Eq. (4.7) into Eq. (D.1), the regularization functional reads

$$
\begin{aligned}
\Phi^{\text{ZOT}} &= \iint\limits_{D} \Big(\sum_{l=-L}^{L} \sum_{m=-M}^{M} C_{lm}\varphi_l(x)\varphi_m(y)e^{-\gamma_{lm}z} \Big)^2 \mathrm{d}x\,\mathrm{d}y \\
&= \iint\limits_{D} \sum_{l_1} \sum_{m_1} \sum_{l_2} \sum_{m_2} \big(C_{l_1 m_1}\varphi_{l_1}(x)\varphi_{m_1}(y) C_{l_1 m_2}\varphi_{l_2}(x)\varphi_{m_2}(y) \big) \\
&\quad \times e^{-(\gamma_{l_1 m_1} + \gamma_{l_2 m_2})z} \mathrm{d}x\,\mathrm{d}y.
\end{aligned}
\tag{D.2}
$$

Interchanging summation and integration gives

$$
\begin{aligned}
\Phi^{\text{ZOT}} &= \sum_{l_1} \sum_{m_1} \sum_{l_2} \sum_{m_2} \Big(C_{l_1 m_1} C_{l_1 m_2} \int_0^{D_x} \varphi_{l_1}(x)\varphi_{l_2}(x)\mathrm{d}x \int_0^{D_y} \varphi_{m_1}(y)\varphi_{m_2}(y)\mathrm{d}y \Big) \\
&\quad \times e^{-(\gamma_{l_1 m_1} + \gamma_{l_2 m_2})z}.
\end{aligned}
\tag{D.3}
$$

The products of the base functions, $\varphi_{l_1}(x)\varphi_{l_2}(x)$ (or $\varphi_{m_1}(y)\varphi_{m_2}(y)$), are products of sine and cosine functions that have the following properties:

$$\int_{-L}^{L} \cos\frac{l\pi x}{L}\cos\frac{m\pi x}{L}\mathrm{d}x = \begin{cases} 0 & \text{if } l \neq m \\ 2L & \text{if } l = m = 0 \\ L & \text{if } l = m \neq 0 \end{cases} \tag{D.4}$$

$$\int_{-L}^{L} \sin\frac{l\pi x}{L}\sin\frac{m\pi x}{L}\mathrm{d}x = \begin{cases} 0 & \text{if } l \neq m \\ L & \text{if } l = m \neq 0 \end{cases} \tag{D.5}$$

$$\int_{-L}^{L} \sin\frac{l\pi x}{L}\sin\frac{m\pi x}{L}\mathrm{d}x = 0. \tag{D.6}$$

For the base functions defined by Eq. (4.4) this means

$$\int_0^{D_x} \varphi_{l_1}(x)\varphi_{l_2}(x)\mathrm{d}x = \begin{cases} 0 & \text{if } l_1 \neq l_2 \\ D_x & \text{if } l_1 = l_2 = 0 \\ D_x/2 & \text{if } l_1 = l_2 \neq 0 \end{cases} \tag{D.7}$$

Using these properties the regularization functional can be written as

$$\Phi^{\text{ZOT}} = \frac{D_x D_y}{4}\, \mathbf{x}^T \mathbf{R}^{\text{ZOT}} \mathbf{x}, \tag{D.8}$$

where the entries of $\mathbf{R}^{\text{ZOT}}$ are given as

$$\mathbf{R}^{\text{ZOT}}_{ij} = \begin{cases} 4\,\delta_{ij}\, e^{-2\gamma_{l_i m_i} z}, & \text{if } l_i = m_i = 0 \\ 2\,\delta_{ij}\, e^{-2\gamma_{l_i m_i} z}, & \text{if } l_i = 0 \text{ or } m_i = 0 \\ \delta_{ij}\, e^{-2\gamma_{l_i m_i} z}, & \text{otherwise.} \end{cases} \tag{D.9}$$

Modification of the base functions

The disturbing potential is expressed by a series of base functions that are the fundamental solutions of Laplace's equation in Cartesian coordinates as (see Eq. (4.7))

$$T(x, y, z) = \sum_{l=-L}^{L} \sum_{m=-M}^{M} C_{lm}\, \varphi_l(x)\, \varphi_m(y)\, e^{-\gamma_{lm}z}, \tag{E.1}$$

where

$$\varphi_l(x) = \begin{cases} \cos \frac{2\pi|l|}{D_x}x, & l \geq 0 \\ \sin \frac{2\pi|l|}{D_x}x, & l < 0 \end{cases} \qquad \varphi_m(y) = \begin{cases} \cos \frac{2\pi|m|}{D_y}y, & m \geq 0 \\ \sin \frac{2\pi|m|}{D_y}y, & m < 0 \end{cases} \tag{E.2}$$

and

$$\gamma_{lm} := \sqrt{\alpha_l^2 + \beta_m^2} = 2\pi\sqrt{\left(\frac{l}{D_x}\right)^2 + \left(\frac{m}{D_y}\right)^2}. \tag{E.3}$$

Because the base functions are periodic but the signal is not, the following base functions that are periodic on a larger domain are introduced (see section 4.5):

$$\varphi_l(x) = \begin{cases} \cos \frac{\pi x}{D_x}, & l = L + 1 \\ \sin \frac{\pi x}{D_x}, & l = -L - 1 \end{cases} \quad, \quad \varphi_m(y) = \begin{cases} \cos \frac{\pi y}{D_y}, & m = M + 1 \\ \sin \frac{\pi y}{D_y}, & m = -M - 1 \end{cases} \tag{E.4}$$

Then for $l = \pm(L + 1), -M \leq m \leq M$ the expression for $\gamma_{\pm(L+1),m}$ is obtained using

$$\Delta\left(\varphi_{\pm(L+1)}(x)\varphi_m(y)e^{\gamma_{\pm(L+1),m}z}\right) = -\left(\frac{\pi}{D_x}\right)^2 - \left(\frac{2\pi m}{D_y}\right)^2 + \gamma_{\pm(L+1),m}^2 = 0, \tag{E.5}$$

which results in

$$\gamma_{\pm(L+1),m} = \pi\sqrt{\left(\frac{1}{D_x}\right)^2 + \left(\frac{2m}{D_y}\right)^2}. \tag{E.6}$$

Similarly, the expressions for $\gamma_{l,\pm(M+1)}$ and $\gamma_{\pm(L+1),\pm(M+1)}$ are obtained as

$$\gamma_{l,\pm(M+1)} = \pi\sqrt{\left(\frac{2l}{D_x}\right)^2 + \left(\frac{1}{D_y}\right)^2} \qquad \text{(E.7)}$$

$$\gamma_{\pm(L+1),\pm(M+1)} = \pi\sqrt{\left(\frac{1}{D_x}\right)^2 + \left(\frac{1}{D_y}\right)^2}. \qquad \text{(E.8)}$$

Bibliography

Alberts BA, Ditmar P, and Klees R (2007a). A new methodology to process airborne gravimetry data: advances and problems. In: Tregoning P and Rizos C, (eds.), *Proceedings of Dynamic Planet - Monitoring and Understanding a Dynamic Planet with Geodetic and Oceanographic Tools*, volume 130 of *IAG Symposia*, pages 251–258, Cairns, Australia.

Alberts BA, Gunter BC, Muis A, Chu QP, Giorgi G, Huisman L, Buist PJ, Tiberius CCJM, and Lindenburg H (2008). Correcting strapdown GPS/INS gravimetry estimates with GPS attitude data. In: *IAG International Symposium on Gravity, Geoid & Earth Observation (GGEO2008)*, Chania, Crete, Greece.

Alberts BA and Klees R (2004). A comparison of methods for the inversion of airborne gravity data. *Journal of Geodesy*, 78: 55–65.

Alberts BA, Klees R, and Ditmar P (2005). A new strategy for processing airborne gravity data. In: Jekeli C, Bastos L, and Fernandes J, (eds.), *Proceedings of the IAG International Symposium on Gravity, Geoid and Space Missions (GGSM2004)*, volume 129 of *IAG Symposia*, pages 161–166, Porto, Portugal.

Alberts BA, Klees R, and Ditmar P (2007b). Gravity field modelling from airborne gravimetry using fundamental solutions of Laplace's equation in Cartesian coordinates. In: *Harita Dergisi, Proceedings of the 1st International Symposium of the International Gravity Field Service 'Gravity field of the Earth'*, pages 283–288, Istanbul, Turkey.

Andersen OB, Knudsen P, Berry P, and Kenyon S (2008). The DNSC08 ocean wide altimetry derived gravity field. Technical report, Presented at the EGU General Assembly 2008, Vienna, Austria.

Arsenin VY and Krianev AV (1992). Generalized maximum likelihood method and its application for solving ill-posed problems. In: Tikhonov A, (ed.), *Ill-posed problems in natural sciences*, pages 3–12. TVP Science Publishers.

Bell RE, Anderson R, and Pratson L (1997). Gravity gradiometry resurfaces. *The Leading Edge*, 16: 55–60.

Bell RE, Childers VA, Arko RA, Blankenship D, and Brozena J (1999). Airborne gravity and precise positioning for geologic applications. *Journal of Geophysical Research*, 104(B7): 15281–15292.

Boedecker G and Stürze A (2006). SAGS4 - Strapdown airborne gravimetry system analysis. In: Flury J, Rummel R, Reigber C, Rotacher M, Boedecker G, and Schreiber U, (eds.), *Observation of the Earth System from Space*, pages 463–478. Springer, Berlin, Heidelberg.

Bouman J (1998). *Quality of regularization methods*. DEOS Report 98.2. Delft University Press.

Bouman J (2000). *Quality assessment of satellite-based global gravity field models*. Publications on geodesy, 48. Netherlands Geodetic Commission, Delft.

Bracewell RN (2000). *The Fourier transform and its applications*. McGraw-Hill, Boston, USA, 3rd edition edition.

Brockwell PJ and Davis RA (1991). *Time series: theory and methods*. Springer Series in Statistics. Springer, New York, 2nd edition.

Broersen PMT (2000). Facts and fiction in spectral analysis. *IEEE Transactions on Instrumentation and Measurement*, 49: 766–772.

Brozena JM (1984). A preliminary analysis of the NRL airborne gravimetry system. *Geophysics*, 49(7): 1060–1069.

Brozena JM (1992). The Greenland Aerogeophysics Project - Airborne gravity, topographic and magnetic mapping of an entire continent. In: *From Mars to Greenland: Charting gravity with space and airborne instruments - Fields, tides, methods, results*, pages 203–214.

Brozena JM, Mader GL, and Peters MF (1989). Interferometric Global Positioning System: three-dimensional positioning source for airborne gravimetry. *Journal of Geophysical Research*, 94(B9): 12153–12162.

Brozena JM and Peters MF (1988). An airborne gravity study of eastern North Carolina. *Geophysics*, 53(2): 245–253.

Brozena JM and Peters MF (1994). Airborne gravity measurement at NRL. In: Cannon ME and Lachapelle G, (eds.), *Proceedings of the International Symposium on Kinematic Systems in Geodesy, Geomatics and Navigation (KIS94)*, pages 495–506, Banff, Canada.

Brozena JM, Peters MF, and Salman R (1997). Arctic airborne gravity measurement program. In: Segawa J, Fujimoto H, and Okubo S, (eds.), *Proceedings of the IAG international symposium "Gravity, Geoid and Marine Geodesy"*, volume 117 of *IAG Symposia*, pages 131–138, Tokyo, Japan.

Bruton AM (2000). *Improving the accuracy and resolution of SINS/DGPS airborne gravimetry*. Ucge report # 20145, Department of Geomatics Engineering, University of Calgary, Calgary, Canada.

Bruton AM, Schwarz KP, Ferguson S, Kern M, and Wei M (2002). Deriving accelerations from DGPS: toward higher resolution applications of airborne gravimetry. *GPS Solutions*, 5(3): 1–14.

Clarke T (2002). Flying free. *Nature*, 417: 582–583.

Crocetto N, Gatti M, and Russo P (2000). Simplified formulae for the BIQUE estimation of variance components in disjunctive observation groups. *Journal of Geodesy*, 74: 447–457.

Czompo J (1994). Testing the rotation invariant scalar gravimeter concept. In: *Proceedings of the International Symposium on Kinematic Systems in Geodesy, Geomatics and Navigation (KIS94)*, pages 483–493, Banff, Canada.

Davis PJ (1979). *Circulant matrices*. John Wiley, New York.

De Saint-Jean B, Verdun J, Duquenne H, Barriot JP, Melachroinos S, and Cali J (2007). Fine analysis of lever arm effects in moving gravimetry. In: Tregoning P and Rizos C, (eds.), *Proceedings of Dynamic Planet - Monitoring and Understanding a Dynamic Planet with Geodetic and Oceanographic Tools*, volume 130 of *IAG Symposia*, pages 809–816, Cairns, Australia.

Ditmar P and Klees R (2002). *A method to compute the Earth's gravity field from SGG/STT data to be acquired by the GOCE satellite*. Delft University Press.

Ditmar P, Klees R, and Liu X (2007). Frequency-dependent data weighting in global gravity field modeling from satellite data contaminated by non-stationary noise. *Journal of Geodesy*, 81(1): 81–96.

Ditmar P, Kusche J, and Klees R (2003). Computation of spherical harmonic coefficients from gravity gradiometry data to be acquired by the GOCE satellite: regularization issues. *Journal of Geodesy*, 77: 465–477.

Ditmar P and van Eck van der Sluijs AA (2004). A technique for modeling the Earth's gravity field on the basis of satellite accelerations. *Journal of Geodesy*, 78: 12–33.

Ditmar P, van Eck van der Sluijs AA, and Kuznetsov V (2004). Modeling the Earth's gravity field from precise satellite orbit data: the acceleration approach works! In: *Proceedings of the Second International GOCE User Workshop "GOCE, the Geoid and Oceanography"*, ESA-ESRIN, Frascati, Italy.

Droge B (1996). Some comments on cross-validation. In: Härdle W and Schimek M, (eds.), *Statistical theory and computational aspects of smoothing*, pages 178–199. Physica-Verlag, Heidelberg.

Eisfeller B and Spietz P (1989). Shaping filter design for the anomalous gravity field by means of spectral factorization. *Manuscripta Geodaetica*, 14: 183–192.

Elieff S (2003). Project report for an airborne gravity evaluation survey, Timmins, Ontario: Report produced for the Timmins Economic Development Corporation on behalf of the Discover Abitibi Initiative. Technical report.

Elieff S and Sander S (2004). AIRGrav airborne gravity survey in Timmins, Ontario. In: Lane RJL, (ed.), *Airborne Gravity 2004 - Abstracts from the ASEG-PESA Airborne Gravity 2004 Workshop*, volume 2004/18 of *Geoscience Australia Record*, pages 111–119.

ESA (1999). *Gravity field and steady-state ocean circulation mission. Reports for mission selection the four candidate Earth Explorer Core Missions*, volume SP-1233 (1). European Space Agency (ESA), Noordwijk.

Featherstone WE, Evans JD, and Olliver J (1998). A Meissl-modified Vaníček and Kleusberg kernel to reduce the truncation error in gravimetric geoid computations. *Journal of Geodesy*, 72: 154–160.

Ferguson ST and Hammada Y (2001). Experiences with AIRGrav: results from a new airborne gravimeter. In: *Proceedings of the IAG International Symposium 'Gravity, Geoid and Geodynamics 2000'*, volume 123 of *IAG Symposia*, Banff, Canada.

Forsberg R (1987). A new covariance model for inertial gravimetry and gradiometry. *Journal of Geophysical Research*, 92(B2): 1305–1310.

Forsberg R (2002). Downward continuation of airborne gravity data. In: *Paper presented at the 3rd meeting of the International Gravity and Geoid Commission 'Gravity and Geoid 2002'*, Thessaloniki, Greece.

Forsberg R, Hehl K, Bastos L, Gidskehaug A, and Meyer U (1997). Development of an Airborne Geoid Mapping System for Coastal Oceanography (AGMASCO). In: *Proceedings of the IAG International Symposium 'Gravity, Geoid and Marine Geodesy'*, volume 117 of *IAG Symposia*, pages 163–170.

Forsberg R and Kenyon S (1994). Evaluation and downward continuation of airborne gravity data - the Greenland example. In: *Proceedings of the International Symposium on Kinematic Systems in Geodesy, Geomatics and Navigation (KIS94)*, pages 531–538, Banff, Canada.

Forsberg R and Olesen A (2006). Broad-band gravity field mapping by airborne gravity and GOCE. Presentation, 3rd International GOCE User Workshop 2006, Frascati, Italy.

Forsberg R, Olesen A, Munkhtsetseg D, and Amarzaya A (2007). Downward continuation and geoid determination in Mongolia form airborne and surface gravimetry and SRTM topography. In: *Harita Dergisi, Proceedings of the 1st International Symposium of the International Gravity Field Service 'Gravity field of the Earth'*, pages 259–264, Istanbul, Turkey.

Forsberg R, Olesen AV, and Keller K (1999). Airborne gravity survey of the North Greenland continental shelf. Technical Report 10, National Survey and Cadastre (KMS), Copenhagen, Denmark.

Forsberg R, Strykowski G, and Bilker M (2004). NKG-2004 geoid model - most recent model. Presentation, NKG geoid meeting, November 2004.

Forsberg R and Tscherning C (1981). The use of height data in gravity field approximation by collocation. *Journal of Geophysical Research*, 86(B9): 7843–7854.

Förste C, Schmidt R, Stubenvoll R, Flechtner F, Meyer U, König R, Neumayer H, Biancale R, Lemoine JM, Bruinsma S, Loyer S, Barthelmes F, and Esselborn S (2008). The GeoForschungsZentrum Potsdam/Groupe de Recherche de Gèodésie Spatiale satellite-only and combined gravity field models: EIGEN-GL04S1 and EIGEN-GL04C. *Journal of Geodesy*, 82: 331–346.

Gabell A, Tuckett H, and Olson D (2004). The GT-1A mobile gravimeter. In: Lane RJL, (ed.), *Airborne Gravity 2004 - Abstracts from the ASEG-PESA Airborne Gravity 2004 Workshop*, volume 2004/18 of *Geoscience Australia Record*, pages 55–61.

Girard DA (1989). A fast 'Monte-Carlo Cross-Validation' procedure for large least squares problems with noisy data. *Numerische Mathematik*, 56: 1–23.

Glennie C and Schwarz KP (1997). Airborne Gravity by Strapdown INS/DGPS in a 100 km by 100 km Area of the Rocky Mountains. In: *Proceedings of the International Symposium on Kinematic Systems in Geodesy, Geomatics and Navigation (KIS97)*, pages 619–624, Banff, Canada.

Glennie CL and Schwarz KP (1999). A comparison and analysis of airborne gravimetry results from two strapdown inertial/DGPS systems. *Journal of Geodesy*, 73: 311–321.

Glennie CL, Schwarz KP, Bruton AM, Forsberg R, Olesen AV, and Keller K (2000). A comparison of stable platform and strapdown airborne gravity. *Journal of Geodesy*, 74: 383–389.

Golub GH, Heath M, and Wahba G (1979). Generalized cross-validation as a method for choosing a good ridge parameter. *Technometrics*, 21: 215–223.

Golub GH and Van Loan CF (1996). *Matrix computations*. Johns Hopkins University Press, Baltimore, MD.

Gumert WR (1998). An historical review of airborne gravity. *The Leading Edge*, 17(1): 113–116.

Gumert WR and Cobb GE (1970). Helicopter gravity measuring system. In: Kattner WT, (ed.), *Proceedings of the symposium on dynamic gravimetry "Advances in dynamic gravimetry"*, pages 79–85, Fort Worth, Texas, USA.

Hammada Y and Schwarz KP (1997). Airborne gravimetry model-based versus frequency-domain filtering approaches. In: *Proceedings of the International Symposium on Kinematic Systems in Geodesy, Geomatics and Navigation (KIS97)*, pages 581–595, Banff, Canada.

Hammer S (1983). Airborne gravity is here! *Geophysics*, 48(2): 213–223.

Hamming RW (1989). *Digital filters*. Prentice-Hall Inetrnational, Inc., 3rd edition.

Harlan RB (1968). Eotvos correction for airborne gravimetry. *Journal of Geophysical Research*, 73(14): 4675–4679.

Hayes MH (1996). *Statistical digital signal processing and modeling*. John Wiley, New York.

Heck B and Grüninger W (1987). Modification of Stokes' integral formula by combining two classical approaches. In: *Proceedings of the XIX IUGG General Assembly, Tome II*, pages 319 – 337, Vancouver, Canada.

Hehl K, Bastos L, Cunha S, Forsberg R, Olesen AV, Gidskehaug A, Meyer U, Boebel T, Timmen L, Xu G, and Nesemann M (1997). Concepts and first results of the AG-MASCO project. In: *Proceedings of the International Symposium on Kinematic Systems in Geodesy, Geomatics and Navigation (KIS97)*, pages 557–563, Banff,Canada.

Heiskanen WA and Moritz H (1967). *Physical geodesy*. W.H. Freeman and Company, San Francisco.

Hestenes MR and Stiefel E (1952). Methods of conjugate gradients for solving linear systems. *Journal of Research of the National Bureau of Standards*, 49(6): 409–436.

Hotine M (1969). *Mathematical Geodesy*. ESSA Monograph 2, US Department of Commerce, Washington, D.C.

Huber PJ (1981). *Robust statistics*. Wiley series in probability and mathematical statistics. Wiley, New York.

Hutchinson MF (1990). A stochastic estimator of trace of the influence matrix for Laplacian smoothing splines. *Communications in Statistics, Simulation and Computation*, 19(2): 433–450.

Hwang C, Hsiao YS, and Shih HC (2006). Data reduction in scalar airborne gravimetry: Theory, software and case study in Taiwan. *Computers & Geosciences*, 32: 1573–1584.

Hwang C, Hsiao YS, Shih HC, Yang M, Chen KH, Forsberg R, and Olesen AV (2007). Geodetic and geophysical results from a Taiwan airborne gravity survey: Data reduction and accuracy assessment. *Journal of Geophysical Research*, 112(B4, B04407).

Jekeli C (1994). Airborne vector gravimetry using precise, position-aided inertial measurement units. *Bulletin Géodésique*, 69: 1–11.

Jekeli C and Kwon JH (1999). Results of airborne vector (3-D) gravimetry. *Geophysical Research Letters*, 26(23): 3533–3536.

Kaula WM (1966). *Theory of satellite geodesy*. Blaisdell Publishing Co., Waltham, Massachusets.

Kay SM and Marple SL (1981). Spectrum analysis - a modern perspective. *Proceedings of the IEEE*, 69: 1380–1419.

Kellogg OD (1929). *Foundations of potential theory*. Springer, Berlin.

Kiefer J (1953). Sequential minimax search for a maximum. *Proceedings of the American Mathematical Society*, 4(3): 502–506.

Klees R (1996). Numerical calculation of weakly singular surface integrals. *Journal of Geodesy*, 70: 781–797.

Klees R and Broersen P (2002). *How to handle colored noise in large least-squares problems - building the optimal filter*. Delft University Press, Delft, The Netherlands.

Klees R and Ditmar P (2004). How to handle colored noise in large least-squares problems in the presence of data gaps? In: Sansò F, (ed.), *Proceedings of the Vth Hotine-Marussi Symposium on Mathematical Geodesy*, pages 39–48, Matera, Italy.

Klees R, Ditmar P, and Broersen P (2003). How to handle colored noise in large least-squares problems. *Journal of Geodesy*, 76: 629–640.

Klees R, Marchenko A, Alberts BA, Wittwer T, and Ditmar P (2005). Comparison of various methods for the inversion of airborne gravimetry data. In: *Proceedings of Dynamic Planet 2005, 'Monitoring and Understanding a Dynamic Planet with Geodetic and Oceanographic Tools'*, Cairns, Australia.

Klees R and Wittwer T (2007). A data-adaptive design of a spherical basis function network for gravity field modelling. In: Tregoning P and Rizos C, (eds.), *Proceedings of Dynamic Planet - Monitoring and Understanding a Dynamic Planet with Geodetic and Oceanographic Tools*, volume 130 of *IAG Symposia*, pages 323–328, Cairns, Australia.

Kleusberg A, Peyton D, and Wells D (1990). Airborne gravimetry and the Global Positioning System. In: *Proceedings of IEEE Plans '90 "The 1990's - a decade of excellence in the navigation sciences"*, pages 273 – 278.

Klingelé E, Halliday M, Cocard M, and Kahle HG (1995). Airborne gravimetric survey of Switzerland. *Vermessung, Photogrammetrie, Kulturtechniek*, 4: 248–253.

Knudsen P (1987). Estimation and modelling of the local empirical covariance function using gravity and satellite altimeter data. *Bulletin Géodésique*, 61: 145–160.

Koch KR (1999). *Parameter estimation and hypothesis testing in linear models*. Springer, Berlin, Germany.

Koch KR and Kusche J (2002). Regularization of geopotential determination from satellite data by variance components. *Journal of Geodesy*, 76: 259–268.

Kotsakis C and Sideris MG (1999). The long road from deterministic collocation to multiresolution approximation. Schriftenreihe der Institute des Studiengangs Geodsie und Geoinformatik 1999.5, Department of Geodesy and Geoinformatics, Stuttgart University, Stuttgart, Germany.

Krarup T (1969). A contribution to the mathematical foundations of physical geodesy. Report 44, Danish Geodetic Institute, Copenhagen, Denmark.

Kress R (1989). *Linear integral equations*. Springer-Verlag.

Kreye C, Hein GW, and Zimmermann B (2006). Evaluation of airborne vector gravimetry using GNSS and SDINS observations. In: Flury J, Rummel R, Reigber C, Rotacher M, Boedecker G, and Schreiber U, (eds.), *Observation of the Earth System from Space*, pages 447–461. Springer, Berlin, Heidelberg.

Kusche J and Klees R (2002). Regularization of gravity field estimation from satellite gravity gradients. *Journal of Geodesy*, 76: 359–368.

LaCoste L, Clarkson N, and Hamilton G (1967). LaCoste and Romberg stabilized platform shipboard gravity meter. *Geophysics*, 32: 99–109.

LaCoste LJB (1967). Measurement of gravity at sea and in the air. *Reviews of Geophysics*, 5(4): 477–526.

Lee JB (2001). Falcon gravity gradiometer technology. *Exploration Geophysics*, 32: 247–250.

Lee JB, Downey MA, Turner RJ, Boggs DB, Maddever RAM, and Dransfield MH (2006). First test survey results from the FALCON helicopter-borne airborne gravity gradiometer system. In: *Extended abstracts of the Australian Earth Sciences Convention 2006*, Melbourne, Australia.

Lemoine FG, Kenyon SC, Factor JK, Trimmer R, Pavlis NK, Chinn DS, Cox CM, Klosko SM, Luthcke SB, Torrence MH, Wang YM, Williamson RG, Pavlis EC, Rapp RH, and Olson TR (1998). *The development of the joint NASA GSFC and NIMA geopotential model EGM96*. NASA Goddard Space Flight Center, Greenbelt, Maryland, USA.

Liu X (2008). *Global gravity field recovery from satellite-to-satellite tracking data with the acceleration approach*. PhD Thesis, Publications on Geodesy, 69. Netherlands Geodetic Commission, Delft.

Liu X, Ditmar P, and Klees R (2007). Estimation of data noise in global gravity field modeling. In: Tregoning P and Rizos C, (eds.), *Proceedings of Dynamic Planet - Monitoring and Understanding a Dynamic Planet with Geodetic and Oceanographic Tools*, volume 130 of *IAG Symposia*, Cairns, Australia.

Lundberg H (1957). Airborne gravity surveys. *Canadian Mining and Metallurgical Bulletin*, Aug.: 465–473.

Marchenko AN (1998). *Parametrization of the Earth's gravity field: point and line singularities*. Lviv Astronomical and Geodetical Society, Lviv.

Marchenko AN, Barthelmes F, Meyer U, and Schwintzer P (2001). Regional geoid determination: An application to airborne gravity data in the Skagerrak. Scientific Technical Report STR01/07, GeoForschungsZentrum Potsdam.

Marchenko DA, Meyer U, and Bastos L (2004). Airborne gravity disturbances in sequential multipole analysis for geoid determination and its test over the Azores. *Bollettino di Geodesia e Scienze Affini*, 1: 101–114.

Meissl P (1971a). On the linearization of the geodetic boundary value problem. OSU report 151, Department of Geodetic Science and Surveying, Ohio State University, Columbus.

Meissl P (1971b). Preparations for the numerical evaluation of second order Molodenskii-type formulas. OSU report 163, Department of Geodetic Science and Surveying, Ohio State University, Columbus.

Meissl P (1976). Hilbert spaces and their application to geodetic least squares problems. *Bollettino di Geodesia e Scienze Affini*, 35: 49–80.

Meyer U (2004). *Airborne Gravity Software - Description for GFZ Software Version 4.5*. GeoForschungsZentrum Potsdam.

Meyer U, Boedecker G, and Pflug H (2003). Airborne Navigation and Gravimetry Ensemble & Laboratory (ANGEL). Introduction and first airborne tests. Scientific Technical Report STR03/06, GeoForschungsZentrum Potsdam.

Meyer U and Pflug H (2003). CHICAGO - Chilean AeroGeophysical Observations - Survey report. Scientific Technical Report STR03/12, GeoForschungsZentrum Potsdam.

Molodenskii MS, Eremeev VF, and Yurkina MI (1962). Methods for study of the external gravitational field and figure of the Earth. *Israel program for scientific translations*, Jerusalem.

Moritz H (1962). Interpolation and prediction of gravity and their accuracy. Report 24, Institute of Geodesy, Photogrammetry and Cartography, Ohio State University, Columbus, Ohio.

Moritz H (1980). *Advanced physical geodesy*. Herbert Wichman, Karlsruhe.

Murphy CA (2004). The Air-FTG. In: Lane RJL, (ed.), *Airborne Gravity 2004 - Abstracts from the ASEG-PESA Airborne Gravity 2004 Workshop*, volume 2004/18 of *Geoscience Australia Record*, pages 7–14.

Nettleton LL, LaCoste L, and Harrison JC (1960). Tests of an airborne gravity meter. *Geophysics*, 25(1): 181–202.

Novák P (2003a). Geoid determination using one-step integration. *Journal of Geodesy*, 77: 193–206.

Novák P (2003b). Optimal model for geoid determination from airborne gravity. *Stud. Geophys. Geod.*, 47: 1–36.

Novák P and Heck B (2002). Downward continuation and geoid determination based on band-limited airborne gravity data. *Journal of Geodesy*, 76: 269–278.

Novák P, Kern M, and Schwarz KP (2000). On the determination of the relative geoid from airborne gravimetry. In: *Paper presented at the IAG International Symposium 'Gravity, Geoid and Geodynamics 2000'*, Banff, Canada.

NRC (National Research Council) (1995). *Airborne geophysics and precise positioning: scientific issues and future directions*. National Academy Press, Washington, D.C.

Olesen AV (2003). Improved airborne scalar vector gravimetry regional gravity field mapping and geoid determination. Technical report, National Survey and Cadastre (KMS), Copenhagen, Denmark.

Olesen AV and Forsberg R (2007a). Airborne scalar gravimetry for regional gravity field mapping and geoid determination. In: *Harita Dergisi, Proceedings of the 1st International Symposium of the International Gravity Field Service 'Gravity field of the Earth'*, pages 277–282, Istanbul, Turkey.

Olesen AV and Forsberg R (2007b). Regional airborne scalar gravimetry for geoid determination. Presentation, IUGG XXIV General Assembly 2007, Perugia, Italy.

Olesen AV, Forsberg R, and Gidskehaug A (1997). Airborne gravimetry using the LaCoste & Romberg gravimeter - an error analysis. In: Cannon ME and Lachapelle G, (eds.), *Proceedings of the International Symposium on Kinematic System in Geodesy, Geomatics and Navigation (KIS97)*, Banff, Canada.

Pavlis NK, Holmes SA, Kenyon SC, and Factor JK (2008). An Earth Gravitational Model to degree 2160: EGM2008. In: *EGU General Assembly 2008*, Vienna, Austria.

Prutkin I and Klees R (2007). On the non-uniqueness of local quasi-geoids computed from terrestrial gravity anomalies. *Journal of Geodesy*, Online first: 10.

Rapp RH and Rummel R (1975). Methods for the computation of detailed geoids and their accuracy. OSU report 233, Department of Geodetic Science and Surveying, Ohio State University, Columbus.

Reigber C, Bock R, Förste C, Grunwaldt L, Jakowski N, Lühr H, Schwintzer P, and Tilgner C (1996). CHAMP phase B - executive summary. Scientific Technical Report STR96/13, GeoForschungsZentrum Potsdam.

Rummel R, Schwarz K, and Gerstl M (1979). Least squares collocation and regularization. *Bulletin Géodésique*, 53: 343–361.

Salychev OS, Bykovsky AV, Voronov VV, Schwarz K, Liu Z, Wei M, and Panenka J (1994). Determination of gravity and deflections of the vertical for geophysical applications using the ITC-2 platform. In: *Proceedings of the International Symposium on Kinematic Systems in Geodesy, Geomatics and Navigation (KIS94)*, pages 521–529, Banff, Canada.

Sander S, Argyle M, Elieff S, Ferguson S, Lavoie V, and Sander L (2004). The AIRGrav airborne gravity system. In: Lane RJL, (ed.), *Airborne Gravity 2004 - Abstracts from the ASEG-PESA Airborne Gravity 2004 Workshop*, volume 2004/18 of *Geoscience Australia Record*, pages 49–54.

Sansò F (1980). The minimum mean square estimation error principle in physical geodesy (stochastic and non-stochastic interpretation). *Bollettino di Geodesia e Scienze Affini*, 39: 111–129.

Schuh WD (1996). Tailored numerical solution strategies for the global determination of the Earth's gravity field. Technical report, Mitteilungen der geodätischen Institute der Technischen Universität Graz, Folge 81, Graz, Austria.

Schuh WD (2003). The processing of band-limited measurements: filtering techniques in the least squares context and in the presence of data gaps. *Space Science Reviews*, 108: 67–78.

Schwarz KP (1979). Geodetic improperly posed problems and their regularization. *Bollettino di Geodesia e Scienze Affini*, 38: 389–416.

Schwarz KP, Cannon ME, and Wong RVC (1989). A comparison of GPS kinematic models for the determination of position and velocity along a trajectory. *Manuscripta Geodaetica*, 14: 345–353.

Schwarz KP, Colombo O, Hein G, and Knickmeyer ET (1991). Requirements for airborne vector gravimetry. In: *Proceedings of the IAG Symposium G3 'From Mars to Greenland: charting gravity with space and airborne instruments'*, pages 273–283. Springer-Verlag, New York.

Schwarz KP and Li Z (1997). An introduction to airborne gravimetry and its boundary value problems. In: Sanso F and Rummel R, (eds.), *Geodetic boundary value problems in view of the one centimeter geoid*, volume 65 of *Lecture notes in earth sciences*, pages 312–358. Springer-Verlag New York.

Schwarz KP and Wei M (1995). Some unsolved problems in airborne gravimetry. In: Sünkel H and Marson I, (eds.), *Proceedings of the IAG International Symposium 'Gravity and Geoid'*, volume 113 of *IAG Symposia*, pages 131–150, Graz, Austria.

Swain CJ (1996). Horizontal acceleration corrections in airborne gravimetry. *Geophysics*, 61: 273–276.

Teunissen PJG (2000). *Testing theory, an introduction*. Delft University Press.

Thompson LGD and LaCoste LJB (1960). Aerial gravity measurements. *Journal of Geophysical Research*, 65(1): 305–322.

Timmen L, Bastos L, Forsberg R, Gidskehaug A, Hehl K, and Meyer U (1998). Establishment of an Airborne Geoid Mapping System for Coastal Oceanography (AGMASCO). In: *Proceedings of the 3rd Marine Science and Technology Conference*.

Tscherning CC, P.Knudsen, and R.Forsberg (1994). Description of the GRAVSOFT package. 4th ed, Geophysical Institute, University of Copenhagen.

Tscherning CC and Rapp RH (1974). Closed covariance expressions for gravity anomalies, geoid undulations and deflections of the vertical implied by anomaly degree variance models. OSU report 208, Department of Geodetic Science and Surveying, Ohio State University, Columbus, Ohio.

Tsuboi C and Fuchida F (1938). Relations between gravity values and corresponding subterranean mass distribution. *Bull. Earthquake Res. Inst. Tokyo*, 15: 636–649.

Valliant HD (1992). The Lacoste & Romberg air/sea gravimeter: an overview. In: *CRC Handbook of Geophysical Exploration at Sea, Hydrocarbons*, The LaCoste & Romberg air/sea gravimeter: an overview. CRC Press, 2nd edition.

Van Kann F (2004). Requirements and general principles of airborne gravity gradiometers for mineral exploration. In: Lane RJL, (ed.), *Airborne Gravity 2004 - Abstracts from the ASEG-PESA Airborne Gravity 2004 Workshop*, volume 2004/18 of *Geoscience Australia Record*, pages 1–5.

Van Loon JP (2008). *Functional and stochastic modelling of satellite gravity data*. PhD Thesis, Publications on Geodesy, 68. Netherlands Geodetic Commission, Delft.

Vaníček P and Kleusberg A (1987). The Canadian geoid - Stokesian approach. *Manuscripta Geodaetica*, 12: 86–98.

Wei M (1999). From airborne gravimetry to airborne geoid mapping - Report of SSG 3.164. In: Forsberg R, (ed.), *Determination of the gravity field. Report of IAG section III*, pages 25–32. Danish National Survey and Cadastre (KMS), Copenhagen.

Wei M and Schwarz KP (1997). Comparison of different approaches to airborne gravimetry by strapdown INS/DGPS. In: Sagawa J, Fujimoto H, and Okubo S, (eds.), *Proceedings of the IAG International Symposium 'Gravity, Geoid and Marine Geodesy'*, volume 117 of *IAG Symposia*, pages 155–162, Tokyo, Japan.

Wei M and Schwarz KP (1998). Flight test results from a strapdown airborne gravity system. *Journal of Geodesy*, 72: 323–332.

Wenzel G (1998). Ultra high degree geopotential models GPM98A, B and C to degree 1800. In: *Proceedings of the Joint Meeting International Gravity Commission and International Geoid Commission*, Trieste, Italy.

Wong L and Gore R (1969). Accuracy of geoid heights from modified Stokes kernels. *Geophys. J. R. astr. Soc.*, 18: 81–91.

Xu G, Hehl K, and Angermann D (1994). GPS software development for aero-gravity: Realization and first results. In: *Proceedings of the 7th International Technical Meeting of the Satellite Division of the Institute of Navigation 'ION GPS-94'*.

Xu G, Schwintzer P, and Reigber C (1998). KSGSoft (Kinematic/Static GPS Software) - software user manual. Scientific Technical Report STR98/19, GeoForschungsZentrum Potsdam.

Xu G, Schwintzer P, Timmen L, and Bastos L (1997). GPS kinematic positioning in AGMASCO campaigns - strategic goals and numerical results. In: *Proceedings of the 10th International Technical Meeting of the Satellite Division of the Institute of Navigation 'ION GPS-97'*, pages 1173–1184.

Xu P (1992a). Determination of surface gravity anomalies using gradiometric observables. *Geophysical Journal International*, 110: 321–332.

Xu P (1992b). The value of minimum norm estimation of geopotential fields. *Geophysical Journal International*, 111: 170–178.

Curriculum Vitae

Bas Alberts was born in Almelo, The Netherlands on February 8, 1977 and grew up in Borne. From 1989 to 1995 he attended secondary school at the Twickel College in Hengelo, after which he moved to Delft to study Geodetic Engineering at the Delft University of Technology. In 2000 he did a three-month internship at the University of New Brunswick, where he was involved in the precise determination of the Canadian geoid. He graduated from Delft University of Technology in 2002 on the topic of geoid determination from airborne gravimetry. For his MSc thesis he compared several integral methods with least-squares collocation for the inversion of airborne gravity data. From September 2002 to March 2003 he extended this study as a Research Associate at the Delft Institute of Earth Observation and Space Systems. After this period he prolonged his stay in Delft and started his PhD at the same research group. From the beginning of 2008 until June 2009 he worked as a Postdoctoral Fellow on the Gravimetry using Airborne Inertial Navigation (GAIN) project, for which he adapted pre-processing software and developed algorithms for attitude determination using GPS and INS data. He has been working at TerraImaging B.V. in Utrecht as Specialist Geodesy and Remote Sensing since August 2009.